ENERGY ANALYSIS OF BRITTLE FRACTURE AND ITS APPLICATION TO ZIRCONIUM OXIDE CERAMICS

By

TOMASZ B. TROCZYNSKI, B.Eng., M.Sc.

A Thesis

Submitted to the School of Graduate Studies

in Partial Fulfilment of the Requirements

for the Degree

Doctor of Philosophy

McMaster University

January 1987

ISBN 0-315-40271-7

Moim Rodzicom

ENERGY ANALYSIS OF BRITTLE FRACTURE AND ITS APPLICATION TO ZIRCONIUM OXIDE CERAMICS

DOCTOR OF PHILOSOPHY (1987) McMASTER UNIVERSITY
(Materials Science) Hamilton, Ontario

TITLE : Energy Analysis of Brittle Fracture and Its Application to Zirconium Oxide Ceramics

AUTHOR : Tomasz B. Troczynski
B.Eng. (University of Mining and Metallurgy, Krakow, Poland)
M.Sc. (University of Mining and Metallurgy, Krakow, Poland)

SUPERVISOR : Professor P.S.Nicholson

NUMBER OF PAGES: x, 225 (text volume)
ix, 139 (illustrations ~~volume~~)

ABSTRACT

An energy approach to fracture of ceramics was undertaken and refined to account for a nonelastic behaviour of these materials. A chevron-notched (CN) four-point bend specimen was recognized as effective experimental arrangement for room and elevated temperature tests. Consequently, a number of theoretical studies of the specimen's performance were undertaken. Modelling of the variation of the strain energy release rate with the crack extension revealed that the subcritical crack growth in a CN specimen causes dependence of the measured fracture parameters on the experimental procedure. Fracture toughness depends on the stressing rate and stiffness of the testing system. Work-of-fracture depends additionally on the crack length, explaining the phenomenon of decreasing effective surface energy with the crack extension. It appears that, as complete fracture is approached (i.e. 100 % of the specimen's cross-section), the measured work-of-fracture approaches that required for crack initiation. An electrical potential drop technique for crack length measurement in the CN specimen was developed for elevated temperatures fracture studies in the ionically conducting zirconium oxide ceramics.

The resistance-to-fracture versus crack extension was determined for a range of temperatures (25 to 1300 °C) for stabilized zirconias and their HfO_2 solid solutions and with second phase β-Al_2O_3 particles dispersed in them. The room temperature results agreed with the literature data and model predictions. Above 1000 °C an energy input of ~1 J/m^2 is required to drive the crack through zirconium oxide ceramics. Viscoelastic effects and crack interaction with β-Al_2O_3 particles result in a total fracture energy dissipation two orders of magnitude higher.

ACKNOWLEDGEMENTS

I would like to express my sincere appreciation to my supervisor, Professor P.S.Nicholson, for his support, guidance, encouragement and friendship.

I am grateful to the members of my committee, Drs D.S.Wilkinson and R.Sowerby, for their advice as to the direction of my work.

Financial support from the National Research Council of Canada and from the Department of Materials Science and Engineering is gratefully acknowledged.

TABLE OF CONTENTS

Page

CHAPTER 1 Introduction.....1

CHAPTER 2 Literature Review.....4

2.1 Brittle Fracture.....4

2.1.1 General Characteristics.....4
2.1.2 Linear Elastic Fracture Mechanics.....11
2.1.3 Fracture Stability.....18
2.1.4 The Microstructural and High Temperature Aspects of Fracture....22

2.2 Zirconium Oxide Ceramics.....34

2.2.1 Materials Development.....36
2.2.2 Toughening Modes.....42

2.3 The Chevron-Notched Four Point Bend Test Specimen.....46

2.4 Theoretical Aspects of Experimental Design and Procedure.....55

2.4.1 Materials Choice and Characterization.....56

2.4.1.1 Zirconia-Hafnia Solid Solutions....56
2.4.1.2 Zirconia-β-Alumina Composites.....57
2.4.1.3 X-Ray Phase Analysis.....58
2.4.1.4 Elastic Modulus Determination.....62

2.4.2 Fracture Testing System and Specimen Design.....68

CHAPTER 3 Theoretical Studies of the Chevron-Notched Beam Bend Specimen.....73

3.1 Subcritical Crack Growth in a Constant Displacement Rate Test.....74

3.1.1 Model and Numerical Analysis.....76
3.1.2 Implications for the Fracture Toughness Test.....80
3.1.3 Implications for the WOF Test.....86

3.2 The Load Relaxation Technique.....92

3.2.1 Model and Calculations.....93
3.2.2 Discussion of Results.....95

3.3 The Electrical Potential Drop Technique to Follow Crack Growth.....99

3.3.1 Plane Solution for Potential Drop in a Notched Conductor.....100
3.3.2 Chevron-Notched Specimen.....102
3.3.3 Sensitivity Analysis of the Potential Drop Method.....108

CHAPTER 4 Experimental Procedure.....112

4.1 Materials Fabrication and Characterization.....112

4.1.1 Zirconia-Hafnia Solid Solutions...112
4.1.2 Zirconia-β-Alumina Composites.....115

4.2 Preparation of Samples for Fracture Test.....116

4.3 Calibration of the Fracture Mechanics Techniques.....118

4.3.1 Compliance Analysis.....118
4.3.2 Use of the Potential Drop Technique for Crack Length Determination.....122

4.4 Fracture Test at Room Temperature.....131

4.5 Fracture Test at Elevated Temperatures....136

4.6 The Determination of Phase Composition and Elastic Modulus of the Zirconia Ceramics.....141

4.7 Model Fracture Experiments with Graphite.....144

4.8 Errors in Determination of the Crack Driving Force.....146

CHAPTER 5 Results and Discussion.....157

5.1 Materials Characterization.....157
5.1.1 Zirconia-Hafnia Solid Solutions....157
5.1.2 Zirconia-β-Alumina Composites.....162

5.2 The Resistance-to-Fracture at Room Temperature Determined via the Load-Fracture-Unload Technique.....165

5.2.1 Zirconia-Hafnia Solid Solutions....165
5.2.2 Zirconia-β-Alumina Composites.....171

5.3 The Resistance-to-Fracture at Room Temperature Determined via Load Relaxation Techniques.....177

5.4 The Resistance-to-Fracture at Elevated Temperatures.....182

5.4.1 Zirconia-Hafnia Solid Solutions....182
5.4.2 Zirconia-β-Alumina Composites.....187

CHAPTER 6 Conclusions and Recommendations for Future Work.....200

APPENDIX 1 Numerical Techniques for Compliance Analysis.....208

APPENDIX 2 Numerical Techniques for Potential Drop Analysis.....210

APPENDIX 3 Numerical Techniques for Room Temperature Fracture Tests.....213

APPENDIX 4 Numerical Techniques for Elevated Temperatures Fracture Tests.....215

APPENDIX 5 Symbolic Names of the Synthesized Materials...216

REFERENCES.....217

PLEASE NOTE : Illustrations are provided in a separate volume.

LIST OF MAIN SYMBOLS

a	crack length
A	crack area
b	crack front length
B	specimen depth
C	relative interprobe distances (C_1,C_2,C_3) ; compliance
d	density ; interprobe distance (2d)
D	displacement
E	Young's modulus (E_s static, E_d dynamic)
f	volume fraction
G	strain energy release rate ; crack driving force
H	interprobe distances H_1, H_2, H_3; summation function H(x)
h	thickness
I	geometric factor for CN specimen, I(x)
k	stiffness constant ; sheer correction factor
K	stress intensity factor
L	bending arm
m	compliance ratio
M	integer number
n	bend span ratio ; integer number
P	load ; numerical factor in PD technique (P_1, P_2, P_3)
Q	relative voltage drop , U(0)/U(x)

R	resistance to fracture (R_e, R_n, R_i) ; electrical resistance
S	bend span (S_1, S_2)
t	time
T	temperature
U	voltage drop ; energy
W	specimen width ; work of fracture (W_e, W_n)
v	velocity
x	relative notch length (x_0, x_1, x_i)
y	interprobe distances (2y,2y')
Y	geometric factor
Z	geometric factor for CN specimen , Z(x)
α, β, θ, ω, ϕ	angles
Γ	surface energy
η	viscosity
ν	Poisson's ratio
τ	time

CHAPTER 1

INTRODUCTION

The most useful properties of ceramics (high temperature strength, chemical inertness and hardness at low density) are accompanied by brittleness. This is still the main factor limiting widespread application of ceramic materials. Brittle fracture is determined by the type of atomic bonding in the ceramic and this in turn characterizes the lattice response to the applied stress in a given environment. At a certain critical stress level, bonds start to break before plastic deformation can take place. The challenge is to develop additional modes of fracture energy consumption in ceramics and thus decrease their brittleness (i.e. increase their strength and their toughness).

One of the proposed solutions is the formation of a so called "process zone" close to the crack tip. The process zone involves crack-microstructure interactions, microcracking, transformation toughening etc. The latter two phenomena have been intensively studied for zirconium oxide ceramics over the past decade. Employment of the stress-induced ZrO_2 phase transformation in the process zone results

in the material toughness approaching that of brittle metals. Structural application of zirconium oxide ceramics however requires retention of the toughness and load-bearing capacity to high temperatures (1000 to 1300°C). Presently the enhanced properties disappear at 500°C. Some solutions to this problem are explored in this thesis.

The modern approach to brittle fracture has followed the Griffith analysis performed more than 60 years ago. Since that time standarization of fracture testing routines has been proposed within the framework of fracture mechanics. In particular, the critical value of stress intensity factor, K_{IC}, is recognized as an intrinsic material parameter. The stress intensity approach to the fracture of inhomogenous ceramics is complicated by microcracking, process-zone genesis, crack-particle interactions and high temperature viscous phenomena. The global energy balance approach or comparison of the crack driving force with the material's resistance to fracture results in a more realistic description of the failure of complex ceramic systems.

The purpose of this thesis is to investigate the fracture characteristics of the new class of zirconia ceramics via the energy approach at room and elevated temperatures. Chevron notched, four point bend specimens were chosen as the optimal configuration for fracture testing. A number of original theoretical and experimental tasks were undertaken, i.e.;

1. an investigation of the effect of subcritical crack growth on the experimental fracture toughness and work-of-fracture tests.
2. the application of the load-relaxation technique to chevron-notched specimens.
3. the utilization of an electrical potential drop technique to monitor high temperature crack growth in chevron-notched conductive ceramic specimens.
4. the high temperature toughening of partially stabilized zirconia ceramics by solid solution and ceramic particle dispersions was investigated.

Theoretical analyses and models were compared with experimental data and a clearer understanding of the fracture of ceramic materials at low and elevated temperatures has emerged.

CHAPTER 2

LITERATURE REVIEW

2.1 Brittle Fracture

2.1.1 General Characteristics

A fracture is brittle when it is not accompanied by permanent deformation of the material. This broad definition merely presents our day-to-day understanding of the process and does not describe the amount or extension of "acceptable" permanent deformation. It is usually assumed for ceramic materials, that the amount of plastic (viscous ; dislocation-active) deformation at the crack tip is negligible. Total permanent deformation of cracking ceramics, generally results from processes taking place far (in terms of interatomic distance) from the crack tip.

Brittle fracture can be considered as the cleavage of adjacent atomic planes. Observation of cracks in ceramics by high resolution transmission electron microscopy confirms this assumption. No plastic deformation has been detected within 10 nm of the crack tip for Si, Al_2O_3 and SiC fractured at room temperature [1,2]. The reverse process of crack healing, i.e. retraction, has also been observed, an impossible phenomenon for any irreversibly-deformed crack-tip

zone. Brittleness does not however exclude large strains, which have been estimated as ≤ 20 % at the crack tip [14], at the moment of the crack propagation.

If a pure "bond breakage" process is responsible for the fracture of brittle materials, it is valid to consider a discrete ionic lattice model. Modelling of this kind was first performed by Orowan in 1945 [3]. He approximated the force between atoms as a function of their separation by a sine wave and obtained a formula for the theoretical bonding strength of a solid as;

$$\sigma_{th} = (E \cdot \Gamma / a_0)^{0.5} \qquad (2.1)$$

where E is the Young's modulus, Γ the surface energy and a_0 the interatomic distance. Substitution into (2.1) of typical E, Γ and a_0 values ($10^{11} N/m^2$, $10 J/m^2$ and $10^{-10} m$ respectively) results in $\sigma_{th} \simeq 0.1E$. Observed values for the strength of ceramics are ≤ 0.001E. The discrepancy arises from ignorance of stress concentrations at defects in the solid [4]. If condition 2.1 is met at any point in a strained body, catastrophic fracture must initiate due to local instability [6]. This condition will most likely be met at the tips of flaws.

Global instability was considered by Griffith [4]. He proposed, that fracture of a brittle material occurs if the decrease of the potential energy of the system on crack

growth is larger than the requisite increase of surface energy. The unstable equilibrium of an elastic plate containing an elliptical crack of length $2c_G$ was analysed by balancing these two energy components and resulted in a critical applied stress, σ_G, of;

$$\sigma_G = [(2 \cdot \Gamma \cdot E)/(\pi \cdot c_G)]^{0.5} \qquad (2.2)$$

When the Griffith condition (2.2) is met, a crack will just start to move in an infinite homogeneous medium. Disturbance from this unstable equilibrium results in crack acceleration and the stress concentration at its tip approaches σ_{th}, heralding criticallity and uncontrollable fast fracture. At equilibrium (2.2) the released elastic energy is equal twice the thermodynamic surface energy 2Γ and thus fracture is a reversible (i.e.controllable) process. For any stress $\sigma > \sigma_G$ (or the crack length $c > c_G$ at $\sigma = \sigma_G$) fracture proceeds irreversibly by thermally-activated atomic jumps and the energy consumed is greater than 2Γ (the excess energy being dissipated as lattice vibrations).

Since the Griffith relation results in fracture initiation, it must be considered as only the necessary and not the sufficient condition for macroscopic body separation [5,6,7]. Confusion between the Griffith condition and the catastrophic fracture state has permeated numerous attempts to explain unusually high surface energy measurements in

fracture experiments and the phenomenon of subcritical crack growth. It must also be recognized, that the homogeneity assumption of elasticity theory fails at the atomic level and crack advance must be considered non-continuous.

A qualitative description of discrete crack propagation between the global and local instability states is provided by the lattice theories of fracture [8]. The authors consider the potential energy of a simplified, one dimensional model of a lattice and crack as a function of the crack length, (Figures 2-1A,B) *. The total potential energy is composed of that due to the external loading system, the strain energy of flexular bonds (spring elements in Fig. 2-1 A) and the cohesive bond energy. The variation of the system potential energy, U, resulting from the crack extension, a, is shown in Figure 2-1B. The "wavy" nature of the plot reflects local metastability sites separated by thermal activation barriers for one atomic distance crack jumps. At $a=a_0$ the thermal activation barriers for crack growth and retreat are equal and equilibrium (i.e. the Griffith condition) is maintained. At this moment the crack driving force, G, is exactly balanced by the resistance force, 2Γ, i.e. $G=G_0$. As the crack grows, the thermal activation barrier decreases and finally vanishes at $a=a_+$ (or $G=G_+$). At this moment spontaneous fracture takes place due to local instability conditions. In

---

* Illustrations are presented in a separate volume.

terms of modern fracture mechanics (discussed in subsequent paragraphs) this moment coincides with the attainment of the critical value of the stress intensity factor, K. Spontaneous closure can take place as the crack heals towards a_- (Fig.2-1 B). For $a_+ > a > a_-$ fracture proceeds subcritically in a "lattice trapped" regime. It is one of the purposes of this thesis to study this regime and its complication by a number of crack-microstructure interactions at elevated as well as at room temperatures.

Another important consideration for even such a simple one-dimensional model of fracture, is the kinetics of the process. If the standard Arrhenius analysis for a thermally activated reaction is applicable, the exponential law for subcritical crack growth velocity, v, emerges, i.e.;

$$v = \alpha[\exp(U_+/kT) - \exp(U_-/kT)] \qquad (2.3)$$

where U_+ and U_- are the thermal activation energies for crack advance and retreat respectively, k is the Boltzmann constant, T the absolute temperature and α a proportionality constant. The thermofluctuation mechanism of fracture, expressed by (2.3), has been proven experimentally for a large number of materials [9]. Subcritical crack growth in ceramics can also be described by an empirical power law which is more amenable to analytical treatment [10,11,12]:

$$v = \beta \cdot G^{N/2} \qquad (2.4)$$

where G is the crack driving force, N is an empirical parameter and β is a proportionality constant.

Although the lattice model explains subcritical crack growth irrespectively of environmental effects, ceramic behaviour is especially sensitive to chemical interactions at crack tips [10,11,12]. The extensive experimental evidence of environmentally-assisted subcritical crack growth in glass and ceramics has been modelled by the discrete lattice and chemical reaction rate theories [13,14]. It is suggested, that the corrosive environment lowers the forward-motion activation energy barrier, U_+, and raises the retreat barrier, U_-. The crack is lattice trapped at a lower applied stress. Equivalently, the surface energy is lowered to that of a chemically reacted surface. The crack driving forces for spontaneous fracture or healing are lowered.

Brittle fracture and subcritical crack growth were recently reviewed by Maugis [15]. It is suggested, that the Griffith condition only applies to the equilibrium crack and cannot describe the critical (fast) fracture event. The crack tip front is modelled as the perimeter of a contact area between two elastic solids and the crack growth kinetic law is expressed as;

$$G - 2\Gamma = 2 \cdot \Gamma \cdot f_T(v) \qquad (2.5)$$

$$G = d(W - U_e)/dA \qquad (2.6)$$

where G is the strain energy release rate (i.e. the crack driving force), Γ is the surface energy, $f_T(v)$ is a function of the crack velocity, v, at temperature T, W is the external work and U_e is the stored elastic energy (kinetic energy is neglected).

Equation (2.5) states that the crack tip dissipation energy (or losses, $G - 2\Gamma$), is proportional to the work of adhesion, 2Γ, and a crack velocity function of the form $v^{1/N}$ (following equation 2.4). The losses are related to viscoelastic processes at the crack tip which are reflected by the frequency dependence of the imaginary part of the Young's modulus, i.e. the loss modulus. As the frequency of bond breaking events increases (or the crack velocity increases), the viscoelastic dissipation and loss modulus decrease. Effectively, the material tends to be more elastic (brittle) and thus the resistance to fracture decreases. As a result, sudden crack acceleration from subcritical velocities v_s, (10^{-8} to 10^{-3} m/s) to the critical velocity v_c ($\geq$ 1 mm/s) takes place and catastrophic rupture follows.

It has been emphasized throughout the above discussion, that the Griffith equilibrium fracture condition must be differentiated from the critical, fast fracture condition. Nondifferentiation leads to the ambiguous characterization of the material properties in terms of a single

"work-of-fracture" test. The energy calculated from the area under the load-displacement curve of a stressed sample depends on the experimental conditions and cannot be directly related to the material's resistance-to-fracture. Some aspects of this pro blem will be discussed in Chapter 3.

The search for a single material parameter characterizing its resistance-to-fracture has resulted in the development of an approach based on linear elastic fracture mechanics (LEFM). Highlights of this discipline will now be discussed.

2.1.2. Linear Elastic Fracture Mechanics

The discipline which considers crack extension behaviour as a function of applied load is called fracture mechanics. If it is based entirely on linear elastic theorems it is called linear elastic fracture mechanics (LEFM). The fundamentals of modern LEFM originate from the works of Irwin [16,17],but the basic concept is the Griffith theory [4]. The idea that the crack driving force is the strain energy release rate G (eq. 2.6) was introduced by Irvin and Kies. In 1954 it was shown [17], that G is equivalent to an elastic force exerted on a crack by an external stress, so the mechanical compliance is related to G, i.e.;

$$G = 0.5 \cdot P^2 \cdot dC/dA \qquad (2.7)$$

$$C = D/P \qquad (2.8)$$

where P is the load, C the mechanical compliance defined via the load application point displacement D at unit load (eq. 2.8) and A is fracture area. When the Griffith condition is attained, $G=G_0=2\Gamma$ and at the catastrophic fracture point, $G=G_C=2\Gamma_e$, where $2\Gamma_e$ is the "effective" surface energy which includes plastic dissipation terms.

A parallel approach, characterized as the "stress-intensity approach" was suggested by Westergaard in 1939 [18]. The crack was modelled as an infinitely sharp slit in a continuum, with walls free of tractions at all stages of loading. The crack tip stress concentration is calculated according to linear elasticity theory assumptions, for three types of loading (opening mode n=I, sliding mode n=II and tearing mode n=III), Fig.2-2A. The general solutions for the near-tip stress field, σ_{ij}, (Fig.2-2B) can be approximated as;

$$\sigma_{ij} = [K_n/\sqrt{(2\pi r)}] \cdot f(\theta) \qquad (2.9)$$

where r is the distance from the crack tip, K_n is the stress intensity factor describing the magnitude of the crack tip stress field in a homogenous linear elastic material for mode n and $f(\theta)$ is an angular function [19], Fig 2.2B. For most loading configurations K_n can be expressed as;

$$K_n = \sigma_a \cdot \sqrt{a} \cdot Y(a) \qquad (2.10)$$

where σ_a is the externally applied stress, a the crack length and Y(a) is a "geometric factor", a function of both crack length and the loading conditions. The assumption of complete homogeneity results in an unrealistic stress singularity at the crack tip (r=0). This inconsistency has been approached by considering a finite crack volume and the crack tip radius [7,20,21].

The relationship between the stress intensity and the strain energy release approaches was shown in 1957 by Irwin [22]. The G and K parameters are related through the elastic properties of the material i.e. for plane stress mode I loading;

$$G_I = K_I^2/E \qquad (2.11)$$

and for plane strain mode I loading (valid for most ceramics)

$$G_I = (1 - \nu^2) \cdot K_I^2/E \qquad (2.12)$$

where ν is the Poisson's ratio and E the Young's modulus. G at the onset of rapid crack propagation is called G_C, the "cri tical-strain-energy-release-rate" (equivalent to G_+ of the lattice concept), or the "fracture toughness", a central concept resulting from LEFM.

Since a negligibly short subcritical crack growth period was assumed, the critical condition has been frequently

treated as the Griffith condition. Modern fracture mechanics results, in large degree, from the works of Srawley and Brown. They questioned the validity of "rapid" crack propagation at $G=G_C$ as an intrinsic material parameter [23]. Instead, the maximum recorded load and the corresponding crack length were proposed as parameters for fracture toughness calculation (from eq. 2.10). These parameters are experimentally dependent however and the resulting G_C does not have clear physical meaning [15].

Irwin and Paris [24] considered the crack velocity versus the driving force, Fig.2-3. It is recognized that the crack can propagate in a stable manner slowly (branch AB) or quickly (branch CE). Unstable propagation takes place at the critical condition $G=G_C$ (branch BC). The kinetics of crack propagation can be modified by the environment, as discussed in the previous paragraph.

In the case of a number of external stresses acting on a body, the corresponding stress intensity factors can only be superimposed for the same mode of crack opening, i.e.;

$$K_I = \Sigma K_{Ii} \quad , \quad K_{II} = \Sigma K_{IIi} \quad \text{etc.}$$

The strain energy release rates for <u>any</u> mode can be superimposed [25], i.e.;

$$G = G_I + G_{II} + G_{III} \tag{2.13}$$

Equation (2.13) suggests, that the G-parameter approach to fracture toughness facilitates a better description of crack propagation under non-ideal (real) conditions under the influence of mixed mode stresses. Ceramics are inherently inhomogenous and crack-microstructure interactions result in mixed-mode fracture. The overall crack driving force is therefore best expressed by (2.13), with unknown particular terms. Direct conversion of the strain energy release rate into a particular mode of stress intensity factor is thus impossible. The local variation of elastic modulus further precludes this conversion.

Fracture mechanical techniques are further complicated if the volume of nonelastically deformed material cannot be neglected compared with the total volume of the body. Since the crack is only driven by the potential energy of the loading system and the strain energy released from the specimen, any irreversible deformation must be excluded from the energy balance [26]. Orowan [27] proposed, that the amount of plastic work , $2\Gamma_p$, per unit increase of crack area, is much larger than the Griffith surface energy so the effective surface energy $2\Gamma_e \simeq 2\Gamma_p$. This transition however is not justified within the framework of LEFM. Even if the plastic zone is minimized in the test specimen, the energy parameter G_C is more meaningful than the derived value of K_C [26].

The application of LEFM is questionable for elastic-

plastic fracture. The global energy balance is a reliable method for analysis of this type of fracture. Eftis and Liebowitz [28] proposed that the external work W is redistributed into stored elastic energy, U_e, dissipated plastic energy, U_p, and effective surface energy Γ_e of a newly created crack area A if the kinetic and residual strain energies are neglected, i.e.;

$$dW/dA = dU_e/dA + dU_p/dA + d\Gamma_e/dA \qquad (2.14)$$

Evans et al. [29] pointed out, that the energy balance (2.14) should contain a phonon energy term associated with the stress waves emitted by the propagating crack. It is assumed at the present stage of analysis and throughout this thesis, that the phonon energy is included in Γ_e.

Comparing (2.14) with the expression for the strain-energy-release-rate from an elastic body, (2.6), the nonlinear crack growth resistance parameter, R, can be defined as;

$$R = dU_p/dA + d\Gamma_e/dA \qquad (2.15)$$

Since $d\Gamma_e/dA$ is the only term responsible for the crack extension (dU_p/dA being dissipated irreversibly into permanent deformation of the body), it will be termed the "Resistance-to-Fracture", R_e in this thesis. The balance, dU_p/dA will be termed the "Nonelastic-Energy-Dissipation-

Rate", R_n and the resistance to fracture will be calculated from;

$$R_e = R - R_n = d(W - U_e - U_p)/dA \qquad (2.16)$$

The analysis of Eftis and Liebowitz was applied to the investigation of nonlinear fracture parameters of graphite and silica refractories by Sakai et al. [32] and Sakai and Bradt [31] . The method involved the retrieval of R_e and R_n from the load-displacement diagrams of repeated load-stable fracture-unload experiments, Figure 2-4. The work performed in each cycle of loading (branch OI)-stable fracture(IN)-unloading(NS) can be divided into the nonelastically dissipated energy W_n (i.e. loop ON'TMNS) and the energy converted into new surface area W_e, (loop OITN'O). If the fracture surface increment in a given cycle is ΔA, the non-elastic energy dissipation rate, R_n, and the resistance to fracture, R_e, are defined as;

$$R_n = W_n/\Delta A \qquad (2.17)$$

$$R_e = W_e/\Delta A \qquad (2.18)$$

The present author believes, that this nonlinear generalization of the fracture mechanical approach should be applied to apparently-elastic ceramic materials,especially if

microcracking or R-curve behaviour is expected or high temperatures are involved.

As will be shown in future chapters, R_n cannot be neglected in the fracture energy analysis for certain ceramics. Therefore the approach proposed by Eftis and Liebowitz, and continued by Sakai and Bradt, will be employed and refined in this thesis.

2.1.3. Fracture Stability

The global energy balance as presented in the previous section, requires that the kinetic energy of the system is negligible during crack growth . Such is the case when the crack propagates slowly and does not accelerate. Fracture stability can be analysed by considering the variation of total energy of the system, U, as a function of the fracture area A. At the equilibrium point, as discussed before (compare eq. 2.14) ;

$$dU/dA = dU_e/dA - dW/dA + dS/dA = 0 \qquad (2.19)$$

where U_e is the stored elastic energy, W is the external work and S the energy stored in the newly created surface. This equilibrium is unstable if U reaches a maximum (the case considered by Griffith, [4]) and at that point, $d^2U/dA^2 < 0$. Stable equilibrium requires U be a minimum so $d^2U/dA^2 > 0$. Any displacement from stable equilibrium results in an increase of the total energy, U, and thus requires an increasing

flux of external work. From the definition of the strain energy release rate, $G_I = d(W-U_e)/dA$, and the resistance to fracture R;

$$R = dS/dA \qquad (2.20)$$

equation (2.19) can be rewritten as;

$$dU/dA = R - G_I \qquad (2.21)$$

Therefore stable fracture requires;

$$dR/dA > dG_I/dA \qquad (2.22)$$

Analysis of the slopes of G_I vs. A and R vs. A curves identifies the range of the crack growth stability.The general condition for stable fracture can be obtained by expressing equation (2.19) in terms of the load P, the load application point displacement D, and the mechanical compliance of the specimen, C = (D/P), [30];

$$dU_e = 0.5 \cdot d(P \cdot D) = P \cdot C \cdot dP + 0.5 \cdot P^2 \cdot dC \qquad (2.23)$$

$$dW = P \cdot dD = P^2 \cdot dC + P \cdot C \cdot dP \qquad (2.24)$$

Substitution of 2.23 and 2.24 into definition (2.6)

results in the expression for the strain energy release rate given in (2.7).

If the fracture resistance curve is flat, i.e. dR/dA=0 (the worst case as far as fracture stability is concerned), substitution of (2.23,2.24) into (2.19) followed by differentiation results in ;

$$d^2U/dA^2 = -0.5\cdot(P\cdot d^2D/dA^2 - D\cdot d^2P/dA^2) \qquad (2.25)$$

If the displacement is written in terms of the compliance, then eq. (2.8) gives;

$$d^2U/dA^2 = -dG_I/dA = -0.5\cdot(P^2\cdot d^2C/dA^2+2\cdot P\cdot dP/dA\cdot dC/dA) \qquad (2.26)$$

Stable crack growth requires, that the bracketted terms of eq. (2.25,2.26) be < 0. Bluhm [119] pointed out that C in equation (2.26) must be considered as the total compliance of the testing system, i.e. the sum of the compliance of the specimen, C_S, and that of the machine, C_M. Thus the machine stiffness is incorporated into the analysis.

The fracture stability depends strongly on the loading arrangement. The two limiting cases thereof are constant load and constant displacement ("fixed grips"), Figure 2-5. For conditions of constant load (path OAB) the crack propagates at dP=0, so the bracketted term of eq. (2.26) reduces to the strongly positive term, $P^2\cdot d^2C/dA^2$, and

fracture is always unstable. There is no such simple answer for the fixed grips test (path OAD_0 for an infinitely stiff machine, path OAD_1 or OAD_2 for $C_M>0$). Even if no energy is stored in the testing system, i.e. $C_M=0$ and $dD=0$, the bracketted term of eq. (2.25) reduces to $-D\cdot d^2P/dA^2$. Manipulation of the compliance definition $P(A)=D(A)/C(A)$, gives $dP/dA = -D\cdot dC/dA\cdot C^{-2}$ and thus;

$$d^2P/dA^2 = -D\cdot C^{-2}\cdot[d^2C/dA^2 - 2\cdot C^{-1}\cdot(dC/dA)^2] \qquad (2.27)$$

i.e. the stability is determined by the competing terms of the compliance function.

It should be noted, Fig.2-5, that the strain energy stored in the specimen decreases (respective triangles OAD_0, OP_0D_0 etc.) in the load relaxation test, whilst it increases in the constant load test (respective triangles OAD_0, OBD_p etc.). Similarily, a specimen of compliance C_S, tested on a system of increasing softness $C_M=0$, C_{M1}, C_{M2} etc. (up to $C_M=\infty$ for the constant load test), would be loaded to $P=P_0$, P_1, P_2 etc. (up to P_C). Since $P_0<P_1<P_2<\ldots\ldots<P_C$ and $G_I \propto P^2$, the strain energy release rate increases as the testing system compliance increases and thus fracture is destabilized.

The above discussion demonstrates the advantage of the fixed grips loading configuration. A detailed analysis of the stability of the chevron-notched, four-point-bend bar was

presented by Bluhm [119] and recently by Troczynski and Nicholson [112]. These results will be discussed in Section 3.2.

The existence of fracture stability is an important part of experimental design. Virkar and Gordon [33] showed that suitable specimen configurations can be determined by compliance analysis. In the present thesis, the chevron-notched four-point-bend specimen was chosen for most fracture tests. This configuration was crack-stability-verified over a range of experimental parameters and loading arrangements using numerical solutions of equations (2.26,2.27). The simulation programs involved and the results therefrom will be discussed in Chapter 3.

2.1.4 The Microstructural and High Temperature Aspects of Fracture

All ceramic materials contain a spatial distribution of structural and elastic inhomogeneities, which is sensitive to their synthesis history and campaign usage. The microstructural influences on the fracture properties of ceramic materials increase in complexity from glass and monocrystals to a variety of anisotropic polycrystals and composites.

A homogenous glass,i.e. the one without bubbles,inclusions and internal stresses, is an ideal material vis a vis LEFM techniques. A stable crack propagates through glass almost undisturbed [34]. As the crack velocity increases

however, the fracture surface becomes rough ("mist" and "hackle" zones respectively), resulting from crack branching at high crack velocities as the maximum local tension plane tends to twist [19,35]. It appears that the consecutive mirror, mist and hackle zones correspond to an increasing crack tip stress intensity factor [35]. The apparent absence of such zones in many polycrystalline ceramics is the result of the grain structure effectively confining these zones to single grains.

The fracture of monocrystals is determined by their anisotropy and depends upon the orientation of the low fracture energy ("cleavage") planes versus the crack plane [35,36]. If a certain amount of plastic deformation occurs the fracture initiation energy can be loading-rate sensitive due to crack tip dislocation emission [36]. Generally the absence of crack-microstructure interactions in monocrystals is manifested by fracture energy values approaching the thermodynamic surface energy [37].

The next step towards real materials requires the introduction of a grain boundary into the crack propagation path. Such an obstacle can stop the crack,cause nucleation of a new crack in the second grain (i.e. transgranular cleavage) or along the grain boundary (intergranular fracture). In the two latter cases the crack most probably will twist (i.e. rotate about the propagation direction) or tilt (i.e. rotate about the crack front line) and the stress intensity experi-

enced by the crack tip will be reduced (for example, by 4 times for a twist of 60 degrees [38]). Even this simple description raises mixed-mode crack propagation questions and throws the single-mode stress intensity approach of LEFM into doubt. The energy analysis of the fracture process is therefore preferred.

Imposition in the crack path of a number of variable size grains, grain bounderies, pores, foreign inclusions (introduced purposedly or accidentally),local stresses caused by thermal expansion mismatch, elastic anisotropy and phase transformations extends the analysis into real ceramic materials. The complexity of the crack-microstructure interactions in such environments makes it impossible to apply any general model. Simplified approaches rely on semiempirical treatments (like the global energy balance treatment) or consideration of one phenomenon at a time ignoring numerous concurrent processes. The key factor to be considered is the scale of fracture events. The growth of natural flaws to critical size (in service, static fatigue or in a simple strength test) is determined by local microstructural conditions, especially local microstress distributions. This is quite different from the propagation of a large crack in a fracture mechanics test specimen which averages multitude of grains and grain boundaries [39,40].

Recently a systematic study was performed on the inert

strength characteristics of ceramics as a function of the flaw size relative to the grain size [42]. The crack size was controlled via a variable indentation load. It was assumed that the fracture toughness of a material, K_C, tends to the "polycrystalline" toughness K_C^{∞}, exclusively for cracks that are large compared with the grain size;

$$K_C^{\infty} = K_m + K_C \qquad (2.28)$$

where K_m represents the combined effect of microstructure on the stress intensity factor at the crack tip and is given by;

$$K_m = \mu \cdot Q/(a^{3/2}) \qquad (2.29)$$

where a is the crack length and $\mu \cdot Q$ is empirically defined as a "microstructural driving force".This assumption is born out by the experimental evidence [39]. It was shown analytically and experimentally [42] that the inert strength of indented specimens vs the indentation loads becomes constant when the size of the crack approaches the microstructural grain diameter (known as the microstructural-influence range). The apparent toughness in the small-crack-size-region (i.e. the microstructure controlled region), measured via the size of the indentation crack, varied substantially even for the same class of material. For certain glass-ceramics, the microstructural influence extended to cracks over 15 grain diame-

ter in size. These results suggest that the practice of gathering fracture toughness measurements from large-crack specimens and thereby predicting the response of natural flaws, should be re-examined.

A dramatic decrease of the apparent fracture energy vs. the size of the critical flaw was reported by Rice et al. for Al_2O_3, stabilized zirconias, MgF_2 and lead zirconate-titanate (PZT),[41]. This effect was attributed to the significant contribution of internal stresses to the failure stress as the critical flaw size approaches the grain size. The effect was particularly significant for non-cubic and multiphase materials.

The influence of grain size and shape and type of lattice on the fracture properties is directly related to the thermal expansion and elastic anisotropy. For cubic materials the variation of the crack path (the "wandering") was attributed to elastic anisotropy and was independent of the grain size [34]. The thermal expansion anisotropy of noncubic materials (e.g. Al_2O_3) leads to local grain boundary stresses and microcracking. Interaction of the main crack with these microcracks and local stress fields results in the grain size dependence of the fracture energy for non-cubic materials [43]. As the grain size increases, the local stresses and the microcrack density increases. The main crack interacts with local stress fields and triggers further microcracking and energy absorption in the "process zone"

close to the cracktip [44]. For larger grains however, the microcracks generate and link spontaneously, so providing easy propagation for the main crack. Effectively,a maximum is observed in the measured surface energy vs. grain size. This was treated theoretically by Fu and Evans [50] and reasonable agreement was obtained between the model predictions and the experimental results for Al_2O_3.

The density of the microcracks in the process zone was modelled by Hoagland at al [45,46]. These authors assumed, that the microcracks did not interact and they found that the microcrack density is independent of the loading conditions. Thus the additional energy dissipation mode should be simply proportional to the damage zone size [45]. A more advanced study [46] predicted an increasing fracture-resistance (R-curve) as a result of microcracking. Hasselman and Singh showed that microcracked materials exhibit increased thermal shock resistance [47].

The process zone concept can be considered as a "shielding" of the crack tip from the externally applied stress. The net effect is to supplement the local negative stress intensity factor K_{IP} [38] such that the crack propagates catastrophically at;

$$K_{IC} = K_{IA} + K_{IP} \qquad (2.30)$$

where K_{IA} is the stress intensity factor due to the

externally applied load (pure mode I fracture is assumed for simplicity). Formulation of the problem in this manner facilitates analysis of the crack interaction with the fibres of composite materials or with the crack tip compressive zones of transformation toughened ceramics [38]. The latter problem will be discussed in more detail in subsequent sections.

Second phase particles appear in ceramics naturally or intentionally (porosity, impurities, inclusions, particulate composites etc.). An exhaustive review of the effect of porosity on the effective fracture energy was undertaken by Rice [49]. If the pores are of regular shape and distribution, an empirical exponential law describes the decrease of fracture energy with porosity;

$$\Gamma = \Gamma_0 \cdot \exp(-b \cdot V_p) \qquad (2.31)$$

where Γ_0 is the fracture energy of a fully dense material, V_p is the volume fraction of pores and b is an empirical factor $\simeq 4$. It was pointed out however, that if the "pores" are microcracks, the effect is reversed due to additional fracture energy dissipation modes (discussed above).

The intentional introduction of second phase into ceramics results in a composite material. In most cases the thermal expansion mismatch between the surrounding matrix and the particles (fibres, rods, discs etc.) induces local stresses

within the inclusions and their vicinity. Davidge and Green [51] argued that the resulting maximum stress is independent of the inclusion size. If the total stored elastic energy equals the energy required to create crack surface, a critical microstructure arises and microcracks are generated in the vicinity of the particles.

Toughening by the microcracks induced by second phase particles was considered analytically by Evans and Faber [52]. These authors recognized that the presence of a variable microcrack density changes the compliance of the process zone and thus modifies the linear elastic stress intensity solution in an unknown fashion. The approach has been attempted wherein the total stored elastic energy is compared with the work required for circumferential fracture around ellipsoidal particles. Optimum toughening is predicted when the particles are of the same size as those required for spontaneous microcracking. This critical particle size depends on its shape, the fracture resistance of the particle-matrix interface, the elastic moduli of the particle and matrix and their thermal expansion coefficients.

A classical example of microcracking induced by non-thermal stresses is found in alumina-zirconia composites [53,54]. The microcrack zone extends ahead of the primary crack and develops due to dilatational strains accompanying the tetragonal-to-monoclinic phase transformation of the dispersed particles of zirconia [53]. Green [54] suggested

the optimum ZrO_2 level for maximum microcrack-induced toughening is 7 vol.%.The presence of microcracks in the composite material was indirectly detected by the dramatic decrease of the composite elastic modulus. A theoretical study by the same author [55] predicts maximization of the applied-stress-induced microcracking at second phase inclusions when the local fracture toughness is low and the size of the inclusions approaches the critical size for spontaneous microcracking.

Residual compressive stresses in the vicinity of monoclinic ZrO_2 inclusions which transformed from the tetragonal phase under the constraint of an Al_2O_3 matrix can serve as an effective surface strengthening agent [56]. 700 MPa of compressive stresses was detected on the surface of an Al_2O_3/30 vol.% ZrO_2 composite. This decayed to 100 MPa 20 μm below the surface.

Under favourable conditions, second phase inclusions can increase a material's fracture toughness by a crack deflection process. This phenomenon was studied theoretically [57] and expermentally [58,59] by Faber and Evans. The local stress intensity factors K_I, K_{II}, K_{III} were expressed as a function of the tilt and twist angle of the crack. The net driving force was calculated as an average value of the strain energy release rate $\langle G \rangle$;

$$E \cdot \langle G \rangle = (K_I^2 + K_{II}^2) \cdot (1-\nu^2) + K_{III}^2 \cdot (1+\nu) \qquad (2.32)$$

Comparison of <G> with the corresponding value for an undeflected crack,G, gave the toughening increment parameter n as;

$$n = \langle G \rangle / G \qquad (2.33)$$

It was shown that the crack tip driving force decreases independently of the particle size and is a function of the particle shape and volume fraction. Twisting of the crack seems the predominant source of toughening. Volume fractions of 10 to 20 % were found optimal. The theoretical predictions were verified qualitatively in experiments on Si_3N_4 and SiC [58,59]. As might be expected, the most significant crack deflection process was obtained in reduced grain-boundary fracture resistance materials.

The complexity of the crack-microstructure interactions in real ceramic materials at room temperature is far from the idealised picture given by the Griffith analysis and the simple single-mode stress intensity factor approach.

A number of additional phenomena can accompany the high temperature failure of ceramics [60]. Typically crack nucleation and propagation stages are involved frequently associated with viscous hole growth, cavitation and creep deformation. The nucleation, growth and coalescence of cavities at preffered microstructural sites depend upon the temperature and loading rate of the test. Accordingly, any microstructural modification that reduces the creep rate

should increase the lifetime of ceramics.

Irreversible deformation of ceramics at high temperatures, especially in the presence of an amorphous grain boundary phase, excludes analysis using the stress-intensity factor approach to failure analysis, extensively used by some researchers. Kromp and Pabst compared the results of the stress-intensity- factor and J-integral energy approaches for different types of alumina [61]. The K_{IC} values obtained from three point notch-bend bar fracture, were dependent on the experimental conditions. In particular, a maximum calculated K_{IC} value was obtained for a crosshead displacement rate of 2 mm/min. Loading-fracture-unloading cycles revealed time-dependent viscous flow of a grain boundary phase, grain slippage and crack closure. The fracture energy was calculated by estimating the crack extension from the unloading compliance. It was concluded [61, 162, 163] that the energy approach alone enables analysis of a fracture process accompanied by significant nonelastic deformation.

High-temperature crack propagation in ceramics can be described by a kinetic law (2.4), wherein the driving force varies between threshold (K_t) and critical values [164], N is close to the steady state creep exponent. In many ceramic materials a viscous grain-boundary phase controls rate of the crack growth. The externally applied driving force G is balanced by a surface tension, which is a function of the temperature and meniscus curvature, Fig. 2-6A, [164]. K_t for

alumina at 1400 °C was reported as 0.5 MPa$\sqrt{m}$ for intrinsic cracks and 1.5 MPa$\sqrt{m}$ for surface-induced indentation cracks, Fig. 2-6B, [164]. According to eq.(2.11), this would give G values of 1 and 7 J/m^2 respectively (for Al_2O_3 E≈300 GPa at 1400 °C [143]). It will be shown in the present thesis that similar values are obtained for zirconium oxide ceramics at 1300°C. It appears that the high-temperature fracture properties of aluminas and zirconias are determined by the grain-boundary glassy phase.

A number of crack-microstructure interactions take place in ceramic materials. Many of these are unpredictable or difficult to describe analytically. The problem is further complicated in ceramic matrix composites and by high temperature phenomena. These observations vindicate the semi-empirical approach taken in this thesis. The global energy balance will be applied to the analysis of high- and low-temperature fracture results for zirconia-based ceramics.

2.2 Zirconium Oxide Ceramics

Zirconium oxide has cubic (C) fluorite type structure stable between the melting point at 2680 °C and 2370 °C, a tetragonal structure (T) between 2370 °C and 1170 °C and a lower density monoclinic (M) structure below 1170 °C, Fig.2-7 [62]. The T ⇌ M transformation is athermal, fast and accompanied by large thermal hysteresis. This was observed by Wolten [63] who identified the martensitic character of the transformation. Further study by optical and electron microscopy revealed surface distortion, twinning and specific orientation relationships between the parent and product phases of the transformation, artifacts characteristic of shear type, diffusionless martensitic transformations [64,65].

The C ⇌ T transformation was studied recently by Heuer and Ruhle [66], who suggested it is massive in type and involves homogenous nucleation. The stability of the T and C phases can be extended by alloying the ZrO_2 with CaO, MgO, Y_2O_3 or simply by heating the ZrO_2 in a reducing environment [62,67]. Since both phenomena produce oxygen vacancies in ZrO_2, it was suggested, that the stabilization of the cubic phase is related to local structural relaxations around anion vacancies [62].

When the dopant concentration is less than that required for complete stabilization, a mixture of C and T phases result. This type of material was recognized by Garvie and Nicholson [68] and Garvie et al [69] as a potentially

transformation-toughened ceramic. Highly dispersed T precipitates (0.1 μm diameter) were grown within C grains at high temperatures and supercooled to room temperature without transformation to the M phase. It was argued that stabilization of the T phase arises from the constraint by the rigid C matrix and surface energy effects. A propagating crack or surface grinding removes these constraints and the T ⇌ M transformation is triggered. The powerful toughening which results from this process is the result of the ~4 % increase in volume involved (and the resultant compressive stress build-up around the crack tip) that accompanies the constrained T⇌ M transformation in ZrO_2.

Zirconium oxide ceramics have been intensively studied for fifteen years. Numerous attempts have been made to optimize the microstructure and mechanical properties of ceramics in the $MgO-ZrO_2$ [71-73], $CaO-ZrO_2$ [74,75], $Y_2O_3-ZrO_2$ [76-78] systems and recently of ZrO_2-containing ceramic matrix composites. The reduction of grain diameter in the sintered ceramics to submicron size and limitation of the amount of Y_2O_3 stabilizer to 2-3 mole% facilitates the synthesis of nearly 100 % tetragonal $Y_2O_3-ZrO_2$ solid solutions [79]. The strength of these materials, (the so called "tetragonal zirconia polycrystals" TZP) exceeds 1 GPa [78] and is by far the highest value ever obtained for a polycrystalline ceramic. It is predicted that the room temperature strength of refined TZP could reach 3 GPa ! [80]. The fracture toughness of the

strong TZP is only moderate (6 MPa√m) and decreases precipitously with temperature.

The point defect structure and concentration in stabilized zirconia is essentially fixed by its dopant content and is independent of temperature and the surrounding atmosphere [81].The introduction of X moles of M^{3+} ions in place of Zr^{4+} ions in the ZrO_2 lattice requires the balance of charge be redressed by X/2 moles of oxygen vacancies. At large dopant concentrations,the electrostatic attraction between the nega tively charged M^{3+} (with reference to lattice) and the ionized, positively charged oxygen vacancies interferes with the random defect distribution. Nevertheless, oxygen ions are transported through the vacancy network in an applied electric field and give a relatively high ionic conductivity to the zirconium oxide ceramics (in the range of 0.1 $\Omega^{-1}cm^{-1}$ at 1000 °C). This conductivity is independent of the oxygen partial pressure over several orders of magnitude and the transport number for oxygen ions is almost unity. The activation energy for this conduction is ~1 eV [62].

In this thesis a unique approach is utilised to the monitoring of crack growth utilising the high-temperature ionic conductivity of ZrO_2 ceramics. The details of the methods used are discussed in subsequent chapters.

2.2.1 Materials Development

Claussen [80] proposed a classification of existing zirconium oxide ceramics and their predicted future develop-

ment. He distinguished three classes; (A)-ceramics based on partially stabilized zirconia, (B)-dispersed zirconia-containing materials and (C)-complex zirconia systems inclusive of all other composites not fitting into (A) or (B). This classification allows partial or full substitution of ZrO_2 by HfO_2 in all cases. Group (A) covers the conventional stabilized zirconia ceramics, usually sintered into the cubic solid solution range at relatively high temperatures (1600-1800 °C) and thus of large grain size (~ 50 μm). The recently reviewed tetragonal-cubic phase field of the ZrO_2-Y_2O_3 system is shown in Fig.2-8, [78]. At 5 m% Y_2O_3 sintering in the cubic phase field can only proceed at T>1700 °C. Coherent tetragonal precipitates are nucleated during cooling and coarsen with ageing between 1300 and 1600 °C. The size of the tetragonal precipitates must be optimised to maximize the extent of the T → M transformation.

It is interesting to note that the solubility of Y_2O_3 in tetragonal ZrO_2 is much higher than either MgO or CaO in ZrO_2. This behaviour difference is attributed to the small ionic radius misfit between Zr^{4+} and Y^{3+}, as compared to that between Zr^{4+} and Mg^{2+} and Ca^{2+}. Consequently, the molar volume change when T-ZrO_2 precipitates from C-ZrO_2 is approximately zero for Y_2O_3-PSZ, whilst it is positive in MgO-PSZ and negative in CaO-PSZ [76]. The compatibility of the T and C-phases in Y_2O_3-PSZ is responsible for the high-temperature stability of this material. This is a reason that yttria-

stabilized ZrO_2 was chosen for the investigations reported in this thesis.

If stabilized zirconia compositions are sintered in the C+T coexistence phase field (2.5 to 7 mole % Y_2O_3 at 1450°C, Fig.2-8), the resulting microstructure contains characteristically large cubic grains, ~5 to ~10 μm size, surrounded by fine (<1 μm) tetragonal grains [82,83]. The content of the C and T phases is within the amounts predicted by the phase diagram, suggesting that equilibrium is reached during sintering. For an average Y_2O_3 content of 4.5 mole%, the C grains contain 7.1 mole% Y_2O_3 and T grains 3 mole%, [83]. This is close agreement with the equilibrium phase diagram.

Decreasing the Y_2O_3 stabilizer content to values such that sintering can be carried out in the single phase tetragonal field results in tetragonal zirconia polycrystals (TZP). In this case the stabilizer content must be limited to 2 to 3 mole% and the sintering temperature (~1400°C) maintained sufficiently low to prevent excessive grain growth. This means the green powder must exhibit significant reactivity at relatively low temperatures. Retention of the T phase at room temperature is only possible under the surface energy constraints imposed by small grains (0.1 to 1 μm).

TZP ceramic is presently considered the toughest and strongest of all ceramics at room temperature. It has been reported however, that it degrades in humid atmospheres at ~200°C [82]. It loses its superb mechanical properties at

moderate temperatures since transformation toughening is neutralised by the stability of the T phase above 500 °C in ZrO_2-Y_2O_3. Another factor limiting the high temperature application of TZP ceramics is the presence of an amorphous grain boundary phase [78].All 11 types of TZP studied in [78] contained a continuous,i.e. perfectly wetting, glassy layer, 2 to 100 nm thick, rich in Y_2O_3, SiO_2 and Al_2O_3. Some triple points at grain boundaries contained glassy pockets up to 100 x 100 nm in thickness. The glassy phase originates from the zircon ($ZrSiO_4$) mineral source of the ZrO_2. This phase aids sintering and final product densification. Grain boundary softening of this kind must be prevented for high temperature applications. With this in mind Claussen [80] has proposed crystallization of the glassy phase by annealing,the introduction of SiO_2 getters and reinforcement by fibres or refractory particles.

A controlled amount of highly dispersed monoclinic phase in zirconium oxide ceramics can activate other toughening mechanisms, i.e. microcracking and crack deflection, leading to an improved thermal shock resistance for the material. This special type of microstructure is obtained by subeutectoid ageing of conventional MgO-PSZ at 1100 °C [72]. Microcracking and crack branching in this material result in increasing fracture resistance (R-curve) behaviour [73]. One of the challanges taken up in this thesis is the triggering of similar toughening mechanisms operating independently of

temperature in yttria-zirconia ceramics.

The dispersion of zirconia particles in matrices other than ZrO_2 has resulted in a new class of ceramic-ceramic composites. The most intensively studied example is the toughening of alumina by zirconia [84-87]. The ZrO_2 particles can be located within the Al_2O_3 grains or at the grain boundaries. They can be monoclinic or tetragonal. The properties of these composites are a function of both the phase composition and the microstructure. The general trend is that monoclinic particles at grain boundaries decrease the composite strength but increase its fracture toughness (by microcracking and crack branching mechanisms). Compressive stresses can be introduced by the surface T → M phase transformation and this leads to an increased bend strength (Al_2O_3-30vol% ZrO_2 has a bend strength of 1.1 GPa !,[86]).

Complex zirconia systems arise if ZrO_2 is crystallized in-situ from a ceramic or glass matrix or is unidirectionally solidified therefrom. These systems are still in the early stages of design. For the purpose of this thesis, the most interesting complex zirconia systems arise from the alloying of ZrO_2 with its sister oxide HfO_2,and from dispersing second phase refractory β-Al_2O_3 particles in a TZP matrix.

The temperature range of transformation toughening of TZP can be increased by alloying with HfO_2. This process can be understood by considering the Y_2O_3-HfO_2 and HfO_2-ZrO_2 phase diagrams (Fig.2-9A,B, [88,89]). The same type of phase

transformations occur in the Y_2O_3-HfO_2 and Y_2O_3-ZrO_2 systems, but the temperature range is different. HfO_2 suffers the M → T transformation on heating between 1350°C and 1750°C. Consequently, transformation toughening via metastable, constrained tetragonal precipitates is theoretically possible in HfO_2 up to 1950 °C. The volume change for the M ⇌ T transformation in HfO_2 is only half that in ZrO_2 [90]. It can be concluded from Fig.2-9 and other data [90,91], that ZrO_2 and HfO_2 form an ideal solid solution over the entire range of composition. Therefore, the alloying of TZP with HfO_2 should result in materials of enhanced high temperature fracture toughness as long as the tetragonal phase in such a solid solution can be suprcooled in metastable form to room temperature. This task is difficult, since the driving force for the T → M transformation at room temperature is 25 kcal/mole for HfO_2 vs. 10 kcal/mole for ZrO_2 [92].

Whilst HfO_2 alloying is aimed solely at widening the temperature range of transformation toughening, the addition of second phase, platey-morphology refractory β-Al_2O_3 particles to TZP is designed to activate microcrack and crack deflection mechanisms of toughening. It was shown [93] that sodium-β-Al_2O_3 reacts with ZrO_2 to form α-Al_2O_3 at the interface, bonding the β-Al_2O_3 particle to the zirconia matrix. The platey structure of the beta-aluminas facilitates easy ion exchange of the basal conduction planes (Na^+, Ag^+, Sr^+ etc.) and thus opens up the possibility of interfacial reaction

control and particle-matrix property adjustment. In this thesis the dispersion of β-Al_2O_3 particles in partially stabilized zirconia is investigated as a possible source of high-temperature toughening. The results of experimental studies in this system are presented and are also summarized in references 95 to 98, 104, 112.

2.2.2 Toughening Modes

At least three types of toughening, acting perhaps concurrently, have been found in stabilized zirconium-oxide ceramics. Firstly, the tetragonal-to-monoclinic (T→M) martensitic, constrained phase transformation of ZrO_2 particles near an advancing crack tip absorbs energy. This is known as stress induced transformation toughening. This effect has been directly observed in transmission electron microscopy [99,100], and has been modelled by several authors [101-106]. The second mechanism involves the nucleation and extension of matrix microcracks caused by the T → M transformation prior to specimen loading. These lead to bifurcation and absorption of energy during crack propagation [44,53,107]. This effect was modelled by Hoagland at al [45,46] and Faber [108]. Finally, multiple crack deflection, branching and blunting has been observed mainly in zirconias containing monoclinic phase [72,73,109,118]. Increase in the high temperature fracture toughness of PSZ single crystals was attributed to crack deflection by stable tetragonal precipitates [110]. The crack deflection source of toughening has been discussed in Section

2.1.4.

Stress-induced transformation toughening can be considered to originate from residual strain fields. These accompany the volume increase during the T → M transformation triggered by local crack tip stresses and tend to "shield" the crack tip in a compressive zone from the externally applied stress (Fig.2-10A). The volume increase can be described by the transformation strain tensor e_{ij}^T [48,101-103,105,106] and is illustrated by a discontinuity on the stress-strain diagram for the material in the vicinity of the crack tip (Fig.2-10B). This crack tip shielding by a process zone of transformed material effectively decreases the stress intensity factor by ΔK, from that value experienced far from the crack tip (K_I^∞) to the value local to the crack tip K_I^1 (Fig.2-10C). Thus on attainment of the critical condition the local stress intensity factor, K_I^1, reaches a value governed by fracture toughness of the fully transformed material ahead of the crack tip, K_C^T, and it follows that;

$$\Delta K_C = K_C^\infty - K_C^T \qquad (2.34)$$

where K_C^∞ is the experimentally measured fracture toughness. Integration of the closure tractions that are exerted on the crack tip surface due to the T → M transformation results in [104,105];

$$\Delta K_C = 0.21 \cdot E \cdot e^T \cdot V_f \cdot \sqrt{h}/(1 - \nu) \qquad (2.35)$$

where E is an average Young's modulus of the material, e^T is a dilatational transformation strain (recognized to be predominantly responsible for the transformation toughening), V_f is volume fraction of the transforming material, h is the transformation zone width and ν is Poisson's ratio. It has been shown, that the stress intensity approach (resulting in equation 2.35) is fully compatible with the energy balance approach [105,106].

If the remote field strain energy release rate, G, is partially deposited in the wake of the crack tip as transformation and residual stress, and partially deposited at the crack tip, G^{tip} (Fig.2-10A), then [105];

$$G = G^{tip} + 2 \cdot \int_0^h U(y)\,dy \qquad (2.36)$$

where U(y) is the residual energy density left behind the crack tip in a wake of thickness h. The contribution of the phase transformation to U(y) can be obtained from the net work associated with the hysteresis loop generated by the residual transformation strain e^T at zero stress (Fig. 2-11). For the simplified case of constant transformation stress σ_C, the loop area is $\sigma_C \cdot e^T$ and thus;

$$\Delta G_C = G - G^{tip} = 2 \cdot h \cdot \sigma_C \cdot e^T \qquad (2.37)$$

It was shown [105], that equations (2.35) and (2.37), which are correlated through the plane strain relationship (2.12), agree within 0.3 %, indicating the equivalence of the two approaches to the transformation toughening phenomenon. Comparison of theory and experiment gave better agreement for the composite Al_2O_3-ZrO_2, i.e. the ΔK was measured as 6 MPa$\sqrt{m}$ vs. the calculated value of 3.8 MPa$\sqrt{m}$. For pure PSZ the measured ΔK was 2.3 MPa$\sqrt{m}$ and the calculated value was 0.81 MPa$\sqrt{m}$ [105].

The energy approach is convenient for analysis of microcrack toughening in zirconia systems [106,108], Fig.2-11. For a fully-developed microcrack process-zone, the toughening increment is related to the residual energy, U(y), left in the wake of the crack front. Via an equation similar to (2.36) U(y) is evaluated geometrically from the loading-unloading hysteresis loop, modified for the microcracked material (Fig. 2-11B). It is assumed for simplicity that microcracking takes place at all potential sites suffering stresses above the critical stress, σ_C. The microcracking results in a decreased Young's modulus, E, and, upon unloading, in permanent residual strain θ. For a complete description, some residual stress, σ^R, must be included in a wake of the crack tip. At a microcrack density of 0.3, the magnitude of the hysteresis loop gives a toughness increase of 1.5 to 2 times [106, 108]. This result agrees with experimental observation [107]. It is interesting to note, that the decrease of the modulus of

elasticity for the microcracked material tends to decrease the hysteresis loop area, i.e. offset the effect of transformation toughening when both phenomena occur concurrently. It is concluded [108] that, in such a case, the permanent strain, θ, must be significantly increased for any substantial toughening.

Special attention is paid to this problem in the present thesis. Efforts are made to optimise the permanent unloading strain by dispersing β-Al_2O_3 particles in the partially stabilized zirconia matrix. The particles generate multiple micro- and macrocracks at the reaction product α-Al_2O_3 interface as well as deflecting cracks. The β-Al_2O_3 therefore contributes to the composite's toughness [97].

2.3 The Chevron-Notched Four-Point-Bend Test Specimen

The idea of introducing a chevron notch (CN) into a fracture test specimen was born more than 20 years ago [111], and has resulted in a variety of geometrical configurations. The geometry of the CN four-point bend bar employed in this thesis is shown in Fig.2-12. The CN specimen is unique for a crack initiates at the notch tip at a low load and then propagates stably to an extension determined by the experimental conditions [112,113]. This means that fatigue precracking is not required (an especially important consideration for ceramic materials) to ensure the sharp crack requisite for fracture toughness testing. The notch is precracked

in-situ during the initial stable crack propagation. The side grooves guide the crack in plane, assuring Mode I fracture.

The symmetrical CN bar was proposed as a suitable work-of-fracture (WOF) specimen, the WOF being defined as the area under the load-displacement record in a controlled fracture experiment [114].

The mechanical compliance (measured as the load application point displacement at unit load) of the CN bend specimen was analysed by Bluhm [115]. The sample was treated as a series of slices, "i" (of total number n) in the span-wise direction. Each slice was considered as having approximately straight-through (ST) notch geometry and compliance C_{iST}. The CN specimen compliance, C_{CN}, is then obtained from the formula;

$$C_{CN} = \{ \sum_{i=1}^{n} [k(\phi)/C_{iST}] \}^{-1} \qquad (2.38)$$

where $k(\phi)$ is an empirical factor accounting for the inter-slice shear effect. Shear between slices effectively decreases the specimen compliance and was experimentally found to depend on the side notch length, x_1, and the notch angle, ϕ=OPR (Fig. 2-12), [119], i.e.;

$$k = 1 + x_1^{3.12} \cdot (2.26\phi - 4.74\phi^2 + 4.7\phi^3 - 1.77\phi^4) \qquad \text{at } 0<\phi<1 \text{ rad}$$

$$k = 1 + 0.444 \cdot x_1^{3.12} \qquad \text{at } \phi>1 \text{ rad} \qquad (2.39)$$

It is claimed [119], that the experimental calibration of the compliance vs. notch length and geometry for a four-point bend, chevron-notched bar satisfactorily agreed with equations (2.38,2.39). Further calibration results will be presented in this thesis. It is obvious however that, as the crack front approaches x_1, the notch ceases to be "chevron" and the shear stresses vanish i.e. k approaches 1. This phenomenon was considered by Sakai and Yamasaki [120] using finite element analysis. k was found to be constant as the crack propagates from x_0 to approximately $x=(x_0+x_1)/2$ and then to diminish gradually to 1 at $x=x_1$. A general formula for the shear correction factor has not been found.

The two approaches [115,119] and [120] differ by a maximum of 10 % in the compliance calculation results as x approaches x_1. Since the majority of the specimens considered in this thesis have $x_1>0.95$ and the compliance equation is uncertain for deep cracks, Bluhms approximated formula for k, eq. (2.39), is utilised.

In order to apply equation (2.38), the compliance of the single ST slice must be obtained by combining equations (2.7,2.10,2.12) and substituting the formula for the outer-fibre-stress in four-point bending, σ_A (Fig.2-12);

$$\sigma_A = 3 \cdot P \cdot (S_1 - S_2)/(2 \cdot B \cdot W^2) \qquad (2.40)$$

If (2.40) is substituted in (2.10) and (2.12) and equated to

(2.7), remembering that for the ST bar dA=BWdx, the result is;

$$dC(x)/dx = 4.5\cdot(S_1-S_2)^2\cdot(1-\nu^2)\cdot x\cdot Y^2(x)/(B\cdot W^2\cdot E) \quad (2.41)$$

where all the parameters have their usual meaning (explained in the preceding formulae and Fig. 2-12). Integration of (2.41) results in [119,120];

$$C(x) = C(0) + 4.5\cdot(S_1-S_2)^2\cdot(1-\nu^2)\cdot I(x)/(B\cdot W^2\cdot E) \quad (2.42)$$

where;

$$I(x) = \int_0^x x\cdot Y^2(x)\,dx \quad (2.43)$$

and C(0) is the compliance of the unnotched ST bar;

$$C(0) = (S_1-S_2)^2\cdot(S_1+2\cdot S_2)/(4\cdot B\cdot W^3\cdot E) \quad (2.44)$$

Y(x) for 0<x<1 can be obtained from the formula [118];

$$Y(x) = \Omega\cdot(0.5\cdot\tan[\pi x/2]/x)^{0.5}/\cos[\pi x/2] \quad (2.45)$$

where;

$$\Omega = 0.923+0.199\cdot(1-\sin[\pi x/2])^4$$

Numerical integration of (2.43) using (2.45) results

in the definition of the I(x). This parameter is useful (in conjunction with 2.42) in determination of the crack length via the compliance analysis for an ST notched bar. Equations (2.43,2.45) are plotted in Fig.2-13. To avoid repeated numerical integration, I(x) can be fitted by a polynomial;

$$I(x) = (1-x)^{-2}\cdot(-0.0273+0.335\cdot x+0.0942\cdot x^2-0.1856\cdot x^3) \quad (2.46)$$

Results calculated using equation (2.46) agree with the numerical ones of (2.43) within 1 % for x>0.2. Finally (2.42) can be utilised slice by slice to obtain the CN specimen compliance according to (2.38).

Since the invention of the CN specimen efforts have been made to correlate the resultant load-displacement diagram with the critical value of the stress intensity factor of the test material. Pook [113] recognized the high stress concentration on the chevron tip and proposed an approximate expression for the plane-strain stress intensity factor, K_I^{CN}, as a function of the crack front length, b, (Fig. 2-12) i.e.;

$$K_I^{CN} = K_I^{ST}\cdot(B/b)^{0.5} \quad (2.47)$$

where K_I^{ST} is a stress intensity factor for ST notched specimen, i.e. b=B.At $x=x_0$, b=0 for an ideal chevron and K_I^{CN} tends to infinity (for the real CN specimen b > 0, so K_I^{CN} is

large but finite, [113]). Since the geometric factor is an increasing function of the crack length (Fig.2-13), K_I^{CN} must drop to minimum at some crack length $x=x_m$.

Assuming that there is no subcritical crack growth, i.e. $K_{IC}=K_0$ (or $G_{IC}=G_0=2\Gamma$, see Section 2.1.1), the method of K_{IC} or G_{IC} determination using the CN specimen is illustrated in Fig.2-14A, [121]. The consecutive curves P_1,P_2,P_3,P_m show the change of the crack driving force, K_I,under applied loads $P_1<P_2<P_3<P_m$. An increase of load from P_1 to P_m drives the crack towards points A,B,C,D respectively. When the maximum load P_m is reached, the crack-driving-force curve is just tangent to the presumably flat crack resistance curve G_{IC} and thus the instability point is reached. The crack then accelerates further under decreasing load P. Therefore the minimum value of K_I ($=K_{IC}$) coincides with the maximum value of load.This simplified analysis is not valid if the material exhibits R-curve behaviour [121] or subcritical crack growth [98]. The latter case will be addressed in more detail in Chapter 3.

Once the compliance function for the CN specimen is known, eq. (2.38), the strain energy release rate (or the stress intensity factor) can be obtained via equations (2.27,2.12). The fracture area A (triangle OPR in Fig.2-12) is given by;

$$A = 0.5 \cdot B \cdot W \cdot (x-x_0)^2/(x_1-x_0) \qquad (2.48)$$

so;

$$dA/dx = B \cdot W \cdot (x-x_0)/(x_1-x_0) \qquad (2.49)$$

Substitution of (2.49) into (2.7) gives;

$$G_I = 0.5 \cdot P^2 \cdot (B \cdot W)^{-1} \cdot [(x_1-x_0)/(x-x_0)] \cdot dC_{CN}(x)/dx \qquad (2.50)$$

Equation (2.50) describes analytically the advantageous feature of the CN specimen, i.e. easy fracture initiation at the chevron triangle tip. Indeed, at $x=x_0$ G_I tends to infinity as soon as the loading commences. Consequently, the chevron tip can be spontaneously precracked (blunted) even during sample machining and handling. Experimentally it has been observed that the CN specimen fracture initiates at loads equal 70 to 90 % of the maximum load value rather than any $P>0$ (compare eq. 2.50). If one assumes that $x>x_0$ at the beginning of the fracture of a CN specimen, subcritical crack growth in this type of specimen can be analysed [98].

If equation (2.12) is substituted again in (2.50), an expression for the stress intensity factor results [126];

$$K_I = P \cdot Y^*(x)/(B \cdot \sqrt{W}) \qquad (2.51)$$

where;

$$Y^*(x) = \{(B \cdot E) \cdot (1-\nu^2)^{-1} \cdot [(x_1-x_0)/(x-x_0)] \cdot dC_{CN}(x)/dx\}^{0.5} \qquad (2.52)$$

$Y^*(x)$ is a function of the sample and bending geometry

(S_1, S_2, x_0, x_1, x) and the specimen width W, via equations (2.38, 2.42, 2.44). Values of $Y^*(x)$ typical for the experimental conditions undertaken in this thesis (S_1/S_2=2, S_2/W=2, x_0=0.3 and 0.5) are plotted in Fig. 2-14B. The minimum of the $Y^*(x)$ curve, $Y^*_m(x)$, corresponds to the crack length x_m which is characteristic of the test geometry and not the material. Since $Y^*_m(x)$ coincides with the maximum load and the start of unstable crack propagation under ideal conditions (i.e. no subcritical crack growth or R-curve), its unique value offers an attractive method of K_{IC} measurement. The value of Y^*_m is determined via the test geometry [146];

$$Y^*_m = Q(x_0,x_1)\cdot(S_1-S_2)\cdot(1+0.007\cdot\sqrt{(S_1\cdot S_2)/W})/W \quad (2.53)$$

where;

$$Q(x_0,x_1) = (3.08+5\cdot x_0+8.33\cdot x_0^2)\cdot(x_1-x_0)/(1-x_0)$$

Simplified K_{IC} measurment procedures, based on equations (2.51,2.53) have gained acceptance for ceramic testing. Munz et al. [126,127] reported the successful application of four-point bend CN geometry for the measurement of the K_{IC} value for Al_2O_3 at room temperature and Si_3N_4 at room and high temperatures. Subcritical crack growth was neglected at high temperatures.

Problems with the use of the CN bend specimen for evaluation of K_{IC} for glass were reported by Chuck et al. [125]. Four-point bend tests with soda-lime-silica glass were

performed in wet and dry environments at various loading rates. A significant number of specimens failed to exhibit stable crack growth prior to catastrophic fracture. The resulting overload overestimated K_{IC} when equation (2.51) was used. It was argued that difficult fracture initiation was caused by a relatively wide notch gap (0.5 mm) and a compliant testing system. The authors recognized that tests on glass will be influenced by a moist environment inducing subcritical crack growth. Consequently, different loading rates could result in different measured values of K_{IC}. This problem will be modelled quantitatively in Chapter 3.

The application of the CN specimen to work-of-fracture tests was recently refined by Sakai et al. [32], Sakai and Bradt [31] and Troczynski and Nicholson [98]. It was shown, that the stability of the CN specimen facilitates multiple loading/stable fracture/unloading experiments and this technique was applied to a silica refractory [31], graphite [32] and zirconium oxide ceramics [96,97]. The nonlinear fracture energy parameters were evaluated for each cycle from the respective areas on the load-displacement record and analysed as discussed in Section 2.1.2.

The chevron-notched four-point bend specimen is extensively employed in fracture experiments in the present thesis because of the relative ease of machining, for fracture initiation and stabilization and the convenient loading geometry (especially at high temperatures). Zirconium

oxide exhibits subcritical crack growth at room temperature [128,129] and presumably nonelastic deformation at high temperatures due to the softening of an amorphous grain boundary phase. Accordingly, analysis of the CN test geometry is refined, beyond the simplified analysis presented above.

The utilisation of the high temperature ionic conductivity of zirconia ceramics to monitor crack growth requires further theoretical treatment of the electrical conductivity of the CN specimen geometry. These problems are addressed in the next chapter.

2.4 Theoretical Aspects of Experimental Design and Procedure

Two groups of zirconium-oxide based ceramic materials were investigated in the present thesis, i.e., stabilized ZrO_2-HfO_2 solid solutions and dispersions of β-Al_2O_3 particles in commercially-available stabilized zirconias.

The major investigation concerned the resistance to fracture of these ceramics. Other properties that were characterized were phase composition (X-ray diffractometry), density (Archimedes principle) and Young's modulus at low and elevated temperatures (using ultrasonic wave propagation techniques and the simple bending of unnotched bars). Extensive imaging by scanning electron microscopy provided a link between the microstructure evolution and the resistance-to-fracture results.

Literature sources of the methods of materials development and characterization will now be discussed.

2.4.1 Materials Choice and Characterization

2.4.1.1 Zirconia-Hafnia Solid Solutions

The transformation toughening range for ceramics containing metastable HfO_2 tetragonal precipitates could reach 1700°C. HfO_2 and ZrO_2 form an ideal solid solution (Fig. 2-9) so a mixture of the two oxides stablised with 4.5 mole % Y_2O_3 should exhibit a linear variation of the tetragonal-to-monoclinic phase transformation (T $\rightleftharpoons$ M). Accordingly, if 30 mole % ZrO_2 is replaced by HfO_2 and the solution stabilized with 4.5 mole % Y_2O_3, the tetragonal phase should be stable above 1100°C. The 4.5 mole % Y_2O_3-ZrO_2 solid solution exhibits tetragonal phase stability at 800°C (i.e., at T > 800°C the transformation toughening mechenism becomes inoperative). Lange [132] has argued that the absolute value of the T → M phase transformation driving force, ΔG, influences the resulting transformation toughening effect, i.e.;

$$K_{IC} = [K_0^2 + (2 \cdot h \cdot E \cdot f \cdot \Delta G)/(1-\nu^2)]^{0.5} \qquad (2.54)$$

where K_0 is the matrix toughness, h the width of the transformation zone, E the Young's modulus, f the volume fraction of transforming material and ν the Poisson's ratio. ΔG changes with temperature and HfO_2 content such that, at 1000°C, ΔG for ZrO_2 is 50 MJ/m^3 and ΔG for 0.7 ZrO_2 + 0.3 HfO_2 is 90 MJ/m^3 [92,131]. If the precipitates in a yttria-

zirconia-hafnia solid solution are maintained in the metastable tetragonal form, the possible fracture toughness increase at 1000°C could be ~30%, i.e., from 2.0 to 2.6 MPa$\sqrt{m}$ according to Lange's formula (2.54).

In the present thesis, solid solutions wherein ≤30 mole % of the ZrO_2 are replaced by HfO_2 will be investigated. To assure a uniform distribution of the Hf^{4+} and Zr^{4+} before sintering, a wet chemical route is employed for powder processing. The traditional oxide-mixing route is also utilised.

2.4.1.2 Zirconia/β-Al_2O_3 Composites

The presence of a dispersed β-Al_2O_3 phase is expected to maximize crack-microstructure interactions and thus provide additional modes of the fracture energy dissipation. Estimation of the stress field in the vicinity of the inclusions can only be obtained for spherical isotropic particles [93] i.e.;

$$p_r = -2 \cdot p_t = -p \cdot R^3/r^3 \qquad (2.55)$$

$$p = [\Delta\alpha \cdot \Delta T]/[(1+\nu_m)/(2 \cdot E_m) + (1-2 \cdot \nu_i)/E_i] \qquad (2.56)$$

where p_r and p_t are the radial and tangential stress in the matrix at a distance r from the centre of a particle of radius R. p is hydrostatic pressure within the particle, $\Delta\alpha$ is difference between the thermal expansion coefficients of the

matrix (m) and inclusion (i) and ν_m, E_m, ν_i, E_i are the Poisson's ratio and Young's modulus for the matrix and inclusions respectively. ΔT is the temperature range over which thermal mismatch stresses cannot be relaxed. Although β-Al_2O_3 particles are not spherical nor isotropic, a numerical estimation based on equation (2.54) gives a compression in the particles of 300 MPa (for E_m=200GPa, E_i=150GPa, ν_m=0.3, ν_i=0.25, ΔT=1000°C, $\Delta\alpha$=$2\cdot10^{-6}\cdot°C^{-1}$). The actual stress distribution in the vicinity of the β-Al_2O_3 particles in a PSZ matrix is complex and cannot be predicted theoretically due to anisotropy, interfacial α-Al_2O_3 formation and porosity.

There is some experimental evidence of a positive interaction (i.e., attraction and arrest) between a PSZ matrix crack and the β-Al_2O_3 particles. The cracks emanating from the corners of a Vickers pyramid indent either run straight into β-Al_2O_3 particles or bend towards the particles to be arrested at the particle-matrix interface [133].

As theoretical analyses are difficult, a range of β-Al_2O_3 inclusion sizes were experimentally investigated. The composite matrices chosen were Y_2O_3-ZrO_2 solid solutions (with 4.5 mole% and 6.9 mole% Y_2O_3).

2.4.1.3 X-Ray Phase Analysis

Phase composition is a key factor controlling the mechanical properties of zirconium oxide ceramics. The relative amounts of the monoclinic (M), tetragonal (T) and cubic (C) phases decide the fracture resistance and

its source mechanism, the thermal shock resistance and the extent of transformation toughening. A number of equations have been proposed to determine the volume fractions of the M, C and T phases in zirconia ceramic microstructures.

Adam and Cox [134] proposed the fraction of C phase (f_C) in a C + M mixture is given by;

$$f_C = I_C(111)/[I_M(111)+I_M(11\bar{1})+I_C(111)] \qquad (2.57)$$

where $I_A(iii)$ is the integrated intensity of the respective peak (iii) for the phase A. A similar equation was used for T + M mixtures [135], i.e.;

$$f_M = I_T(111)/[I_M(111)+I_M(11\bar{1})+I_T(111)] \qquad (2.58)$$

It was shown however, [136], that (2.58) considerably (up to 30%) underestimates the T-phase content in an M+T mixture and a more accurate expression was proposed;

$$f_T = I_T(111)/[I_T(111)+I_M(111)] \qquad (2.59)$$

Garvie and Nicholson [68] assumed that the intensity of the C or T (111) peak is equal to the sum of the intensities of the M ($\bar{1}11$) and M ($11\bar{1}$) such that a simple linear formula similar to (2.57) resulted.

The most complete treatment of this problem is the

recent work of Toraya et al. [137]. These authors assume that, for a T+M mixture, the integrated intensity ratio, X_M, is related to the volume fraction of monoclinic phase, f_M, and the intensity of the reflection H(hkl) of the pure phase by the relations;

$$X_M = [I_M(111)+I_M(11\bar{1})]/[I_M(111)+I_M(11\bar{1})+I_T(111)] \quad (2.60)$$

and;

$$X_M = f_M \cdot [H_M(111)+H_M(11\bar{1})]/\Omega \quad (2.61)$$

where;

$$\Omega = f_M \cdot [H_M(111)+H_M(11\bar{1})]+H_T(111)\cdot(1-f_M)$$

Solution of (2.61) for f_M gives;

$$f_M = P \cdot X_M/[1+(P-1)\cdot X_M] \quad (2.62)$$

where;

$$P = H_T(111)/[H_M(111)+H_M(11\bar{1})] \quad (2.63)$$

The calculated value of parameter P is 1.340 and its experimental value is 1.311 (by a least square fit of equation 2.62 to data for calibration mixtures). Equation (2.62) takes account of the nonlinear dependence (maximum 6.8%) of the volume fraction f_M against the integrated intensity ratio X_M. This was neglected in previous formulae.

The small differences in the lattice parameters of the C and T phases for Y_2O_3-ZrO_2 solid solutions causes their

diffraction peaks to overlap. Therefore, in the present thesis, the volume fraction, $f_{C,T}$, of C+T phase will be determined jointly, [77], such that the final formula employed for determination of f_M is (based on 2.60 and 2.58, P=1.311);

$$f_M = \{1 + 0.76 \cdot I_{C,T}(111)/[I_M(111)+I_M(11\bar{1})]\}^{-1} \quad (2.64)$$

Unfortunately, an analysis leading to an equation for hafnia and hafnia-zirconia systems similar to (2.64), has not been reported. HfO_2 has a structure similar to ZrO_2 and undergoes the same phase transformations. The X-ray data for both oxides are compared in Figure 2-15B for the 2θ range 28-32° for Cu-K_α radiation with λ = 0.154 nm. Calibration via mixtures of cubic and monoclinic HfO_2-Y_2O_3 solid solutions and the ratio of the intensities $I_C(111)/I_M(111)$ was performed by Buckley [144]. To compare these calibrations with the results via the method proposed by Toraya et al. [137] for the ZrO_2-Y_2O_3 system, the following calculations were performed. Knowing the ratio of the intensities of $I_M(111)/I_M(11\bar{1})$ for ZrO_2, (equal to 1.4 [136]), the integrated intensity ratio, X_m, (equation 2.60) can be expressed as;

$$X_M = 2.4/(2.4 + r) \quad (2.65)$$

where $r = I_T(111)/I_M(111)$. If equation (2.65) is substituted

into (2.62), letting P = 1.311, the volume fraction of tetragonal phase, f_T, as a function of r is obtained;

$$f_T = r/(3.14 + r) \qquad (2.66)$$

This equation is plotted as r vs. volume fraction in Figure 2-15A ($r=r_2$ for ZrO_2). Also displayed are the original calibration results of Buckley for C + M mixtures of stablized HfO_2 ($r=r_1$). Clearly the calibration results for the T and C phases of both ZrO_2 and HfO_2 can be applied interchangeably. Accordingly, equation (2.64) was employed for the M phase content determination in the Y_2O_3-ZrO_2-HfO_2 solid solutions investigated in this thesis.

The phase composition of the zirconia-β-alumina ceramics was not studied as a separate project. Based on literature data [94, 133], it was recognized that the only phase change in the input products involves the formation of α-Al_2O_3 and sodium zirconate at the interface between the β-Al_2O_3 particles and the PSZ matrix. These levels are so low as to be beyond the sensitivity range of x-ray analysis for the 20 vol. % β-Al_2O_3/ZrO_2 composites.

2.4.1.4 Elastic Modulus Determination

The elastic modulus of ceramics depends on their phase composition and phase distribution, especially when cracks or voids are present. In this respect both the HfO_2-ZrO_2 solid solutions and the ZrO_2-β-Al_2O_3 composites are complicated

systems. No attempt is therefore made to model the elastic properties of these ceramics as a function of composition or microstructure. However, an average value of their elastic modulii (E) must be determined as input data for the compliance and fracture energy analyses.

There are several available techniques to determine E at room temperature and a few applicable at high temperatures. The simplest low temperature technique involves the attachment of a piezoelectric sound wave generator to the flat surface of a specimen and measurement of the transit time, t, for a pulse reflected from the flat, parallel opposite face to return to the original surface. The attenuation of the ultrasonic pulse is minimized by choosing a low frequency wave. The velocity of the longitudinal (v_l) and transverse (v_t) waves in an isotropic medium of density d is given by [138];

$$v_l = \{[E\cdot(1-\nu)]/[d\cdot(1+\nu)\cdot(1-2\cdot\nu)]\}^{0.5} \qquad (2.67)$$

$$v_t = \{E/[2\cdot d\cdot(1+\nu)]\}^{0.5} \qquad (2.68)$$

where E is the Young's modulus and ν the Poisson's ratio. At room temperature the transit time can be determined with an accuracy better than 1% so the key factors for error minimisation are the parallelism of the reflection surfaces, the determination of the specimen thickness and its density.

A dynamic value of the Young's modulus is obtained in this way.

Stable fracture experiments are performed at slow stressing rates and the energy stored in the specimen during static loading is governed by the compliance law and the static value of Young's modulus, E_s. Therefore an alternative technique was also used to determine E_s. If an unnotched bar is four-point-bent by a load P and the load-application point displaced by D, the static Young's modulus E of the material can be obtained from equation (2.44), where C(0)=D/P. The static modulus value is usually lower than that obtained by ultrasonic (dynamic) measurement. This is not surprising as time-dependent phenomena (perhaps delayed grain boundary microcracking and healing) are involved in the static loading process. In the present thesis both methods are utilised.

As the temperature is raised above 900°C, the concept of elastic modulus and its measurement becomes complex due to the presence of grain boundary amorphous phases. The material starts to deform viscoelastically and its behaviour can be modelled by a combination of dashpot and spring elements (Fig. 2-16). If a spring corresponds to the elongation rigidity k and a dashpot to the viscosity η, the relaxation time, τ, of the element is defined as;

$$\tau = \eta/k \qquad (2.69)$$

τ is a measure of the time required for stress relaxation in the deformed element. The deformation of a viscoelastic body can be described by considering a large number of such elements with a spectrum of relaxation times, τ_i. If such a body is periodically stressed, U' of the total input energy, U, will be reversibly stored and, if no fracture takes place, this energy can be completely recovered (like the strain energy in an elastic body), Fig. 2-16. A part of U can be used to create fracture surface above a certain critical value of stress. If a portion U" (U"=U-U') is irreversibly dissipated by deformation of the body, this energy is not available for the fracture process. The elastic energy stored in a viscoelastic body is a measure of the "storage" modulus E' (or Young's modulus) and the energy dissipated in the "dashpot" network is a measure of the "loss" modulus E". E'and E" for a single spring/dashpot element can be simply expressed in terms of the relaxation time τ and the frequency ω [139]. For a real body, a spectrum of relaxation times must be considered and integrated.

Consider the stress-strain curve for a viscoelastic body, Fig. 2-16. If no fracture occurs during loading, the curve OB can be described by the equation;

$$\sigma(t) = \epsilon \cdot E(t) \qquad (2.70)$$

where E(t) is a relaxation modulus, a time dependent analog

of the Young's modulus for an elastic solid. If the specimen is unloaded at point B to the zero stress level D, the loop OBD represents the nonelastically dissipated energy U''_1, if the residual strain energy at point D can be neglected. If further loading along the line OBC leads to crack extension, the nonelastic dissipation is represented by loop OBB'FDO (i.e., U''_1 and U''_2), while the energy spent for new surface creation is loop FB'C (i.e., U'_2). The unloading paths BD and CF are governed by the test geometry, the storage modulus E' and the notch length at B and C respectively (Fig. 2-16). The relaxation modulus E(t) is a function of the relaxation spectrum of a viscoelastic body [139];

$$E(t) = E_e + \int_{\tau=0}^{\infty} H \cdot e^{-t/\tau} \, d\ln\tau \qquad (2.71)$$

where H is called a rigidity function and E(t) has an elastic value, E_e, at $\tau=\infty$. The relation between E(t) measured along line OB (Fig. 2-16) and the storage modulus $E'(\omega)$ must be established for the purpose of this thesis. These two quantities are related through [139];

$$E'(\omega) - E(t) = \int_{\tau=0}^{\infty} H \cdot \{\omega^2\tau^2/(\omega^2\tau^2+1) - e^{-t/\tau}\} d\ln\tau \qquad (2.72)$$

According to equation (2.72), the storage modulus E' is a function of the frequency, ω, of the stress application.

Therefore it is important that the static value E' be measured at the same stressing rate as used in the fracture experiments. The spectrum of relaxation times and the rigidity function, H, are unknown for viscoelastic zirconia ceramics. As the right-hand side of equation (2.72) is always positive [139], it will reach a minimum at t=0 or it will be negligible when $t \to 0$ and $\omega^2\tau^2 \gg 1$ (i.e., the dynamic measurement). Therefore, the right-hand side of equation (2.72) will be neglected for the static loading pattern presented in Figure 2-16 if E(t) is calculated via the tangent to the origin O, i.e., at t=0. Such an approximation is with agreement with Krausz and Eyring [174] analysis of the spring/dashpot model. They showed that at constant displacement rate a spring/dashpot unit should have initially a stress-strain curve that is characteristic of the spring. As the force increases the dashpot will start slipping and the stress-strain curve will not indicate the spring stiffness [174].

A similar technique was suggested for the determination of the elastic (E) and anelastic (M) moduli in uniaxial tension for a viscoelastic metallic specimen [169] (an anelastic strain ϵ^a is defined as that reflecting the magnitude and direction of prior deformation history. The sum of ϵ^a and the permanent strain, ϵ^p, gives the total nonelastic strain, ϵ^n). The initial portion of the plot of stress (σ) vs. accumulated strain (ϵ) shows the transition of slope from

E to M·E/(M+E).

Consequently the high-temperature static storage modulus for a viscoelastic solid has been estimated in the present thesis using eq. 2.44 and measuring the initial slope of the load-displacement record of an unnotched bar at a strain rate similar to that used in the fracture experiments.

To evaluate this technique, literature data [140, 141, 142] for the dynamic Young's modulus of ZrO_2 were normalized to room temperature values and compared with the static results obtained in the present thesis for similar materials (Fig. 2-17). As expected, the static values are consistently smaller, although the temperature variation is similar. It is felt that the static measurement better describes the material behaviour in slow fracture experiments at high temperatures (in particular the release of the stored elastic energy into the surface of a newly-created crack).

The values of high-temperature static Young's modulus obtained in this thesis, lower than the dynamic data from Fig. 2-17, should be treated as a lower-bound estimation. The possible associated error of the calculated crack driving force will be discussed in Section 4.8.

2.4.2 Fracture Testing System and Specimen Design

The energy involved in brittle fracture is analysed in the present thesis using four-point bend testing of chevron-notched (CN) specimens at low and elevated temperatures. The tests are performed via load relaxation (LR) and loading-

fracture-unloading (LFU) routines, using compliance analysis (CA) and potential drop (PD) techniques to calculate crack lengths. The choice of specimen type and experimental arrangement will now be discussed. Areas for further theoretical analyses of the CN specimen are also identified.

The bend test was chosen as a simple and reliable method of crack-driving-force application. This is especially important for hard ceramic materials, as machining is limited to the cutting and polishing the four faces and the chevron notching. Another advantage is that little material is required for each specimen. No holes, grooves or holders are required as the load is applied in compression (especially convenient at high temperatures). Therefore, apart from the chevron notch, no unnecessary stress concentrators are introduced. The technique is well established experimentally and stress and error analyses are available in the literature. CN and straight through (ST) calibrations of specimen compliance have been widely reported. In addition, four-point-bending offers a uniform bending moment between the upper (shorter) bend span so precise notch centering between the load application points is not required as per three-point-bending.

Although the ST bend specimen geometry is well established in fracture mechanics practice, this specimen geometry is not suitable if fracture stability is the main concern. A crack must initiate simultaneously along the

whole length of the straight-through notch, which has frequently been cut with a thick (300-500 μm) blade. This renders the ST specimen susceptible to overload and, once initiated, catastophic uncontrollable fracture follows. As discussed in the previous chapter, the stress concentration at the chevron notch tip reduces the danger of overload and increases the fracture stability.

The use of the CN specimen in constant strain rate experiments is not sufficient to maintain fracture stability for certain materials and testing systems. In these cases the alternative LR test should be considered and was used in this thesis. The theoretical analysis of the LR-CN test is not available in the literature and is presented in the next chapter.

Although the LR configuration is unique in its stability and ability to identify crack-microstructure interactions (the crack velocity is measured in the LR test), the analysis requires the assumption of ideal elasticity. This is questionable for ceramic and composite materials at room temperature and is not true at elevated temperatures. Moreover, as the ideal LR test proceeds to full fracture, it does not allow the experimenter to intervene in case of undesirable developments, eg., crack acceleration towards a critical veolcity. In such a case the strain energy release rate could be reduced (i.e., the crack deccelerated) if part (or all) of the load is decreased. This is the characteristic

of the LFU experimental routine. Properly chosen unloading points allow one to preserve the condition $G_I<G_{IC}$ and so maintain fracture stability (this task is not easy for high-stiffness brittle ceramics). The variation of the crack driving force in LFU experiments is modelled in the next chapter. Guidelines for the experimental procedure and design of the testing system are developed therein.

The room temperature ZrO_2 tests utilised specimen compliance analysis (CA) as an indication of the crack length (through equations 2.38 and 2.42). This technique is convenient and accurate (as shown by the calibration results) if the load, P, and load application point displacement, D, can be measured accurately (at ±0.1N and ±0.1μm respectively the accuracy of the compliance calculation is better than 3%).

To use the CA technique at elevated temperatures requires the use of an extension rod from the specimen surface inside the furnace to the displacement measuring device outside the furnace. If μm-range distances are to be measured, this technique is difficult to implement and unreliable (instead, direct crack observation was recommended [162,163]). An alternative procedure involves utilization of the high temperature ionic conductivity of ZrO_2 ceramics in atmospheres containing oxygen (O^{2-} ions diffuse through oxygen vacancies). If this conduction is described by Ohm's law (i.e., there is no interference from electrode

polarization), the crack length can be calculated from the increase of the resistance (or the potential drop at constant current) due to reduction of the specimen cross section available for conduction as the crack grows.

Potential drop (PD) applications have been reported in the literature for ST-notched electronically conducting specimens. New theoretical and experimental developments were required for CN specimens utilising ionic conduction. This analysis is presented in the next chapter.

From the above discussion, both low and elevated temperature experimental design with chevron-notched specimens required a number of new theoretical analyses. As these analyses constitute a significant part of the original research reported herein, they are included in a separate chapter .

CHAPTER 3

THEORETICAL STUDIES OF THE CHEVRON-NOTCHED BEAM BEND SPECIMEN

The energy analysis of brittle fracture requires, that the crack driving force be within the limits of the threshold (K_t or G_t) and critical (K_{IC} or G_{IC}) values. Equivalently, the most informative experiments are performed in the subcritical crack growth range. This was the primary reason for choice of the four-point-bend chevron-notched specimen in the present thesis.

A fundamental deficiency of the CN-analyses available in the literature is the neglect of subcritical crack extension. Simplified two-state analysis is preferred, i.e. the crack is assumed to be stationary at $K_I < K_{IC}$ or the crack propagates catastrophically at $K_I = K_{IC}$. This is hardly applicable as the CN specimen was originally designed for work-of-fracture (WOF) tests which intrinsically require the whole experiment to be performed in the subcritical crack growth (SCG) regime.

In this chapter the CN specimen is studied assuming that the crack velocity for $K_t < K_I < K_{IC}$ is governed by a widely accepted power law (2.4). Recognition of SCG in the CN specimen results has important implications for the fracture

testing techniques. It will be shown, that the WOF technique results in values characteristic for the material and not for the experimental conditions only if the WOF values are analysed against the crack extension up to complete fracture. The fracture toughness can be calculated from the maximum load only if a specific displacement rate is utilised.

Section 3.2 of the present chapter is devoted to stability analysis of the CN specimen as a function of a number of experimental parameters in the load-relaxation test.

Finally, an original method is proposed for the application of the electrical potential drop (PD) technique for crack length measurement in test specimens exhibiting not-straight-through crack fronts (in particular for the CN specimen). The technique is verified by calibration experiments and used for the first time for ionically conducting materials ,i.e ZrO_2-based ceramics, (Chapter 4).

Sections 3.1 to 3.3 present the results published in references [95,96,98,112,172,173].

3.1 Subcritical Crack Growth in a Constant Displacement Rate Test

An empirical law (2.4) governing subcritical crack growth can be expressed as;

$$v = v_C \cdot (K_I/K_{IC})^N \qquad (3.1)$$

where v is the crack velocity ($v=v_C$ at $K_I=K_{IC}$) and N is a

parameter characteristic of the material and the environment. At crack initiation, $K_I=K_t$, and the crack velocity can be as low as 10^{-9} m/s or "zero" in experimental practice. In a constant displacement-rate test the specimen is likely to be loaded in an apparently linear-load-displacement regime (Fig. 3-1), before apparent fracture initiation at P_i (70 to 90 % of the maximum load value, P_m). The apparent fracture initiation point indicates that the crack has already grown by a certain length Δx ($x=a/W$, according to the standard notation in Fig. 2-12). The true fracture initiation which occurs at loads between P_i and 0 (i.e. at $K_I=K_t$ and load P_0) must be located by some other technique.

As indicated in the previous chapter, the "ideal" chevron notch shape implies, that the strain energy release rate at the tip tends to infinity at any applied load (eq. 2.50). Accordingly, the closer the notch is to the ideal shape, the more probable it is that it will spontaneously precrack (blunt) during the specimen machining and handling. The resulting blunted tip is equivalent to the ideal shape when the initial crack x_0 has extended by Δx. In the present thesis $\Delta x=0.002$ is arbitrarily assumed such that the apparent fracture initiation load, P_i, is within the values observed experimentally. This is equivalent to assuming that subcritical crack growth starts at some non-zero load value, P_0, and thus a real description and analytical treatment of fracture initiation and propagation in the CN specimen can be

undertaken.

Usually fracture is out of control when the crack velocities reach 10^{-3} to 10^{-1} m/s. In the present work the CN specimen performance is analysed at $v_C/v_t \simeq 10^5$ to 10^8. Despite the fact that N can vary widely, the fastest change of material properties occurs if N varies between ~2 and 40 [145]. In the present thesis values of $N \leq 35$ are considered.

Knowing K_{IC} (from literature data or independent measurements), v_C/v_t and N, the threshold stress intensity factor, K_t, can be obtained from equation (3.1). Integration of this equation gives the time dependence of the crack length. The CN specimen compliance is calculated via the slice model proposed by Bluhm [115], eq.(2.38-2.46), Appendix 1. The load is obtained from the displacement and compliance data and the crack driving force follows from eq. (2.50) and K_I from eq. (2.12).

3.1.1 Model and Numerical Analysis

The total compliance of the system is composed of that of the machine (C_M) and that of the specimen (C_S), so that for the constant displacement rate conditions, the load is given by;

$$P = (D_S+D_M)/(C_S+C_M) = \dot{D}\cdot t/(C_S+C_M) \qquad (3.2)$$

where D_S is deflection of the specimen (or the load applica-

tion point displacement), D_M is deflection of the machine, $\dot{D}$ is the displacement rate, t is time of loading and P is load. Assuming the reality of a blunt chevron tip, the specimen is initially loaded in a linear regime (no crack growth) up to time $t=t_0$. At this moment (point T, Fig. 3.1), $K_I=K_t$, the total deflection is D_0, the load is P_0 and a new count of time, τ, is initiated. Equation (3.2) now becomes;

$$P(\tau) = (\dot{D}\cdot\tau+D_0)/(C_S[\tau]+C_M) \qquad (3.3)$$

where $\dot{D}_0=\dot{D}\cdot t_0$. At $P=P_0$ τ is taken as zero and at fracture initiation the specimen compliance, C_S, is taken as the initial value, C_{Si};

$$P(\tau=0) = D_0/(C_{Si}+C_M) = P_0 \qquad (3.4)$$

As the crack propagates, the values of K_I and G_I are obtained from standard fracture mechanics formulae (2.7). Equations (2.51, 2.50) will be utilised for the CN geometry.

The threshold values of load (P_0), time (t_0) and deflection (D_0) are obtained from equations 3.3 and 2.51, i.e.;

$$P_0 = K_t\cdot B\cdot\sqrt{W}/Y^*(x_i) \qquad (3.5)$$

$$t_0 = P_0\cdot(C_{Si}+C_M)/\dot{D} \qquad (3.6)$$

$$D_0 = \dot{D}\cdot t_0 \qquad (3.7)$$

Substituting (3.3) into (2.51) and combining with (3.1);

$$v = v_c \cdot \left[\frac{\dot{D}\cdot\tau + D_0}{K_{IC}\cdot(C_S+C_M)}\right]^N \cdot \left[\frac{E}{2BW} \cdot \frac{C'\cdot(x_1 - x_0)}{(x - x_0)}\right]^{N/2} \qquad (3.8)$$

where $C' = dC/dx$ for simplicity.

Rearrangement of the parameters in equation (3.8) to assemble together the constants, the variables with τ and the variables with x gives;

$$dx/d\tau = F\cdot f_1(\tau)/f_2(x) \qquad (3.9)$$

where;

$$F = \text{const} = v_c/W\cdot\{E\cdot(x_1-x_0)/(2\cdot B\cdot W\cdot K_{IC}^2)\}^{N/2} \qquad (3.10)$$

$$f_1(\tau) = (\dot{D}\cdot\tau + D_0)^N \qquad (3.11)$$

$$f_2(x) = \{(x - x_0)\cdot(C_S + C_M)^2/C'\}^{N/2} \qquad (3.12)$$

Separation of the variables in (3.9) and integration yields;

$$\int_{x=x_i}^{x} f_2(x)\,dx = F\cdot\int_{\tau=0}^{\tau} f_1(\tau)\,d\tau \qquad (3.13)$$

or;

$$I(x) = F\cdot(\dot{D}\cdot\tau + D_0)^{N+1}/\{\dot{D}\cdot(N+1)\}\Big|_{\tau=0}^{\tau} \qquad (3.14)$$

where I(x) is the left-hand side of equation (3.13), solved numerically in steps of x = 0.01. Evaluation of (3.14) between τ and τ=0 gives the time after which the crack would

extend from its initial length x_i, to x, i.e.;

$$\tau = \dot{D}^{-1} \cdot \{[\dot{D} \cdot (N+1) \cdot I(x)/F + D_0^{N+1}]^{1/(N+1)} - D_0\} \quad (3.15)$$

The time τ can only be obtained by proper integration of $I(x)$. To simplify the problem, each parameter was normalized using the following constants : time(1 sec) ; length (1mm) ; deflection rate (1 µm/sec) ; compliance (1µm/N) ; K_I (1MPa$\sqrt{m}$) ; G_I (1J/m^2) ; E(1GPa) ; The Poisson's ratio was assumed constant and equal to 0.3. This procedure resulted in dimensionless formulae suitable for numerical analysis. The specimen compliance and its derivative, required for numerical representation of eq. (3.12, 3.13) were calculated via the Bluhm slice model, utilizing a crack increment between slices of 0.002 (subroutines XCOM, COMX, Appendix 1). $I(x)$ was obtained numerically following the trapezoidal rule with Δx steps of 0.002.

The primary purpose of this analysis is to model the fracture toughness and work-of-fracture tests utilising CN bars of ceramics. The variable parameters were chosen as characteristic of the three main groups of ceramic materials (Young's modulus E is given in GPa, K_{IC} and K_t in MPa$\sqrt{m}$) i.e. ; Type I, high stiffness and medium toughness (Al_2O_3, SiC), E=400, N=30, K_{IC}=3, K_t=2 ; Type II, medium stiffness and enhanced toughness (PSZ), E=200, N=25, K_{IC}=4, K_t=2.5 ; Type III, low stiffness and toughness (microcracked ceramics,

graphite), E=11,N=10, K_{IC}=1.1, K_t=0.3. Some results are also presented for glass (E=70, N=15, K_{IC}=0.8, K_t=0.4).

Unless othewise stated, the testing system parameters are fixed at C_M=0.1 μm/N, the bend span ratio n=S_1/S_2=2, the specimen depth and width B=W=4 mm and $v_C/v_t=10^5$. The results are presented as a function of specimen deflection, D_S [μm], or the fractured area, A, normalized to the maximum area available for fracture. For example, in Fig.2-12 at a crack extension of x, A = ORP/MNOPRST.

3.1.2 Implications for the Fracture Toughness Test

Figures 3-2 A,B show the variation of K_I for material Type I with crosshead displacement rates between 0.1 and 2.0 μm/s. The "hump" on the K_I vs D_S graph (Fig. 3-2A) originates from the characteristic variation of the geometric factor $Y^*(x)$ for the CN specimen, (eq. 2.52, Fig. 2-14B). Initially $Y^*(x)$ is large and constant since there is no crack growth. As the crack initiates at $K_I=K_t$ and grows, $Y^*(x)$ drops to a minimum value, Y_m, and then increases again. The combination of load, P, specimen compliance and $Y^*(x)$ variation results in K_I curves as shown in Fig. 3-2A.

It is clear from Fig. 3-2A that the maximum load, P_m, can only be correlated with K_{IC} for a displacement rate of 2 μm/s. For slower cross-head velocities, critical conditions occur after P_m has been passed. The complete load-displacement curve is only drawn for $\dot{D}$=2μm/s, but the displacement at maximum load is independent of the cross-head velocity

(compare the two dashed $P-D_s$ curves for $\dot{D}$=0.5 and 0.1 μm/s, Fig. 3-2A). If equation (3.1) holds true above $K_I=K_{IC}$ (i.e. the fracture toughness is larger, than the assumed 3 MPa√m) or if the critical velocity is larger than the assumed 10^{-3} m/s (continued dashed lines, Figs.3-2 A,B), the maximum value of K_I is reached after the maximum load. Since a sharp increase in N is expected in this range, quantitative conclusions are meaningless. However, a qualitative description of stick-slip crack motion has been attempted [16].

The correlation of P_m and K_{IC} proposed by Munz et al. [126,127,146], requires $P=P_m$ and $Y^*=Y^*_m$ at $x=x_m$ (Fig. 2-14), resulting in equation (2.51);

$$K_{IC} = P_m \cdot Y^*_m/(B \cdot \sqrt{W}) \qquad (2.51)$$

Y^*_m can be conveniently calibrated [146], simplifying fracture toughness testing of ceramics. According to Fig. 3-2A, if subcritical crack growth is taken into account, the above procedure is only correct when a certain value of displacement rate is utilised.

In Fig. 3-2B K_I is plotted vs. the normalized fracture area A ($A=A_m$ at $Y^*=Y^*_m$ as indicated), for the same experiments. The calibration procedure [146] demands are only met for a discplacement rate of 2 μm/s. This conclusion agrees with the experimental observation that, upon decreasing the cross-head speed, the slow fracture range increases beyond

the maximum load (sometimes up to complete fracture, as required for WOF experiments).

Figure 3-3 duplicates Fig.3-2B for the Type II material (PSZ). Below $\dot{D}$=0.5 μm/s, it is impossible to measure K_{IC} with the present experimental parameters (n=2, C_M=0.1 μm/N). This situation makes the WOF experiment attractive, but the value of resistance-to-fracture calculated therefrom will depend on the displacement rate. For this case, the fracture toughness can be calculated from the maximum load via calibration utilizing $\dot{D}$=4 μm/s, i.e. twice the value for the Type I material.

Similar plots for Type III materials are shown in Fig. 3-4A,B. The most striking difference between this material and the previous two is the slow K_I variation with A. The cross-head velocity must reach the high value of 20 μm/s (1.2 mm/min) for critical conditions to be attained at the maximum load value in the constant displacement rate experiment. The dashed lines in Fig. 3-4A,B show the variation of the load and stress intensity factor assuming a wider range of subcritical crack growth, i.e. $v_t=10^{-10}$ and $v_C=10^{-2}$ m/s. In such cases even higher $\dot{D}$ values are necessary to measure the K_{IC} (now defined as K_I at a crack velocity of 10 mm/s).

The stress analysis error for the four-point bend bar (discussed in detail in Section 4.8) can be reduced by increasing the bend span ratio,n [147]. The influence of an increased n ratio is shown in Fig. 3-5. Increasing n promotes

fracture stability and this must be considered in the K_{IC} test. The cross-head velocity for K_{IC} measurement at n=2 is 2 μm/s, Fig. 3-2A,B. If the span ratio is increased to 4, this velocity must be doubled in order to meet the calibration procedure [146] requirements.

In the following analysis, an attempt is made to estimate the error resulting from the application of equation (2.51), if the subcritical crack growth that occurs before the maximum load P_m is reached, is different from $(x_m - x_0)$. If the true value of K_{IC} is known, the relative error, e, in the fracture toughness measurement can be obtained from the formula;

$$e = (\bar{K}_{IC} - K_{IC})/\bar{K}_{IC} \qquad (3.16)$$

where $\bar{K}_{IC}$ is calculated from eq. (2.51). It is assumed that fracture initiates at the chevron tip before P_m is reached. The cases of difficult fracture initiation due to, for example, an excessively wide notch [125], are not considered relevant here and will be discussed in Section 3.2.

Consider the load-displacement curve, Fig.3.1, as recorded in the fracture toughness test. At a slow loading rate, the $K_I = K_{IC}$ condition will be reached (if at all), somewhere between points M and Z. An increase in the loading rate reduces the subcritical crack growth to such an extent that $K_I = K_{IC}$ at $P = P_m$ (i.e. the condition which allows aplication of eq. 2.51) or even at some load, P_z, such that

$P_0<P_z<P_m$ somewhere between points T and M (Fig. 3.1). The recorded maximum load is now P_z. In both cases equation (2.51) results in a value of $\bar{K}_{IC}$ smaller than the true K_{IC}. It is characteristic of the CN specimen that suppression of subcritical crack growth in fast-displacement rate fracture toughness test would result in erroneous measurements (quite the opposite for ST specimens). The reason is that the CN specimen requires a precisely determined (and not minimised) amount of subcritical crack growth Δx ($=x_m-x_0$) at the moment of catastrophic fracture to utilise the calibration equation (2.51).

Generally the fracture toughness test using the CN specimen with an easily-initiating crack gives a conservative estimate of K_{IC}.

This discussion is quantified by numerical simulation for the three types of materials and glass. $\bar{K}_{IC}$ was obtained from eq. (2.51) wherein P_m was taken as the true maximum load if the specimen fractured catastrophically between points M and Z (Fig. 3-1) or as P_z at catastrophic fracture between points T and M. The K_{IC} value is assumed to be the true one at the outset of the model calculations. The results, obtained from eq. (3.16), are plotted against the exponent N, Fig. 3-6, against the displacement rate in Fig. 3-7A and against the displacement rate and machine compliance (for glass only) in Fig. 3-7B.

Figure 3-6 shows that the fastest changes of e occur

for materials of Type I or II when N<30 whilst for graphite or glass they occur for N<15. These observations satisfy the choice of N values in the simulation experiments. The value of e levels at -8% and N>40 for Type I and II materials and at -2% for glass and graphite with N>20 (Fig. 3-6 for typical experimental conditions).

In slow displacement rate tests, the underestimation, e, is linear with log $\dot{D}$ and can reach -20 to -30 % (Fig. 3-7A). As $\dot{D}$ increases (the branches A_iB_i, i=1,2,3), the curve reaches a maximum (e=0) for the conditions predicted in Figs. 3-2 to 3-4. As $\dot{D}$ further increases, the increase of the absolute error value is predictable as long as the fast displacement rate does not hinder fracture initiation at the chevron tip (in this case, an overload results and the calculated K_{IC} is an overestimation, [12S]). If the ideal displacement rate (resulting in e=0) is unknown, the initial values of $\dot{D}$ should be such that catastrophic fracture takes place after P_m is reached (branch A_iB_i of Fig. 3-7A or MZ of Fig. 3-1). Subsequent experimentation with increased $\dot{D}$ values should result in a coincidence point where $P=P_m$ at $x=x_m$ as required for accurate K_{IC} calculation from equation (2.51).

Figure 3-7B shows curves for glass similar in shape to those in Fig. 3-7A. The testing system compliance, C_M, can have a profound effect on the accuracy of the fracture toughness test. A displacement rate of 2 μm/s will result in an accurate measurement for a stiff system (C_M=0.1 μm/N) but

in an underestimation of 15 % for a soft system (C_M=10 μm/N). Use of a soft testing system requires faster loading rates, since an increased portion of the cross-head displacement is expended on machine deformation. For large C_M values (i.e. a soft system), the error of measurement is less sensitive to changes of the displacement rate.

3.1.3 Implications for the WOF Test

The idea of the WOF experiment is to convert the work done by the loading system exclusively to an increment of the surface energy of the broken specimen. In practice, it is either performed in one cycle to yield an average value over the entire surface created [114] or by repeated loading-fracture-unloading cycles [96, 120, 130] resulting in the resistance-to-fracture as a function of the crack extension.

Both types of work-of-fracture experiments are modelled in terms of the stress intensity factor. Considering the constant displacement rate test, curves similar to those in Fig. 3-2B, but for increasing initial crack length are presented in Fig. 3-8A for a Type I material. The consecutive K_I vs. A curves, numbered 1 to 7, represent variations of the stress intensity factor during hypothetical WOF tests for specimens having an initial crack length x_i equal to 0.42, 0.50, 0.55, 0.60, 0.65, 0.70, 0.80 respectively (at constant x_0=0.40). The broken curve (#8) is expected when x_i=0.90. Consequently, the curves also represent the variation of the stress intensity factor in the loading-fracture-unloading

experiment.

For samples #1 to #5 it is not possible to perform continuous WOF tests since the crack accelerates to a critical velocity (points M,N,S, Fig. 3-8A) and failure follows. For an initial crack length larger than 0.65 (curve #6), full stability is expected for a continuously loaded specimen. The "effective surface energy", 2Γ, calculated from such an experiment will be equivalent to the area under the curve type 6,7,8, expressed in terms of the strain energy release rate G_I, divided by the total fractured area. The resultant value will depend on the initial crack length and it seems will approach the threshold K_t or G_t as defined by equation (2.12), for crack lengths approaching 100% of the specimen width. This result explains the dependence of the WOF-2Γ on the crack length [120,130].

Considering the repeated loading-slow fracture-unloading experiment for one specimen, a similar set of curves, Fig. 3-8A, would be generated, but cut at unloading points $U_1, U_2 \ldots U_i$ (i.e. after crack extension in cycle #1 by 0.08, in cycle #2 by 0.05 etc.). The experiment proceeds in sequence A_1-U_1-A_2-U_2-A_3-U_3- etc. It is assumed that unloading is fast enough to suppress any accompanying subcritical crack growth and proceeds at least to the point when $K_I = K_t$ (in the present thesis unloading was performed down to $K_I = 0$). The danger of uncontrolled fracture appears on cycle #5 when $U_5 \simeq S$ (Fig. 3-8A). For such a sequence of repeated load-fracture-unload

(LFU) tests, the calculated 2Γ will initially increase and subsequently diminish (after cycle #5) to the limit, G_t.

To illustrate this point quantitatively, the following numerical integration was performed;

$$WOF = \left(\int_{A_i}^{A_{i+1}} G_I dA \right) / \Delta A \qquad (3.17)$$

where $\Delta A = A_{i+1} - A_i$ is an increment of the fracture area in subsequent LFU cycles. G_I was obtained from Fig.3-8A using equation (2.12). Equation (3.17) is valid for a perfectly elastic material or for that part of the total work-of-fracture which was converted into fracture surface energy. The results are presented as curve F (at C_M=0.1 μm/N and displacement rate 0.1 μm/s) in Fig. 3-8B. It appears that the WOF values decrease towards G_t as full fracture is approached. If an infinitely stiff testing system is considered (i.e. C_M=0, curves B, C), the predicted values of WOF are different. The WOF values also change for varying displacement rates (compare curves B, C and F in Fig. 3-8B). As A=100% is approached however, the differences decrease and all the curves appear to approach WOF = G_t.

Similar plots for Type III material are shown in Fig. 3-9. None of the curves (numbered 1 to 8) cross the critical fracture line (K_I=K_{IC}) so the test is stable both for continuous and intermittent WOF experiments. The resulting 2Γ does not increase in the initial LFU cycles due to the flat

K_I vs. A curve. As noted for the Type I material, 2Γ tends to G_t in the limit. A uniform decrease of the quantities characterising the fracture of Type III materials with crack extension suggests that the threshold values G_t and K_t can be determined by simple extrapolation [32]. Integrated G_I curves for graphite for (C_M=0.1 μm/N and C_M=0) are shown in Fig. 3-98. As full fracture is approached, the differences between the two plots decrease and both tend to G_t.

The variation of measured resistance-to-fracture with crack extension predicted by the present analysis (Fig. 3-88, 3-98) was recently reported for glass specimens [130]. Since subcritical crack growth was neglected (i.e. during crack propagation G_I=constant=G_{IC}), the decrease observed in the calculated values of G_{IC} was inexplicable. Characteristically, the effect was more profound in air than in an inert atmosphere. Correlations between the present model and experimental results for fully and partially stabilized zirconia, SiC and graphite are in press [96] and are presented in the experimental sections of this thesis.

It must be emphasized that numerical analysis cannot be performed at A>80% (or x>0.95) due to uncertainties in the compliance equation. Therefore, the limit of the strain energy release rate (or WOF) curves cannot be unequivocally defined. The expected variation for A>80% is indicated by broken lines in the figures.

It can be concluded from the above analyses that the

occurence of subcritical crack growth during constant displacement rate experiments on chevron-notched beams explains the observed specimen behaviour and influences the fracture testing routines.

The main advantage of the CN sample over other configurations is the in-situ initiation of a sharp crack. The fulfillment of two exclusive requirements, (i.e. sharp, semi-static crack initiation followed by propagation) is intrinsic to valid fracture toughness tests. For metallic specimens this has resulted in two stages to the tests, i.e. fatigue crack initiation followed by loading to K_I-K_{IC}. For CN brittle specimens the two stages can immediately follow one another but a predetermined displacement rate must be utilised. The less-than-ideal shape of the real chevron notch tip requires that an overload be applied to initiate fracture, especially if there are any compressive surface stresses or an excessively wide notch. This is the main reason that most experiments on CN specimens are confined to relatively low displacement rates (0.02 to 0.05 mm/min). Such conditions promote subcritical crack growth but, once fracture has been initiated, the displacement rate must be increased to relate the maximum load to the K_{IC}.

If the stress intensity factor at "fast" (i.e. critical) fracture is to be measured, the following steps must be taken; (A) a stable crack must initiate before the maximum load is reached ; (B) ceramics Type I (Al_2O_3, SiC) must be

tested at a cross-head speed 0.12 mm/min for $S_1/S_2=2$. If the bend span ratio is increased, the displacement rate must be increased by the same factor ; (C) for Type II (partially stabilized zirconia) specimens to yield valid K_{IC} values, the displacement rate must be 0.24 mm/min at an assumed value of N=25 ; (D) the testing of low stiffness, low toughness ceramics (Type III) requires extremely high displacement rates $\geq$ 1.2 mm/min.

The above conclusions evolved from the assumption of numerical values to simplify the analysis. Whilst N$\leq$35 may be justified (Fig. 3-6), the ratio v_c/v_t can be larger than assumed (10^5). Such would increase the range of subcritical crack growth (Fig. 3-4). The proposed displacement rates must only be considered therefore as guidelines. In most cases, the coincidence point of maximum load at $K_I=K_{IC}$ for given experimental conditions (i.e. loading rate, geometry, machine stiffness etc.) is not known. Therefore a series of fracture toughness tests must be performed at constant displacement rates such that instability occurs after the maximum load is reached. Subsequently, the displacement rate can be increased so that instability occurs at the maximum load value and equation (2.51) is valid.

It is not possible to measure K_{IC} via a WOF experiment because the two quantities are juxtaposed. A knowledge of the crack growth kinetics and the parameters of the testing system are an essential factor in the experiment. Subcriti-

cal crack growth is responsible for the decreasing "partial" work-of-fracture, 2Γ, with crack extension in multiple loading-fracture-unloading tests. In the limit as the crack length approaches 100% of the specimen width, the work-of-fracture seems to approach the resistance of the material to fracture initiation.

3.2 The Load Relaxation Technique

The constant displacement rate experiments, discussed above, are used for fracture toughness or WOF measurement. If the testing system is not hard enough however, destabilization and catastrophic fracture can occur at an undesirable moment.

In order to increase fracture stability, the energy flux from the testing system into the specimen must be reduced. In the limit of an ideally stiff machine, no external work is performed on the cracking material during a zero-displacement rate test (known as a load relaxation, LR, or fixed grips test). Since this technique provides a record of load relaxation against time, it is possible to determine the crack velocity vs. the externally applied stress intensity factor.

Some consideration of fracture stability was presented in Section 2.1.3. In the present chapter the general expression (2.26) is anlysed for the LR test on a CN specimen for particular experimental conditions.

The bending geometry and the testing system stiffness

will receive particular attention. It is assumed that a non-ideal chevron notch influences the load at apparent fracture initiation. Equivalently, a larger deviation of the notch from ideality results in a larger overload at the moment of fracture initiation.

3.2.1 Model and Calculations

Consider the load relaxation experiment (Fig.3-10A,B). The specimen is loaded at a constant deflection rate above the fracture initiation point M. The machine crosshead movement is stopped after the crack has extended from x_0 to x_i (point Y),i.e. after deviation from linearity of the load-deflection curve.Since the crack has moved, the condition for crack position instability is satisfied,i.e.;

$$G_I \geq G_t \qquad (3.18)$$

At the moment the crosshead stops, the specimen is loaded to P_i and deflected to $D_i=D_i(x_i,P_i)$. Subsequently the specimen deflection increments are taken up by the machine [33];

$$D(x,P) = D_i + C_M\cdot(P_i - P) \qquad (3.19)$$

If the compliance of the testing machine, C_M, is constant, the deflection of the specimen increases linearly (eq. 3.19, Fig. 3-10A). Since the total deflection D_{tot} is constant, the relaxation load, P, is governed by the equation;

$$D_{tot} = P\cdot[C_M + C_S(x)] = D_i + C_M\cdot P_i \qquad (3.20)$$

where $C_S(x)$ is the compliance of the sample with arbitrary crack length x. Equations (3.19,3.20) define the hypothetical load-deflection curve in terms of the machine characteristics. According to the definition of compliance, at the outset of the LR experiment;

$$D_i = P_i\cdot C_S(x_i) \qquad (3.21)$$

If the crack moves to $x=x_i+\Delta x$, then, from eq. 3.20;

$$P = [D_i + C_M\cdot P_i]/[C_M + C_S(x)] \qquad (3.22)$$

The compliance C_S is obtained from the Bluhm slice mo del [115] (Appendix 1). The strain energy release rate is determined using eq. (3.22, 2.50).

Due to the notch blunting (discussed in the previous section) fracture initiation requires a certain overload, the value of which depends strongly on the specimen preparation routine. In the present analysis values of G_I were calculated at variable fracture initiation loads and compared with the arbitrary fracture resistance function R(A). Following the discussion of fracture stability (Section 2.1.3), three types of conclusion can be drawn regarding the crack extension: (A)

that fracture arrests at $G_I(A)<G_t$; (B) that fracture advances at $G_I(A)\geq G_t$, stably at $dG/dA<dR/dA$ and unstably at $dG/dA\geq dR/dA$. For simplicity, it will be assumed that $R(A)=G_t=R_i$ for most cases and all G_I values will be normalized to R_i. For the case of an increasing fracture resistance curve, both G_I and $R(A)$ are normalized with respect to R_i (Fig. 3-11). The testing system parameters are similar to those assumed in the previous section ($S_1/S_2=2$, $S_2/B=S_2/W=2$). The material parameters are those of an average PSZ [148] ($E=170GPa$, $R_i=21J/m^2$, $\nu=0.3$). Unless other stated, the crack length at the load relaxation start is $x_i=x_0+0.1$. The variation of G_I is plotted against the normalized fracture area, A/A_0, counted from the LR start. In Fig. 3-10B A=MNPR and A_0=KLMNOPRST at $x=x_j$. Therefore, at the fracture initiation moment $A/A_0=0$ but at the completed fracture $A/A_0<1$, depending on the initiation crack length x_i.

3.2.2 Discussion of Results

Fig. 3-11A shows the influence of the apparent fracture initiation load, P_i, on the shape of the G_I/R_i curves. As previously discussed, for a non-ideal CN specimen, P_i is sensitive for the notch preparation routines. At constant relative machine compliance $m=C_M/C_{Si}$ (where C_{Si} is C_S at $x=x_0$) the value of P_i would not influence the amount of stable crack extension as all the curves have a minimum at constant $(A/A_0)_{min}$. The magnitude and slope of G_I/R_i changes markedly. When P_i is increased, only those specimens with

significant R-curve behaviour (at each point $dR/dA > dG_I/dA$) or high fracture toughness G_{IC} (at each point greater than G_I) will survive the crack acceleration region (between MIN and MAX in Fig.3-11A). For such a specimen, once the fracture area is bigger than $(A/A_0)_{max}$, the crack will proceed stably up to the arrest point at $G_I/R_i=1$ or complete fracture, whichever comes first.

The two dashed-line curves in Fig. 3-11A represent deviations from the "standard" test conditions. The curve $R/R_i=f(A)$ simulates a hypothetical rising fracture resistance for the material which will survive the crack acceleration region MIN to MAX, i.e. the slope of the dotted line is greater than that of the G_I/R curves. Now the arrest point (AR) at $G_I=R$ is reached sooner and additional flux of strain energy is required to continue the fracture. The second, opposite type of behaviour is expected for the specimen suffering constant load, P_i, (here $P_i=80$ N) giving the relative strain energy curve G_I/R. According to relation (2.7), this curve is obtained simply as;

$$G_I = G_I \cdot (P_i/P)^2 \qquad (3.23)$$

After a short period of stable crack extension, the G_I/R curve soars steeply and the crack accelerates to a critical velocity immediately after the minimum point.

As the fracture initiation load, P_i, is lowered, the

difference between the maximum and minimum values of G_I/R_i diminishes, giving an almost flat curve at P_i=50 N (assuming no arrest due to an increasing fracture resistance). So careful preparation of the experiment can result in crack propagation under approximately constant (within 5%) G_I conditions. This is particularly attractive in view of the simplicity of CN specimen preparation when compared with other "constant-G_I" specimen geometries (tapered or constant moment DCB, double torsion). Certainly, one can expect extremely slow crack propagation for G_I values close to R_i.

For a stiffer testing system relative to the initial stiffness of the sample (m=1, Fig. 3-11B), the instability region disappears and an initiation load of 50 N will result in quick fracture arrest. Such behaviour opens up the possibility of repeated fracture initiation-arrest studies on one sample. After apparent crack arrest at point B, the crosshead is moved to the apparent initiation moment C and stopped. Again the G_I/R_i curve will follow a decreasing path CD to the next arrest moment at G_I=R_i. Of course, the dead-load curve G_I/R_i is uninfluenced since, for these conditions, m is infinitely large.

Substantial crack extension before the start of LR can cause destabilization due to crossing beyond the minimum point on the G_I/R_i curve. This effect is shown in Fig. 3-11C, at x_i = 0.5, 0.6 and 0.7. Stability can be regained if the crack is deep enough to initiate the test after the maximum

on the G_I/R_i curve.

An increase of the depth of the initial notch, x_0, by 0.2, results in a twofold increase of the crack driving force for the same fracture initiation load.This effect is compared in Fig. 3-11D (x_0=0.3, x_i=0.4) and Fig. 3-12A (x_0=0.5, x_i=0.6), together with its dependence on the machine compliance. The crack extension before arrest for a stiff testing system is larger in the second case. The critical value for the system stiffness against fracture stability is m=1.

Figure 3-12B illustrates the effect of increasing the bend span ratio, $n=S_1/S_2$, for constant C_M=0.15 μm/N. A decrease of n at constant C_M causes an increase of m and decreases the stability.

Finally, Fig. 3-12C shows the effect of the side notch length, x_1. This is the only case where the discontinuity in the G_I curve at $x=x_1$ (due to the assumed constant value of the shear correction factor k, even at $x=x_1$, i.e. the ST specimen) is observed. The shorter x_1, the less the influence of the chevron notch shape and the G_I/R_i curve becomes similar to that of a straight-through-notch specimen.

It can be concluded that, for the CN-LR test, there is always a stable crack extension regime at the beginning of the fracture due to the negative slope of the G_I curve. For specimens which survive the fracture acceleration region, the crack is inevitably arrested at G_I/R_i=1. The slope of the G_I curve can be controlled by choice of appropriate x_0, x_1, x_i,

P_i, C_M, S_1/S_2 values. This analysis provides an essential data for experimental design.

3.3 The Electrical Potential Drop Technique to Follow Crack Growth

The potential drop (PD) technique has attracted interest in the study of fracture and fatigue in electrical conductors for more than 20 years . The first calibration results were reported by Anctil et al. in 1963 [149]. The analytical solution of Laplace's equation, governing the electrical potential distribution in the vicinity of a crack was attempted by Johnson in 1965 [150] and Gilbey and Pearson in 1966 [151]. Since that time numerous works have appeared utilising the analytical solution for the PD and comparing it with experimental results.

The electrical equipotential line distribution around a crack was investigated by Richtie et al. [152]. They suggested opti mal conditions for current input and potential probe posi tion. Aronson and Richtie continued by optimizing the tech nique via finite element analysis [153].

The nonzero volume crack effect was considered by Clark and Knott [154] and Knott [155] and the sources of error in the technique were reviewed by Druce and Booth [156]. The important conclusions from these investigations are, that the method is highly sensitive and variation of the potential probe position close to the crack has relatively little effect.

The cited works assumed a straight-through crack front except [156] in which the errors resulting from crack bowing were considered. The solution for the Laplace's equation for polygonal domains was undertaken by Papamichael and Whiteman [159,160]. These authors admit that complicated boundary conditions (e.g. for a three-dimensional solution) may result in serious difficulties for the analytical approach. As an alternative, a finite element method [160] or a purely experimental calibration is suggested [155, 156, 161] as being more viable.

Frequently, the crack front cannot be approximated by the ST shape. The most obvious case is the CN sample (Fig. 3-138) utilised in this thesis.

3.3.1 Plane solution for Potential Drop in a Notched Conductor

Modification of the solution of the Laplace equation for the electrical potential distribution around a crack [157] gave the following equation for dimensionless crack length, x;

$$x = (2/\pi)\cdot\cos^{-1}[(1 - P_1^2)/(P_2 - P_1^2\cdot P_3)] \qquad (3.26)$$

where;

$$P_1 = [\exp(U/2k) - 1]/[\exp(U/2k) + 1] \qquad (3.27)$$

$$P_2 = \operatorname{sech}^2(\pi y/2W) \qquad (3.28)$$

$$P_3 = \operatorname{sech}^2(\pi d/2W) \qquad (3.29)$$

The parameters in this equation are described in Fig. 3-13A showing the geometry and cross-section of ST sample. U=U(x) is the electrical potential drop between surface points E,F (distance=2y) for a normalized crack length x and constant direct current applied between the surface points A and G (distance apart=2d). The proportionality constant k is found by measurement of $U(x_0)$, for a known initial crack length $x=x_0$. In particular, it follows from eq. (3.26) that, if d>2W (the normal experimental situation for bend bar), then for $x_0=0$;

$$k = U(0) \cdot W/(2 \cdot \pi \cdot y) \qquad (3.30)$$

Equations (3.27, 3.30) imply that drop of potential-crack growth data should be stored in the dimensionless form suggested by Anctil et al. [149];

$$Q(x) = U(0)/U(x) = R(0)/R(x) \qquad (3.31)$$

where R(0) and R(x) are the electrical resistances of the reference, unnotched and notched (ST) samples respectively. R(x) is measured across the crack between the lines $Y=\pm y$ (current is applied between lines $Y=\pm d$), Fig. 3-13A. R(0) is measured either as R(x) if the initial notch has not been cut

yet, or between any lines C,D (2y' distance apart), while the current is applied between lines Y=0 and Y=-d.

Further simplification of the numerical analysis and data collection procedure results if the distances 2d,2y' and 2y are normalized to the sample width W;

$$C_1 = 2y'/W \; ; \; C_2 = 2y/W \; ; \; C_3 = 2d/W \qquad (3.32)$$

with the result that;

$$P_1 = [\exp(\pi \cdot C_1/2 \cdot Q) - 1]/[\exp(\pi \cdot C_1/2 \cdot Q) + 1] \qquad (3.33)$$

$$P_2 = \operatorname{sech}^2(0.25 \cdot \pi \cdot C_2) \qquad (3.34)$$

$$P_3 = \operatorname{sech}^2(0.25 \cdot \pi \cdot C_3) \qquad (3.35)$$

The agreement between this theory and experiments is good [149,151].

3.3.2 Chevron-Notched Specimen

Consider the hypothetical process of slicing the ST specimen in the direction normal to the crack front (Fig. 3-13A). The system can be treated as a set of resistors connected in parallel. Clearly, the process neglects the interaction between "slices" in contact in real sample.The validity of this assumption is tested by experimental calibration.

Due to the specimen symmetry, the interlaminar current

density in the Z-direction should be negligible. The proposed equivalent circuit would therefore possess interlaminar resistances much larger than those along the slice, i.e. the parallel configuration. The appropriateness of this analysis is vindicated by the good experimental agreement obtained (Section 4.3.2). The simplicity of the final formula facilitates its application (the complex three-dimensional finite element analysis requisite for exact solution is avoided).

If the ST sample is "sliced" into n slices in a direction normal to the crack front, each slice having the same notch length x and resistance $R_i(x)$, then, from eq.(3.31);

$$Q(x) = Q_{ST} = R(0)/R(x) = R(0)/[n \cdot R_i(x)] \qquad (3.36)$$

Since the current density in any plane parallel to the XY plane is the same in each point along an arbitrary line (x_0, y_0, z), the following relation is valid;

$$1/n = A_i/A_0 \qquad (3.37)$$

where A_i is the area of the uncracked section of slice i and A_0 is the area of the uncracked part of the specimen (Fig. 3-13A). Accordingly;

$$Q_{ST}(x) = [R(0)/R(x)] \cdot [A_i/A_0] = n \cdot [R_i(0)/R_i(x)] \cdot [A_i/A_0] \qquad (3.38)$$

or $Q_{ST}(x) = \sum_{i=1}^{n} Q_{iST}$ where $Q_{iST}(x) = Q_{ST}(x)/n = R(0)/R_i(x)$. For the ST sample, $Q_{ST} = R_i(0)/R_i(x)$ and equation (3.38) is always fulfilled.

However, the slicing procedure for the CN specimen (Fig. 3-138) results in a series of approximately straight-through samples of changing conduction area $A_i(x_i)$ and resistance $R_i(x_i)$. For each slice therefore eq. (3.38) is applied with a particular $Q_{iST}(x_i)$ and a particular $A_i(x_i)$.

Defining the Q parameter for the CN sample as;

$$Q_{CN}(x) = R(0)/R(x) \qquad (3.39)$$

and approximating the system as a set of parallel resistances and applying Ohm's law, gives;

$$Q_{CN}(x) = \sum_{i=1}^{n} R(0)/R_i(x_i) = \sum_{i=1}^{n} Q_{iST}(x_i) \qquad (3.40)$$

or, from eq. (3.38);

$$Q_{CN}(x) = \sum_{i=1}^{n} Q_{ST} \cdot A_i/A_0 \qquad (3.41)$$

It can easily be shown (for notation see Fig. 3-138), that, for $x \leq x_1$;

$$A_0 = 0.5 \cdot B \cdot W \cdot [2 - x - x_1 + (x - x_0) \cdot (x_1 - x)/(x_1 - x_0)] \qquad (3.42)$$

or;

$$A_0 = 0.5 \cdot B \cdot W \cdot V(x)$$

and for $x \geq x_1$;

$$A_0 = B \cdot W \cdot (1 - x_1) \tag{3.43}$$

and;

$$A_i = \Delta B \cdot W \cdot (1 - x_i) \tag{3.44}$$

For $x \geq x_1$ the plane solution (3.26) is applied directly. The influence of the chevron shape notch on the specimen properties is proportional to the difference, $(x_1 - x_0)$. The limiting case $(x_1 = x_0)$ is the ST sample. The number of "slices" necessary to approximate the CN bar properties is therefore proportional to $(x_1 - x_0)$;

$$n = B/\Delta B = 2 \cdot N \cdot (x_1 - x_0) \tag{3.45}$$

where 2N is the number of slices necessary to approximate the longest chevron, i.e. $x_1 - x_0 = 1$. Thus the notch length increment, $(x_{i+1} - x_i)$, between slices is always equal to (1/N). N was chosen in this thesis as 100 or 500. From eq. 3.41-3.44;

$$Q_{CN}(x) = \sum_{i=1}^{n} \{Q_{ST}(x_i) \cdot (1 - x_i) / [N \cdot (x_1 - x_0) \cdot V(x)]\} \tag{3.46}$$

As the crack grows, a fraction of the "n" slices (n_2 say) have a constant notch length, $x_i = x$, and $Q = Q_{ST}(x)$ (for any other known or assumed crack-front-shape this is simply replaced by $x = f(z)$ and eq. 3.42, 3.43 modified accordingly). For the rest, $(n_1 = n - n_2)$ slices, x_i changes linearly up to x_1. Therefore;

$$Q_{CN}(x) = \sum_{i=1}^{n_2} \{Q_{ST}(x)\cdot(1-x)/[N\cdot(x_1-x_0)\cdot V(x)]\} +$$

$$+ \sum_{i=n_2+1}^{n_1} \{Q_{ST}(x_i)\cdot(1-x_i)/[N\cdot(x_1-x_0)\cdot V(x)] \quad (3.47)$$

and, since;

$$b/B = (x - x_0)/(x_1 - x_0) \quad (3.48)$$

then; $$n_2 = b/\Delta B = (B/\Delta B)\cdot(x - x_0)/(x_1 - x_0) \quad (3.49)$$

or, according to eq. (3.45);

$$n_2 = 2\cdot N\cdot(x - x_0) \quad (3.50)$$

$$n_1 = n - n_2 = 2\cdot N\cdot(x_1 - x) \quad (3.51)$$

Substitution of eq. (3.50,3.51) into (3.47) gives;

$$Q_{CN}(x) = 2\cdot[(1-x)\cdot N\cdot(x-x_0)\cdot Q_{ST}(x)]/[N\cdot V(x)\cdot(x_1-x_0)] +$$

$$+ \sum_{i=n_2+1}^{n_1} [Q_{ST}(x_i)\cdot(1-x_i)]/[N\cdot(x_1-x_0)\cdot V(x)] \quad (3.52)$$

Finally, replacing the summation in eq. (3.52) by H(x) and letting x_i vary from x to x_1, the final formulation is obtained;

$$Q_{CN}(x) = [2\cdot(1-x)\cdot(x-x_0)\cdot Q_{ST}(x) + H(x)/N]/[V(x)\cdot(x_1-x_0)] \quad (3.53)$$

where $Q_{ST}(x_i)$ for $x_i = x$ to x_1 are evaluated via eq. 3.26-3.35.

Equation (3.53) has been verified for a number of model graphite chevron-notched samples of different geometry and probe location. The numerical procedures used are presented in Appendix 2. The results are discussed in Section 4.3.2.

The proposed semiempirical approach leads to a simple relationship between the potential drop and the crack length for a not-straight-through notch in a bar sample. The resulting equation was worked out for the particular case of a CN specimen and was suitably normalized for computer routines.

Despite treatment of the non-straight-through notch specimen as a set of electrically-independent resistances, experimental calibrations agreed with the numerical results with an accuracy comparable to that for the ST crack-front case.

The results presented can be applied to any electrically-conducting material and any defined crack front shape. The method is potentially powerful for fracture studies of materials wherein initiation of atomically sharp notches is difficult. Application of the method to the study of high resistance ceramic conductors is particulary attractive. Such require a relatively low, constant direct current (1 to 300 mA) to obtain an easily-measurable drop of potential (0.1 to 100 mV).

3.3.3 Sensitivity Analysis of the PD Method

In this section the relative potential drop for a CN specimen is calculated via equation (3.53) and plotted in Figures 3-14A to D. The numerical procedures are outlined in Appendix 2. Typical experimental conditions were used to construct these figures, i.e. fixed x_0=0.4, x_1=1.0, except for the ST case where x_0=x_1=0.4, Fig. 3-14D. C_1 is varied from 0.1 to 1.1 in 0.1 steps, C_2 from 0.2 to 0.8 in 0.05 steps and C_3 from 2.0 to 12.0 in 1.0 steps. x is varied from 0.4 to 0.95 in 0.05 steps. Since these three-dimensional plots show general trends only, a sensitivity parameter S (=$\Delta Q/\Delta x$) and an error parameter R (=$\Delta Q/Q$) were also defined. For simplicity, S and R are calculated at Δx=0.1 and in the middle of the scanned x values (i.e. x=0.6 to 0.7), Fig. 3-14E. S indicates the change of Q for crack growth Δx= 0.1. Analysis of the variation of S with C_1, C_2 and C_3 facilitates estimation of the consequences of erroneous measurments of C_i (i=1,2,3) in relation to the crack length, x, calculated therefrom. The parameter R indicates the Q-reading error that would give an x error of 0.1. The optimum combination of C_i should result in maximum S and R values.

The variation of Q with C_i is shown in Figures 3-14 A to C for CN specimen and in Fig. 3-14 D for ST specimen. The corner A is common and x is plotted to the left and C_i (i=1,2,3) to the right of A. Q is plotted vertically from A. The sensitivity,S, and error,R, parameters for the respective

plots are compiled in Figure 3-14 E.

Considering Fig. 3-14A (i.e. plots E1, E2, E3) and the respective first section of Figure 3-14E, the sensitivity improves markedly as C_1 increases and less markedly as C_2 decreases. The error in Q which results in uncertainity in the crack length calculations of $\Delta x=0.1$ is approximately constant and equals 13 to 16%. The sensitivity of the PD technique to detect crack initiation in a CN specimen is low. This is indicated by the leveling of the Q vs. x curves at $x \cong x_0$ (i.e. at point A).

Figure 3-14B (plots E4, E5, E6) shows that an increase of C_2 (at constant C_1) decreases S slightly (see also Section II of Figure 3-14E). Variation of the voltage probe distance, C_2, by 100% (from 0.25 to 0.50) causes a decrease of the output signal Q of only 4%. In other words a large error in the C_2 measurement (resulting, for example, from a large area of contact between the probes and the material) only causes small errors in the crack length calculation, x. This is an important feature of the PD technique and was pointed out previously for the two-dimensional specimen [156].

The last section (III) of Figure 3-14E and Fig. 3-14C (plots E7, E8) illustrate the variation of R, S, and output, Q, with the current probe distance, C_3. S and Q are constant as long as $C_3>3$ (a slight bending of the Q vs. C_3 lines is evident in Fig. 3-14C for $C_3<3$). Thus it is concluded that precise measurement of the distance between the current leads

is also non-crucial.

Similar graphs for the ST specimen are shown in Fig. 3-14D (plots E1A to E4A). The effect of variation of C_1 and C_2 is similar to that for the CN specimen. Small C_2 and large C_1 hinder detection of fracture initiation in the ST specimen. This is indicated by the leveling of the graph E2A at $x \simeq x_0$ and $C_1 = 0.8$ to 1 and $C_2 = 0.25$. In other cases, curvature of the graphs is consistently positive.

It is instructive to compare the sensitivity of the PD technique with that of compliance analysis (CA). In the latter the basic parameter utilised as indicators of the crack length, x, is the slope of the load-displacement line (i.e. the compliance $C(x)$). The potential drop across the crack $U_2(x)$ is used in the PD technique. To compare the response of the "indicator" $C(x)$ or $U_2(x)$, to the crack length increment, two dimensionless functions are defined;

$$S_C = \log\{d[C(x)/C(x_0)]/dx\} \qquad (3.54)$$

$$S_U = \log\{d[U_2(x)/U_2(x_0)]/dx\} \qquad (3.55)$$

S_C and S_U are plotted in Fig. 3-15 for typical experimental conditions (x_0=0.4, S_1/S_2=2 to 4, B/W=0.5 to 2.0, E=100 to 200 GPa, C_1/C_2=0.5 to 2.0). The evaluation was performed numerically (Appendix 1, 2) using a crack length increment $dx \simeq \Delta x = 0.01$.

It turned out that the assumed variation of the specimen parameters does not influence the response curves S_C and S_U. S_U drops to small values on initial crack extension, as expected from the flat portion of the surfaces in Figs. 3-14A to C. It increases significantly only at $x>0.9$. Over the whole range of the crack lengths, the response of the compliance function S_C is larger than the potential drop function S_U (Fig.3-15). Therefore, whenever the CN specimen compliance can be measured with sufficient accuracy (for example at room temperature), CA is favourable over the PD technique. The potential drop method should be applied if compliance measurements are difficult or uncertain, i.e at high temperatures.

The new approach to the CN specimen, taking into account the subcritical crack growth, discussed in the present chapter, facilitates explanation of the experimental data and results in a better understanding of specimen behaviour. The theoretical studies provide invaluable guidelines for the design of the testing system and techniques, the choice of the specimen geometry and experimental planning. These subjects are addressed in the following chapter.

CHAPTER 4

EXPERIMENTAL PROCEDURE

4.1 Materials Fabrication and Characterization

4.1.1 Zirconia-Hafnia Solid Solutions

Two techniques were employed to prepare ZrO_2-HfO_2 solid solutions. The traditional, more efficient and economical method is based on the mixing and sintering of ZrO_2, Y_2O_3 and HfO_2. The main drawback of this route is the long-time/high-temperature sintering required to ensure the formation of a dense, uniform solid solution from the initial > 20 μm powder grains. The material is therefore subject to excessive grain growth and strength deterioration. The second, more sophisticated technique provides for intimate component mixing before the sintering stage. This route starts with soluble salts of Y^{3+}, Zr^{4+} and Hf^{4+} in the required proportions in a common solvent. These are subsequently converted to the oxide form without elemental redistribution.

For the oxide-mixing (OM) route, HfO_2 (97%+, Alfa Prod.), Y_2O_3 (99.99%, Nucor) and ZrO_2 (99+%, Alfa Prod.) were mixed with 5.5 wt% polyvinyl acetate binder (Gelva,

multipolymer solution, Monsanato) and 1.5 wt% of polyethylene glycol lubricant (Fluka Ag) and dispersed in methanol. The slurry was vibromilled (Vibro-Energy Grinding Mill, Sweco) for 3 hours at room temperature in a plastic jar. Stabilized zirconia cylinders were introduced into the slurry to ensure non-agglomeration, intimate mixing and binder and lubricant distribution. Subsequently the solvent was evaporated at 60-80°C under reduced pressure (Rotovapor, Buchi) and then at 120°C and atmospheric pressure overnight. The resulting powder was sieved through 120 mesh, mould shaped into bars at 30 MPa pressure and isostatically pressed at 350 MPa. After shaping the binder and lubricant were carefully burned-out increasing the furnace temperature 40°C/hour to 400°C overnight.

The wet chemical (SFFD) route started from the water soluble sulphates of yttrium (99.9%, Alfa Prod.), zirconium (Alfa Prod.) and hafnyl chloride (reactor grade, Atomergic Co.). The chemicals were dissolved and thoroughly mixed in deionized water in proportions to obtain the appropriate oxide content after calcination. The solution was filtered and gelled with ammonium hydroxide. The gel was allowed to settle and was washed five times with distilled water to remove SO_4^{2-}, NH_4^+ and Cl^- groups. The resultant milk-like hydroxide slurry was spray-frozen into liquid nitrogen to avoid redistribution of the chemicals during drying. The water was then vacuum (0.1 Tr) resublimated for 72 hours and

the dry gel calcined to oxides at 1200°C for 1 hour. The mixture of oxides was treated with binder and lubricant and shaped in the same fashion as the oxide route. The materials contained 4.5 mole % Y_2O_3 and 0, 10, 20, 30 and 100 mole % of the ZrO_2 replaced by HfO_2. The compositions and sample codes are compiled in Appendix 5.

Two similar sintering schedules were followed for both groups of solid solution. High-temperature sintering was carried out at 1800±10°C for 2 hours in a gas furnace. The temperature was controlled pyrometrically on the sample surface. The temperature-composition conditions assured formation of single cubic phase during sintering. At the end of the schedule, the specimens were quenched to 1000°C in ~4 minutes and to room temperature in ~40 minutes. The phase diagrams, (Figs. 2-8, 2-9), predict tetragonal phase nucleation within the large cubic grains during quenching. These nuclei were subsequently grown by heat treatment at 1400°C for 4 hours. As the high-temperature sintering was followed by quenching, this route is called HTQ.

Lower temperature sintering was carried out at 1500± 1°C for 6 hours in an electric furnace within the cubic + tetragonal stability coexistence field. The resultant equilibrium mixture of tetragonal and cubic grains did not require additional heat treatment. After sintering the specimens were furnace cooled to room temperature to induce further precipitation and growth of tetragonal phase within

the cubic grains. This low-temperature sintering followed by cooling route is called LTC.

4.1.2 Zirconia-Beta-Alumina Composites

The preparation of the ZrO_2-β-Al_2O_3 composites was based on commercially available ceramics; zirconia stabilized with 8wt.% and 12wt.% Y_2O_3 (type ZYP, 99.3%, Zircar Prod. Inc.) and refractory single phase β-Al_2O_3 (type Monofrax H, 93.9% Al_2O_3, 5.6% Na_2O, Sohio Eng. Mat.). The ZYP powders are fine-grained with > 90% 0.1 µm agglomerate size and a specific surface area of 40 to 60 m^2/gram. No binders or lubricants were necessary for shaping. The high surface area of the starting powder triggered sintering at 900°C and a 99% dense body of average grain size < 5 µm was achieved after sintering for 6 hours at 1500°C (LTC route).

The beta-alumina particles were obtained by crushing and grinding fusion-cast Monofrax H in an alumina lined vibromill with alumina balls. After milling, the powder was sieve-separated into fractions of the grain size d < 45 µm, 53 > d > 45 µm, (called fraction "50"), 75 < d < 106 µm (fraction "90") and 106 < d < 150 µm (fraction "120"). The consecutive fractions (50, 90, 120) were mixed with the stabilized zirconia (ZYP) powder to give composites containing 20 vol.% particles. The compositions and code names of the investigated specimens are listed in Appendix 5. To assure intimate mixing of the constituents whilst avoiding reduction of the particle size of the brittle β-Al_2O_3, the

batch was loaded into a plastic jar and vibromilled (Sweco vibro-mill) for 2 hours with no milling medium. It was found that dry or wet (the constituents suspended in alcohol) milling/mixing resulted in equal mixing and similar fired densities of the fired composites. Test bars were mould and isopressed. The sintering cycle involved the heating at 200°C/hour to 1000°C and soaking for 9 hours. Subsequently the temperature was increased at the same rate to 1500°C and the material sintered for 6 hours. The samples were cooled to room temperature at -200°C/hour.

4.2 Preparation of Samples for Fracture Tests

The as-sintered specimens were in the form of rectangular plates (30 x 30 x 5 mm) or bars (5 x 5 x 30 mm). The plates were cut into bars using a high speed diamond saw and the load-application faces were polished with 400 grit SiC. The grinding and polishing of the as-sintered bars was more elaborate as some samples warped after isopressing and sintering. The grinding time of the individual bars was reduced substantially if the isopress warpage was corrected before the sintering stage. The isopressed bars were strong enough to be dry polished on 600 grit SiC paper. Thus the parallelism of the load-application faces was assured before sintering. This was especially important in case of the partially stabilized zirconias as surface grinding triggers the tetragonal-to-monoclinic phase transformation and the resulting compressive surface stresses inhibit further

grinding.

The majority of the fracture tests were performed on chevron-notched, four-point bend bars (Fig. 2-12). The notch was introduced using a 150 μm-thick diamond coated blade in a slow-speed cutter (type Isomet, Buhler Inc.). The specimen was positioned against the blade in such a way that the side arms of the chevron triangle (AB and AC, normal to the radius OR, OR' at R and R', Fig. 4-1) resulted in an initial notch length of x_0 = 0.3 to 0.5. With typical arms length of ~ 4 mm, the 39 mm curvature radius, OR, resulted in concave cuts of maximum deviation from linearity of 50 μm. This deviation is considered negligible for the purposes of the present thesis.

Since easy fracture initiation is crucial for stable fracture tests, the compressive surface stresses introduced during the notch cutting process were relaxed before the testing. This can be done by heat treating the samples above 1000°C or by etching the machined specimen in cold concentrated hydrofluoric acid for 20 minutes. The latter technique was used. Micrometric measurement (Mintutoyo Micrometer type 293-301) indicated that a surface layer of ZrO_2 ~10 μm deep was uniformly removed from the specimen surface. After HF etching, the load-application faces were re-polished on 400 grit SiC paper. The etched surface layer depth was neglected in measurements of the initial notch length x_0. The exact geometry of the chevron triangle was determined

after the fracture tests, using a travelling microscope with an accuracy better than 0.1 mm.

4.3 Calibration of the Fracture Mechanics Techniques

4.3.1 Compliance Analysis

It was shown in Chapter 2 that the mechanical compliance of the four-point bend CN specimen can be related to the crack length through equations (2.38) to (2.45). Implementation of this technique is now described and the calibration results presented.

The experimental setup for the room temperature compliance analysis and fracture testing is shown in Fig.4-2. CN bar (1) is seated onto free-to-rotate sapphire rollers (2), 3.2 mm in diameter. The lower plate (3) is fixed through a stiff, piezoresistive load cell (4) (type TC-2000-500, Kulite Semicond Prod. Ltd.) to the movable crosshead (11) of a universal testing machine (type WF 10052, Wykeham Farrance Inc.). The core (5) of a high-sensitivity linear variable differential transformer, LVDT, (6) (type 100 DC-D, Schaevitz Eng.) is also attached to the lower plate (3). The upper loading plate (7) is free to adjust via a hemi-spherical lubricated joint (8). Retainer springs (9) provide minimal force to keep the plate (7) and joint (8) in contact whilst allowing for self-adjustment of the plate to the specimen's surface. The displacement transducer (6) and ball-joint (8) are attached to the immobile upper crosshead (10) of the testing machine. The LVDT was calibrated by a micrometer and

its sensitivity was 0.264 μm per 1 mV of the output signal at ± 15 V input.Similar values for the load cell were 14.8 N/mV at 10 V input.The LVDT and load cell outputs were recorded on the X and Y respectively of an x-y recorder (12) (type PL3, JJ Instruments). The resolution of the recorded signal was 0.3 N and 0.02 μm.

Pressing of the upper (7) against the lower (3) plate with no specimen gave the bending rig compliance, C_R. The results of five repeated loadups are shown in Fig. 4-3 (the coincident loading-unloading paths prove elastic behaviour of the testing system). The load vs. displacement line reaches a constant slope soon after loading commences (at P > 2 N) and gives C_R = 0.04 μm/N. This value of compliance of the bending device is corrected into the actual specimen compliance analyses. The displacement obtained from the machine crosshead displacement rate and time gives the total machine compliance, C_M. Although C_M does not enter the compliance analysis, it characterizes the stiffness of the testing system and lends perspective to the fracture stablization and thus also must be determined. In order to determine C_M, it was initially assumed that the displacement, D, indicated by the calibrated LVDT was much more accurate than the simple multiplication $D=\dot{D}\cdot t$ of the fixed displacement rate, $\dot{D}$, and the time of displacement t. Subsequently, the machine settings were calibrated using the LVDT (measured displacement D_L) and a travelling microscope (measured

displacement D_{TM}). The difference between the three values of displacement, $\dot{D} \cdot t$, D_L and D_{TM} was less than 2% so the machine settings were considered accurate enough.

$\dot{D}$ was typically set at 5 μm/min and the increase of load against time was recorded (Fig. 4-4 for three loading tracks). These graphs are nonlinear up to 20 N. Above this value C_M stablized at 0.07 μm/N. This value is still low enough to guarantee successful fracture stablization. The lines shown in Fig. 4-4 were fitted by linear, multiparameter least squares regression analysis into the polynomial expression, D=D(P). The instantaneous machine compliance was obtained as the derivative of this function, dD(P)/dP, and is plotted vs. load in Fig. 4-5 (curve A). For comparison, curve B presents similar results for the high temperature testing system (based on a different design, load cell and discussed in Section 4.5). The increased sophistication of the high-temperature testing system resulted in a two-fold increase of its compliance.

Once C_R was determined, the compliance equations for the CN bars were verified using graphite (type AXM, POCO, E=10.5 GPa, ν = 0.15). These bars were cut and polished to 10 x 10 x 100 mm and chevron-notched to obtain a 0.8 mm wide slot. The specimen was positioned between bending spans, S_1 = 88.9mm and S_2 = 38.1 mm, stressed at a displacement rate of 5 μm/min up to the linear portion of the load-displacement line and then unloaded. The specimen compliance was deter-

mined from the inverse slope of the load-displacement curve, reduced by C_B. The notch was then saw-extended and its new length measured by travelling microscope with 0.2 mm accuracy. The loading-unloading cycle was then repeated.

The experimental results were compared with calculations for the CN bar using equations (2.38) to (2.45). A Fortran IV program was compiled to generate the compliance values as a function of crack length and test geometry, for various values of the shear correction factor, k. The central part of the program is the subroutine XCOM that returns the compliance C(x) and its derivative dC/dX as a function of the crack length, specimen properties and test geometry. The flowchart of XCOM is listed in Appendix 1. The same appendix also includes the complementary subroutine, COMX which returns the crack length, x, and the compliance derivative, dC/dx, using as input the compliance values, C, the specimen properties and the test geometry. Both subroutines are universal for any CN shape up to the ST configuration. XCOM was utilised for the compliance calibration (i.e., the crack length was measured by methods other than the compliance, eg. optical or electric potential drop), whilst COMX was utilised for the compliance analysis (i.e., the crack length and driving force were obtained from the compliance measurement).

The experimental and numerical results of the compliance calibration for two samples coded I and II are

compared in Fig. 4-6. Curve A was obtained assuming no "interslice" shear, i.e., $k = 1$, curve B assumed Bluhm's correction factor of $k = 1.35$ (equation 2.39) and curve C used the Sakai and Yamasaki analysis, $k = f(x)$. The experimental results are shown as open circles. All curves and points converge at $X>0.8$. Bluhm's approximation seems better for short cracks whilst Sakai and Yamasaki's is superior for intermediate crack lengths.

The Bluhm approach will be used in this thesis as it provides an analytical expression for the correction factor, k, and the accuracy of the analysis was confirmed.

4.3.2 Use of the Potential Drop Technique For Crack Length Determination

The validity of the correlation between the relative potential drop (PD) across a crack with the crack length for ST samples (eq. 3.26) was verified at room temperature using aluminum foil and graphite bars and at elevated temperatures using stabilized zirconia. CN samples (eq. 3.53) were calibrated at room temperature (graphite bars). As the plane solution (3.26) for the PD technique is independent of the specimen depth, B, notched aluminum foil was first considered. 20 μm thick foil of resistivity 2.7 μΩ·cm was cut into strips with proportions similar to the real test bars (3 cm wide and 20 cm long) and glued to a stiff surface. Current and potential probes were positioned as schematically

shown in Fig. 3-13. Electrical contact was made by pressing copper leads into the Al foil. The "crack" was introduced with a razor blade and the notch length was measured by a travelling microscope with 0.1 mm accuracy. The potential drop, $U_2(x)$, was measured across the notch at a constant current of 200 mA (drawn from a Precision Potentiostat type 251 of H.B Thompson and Associates). The values obtained were 0.1 mV at $x = 0$ and 2 mV at $x = 0.97$. The reference potential, U_1, was measured between the same points as U_2 before the initial notch was cut, i.e., $U_1 = U_2(0)$ and $C_1 = C_2$ (for notation, see Section 3.3). The measured values of $U_2(x)$ were normalized to $U_2(0)$ and the ratio $Q(x) = U_2(0)/U_2(x)$ was plotted against the crack extension, x.

In order to compare experimental results with theory, a Fortran IV program was compiled based on solutions for the potential drop in the vicinity of the notch (equations 3.26 to 3.53). The program was universal for any CN geometry and in the limit gave a solution for the ST specimen. The central part of the program is a subroutine XDOP which returns the relative potential drop, $Q(x)$, as a function of the crack length, x, and test geometry (especially, the inter-probe distances C_1, C_2, C_3). A flowchart of XDOP is listed in Appendix 2. The same appendix includes a complementary subroutine DOPX which returns the length x at a given relative potential drop, Q, and test geometry. XDOP is utilised for the PD calibration wherein the crack length is

measured by methods other than the potential drop (i.e., optical or compliance analysis). DOPX is utilised for the crack length determination at high temperatures. Assembly of the two subroutines (DOPX and XCOM) allows determination of the specimen compliance C(x) and its derivative dC(x)/dx at high temperatures. This provides a method of analysis of the high temperature fracture experiments (program LFUHT, Appendix 4).

As the normalized interprobe distances C_1, C_2, C_3, are never known exactly (especially where a metal-ceramic connection is concerned) an essential part of the calibration program was the calculation of the effective distance between the reference probes, C_{1eff}. The accepted method is based on the adjustment of C_1 (resulting in C_{1eff}) such that the crack length calculated from the measured initial potential drop is equal to the initial crack length measured optically.

In the calibration program, once the C_{1eff} value has been obtained, the simulated crack is extended in $\Delta x = 0.01$ steps and the expected Q(x) values are calculated. A number of such calibrations were performed and the numerical results (continuous curve A) are compared with typical experimental data for an ST aluminum foil (circles) in Fig. 4-7. The largest discrepancy between the theory and experiment is < 4% for short cracks. Curve B was obtained by a similar numerical procedure using three-dimensional graphite specimens. This material was suitable for PD calibration procedures (as

well as for compliance analysis and model fracture experiments), since it is easy to machine, isotropic and possesses a reasonably high resistivity (320 μΩ·cm) and a grain size < 25 μm. The bars were cut and polished to ~ 10 x 10 x 40 mm and ST notched with a saw to give an 0.8 mm wide slot. The current and potential probes (copper) were electrically contacted with the graphite surface by mechanical pressing. The reference potential drop, U_1, and C_{1eff} were obtained in the same way as for the aluminum foils. The notch was saw-extended to simulate an advancing crack and the new length was measured by a travelling microscope to 0.2 mm accuracy. The drop of potential across the crack, $U_2(x)$, varied between 0.1 and 2.0 mV for a constant DC current of 200 mA. Several calibrations were performed and the triangles of Fig. 4-7 are typical results. The scatter of the experimental measurements is larger than for the aluminum foils and is attributable to the difficulty of optical crack length determinations. Agreement between theory and experiment is still satisfactory.

The next step was the calibration of CN specimens of graphite at room temperature. The sample and notch preparation, the electrical probes introduction and the data collection were the same as for the ST case. Numerical analysis involved application of the same calibration program utilising the full chevron notch (equation 3.53). A wide spectrum of specimen geometry and interprobe distance was

investigated. The calibrations gave satisfactory results and typical values for four CN specimens are shown in Fig. 4-8 (the lines represent the theory and the points the experimental results). As expected, during the initial stages of crack extension ($x-x_0 < 0.05$) the area lost for electrical conduction was small and the output signal changed slowly (in contrast to ST case). The PD method is therefore not suitable for fracture initiation investigations of CN samples. Following the initial stage the slope of the Q(x) curve for the CN specimen is similar to that of the ST sample. The results shown in Fig. 4-8 vindicate the slice analysis of the PD technique for the CN specimen (Section 3.3) and application of its solution (3.53) to crack length measurement.

All the above experiments involved materials with purely electronic conduction. The final fracture experiments were performed on a purely ionic conductor, PSZ. Since the validity of the PD technique vis a vis the geometry of the test specimens has been proved, calibration utilising ionically conducting PSZ was performed at 700°C using the simpler-to-manipulate, ST specimens.

A technique of providing reliable electrical contact between the probes (Pt wire) and the ceramic surface was developed (Fig.4-9). This figure shows the bottom, B, top, T, and two sides, S, of the specimen. Before cutting the main, fracture-initiation notch, four grooves 0.1 mm deep and 0.3

mm wide were introduced into the bottom face of the specimen, for the current (1) and voltage (2) probes. As the final test notch was much deeper, it was assumed that the 2% reduction of specimen width due to the grooving does not influence the compliance analysis and fracture process. Rectangular Al_2O_3 plates (3), 4 x 8 x 1 mm, grooved on two sides were positioned on top of the specimen over the probe grooves. Subsequently these plates were attached to the specimen by wrapping 0.3 mm thick Pt wire probes such, that the only contact line of the probe and specimen was the groove (4), Fig. 4-9. The probe wires were additionally mechanically pushed into the grooves, guided and isolated from the specimen's top and side surfaces by the grooved alumina plates. In this way, good mechanical contact was provided between the probe and specimen's tensile surface.

Electrical contact was established by applying conducting high-temperature platinum-based enamel (type E-831, Johnson-Matthey Chemicals Ltd.) over the wire-filled grooves (4) and over any other mechanically-supported electrical contacts (for example contacts (5) between the temporary specimen probes and the permanent Pt leads providing connection between the furnace chamber and the exterior electronic instruments). The platinum enamel was allowed to dry, razor cut to give uniform edges in the contact area and sintered immediately prior to the test to give a porous electrode (the porosity is necessary to allow

free penetration of oxygen into the contact area). The enameled surface extended 1 to 2 mm along the specimens' long axis such that the true interprobe distance was difficult to define (this was the main reason for implementation of the C_{1eff} calculation routine). The interprobe distances H_1, H_2, H_3, (equivalent to 2y', 2y and 2d respectively in the theoretical analysis, Section 3.3.2, Fig. 3-13) were measured between the inner edges of the platinum enamel contacts.

The reference potential, U_1, was determined after the calibration (or fracture) experiment was completed. One half of the broken specimen was additionally grooved and the voltage probes for the U_1 determination were attached at lines (6), Fig. 4-9, whilst current was passed between lines (1) and (2). This method assumes homogeneity of the specimen and an insensitivity of its properties to multiple heating and cooling. For the purpose of analysing the fracture experiments, the reference voltage measurements, U_1, were performed up to 1300°C. Typical results are shown in Fig. 4-10 for partially (A) and fully (B) stabilized zirconia ceramics. The DC current used was 3mA. The temperature was increased at 5°C/min.

The plot of ln (U_2) vs. the inverse of absolute temperature at constant crack length (Fig. 4-11) is characteristic of ionic conductors. The change of the slope of the lines at 1100°C has been reported in the literature as evidence of a change of the ionic transport mechanism. At

higher temperatures the conductivity is thought to be controlled by lattice diffusion with a higher activation energy than the lower temperature grain-boundary diffusion with its lower activation energy.

The zirconium oxide specimen for calibration of the PD technique at elevated temperatures was attached to an alumina rod by permanent current and voltage probes. All high temperature electrical connections were enamelled and the rod slowly introduced into the furnace at 700°C (these operations were repeated after each notch extension and optical measurement). The calibration results are compared with the numerical calculations in Fig. 4-12. The functional dependence and scatter is similar to the room temperature graphite calibration. An exceptionally high value of distance between the voltage and reference probes ($C_1 = C_2 = 1.17$) resulted in an almost-linear relationship between Q and x. The broken line at short crack lengths represents the expected variation as, for this particular specimen geometry (large C_1, C_2; small x), the Q(x) response cannot be obtained numerically.

The current density increases in the specimen's web as the notch is artificially or naturally extended. At a certain current density, polarization problems can arise as the amount of oxygen entering specimen at the cathode cannot be transported sufficiently fast through the bulk of the "narrow throat" that constitutes the uncracked cross-section.

As a result, the surface and bulk gradient of oxygen vacancies causes non-ohmic current-voltage behaviour. Effectively, at constant current the potential drop across the crack increases disproportionally (faster) when compared with the increase expected due to the reduction of conducting area alone. This effect was investigated between 700 and 1300°C The current density was increased for constant conducting area (the notch web). The voltage, U_2, vs. the current was recorded across the crack.

Typical results for a Z4A120 type specimen are shown in Fig. 4-13. The linear, ohmic current-voltage dependence was verified for a total current up to 40 mA. The current was increased in 5 mA steps and the potential (U_2) increase followed immediately and was stable for > 0.5 hours (the typical duration of a high temperature fracture experiment). The polarization-free current density is 8 mA/mm^2 for a specimen cross-section of 4 x 4 mm, an initial notch length of x_0=0.4 and a chevron notch web area of ~ 5 mm^2. Since most of the high-temperature fracture experiments were conducted at a constant current of 3 to 5 mA, the current density only reached 8 mA/mm^2 at a relative crack length > 0.95 to 0.98. This value was therefore set as the safety limit for the polarization free, ohmic behaviour of the specimens tested at high temperatures.

4.4 Fracture Tests at Room Temperature

Two types of fracture tests were performed at room temperature, i.e., load relaxation, LR (analysed in Section 3.2) and load-fracture-unload, LFU (analysed in Section 3.1). Although both techniques have some deficiences and each provides data unavailable by the other, the majority of experiments were performed using the LFU method.

A schematic of the variation of the load vs. time for the LR technique is presented in Fig. 3-10 B. The specimen is prepared and positioned in the bending rig (as described in Section 4.3.1) and loaded at a low crosshead displacement rate (typically 1 to 5 μm/min.). The first deviation of the apparently linear load-displacement record is noted at point M and represents an increase of crack length and compliance. Immediately after point M, the machine crosshead is stopped (point Y) and the load relaxation vs. time recorded. The total displacement D (i.e., that of the sample D_s and machine D_m) up to the point Y is $\dot{D}\cdot t$, where $\dot{D}$ is the displacement rate. The load relaxation starts at $t=t_0$, $P=P_i$ and $D_s=D_i$ (Fig. 3-10 A). Subsequently the load-application point displacement, (i.e. D_s), is governed by equation (3.19), where C_M is a function of the load (of Fig. 4-5);

$$D_s = D_i + C_M\cdot(P_i - P) \qquad (3.19)$$

As the displacement $D_s=\dot{D}\cdot t-C_M\cdot P$ and load P are known,

the specimen compliance $C_s(x)$ can be obtained and used as input for the COMX subroutine (Appendix 1). As a result, the crack length, x, and the compliance derivative, dC/dX, is returned and the crack driving force can be calculated from equation (2.50). The advantage of the LR over the LFU technique is that time enters the calculations and therefore the crack velocity can be analyzed. This is conveniently done by differentiation of the relaxation curve. Equation (3.19) can be expressed as;

$$dD_s/dt = d(C_s \cdot P)/dt = -C_M \cdot dP/dt \qquad (4.1)$$

where C_M=const. Since both the specimen compliance, C_S, and the load, P, change with time, rearrangement of (4.1) gives;

$$da/dt \cdot dC_s/da \cdot P + dP/dt \cdot C_s = -C_M \cdot dP/dt \qquad (4.2)$$

If the crack velocity, v, is defined as da/dt, then transformation of equation (4.2) results in;

$$v = -dP/dt \cdot (C_M + C_s)/(P \cdot dC_s/da) \qquad (4.3)$$

The load-time relaxation curve was digitized and compiled into an input data file for the main analysis program called LR (for flowchart see Appendix 3). The output data file was plotted as the strain energy release rate and

the crack velocity vs. the percentage of the fracture area.

It was found in numerical practice that it is more convenient and accurate to analyze the specimen's compliance in increments relative to the initial value rather than the absolute values. This is because some scatter and deviations from the model are to be expected. This is especially true at fracture initiation, despite the compliance calibrations (Fig. 4-6) and their verification by the numerical calculation. The most accurate way to determine the initial crack length, x_0, is by post fracture optical measurement on the fracture surface. Knowing x_0, the initial compliance C_0 is calculated using subroutine XCOM. As the LR experiment progresses, increments of crack length are obtained by adding to C_0 the increments of the compliance recorded by load-relaxation curve and utilizing of the COMX subroutine. This technique assumes ideal elasticity and is therefore limited to certain types of ceramic which exhibit negligible permanent deformation. Difficult fracture initiation in the LR test will cause overload and prompt catastophic fracture (as discussed in Section 3.2). If the machine crosshead is stopped too soon, the crack will arrest, if too late - it will propagate catastrophically.

If the material under test exhibits nonelastic deformation, the LR technique overestimates the crack length and crack driving force values. It is also difficult to conduct this test if the material exhibits R-curve behaviour.

These were the main reasons for the development of the LFU routines used in the present thesis. This technique facilitates determination of the true compliance and the elastic and nonelastic input into the fracture energy of a partially cracked specimen (see literature review, Section 2.1.2). The test specimen was prepared and the experiment initiated using the same equipment as for the compliance calibration and LR tests. The sample is loaded at a slow rate. Immediately after loading ceases (point Y in Fig. 3-10 A), the crosshead movement is reversed and the specimen is unloaded at a much faster rate (105 μm/min. vs. 5 μm/min. for loading). Thus crack growth during the unloading cycle can be neglected. These fast changes of the crosshead direction and velocity were possible as it was driven by a variable-speed, DC motor.

The load-fracture-unload cycles were repeated, typically 5 to 15 times for each specimen. Load vs. displacement was plotted and corrected for the bending rig compliance, C_R. The experimental data read from the load-displacement record, Fig. 4-14, was inputed for the analysis program LFURT (a flowchart is presented in Appendix 3). The data file contains the value of permanent deformation at zero load, $z=D_F-D_A$, the maximum load in a given cycle, P_M, the load at the unloading moment, P_U, and the loading compliance (i.e., inverse slope of the D_AM line) reduced by the rig compliance C_R for each loop of LFU (eg. loop #2). The initial

compliance of the specimen, C_0, at $x=x_0$, was obtained via the slice model. The consecutive crack length (Δx) and fracture area (ΔA) increments were calculated from the compliance increments. The total work-of-fracture-loop, $D_A MUD_F$, was divided into its elastic ($\Delta W_e = D_A MX$) and nonelastic parts ($\Delta W_n = D_A XMUD_F$), Fig. 4-14. The respective areas were calculated in micro-joules (the plot is vs. μm), using the simple geometrical relations;

$$\Delta W_e = 0.5 \cdot b \cdot c \cdot \sin(\alpha - \beta) \qquad (4.4)$$

$$\Delta W_n = 0.5 \cdot z \cdot (P_M - P_U) + z \cdot P_U = 0.5 \cdot (P_M + P_U) \qquad (4.5)$$

where the parameters are shown in Fig. 4-14. The average values of the resistance-to-fracture, R_e, and the nonelastic energy dissipation rate, R_n, for each cycle were obtained from equations (4.4, 4.5, 2.17, 2.18) and plotted against the fracture area corresponding to the middle of the increment, ΔA. For an ideal elastic solid, R_e is equal to the strain energy release rate, G_I, in the limit as $\Delta A = dA$. R_n cannot be related to any LEFM formulae however, as discussed in the literature review. As the experimental equipment allows complete control of the fracture process, the LFU technique is unique for the determination of the R_n of brittle materials. This is especially important if R-curve or high-temperature processes are investigated.

The overall error of the LFU technique is related primarily to inaccurate determination of the crack length. Since the compliance of the CN specimen is not simply related to its geometry, the calibrations (Section 4.3) and model experiments (Section 4.7) provided valuable complementary information for error analysis. For short cracks (i.e., in the slow compliance variation range), the scatter between the measurements and calculations reaches 15% (Fig. 4-6). For longer cracks, the agreement is within 5%. It will be shown in further model experiments with graphite (Section 4.7) that the discrepancy between the resistance to fracture obtained simultaneously by the potential drop and compliance analysis techniques is within 20%. This is irrespective of the relative immunity of the PD technique to the experimental error as discussed in Section 3.3.3 and estimates the accuracy of the techniques under consideration. This problem is discussed further in Section 4.8.

4.5 Fracture Tests at Elevated Temperatures

The testing system designed for elevated temperatures is schematically shown in Fig. 4-15. The distance between the cross-heads (1,2) of the universal testing machine (WF10052) was increased to a maximum of 1 m. An alumina pushrod (3), 30 cm long and 1.2 cm diameter, was attached to the fixed upper crosshead (1). An alumina support tube (4),38 mm OD and 25 mm ID, was connected to the movable crosshead (2) through a stainless steel rod (14) and load cell (5).

The load cell was positioned at the bottom to avoid convection heating. Nevertheless, the stiff piezoresistive cell, successfully employed for room temperature testing was found to be too unstable for use at elevated temperatures. It was therefore replaced by a standard cell (type T263A-500-10P1, Transducers Inc.) designed as a pair of cantilever beams with a built-in LVDT element. The response of the LVDT was calibrated in units of force. The load cell output was fed into the Y-input of a recorder (10).

The specimen (S) was positioned between alumina supporting plates (6,7), previously grooved by a circular profile high-speed diamond saw to accomodate the sapphire loading rods (3.2 mm in diameter) (8). The movable upper support plate (6) allowed adjustment to the specimen surface via an additional sapphire rod joint. Electrical probes were attached to the specimen's tensile surface (as described in Section 4.3.2, Fig. 4-9) and connected to the constant current source (9) (current probes) and the x-input of the recorder (10) (U_2 voltage probes).

A tubular triple-heating zone furnace (11) (Pt-30% Rh heating elements) was movable along the axis of the support tube (4). A uniform temperature distribution (controlled within ± 2°C) was achieved in the central specimen chamber. The core (12) of the LVDT element (13) was attached to the support tube (4) outside the furnace for approximate displacement measurement. It was assumed that, at elevated tempe-

ratures, the elastic deformation and creep of the loading alumina components (of smallest cross-section > 1 cm^2) is small compared with that of the test specimen. Accordingly, the crosshead displacement measured outside the furnace and corrected for the machine compliance, C_M, is the approximate load-application point displacement. This method is not accurate enough for crack length determination (this was accomplished at elevated temperatures by the PD technique), but was considered adequate for estimation of the nonelastic energy dissipation rate in the sample.

The specimen was positioned in the bending rig and a small load (< 20% of the expected fracture load) was applied to immobilize the specimen and maintain alignment. The furnace was slid into place with the hot central zone positioned around the specimen. The temperature was increased at 20 °C/min. Having reached the test temperature, a constant current of 3 mA and a constant displacement rate of 5 μm/min. were initiated. The fracture experiment proceeded in the LFU pattern recording load vs. potential drop (U_2) across the crack. A schematic of this output is shown in Fig. 4-16. Fracture initiates at point S but, due to the slow initial crack advance, the first increase of U_2 is recorded at point I. A period of stable crack growth follows (between point S and T) and the sample is unloaded at point T. The potential drop can decrease during the last stages of unloading due to partial crack closure and restoration of electrical contact

between the fractured surfaces. This phenomenon depends on the test temperature and is absent in the case of extensive permanent sample deformation.

The data file is extracted from the load-potential drop record as input for the high temperature fracture analysis program LFUHT (Appendix 4). The data file contains values of the maximum load, the load at the moment of unloading and the increment of potential drop ΔU_2 for each cycle. C_{1eff} is determined as described in Section 4.3.2. The crack length increment is calculated using subroutine DOPX knowing ΔU_2. The compliance is determined using subroutine XCOM. The loading and unloading values of compliance and the loading record facilitate numerical recreation of the elastic part of the P-O graph. The resistance-to-fracture, R_e, is obtained as per the room temperature LFU experiments (Fig. 4-14). Since all the fracture experiments were relatively fast, the effects of creep and creep damage accumulation on the test specimen properties were neglected.

The nonelastic energy dissipation rate, R_n, can only be obtained if the displacement of the load-application points is recorded. An LVDT element was mounted outside the furnace (Fig. 4-15) for this purpose. Thus the load vs. displacement and load vs. potential drop was recorded simultaneously. The increments of fracture area, ΔA, were obtained from the potential drop in the usual way. Consecutive loops of the load-displacement graphs were integrated planimetrically to

obtain the total work-of-fracture, ΔW_t, for each cycle. At elevated temperature, $\Delta W_t \gg \Delta W_e$ and so the nonelastic energy dissipation rate, R_n, was obtained as $\Delta W_t / \Delta A$.

It is interesting to compare the methods of fracture energy determination employed in the present thesis (Fig. 2.4, equations 2.17, 2.18) with the techniques of elastic-plastic fracture mechanics utilised for metallic materials. As pointed out by Turner [166], the effect of plasticity on the elastic energy release rate can be analysed on the load, P, vs. displacement, D, diagram for an elastic-plastic material (Fig. 4-17). If the crack in the specimen extends under fixed grips conditions, the drop of load for elastic body would be equivalent to AB and that for plastic body to EC (generally, AB is different than EC). Since the elastic-plastic specimen behaves as a unit, the drop of load (say EC) must be the same for all parts. Accordingly, the path for the elastic body is ABT and thus the elastic contraction $\Delta D = SR$ results. This must be accompanied by a plastic expansion of the same amount, S'R', since the grips are fixed. The elastic contraction SR releases additional strain energy TBRS. The total strain energy release rate, defined as I, is proportional to sum of the areas OAB and TBRS.

It is argued [166] that G (i.e. the area OAB per unit fracture area created) is the free potential energy rate available for the crack extension, whereas I is the total (free plus bound) potential energy rate available, the bound

component being related to the plastic work done during the crack growth. The relation between G and I depends on the loading configuration and the crack length. For three-point bending (S/W=4 and 0.4<x<0.8) the elastic contraction term can be neglected and I≅G. Although data for the four-point bending are not available, the two configurations are similar enough to assume I≅G also (especially as x>0.4 for most of the tested specimens). Consequently, the quantity defined in the present thesis as the resistance to fracture R_e for a brittle-nonelastic ceramic is equivalent to the elastic energy release rate for metals computed according to the methods of elastic-plastic fracture mechanics.

The application of LFU and PD techniques to ionically-conducting, viscoelastic materials at high temepratures has been undertaken for the first time in this thesis. The global energy analysis approach is considered appropriate and self-consistent enough to produce meaningful data. In fact, the results generated by these techniques allowed quantification of the energetics of high-temperature crack-microstructrue interactions in the zirconium oxide ceramics studied.

4.6 The Determination of Phase Composition and Elastic Modulus of the Zirconia Cermics

The monoclinic content of the ZrO_2-HfO_2 solid solutions and the matrix of the ZrO_2-β-Al_2O_3 composites was determined by surface x-ray diffraction and application of

equation (2.62). Specimens were tested as-sintered to avoid the surface phase transformation upon machining, i.e., specimens were not ground to powder. The bars were attached to a glass slide in such a way that the scanned surface of the bar coincided with the surface of the slide. The assembly was mounted in a Philips PW1720 diffractometer and scanned between 2θ=27 to 33° by Cu-K_α radiation at 1 deg/min. The intensities of the [C + T](111) and M(111), M($11\bar{1}$) were planimetrically integrated and the results substituted into (2.62). Two to four samples of each material were scanned and average values of the volume fraction of monoclinic phase were determined.

The room-temperature elastic modulus was measured by the four-point-bending of unnotched bars (static value E_s) and by measuring the transit time of an ultrasonic wave through the material (dynamic value E_d). The static experiment was performed using equipment and procedures described in Section 4.3.1. However, the specimen was purposely made thin (W=1 to 2 mm). As the compliance, $C \propto W^{-3}$, the reduction of W to ~1.5 mm (on average) gave C≅1.0 μm/N, i.e., at least order of magnitude larger than C_M, the machine compliance. Thus the slope of the load vs. displacement record was linear and any machine nonlinearity effects (Fig. 4-3, 4-4) were taken up by the compliant specimen. The calculated total compliance (rig and specimen) was reduced by C_R and the static value of elastic modulus was obtained via

equation (2.44). Three to four specimens of each material were investigated. The errors involved in the static bend test are discussed in Section 4.8.

The transit time of an ultrasonic wave was determined using the paralleled and polished pieces of broken bars. A diagram of the equipment is shown in Fig. 4-18. The material (1) was coupled through natural honey with commercial piezoelectric transducers (2) producing a 5 MHz shear wave and a 15 MHz longitudinal wave. The transducers were excited by a high frequency signal from the generator (3). The main and reflected pulses were transmitted through the receiver/amplifier to the oscilloscope (5) (Tektronix 2445), triggered through the synchronization line (6). The time between the consecutive reflection pulses was obtained with an accuracy better than 1%. Equations (2.65) and (2.66) were used to calculate Young's modulus and Poisson's ratio.

The high temperature elastic ("storage") modulus was estimated following the precautions discussed in Section 2.4.1.4. Unnotched, thin specimens were stressed in the high-temperature, four-point-bend rig, described in Section 4.5 (Fig. 4-5). The change of load P vs. displacement D was monitored outside the furnace. D was then reduced by the bending rig deformation inside the furnace (D_R) via:

$$D_R = P \cdot C_R \qquad (4.6)$$

For all elevated temperature tests $D >> D_R$, i.e., the bending rig compliance can be neglected as compared with that of the specimen. The slope of the tangent line OA on the load-displacement plot was calculated (as per Fig. 2-16). The static high temperature elastic modulus, E_s, was estimated from equation (2.44) knowing the specimen's storage compliance.

4.7 Model Fracture Experiments with Graphite

High quality graphite (type AXM, POCO Graphite Inc.) was used throughout this thesis as a model material for calibration purposes. In this paragraph a comparison is made between simultaneous compliance and PD analyses at room temperature.

The experimental load-displacement output for graphite specimen GR62 is shown in Figure 4-19. Some fluctuation of the zero load line (Fig.4-19A) is characteristic for a piezo-resistive load cell. Fracture energy analysis results for specimen GR62 and two additional specimens are compiled in Figure 4-19B. The scatter of R_e was ± 15 J/m^2 and R_e steadily decreased as predicted by the model (Fig. 3-9), approaching a limiting value of 80 J/m^2 at full fracture. This result agrees with literature data [32]. The scatter of the nonelastic energy dissipation rate, R_n, was ± 20 J/m^2 and the average R_n value decreased with the crack extension.

Similar LFU experiments were repeated with graphite whilst simultaneously monitoring load vs. potential drop and load vs. displacement (Fig.4-20A and 4-20B respectively).

Nineteen cycles were performed generating crack length data from PD measurements. The slope of the load-displacement curves at long crack lengths was so small that record overlap excluded quantitative analysis. The crack length calculated via the PD method (x_{PD}) for 12 cycles is compared with that from compliance analysis (x_{CA}) in Fig. 4-20C. Except for the second point, the results agree within 3%. The larger scatter is expected for short cracks as both the relative potential drop and compliance curves are flat in the initial crack extension regime. Consequently small errors in compliance or potential drop measurement can result in larger errors in the calculated crack length for short cracks.

The fracture energy was determined from Fig. 4-20B (and the analysis program LFURT) and Fig. 4-20A (and the analysis program LFUHT). The results for both methods are compared in Fig. 4-20D. The open circles (compliance technique) and closed circles (PD technique) are in satisfactory agreement. An unexpected rise of R_e was observed for A > 50% (A is the percentage of available area fractured). This can be explained by the influence of the relatively large constant current of 200 mA ($\sim$ 10 A/cm^2 at A $\simeq$ 80%) on the fracture process. This current was necessary to obtain a measurable potential drop of 1 to 2 mV. The passage of this current does not appear to influence the measurement procedures as the results for both methods are in reasonable agreement. Compliance analysis results for two other speci-

mens (tested with DC=100 mA and without any current) are also shown in Fig. 4-20D for comparison. It does appear that the application of high current densities does change the fracture properties of graphite. These experiments illustrated the compatibility of the two methods vis a vis the geometry of the specimen.

4.8 Errors in Determination of the Crack Driving Force

The fracture mechanics and compliance derivations used in the present thesis are based on simple beam theory and its inherent assumptions. It is assumed that transverse sections of the specimen perpendicular to its longitudinal axis remain plane during bending, the the maximum deflection is small compared to the beam width W, and there is no twisting. It is further assumed that the material is isotropic, homogenous and of equal elastic modulus in bending and compression. Violation of any of these assumptions will result in stress analysis errors. Further errors arise, if the load application or specimen geometry is non-ideal. The uncertainty is increased by the usual scatter of properties from sample to sample, instrumental reading errors and unstable experimental conditions (temperature, humidity, power supply, etc.). In the present paragraph, the overall effect of experimental errors on the uncertainty of the calculated value of the crack driving force is estimated.

Suppose equation (2.10) is substituted into (2.12) to give a general formula for the crack driving force;

$$G = \sigma^2 \cdot f(a)/E \qquad (4.7)$$

where σ is a surface tensile stress in a bend bar, E the Young's modulus already reduced by the Poisson's ratio term $(1-\nu^2)$ and $f(a)$ is some geometric function of the crack length a. For the ST specimen;

$$f(a) = Y^2(a) \cdot a \qquad (4.8)$$

For the CN specimen an additional term appears (cf. equation 2.50), i.e.;

$$f(a) = Y^2(a) \cdot a \cdot (a_1 - a_0)/(a - a_0) \qquad (4.9)$$

In equation (4.9) it is assumed for simplicity that the slope of the plot of compliance vs. crack extension is the same for the ST and CN specimens [126]. The standard deviation of G (ΔG) can be estimated from formula (4.7) using the error propagation method [123];

$$(\Delta G/G)^2 = 4 \cdot (\Delta\sigma/\sigma)^2 + (\Delta f/f)^2 + (\Delta E/E)^2 \qquad (4.10)$$

where $\Delta\sigma$, Δf and ΔE are estimates of the variance of measurement of the stress, geometric function and Young's modulus respectively. The right-hand terms of equation (4.10) are the errors in stress, stress concentration and

stiffness measurement respectively. The covariance terms are neglected. This is equivalent to assuming that the values of σ, $f(a)$ and E were obtained independently. This is true if the PD technique is used to determine the crack length and is used in the subsequent $f(a)$ calculation. In the compliance analysis however, the calculated crack length (and thus $f(a)$) and the bend stress, σ, depend on the same set of parameters (eg. specimen and loading geometry). Therefore the errors in $f(a)$ and σ are interdependent and the covariance term should be included in (4.10). The complications of this task however negate the provision of quantitative covariance data at the present stage of analysis. In particular, it is not known how non-ideal four-point bending is nor are violations of the simple bending assumptions known which would influence the geometric factor $Y(a)$ and the compliance of the CN specimen. Some indication of the variance of the geometric function, $f(a)$, under non-ideal conditions should be given by the scatter of the compliance calibration results (Fig. 4-6) and those of the relative potential drop (Figs. 4-7, 4-8). The calculated and measured values for compliance analysis agreed within 10% and for potential drop within 4%. From equation (2.45) any errors in determination of crack length propagate into the determination of the geometric factor $Y(a)$.

The single effect of an erroneous crack length determination on the resulting crack driving force determination

was therefore modelled (i.e., assuming errorless stress and stiffness analysis, $\Delta\sigma$-ΔE-0). As the accuracy of the compliance measurement decreases with crack length (see Fig. 4-20), the relative error can be approximated by ;

$$\Delta C/C = Z\cdot(x - x_0) \qquad (4.11)$$

For a typical specimen with relative initial crack length x_0=0.4, the error of the compliance reading can reach 20% at long cracks so Z = 0.3 reflects the capability of the present experimental setup for CN specimens. A program based on subroutine COMX (Appendix 1) was compiled and calculations of the crack length and driving force performed for compliance values C and C±ΔC with Z = 0.1 to 0.5. The resulting error of the crack length calculation, $\Delta x/x$, is plotted in Fig. 4-21A. At Z = 0.3, the maximum $\Delta x/x$ is ≃7% at $x-x_0$= 0.2 (i.e., in the early stages of crack extension). Simultaneously, the relative error of the strain energy release rate was (cf. equation 2.7);

$$\Delta G/G = [dC/dx - d(C+\Delta C)/dx]/[dC/dx] \qquad (4.12)$$

This term is plotted in Fig. 4-21B. Equations (4.11) and (4.12) result in almost identical values as a function of crack extension. Thus, for the room temperature compliance analysis of the fracture test, the single effect of erroneous

crack length determination on the variance of the crack driving force is;

$$\Delta G/G \cong \Delta C/C \cong \Delta f/f \cong 0.3\cdot(x - x_0) \qquad (4.13)$$

Similar numerical analyses were performed for the PD technique. The parameters most susceptible to experimental error are the inter-probe distance C_1, C_2 and C_3 (the accuracy of measurement of the voltage and current is high). The simulation program, based on subroutines XDOP and DOPX assumes a knowledge of the true values of C_1, C_2, C_3 and an array of crack lengths, x_i. It then introduces an "error" into either C_1, C_2, or C_3. The routine for the calculation of C_{1eff} is applied (see Section 4.3.2) and consecutive "erroneous" values of the crack length, x_e, are calculated.

As expected from the sensitivity analysis of the PD technique, (Section 3.3.3), variation of C_2 is the only source of significant error in the crack length calculation (variations of C_1 or C_3 up to + 40% give a $\Delta x_e < 1\%$). The effect of the variation of the calculated value of x_e vs. the true value of x at $C_2=\pm 40\%$ is shown in Fig. 4-22. $(x-x_e)/x$ vs. crack length (x) is shown in Fig. 4-23A at $\Delta C_2=+10\%$, +20% and +40%. The estimate of C_2 reflects in the crack length. The dependence is similar for $\Delta C_2 < 0$ and an underestimation of the crack length results. It is interesting to note, that now a relatively large error in x persists to longer crack

lengths (cf. compliance technique, Fig. 4-21A). Consequently, the simulated error of the crack driving force, Fig. 4-23B (obtained by application of eq. 4.12 and the subroutine XCOM for the "erroneous" crack length x) increases faster, than observed with the compliance technique (Fig. 4-21B). Nevertheless, the error $\Delta G/G$ can be approximated by a linear equation for the crack lengths $x_0 < x < 0.9$, , i.e. ;

$$\Delta G/G \simeq \Delta f/f \simeq 0.65 \cdot (x - x_0) \qquad (4.14)$$

where a reasonable maximum value of ΔC_2=20% has been assumed (from Fig. 4-23A, a consistent error in the calculated crack length at ΔC= 20% should not exceed 2%, in agreement with the calibration data, Fig. 4-8).

Fluctuations of temperature will cause a potential drop variation across the notch without crack growth. Since these fluctuations are limited to ± 2°C, the resulting voltage fluctuation is less than 0.2 mV for a typical specimen at 1300°C and i = 3 mA, i.e., 0.01 in terms of the Q values (compare Fig. 4-10). This results in an uncertainty in the crack length calculation of 4% from Fig. 4-8, i.e., within the limits of the above simulation model.

Errors in the calculation of the tensile stress in a bend specimen under non-ideal conditions have been extensively discussed by Baratta [147]. He expressed the errors, e, as;

$$e = (\sigma_i - \sigma_x)/\sigma_x \qquad (4.15)$$

where σ_i is calculated for ideal conditions (i.e., a simple beam of errorless geometry) and σ_x is close to the true bending stress including deviations from ideality. He tabulated results for a number of experimental conditions, eg. for the bending span ratio $n=S_1/S_2$, for the specimen's depth to width ratio, $m=B/W$ and for the span to width ratio, $l = S_1/W$. In term of the present study appropriate values are : $n=2$, $m=1$, $l=6$.

If the stress distribution along a cross-section of the specimen is nonlinear (a possibility for the high-temperature tests), $|e|<6\%$ (and $e<0$) for $l>2$. The effects of anisotropy and inhomogeneity were neglected, as specimens were polycrystals with the largest inclusion size (120 μm large β-Al_2O_3) < 2% of the specimen width. If the specimen is initially curved to radius r, an underestimation of the true stress can be expected. For an estimated $r/W > 45$, $|e|<1\%$ and $e<0$.

Errors also arise in the bend stress calculation if the maximum deflection is significant compared with the beam width, W, or if friction exists between the loading rollers and the specimen surface. It has been suggested [147] that these effects are negligible if the slope between the beam in the loaded and unloaded positions at the outermost support point is <15 degrees. Simple trigonometric calculations show

that the angle is less than 15° if the load application point displacement is <1.6 mm for the bending rig presently utilised. This condition was met in all fracture tests.

The transmission of the load through the rollers causes local contact stresses but these decay quickly with distance and do not cause errors in notched specimen testing.

It appears the most serious errors in stress analysis are the result of non-ideal bending geometry, load mislocation and beam twisting. The load mislocation (i.e., shift of the centre of the upper bend span vs. the lower span) is related to the precision of the bending fixture alignment. The high-temperature Al_2O_3-set (Fig. 4-15) limited alignment accuracy to ± 0.5 mm. The room temperature steel fixture gave ± 0.3 mm. These values normalized to lower bend span are 0.02 and 0.01 respectively giving a possible stress underestimation of 15% and 8% respectively [147].

If the line loads between the pairs of load-contact points are nonuniform or nonparallel or if the cross-section of the specimen is skewed along its length, a net torque (i.e., beam twisting) results. Input data for the resulting stress error includes the skew angle along the total length of the specimen and the displacement angle along the fixtures from one support point to the adjacent load point. It is not unusual for both angles to be within 2 degrees for the ceramic specimen and fixture. For these values the resulting

torque causes a 15% stress underestimation.

To determine the overall variance of the stress analysis $(\Delta\sigma)^2$ the square of each of the error spans were added together. The maximum overall error (i.e. the square root of the variance) in the outer-fibre stress determination at room temperature was estimated as 18% and at high temperatures as 22%.

The last value required for the error progagation formula (4.10) is the variance of the elastic modulus, E. This is taken as the square of the standard deviation (ΔE) of measurements made at room ($\Delta E/E \simeq 0.10$) and high temperatures ($\Delta E/E \simeq 0.15$).

Compiling the estimated maximum values of the room and high temperature variances, the respective formulae are obtained from (4.10);

$$\Delta G/G = [0.04 + 0.09\cdot(x - x_0)^2]^{0.5} \qquad (4.16)$$

$$\Delta G/G = [0.07 + 0.42\cdot(x - x_0)^2]^{0.5} \qquad (4.17)$$

Equations (4.16) and (4.17) are plotted against the crack extension, $(x-x_0)$, in Fig. 4-24. The maximum standard error of the compliance technique increases slowly with crack extension (x) and is within 20% to 30% as long as $x < 0.9$.

The maximum error in the crack driving force obtained via the PD technique increases from 26% to 50% as the crack grows from its initial length, x_0, to x=0.9.

The evaluation of the standard error herein presented pertains to the LEFM formulas (2.7, 2.10, 2.13 and so to (4.10). The resistance-to-fracture for the high-temperature experiments is calculated as an increment of the work-of-fracture vs. the fracture surface, i.e., $\Delta W_e/\Delta A$. Both of these quantities depend on the crack length obtained via the PD technique. Thus, the covariance terms involved will have a significant effect on the calculation of the crack driving force. Consequently, it is assumed that the analysis pertains to room as well as high temperature testing.

It is probable that the determination method for the high temperature static Young's modulus gives a lower-bound estimation (Fig. 2.19) and it is instructive therefore to consider the effect of these underestimated-values on the calculation of the resistance to fracture at high temperature.

A schematical load-displacement graph, reconstructed from the crack length data, is presented in Figure 4-25. This shows the variation of specimen compliance with crack growth. For simplicity, it is assumed that the crack extends at constant load, P, i.e., the fracture initiation points are A or F. If the static Young's modulus (E) is known exactly, the loading and unloading compliances are C_1 and C_2 respec-

tively. If an underestimated value E' is used for the calculations, C_1' and C_2' result. The compliances can be expressed as;

$$C_1=b_1/E \;; C_2=b_2/E \;; C_1'=b_1/E' \;; C_2'=b_2/E' \qquad (4.18)$$

where b_1, b_2 are numerical constants characteristic for the specimen geometry (Equations 2.42 - 2.44). The work-of-fracture for the first case is $W_e = 0.5 \cdot P \cdot D$ and for the second is $W_e' = 0.5PD'$ where D or D' is a recovered displacement of the loading roller during crack growth (not measured in the high-temperature test). From equation (4.18) and the compliance definition (2.8);

$$D = P \cdot (b_2 - b_1)/E \qquad (4.19)$$

$$D' = P \cdot (b_2 - b_1)/E' \qquad (4.20)$$

so;

$$W/W' = E'/E \qquad (4.21)$$

i.e., the underestimation of the elastic modulus results in a similar overestimation of the work-of-fracture. The errors introduced by the Young's modulus measurement and those due to non-ideal bending conditions (discussed above) act in the opposite manner.

CHAPTER 5

RESULTS AND DISCUSSION

5.1 Materials Characterization

5.1.1 Zirconia-Hafnia Solid Solutions

The yttria-stabilized zirconia-hafnia solid solutions were obtained by simple oxide mixing (called OM technique) giving materials type P0, P1, P2 and P3 and by spray-freezing freeze-drying (called the SFFD technique) giving materials type P0A, P1A and P2A (Appendix 5). For comparative studies, limited quantities of fully stabilized yttria-zirconia-hafnia specimens were prepared. Two sintering routes were used, i.e., 1500°C, followed by furnace cooling (called LTC) and 1800°C, followed by quenching (called HTC).

The XRD phase analysis results as a function of HfO_2 content are presented in Fig. 5-1. The HTQ route (open symbols) resulted in low monoclinic (M) phase content for the SFFD materials up to 20 mole % HfO_2. For the OM-type ceramics, the M-phase content was larger and increased with mole % HfO_2 to a maximum of 40 vol.%. Incomplete stabilization of the ZrO_2-HfO_2 solid solution results when the starting powders are relatively coarse. SFFD materials of the same

composition are highly dispersed and homogenized ensuring a uniform distribution of the stabilizer (Y^{3+}). On quenching of these materials from high temperature, the single-phase cubic field inhibits the nucleation of significant monoclinic phase.

Similar compositions prepared by the LTC sintering route exhibited high contents of M phase with the exception of the POA samples (i.e., without HfO_2). 1500°C is within the coexistence field of the cubic (C) and tetragonal (T) phases and results in an equilibrium composition of 60% C and 40% T. Further T phase precipiates within the C grains during cooling. Large grains (1 to 5 μm) of T phase transform to M upon slow furnace cooling, the driving force for this transformation being proportional to drop of temperature and HfO_2 content. All LTC-OM materials exhibited a high M-phase content. Typical XRD scans (2θ = 28 to 32°) for LTC-OM and LTC-SFFD materials are shown in Fig. 5-2 and 5-3 respectively. The high intensity central peak $(111)_{C+T}$ has been foreshortened for clarity. The fully stabilized (with 6.9 mole % Y_2O_3) reference specimen exhibited no detectable monoclinic phase.

The microstructures of polished and HF-etched sections of the LTC materials are shown in Figs. 5-4 to 5-7. The phases were identified via XRD data and similar microstructures reported in the literature. On the typical PO section (Fig. 5-4A), a mixture of T and M phases separate the

10-15 μm size cubic grains. The estimated porosity is 10 vol.% and this was verified by subsequent density measurements. The pores are distributed on grain boundaries and trapped within the cubic grains.

Fig.5-4 B,C and D show similar microstructures for the P1,P2 and P3 materials respectively. Unlike P0, the ceramics containing HfO_2 suffer grain pull-out during polishing due to weak and microcracked grain boundaries. The M phase forms a continuous layer between the cubic grains of these microstructures. The damage is most severe for pure and partially stablized hafnia (with 4.5 mole % Y_2O_3), Fig. 5-5A. The surface M phase is completely removed during cutting and polishing. Porosity is located between and within the large grains (20 to 50 μm). Clusters of M phase can clearly be seen on the fracture surface, Fig. 5-5B. Full stablization of HfO_2 by 6.9 mole % Y_2O_3 results in pure cubic phase (Fig. 5-6A) with no grain pull-outs. The porosity pattern is similar to that observed in other compositions. Fracture was transgranular and revealed traces of M phase (Fig. 5-6B).

The LTC-SFFD synthesis route gave material microstructures summarized in Figs. 5-7 A, B and C (P0A, P1A and P2A respectively). The sample free of HfO_2 (i.e., P0A, Fig. 5-7A) is 97% dense with cubic (< 10 μm size) and tetragonal (< 5 μm size) grain intergrowths (the M phase content is < 8 vol %). The cubic (C) grain size does not change with HfO_2 addition but the shear associated with the increasing M phase

weakened the grain boundaries and the specimen surfaces crushed during polishing. P2A ceramics (Fig. 5-7C) exibited multiple intergranular cracks.

The elastic constants (the Young's modulus, E, and Poisson's ratio, ν,) and densities, d, for the zirconia-hafnia SFFD materials are compiled in Figs. 5-8 to 5-11. The variation of room temperature E, ν and d with HfO_2 content is shown in Fig. 5-8 (HTQ) and 5-9 (LTC). In order to separate the density and elasticity effects, the longitudinal ultrasonic wave velocity v_l is also plotted. For clarity, the average values are connected by straight lines. These do not however suggest a linear variation of properties.

The dynamic modulus value, E, of 210 GPa was obtained for pure PSZ using HTQ-SFFD samples. This value agrees with literature data. Unexpected behaviour was observed for the P1A ceramics (HTQ-SFFD). Some samples had E > 200 GPa while others had E < 100 GPa. Further increase of the HfO_2 content to 20 mole % gave a uniform low value of E ≃ 30 GPa. Multiple cracks were detectable by eye on the P2A specimen surfaces. Evidently, high-temperature sintering followed by quenching thermally shocks these materials. The resulting properties were also found to depend on the sample location in the quenched batch. For this reason, fracture investigations were pursued on the LTC materials. The variation of density, d, for these materials (and HTQ for comparison) is shown in Fig. 5-9. E and v_l are shown in Fig. 5-10. The

properties scatter within ~15% and E stabilized at 150 GPa for specimens containing 20 mole % HfO_2.

High temperature static modulus values were determined for the LTC-SFFD ceramics containing < 10 mole % HfO_2 (for higher HfO_2 contents, the devastating M→T transformation takes place), Fig. 5-11. The results for pure PSZ (sample type P0A), normalized to the room temperature value of E, are compared with literature data in Fig. 2-17. The results obtained in this thesis are consistently smaller than the dynamic measurements reported in the literature. It is felt, that the static test provides a more realistic result as far as the strain energy released in a fracture process is concerned. Accordingly, the static high temperature value of E was measured at a strain rate similar to that used in the fracture experiments and is utilised in this thesis for the crack driving force determination. The possible influence of the underestimation of E on crack driving force calculations has been discussed in Section 4.8.

Fig. 5-12 shows the effect of HfO_2 content on the elastic properties of the HTQ-OM ceramics, partially stabilized with 4,5 mole % Y_2O_3 (P0 to P3, Fig. 5-12A) and fully stabilized with 6.9 mole % Y_2O_3 (F0 to F3, Fig. 5-12B). The E values of the partially stabilized materials drop from 180 GPa for P0 and P1 to 130 GPa for P3. The scatter is ±15%. The E values for the fully stabilized samples increased from 140 GPa for F0 (no HfO_2) to 170 GPa for F3 (30 mole % HfO_2)

(scatter ± 4%). Similar trends were observed for the Poisson's ratio. The sintering of fully stabilized zirconia-hafnia is difficult and the maximum density achieved was 87% theoretical (Fig. 5-13). Partially stabilized materials sintered to > 90% density irrespectively of the method of heat treatment. The elastic properties of the LTC-OM ceramics are consistent with their phase composition (compare Fig. 5-1 and 5-14). The modulus, E, is weakly dependent on the HfO_2 content and equals ~130 GPa. The sintering conditions of these materials were such that their monoclinic phase content was high and independent of the HfO_2 alloying.

As the static Young's modulus must be known to analyse the stable fracture experiments, its values are compiled as a function of HfO_2 content in Fig. 5-15. For the large-grained OM-type materials the difference between the static and dynamic E values increased with HfO_2 content, i.e., with the content of M phase which in turn increases the microcrack density (compare Figs. 5-10, 5-12A, 5-14 and 5-15. The room temperature dynamic and static values of E for the small-grained microcrack-free SFFD-type materials were in good agreement. Apparently time or frequency-dependent phenomena (eg. the delayed frictional closing and opening of microcracks) is active in high monoclinic-phase-content materials.

5.1.2 Zirconia-Beta-Alumina Composites

The zirconia-β-alumina composites were analysed in the same way as the ZrO_2-HfO_2 solid solutions. XRD of the as-

sintered surfaces revealed the presence of 19 to 31 vol % of monoclinic (M) ZrO_2 phase. This level exhibited a weak dependence on the size and content of β-Al_2O_3 particles (Fig.5-16, for the materials type Z4, stabilized with 4.5 mole % Y_2O_3). The type Z8 materials (stabilized with 6.9 mole % Y_2O_3) exhibited a single $(111)_{T,C}$ peak in the considered 2θ range indicating no M-phase was present. β-Al_2O_3 peaks were not detected in the surface diffraction experiments at 20vol. % particles. XRD of high β-Al_2O_3 content composites [133] revealed α-Al_2O_3, β-Al_2O_3, zirconia (M,T,C) and possibly sodium zirconate. Since stabilization of the tetragonal phase at room temperature involves constraint of the transformation, the specimen bulk contains mostly tetragonal and cubic ZrO_2 phases (this was further verified by the elastic property measurements).

The change of static elastic modulus with temperature and β-Al_2O_3 inclusion size is shown in Fig. 5-17. The uncertainty of the high-temperature measurements reached ±20% of the average value. A dramatic change of E was observed at room tempeature when the β-Al_2O_3 particle size exceeded 50 μm (E=175 GPa for pure Z4, 150 GPa for Z4A50 and 75 GPa for both Z4A90 and Z4A120). The drop of static E for the large-particle composites at high temperatures was slower when compared with pure Z4 (Fig. 5-17).

The microstructures of the Z4 series materials are shown in Fig. 5-18A to D. The tetragonal and cubic phases are

recognizable on the polished and etched section of pure Z4 (i.e., partially stabilized zirconia, PSZ, Fig. 5-18A). A continuous α-Al_2O_3 interface forms on the small β-Al_2O_3 particles (Fig. 5-18B), whilst a discontinuous α-Al_2O_3 layer, macrocracks and porosity are associated with the large β-Al_2O_3 particles (Figs. 5-18C, D). The microstructures of the composites based on fully stabilized zirconia, FSZ, (Fig. 5-19A to D) show extensive macrocrack networks linking the large β-Al_2O_3 particles. It is clear that the thermal expansion mismatch stresses exceed the strength of the FSZ.

The microstructural observations explain the measured elastic properties and density values (Fig. 5-20A). Both decrease with the particle size for the 20 vol.% β-Al_2O_3 composites. The data are compared with that for fully and partially stabilized matrices (Z8 and Z4 series respectively). The particle size effect is stronger in the Z8-type ceramics. For 20 vol.% of 50 µm size inclusions the drop of E relative to the pure matrix material is 40% for Z8-type ceramics and 20% for the Z4-type ceramics. At elevated temperatures, E decreases in a similar fashion to the Z4 materials (Fig. 5-20B).

The elasticity, density and microstructures of the zirconia-β-alumina composites suggest that the inclusion size should not exceed 50 µm if spontaneous matrix fracture is to be avoided (i.e., to maintain the high strength of the material). As will be shown, the continuity of the α-Al_2O_3

layer on the β-Al_2O_3 inclusions plays an important role in the high-temperature fracture characteristics of the ZrO_2-β-Al_2O_3 composites. On the other hand, the porous and discontinuous interfaces associated with the larger β-Al_2O_3 particles promote their pull-out on crack propagation at room temperature. The complete results of the fracture studies are presented in the following sections.

5.2 The Resistance-to-Fracture at Room Temperature Determined via the Load-Fracture-Unload Technique

5.2.1 Zirconia-Hafnia Solid Solutions

A typical room-temperature record of the load-fracture-unload and compliance analysis experiment (reffered to as LFU-CA) for the specimen type P0 is shown in Fig. 5-21A (for clarity only the loading paths are plotted). The maximum load did not exceed 40 N and the maximum permanent deformation was 15μm (0.5 to 1μm in each cycle). As the crack length increased, the loading path can be divided into two characteristic stages: an initial one of higher slope (i.e., lower specimen compliance, path AB in Fig. 5-21A) and a final one of lower slope, i.e., higher specimen compliance, path BC. The initial stage of lower compliance is related to the opening of microcracks generated in the previous fracture cycle which closed during unloading. This interpretation was verified by simultaneous potential drop and compliance analysis of LFU model graphite specimens (Fig.4-20). The effective crack length is represented by the slope of

path BC. The main crack starts to advance between B and C.

The results of the calculation of the resistance-to-fracture, R_e, and the nonelastic energy dissipation rate, R_n, based on Fig. 5-21A (and for one another specimen type P0) vs. the percentage of the fracture area are plotted in Fig. 5-21B. R_e initially increases and the R_n values scatter between 0 and 30 J/m^2. This scatter is due to real physical effects and not experimental error (the error in the R_n calculations should be similar to that for the more-uniformly-varying R_e). As full fracture is approached, R_n=60 and R_e=20 J/m^2.

The crack arrested after the last unloading cycle and the fracture surface of the P0 specimen is shown in Fig. 5-22 A,B. The crack opening displacement is > 10 μm, the fracture is intergranular with extensive grain pull-out and micro-cracking. The crack front has been deflected by as much as 80 degrees, implying mixed-mode fracture. The crack propagation path (Fig. 5-24A and many subsequent figures) vindicates the energy approach utilised in this thesis. The fracture surface of the P0 material (Fig. 5-22B) indicates a tortuous crack path with transgranular cracking of the C grains and intergranular cracking of the M grains. The fracture morphology explains the large and scattered nonelastic energy dissipation rate. Crushed and microcracked M-phase debris resist elastic crack closure resulting in permanent deformation of the specimen and thus large R_n values.

A similar set of figures for the P1-type ceramic is presented in Fig. 5-23 and 5-24. The R_e values are now more scattered and decrease to 20 J/m^2. The dispersed R_n values oscillate around 30 J/m^2. The arrested crack exhibits multiple birfurcation with an opening displacement of 10 μm (Fig. 5-24A) and mixed trans- and intergranular propagation modes (Fig. 5-24B). The origin of the large R_n values is similar to that of the P0 ceramics.

No significant change in the resistance to fracture was observed when the amount of ZrO_2 replaced by HfO_2 was increased to 20 and 30 mole % (materials P2 and P3 respectively, Fig. 5-25 and 5-26). If maximum ±20% error bands are imposed, the limiting R_e values are between 10 and 30 J/m^2 as full fracture is approached. The unusual variation of R_e observed for the specimen coded P351 (Fig. 5-26) is attributed to crack branching (the R_e calculated at A=50% is 80 J/m^2 instead of the expected 40 J/m^2). The high R_e values for short cracks decrease to a limiting value of ~20 J/m^2 for the P2 and ~30 J/m^2 for the P3 type ceramics. This does not indicate "negative" R-curve behaviour but rather manifests a changing strain energy release rate with crack propagation.

The geometry and stiffness of the testing system and specimen results in a variable crack driving force, as predicted in Section 3.1. As the static Young's modulus of materials P0 to P3 decreases, the R_e vs. A variation does not exhibit a maximum as predicted by the model data of

Figs. 3-8, 3-9. During the initial stages of fracture, the large driving force causes faster crack propagation, the excess energy being dissipated as heat and process-zone creation. The smallest R_e value still capable of driving the crack should be considered as the resistance-to-fracture. Such R_e values are reached as full fracture is approached and these values are 20 to 30 J/m^2 for the materials under consideration.

Fractography of P2 and P3 materials (Fig. S-27 and S-28) shows features similar to those for P0 and P1 type ceramics. The grains are separated in a 20 μm-deep damage layer below the crack plane. The permanent opening displacement is 10 μm. This so-called "process zone" contributes to the increased resistance-to-fracture.

A typical LFU-CA record for the SFFD material with zero HfO_2 content (i.e., P0A type) is shown in Fig. S-29. The permanent deformation after the last cycle does not exceed 3 μm. The two-stages of loading compliance discussed previously, are absent for this material. The resulting resistance-to-fracture, R_e, compiled for two specimens (circles and triangles in Fig. S-29A) increases and subsequently decreases to 40 J/m^2 as full fracture is approached. In the same figure the results for two samples of the P1A material are plotted (squares). A qualitatively similar variation of R_e is observed giving a limiting value of 20 J/m^2 (characteristically, the less stiff material, P1A, results in

a more flat R_e curve than the P0A material).

The difference between the resistance to fracture of the two types of ceramics is determined by their M-phase content (Fig.S-1). This is verified by the microstructural observation of arrested cracks (Fig.S-30A for P0A and S-30B for P1A). The crack opening displacement for P1A is at least two times that for P0A (8 vs.4 μm). The prsence of M-phase facilitates seperation and pull-out of the cubic grains giving predominantly intergranular crack propagation for P1A. The fracture of P0A is of mixed type, i.e., transgranular cracking of the cubic grains and intergranular cracking of the tetragonal/monoclinic mixture.

Increase of the HfO_2 content of the SFFD ceramics to 20 mole % causes the generated microcracks to influence the load-displacement curves and give the characteristic two-mode loading compliance (Fig. S-31A). The effect is similar to that observed for the other high M-phase content materials (P0 to P3). The total permanent deformation exceeds 20 μm and is ~1 μm in each cycle. The scatter of the calculated values of R_e and R_n (Fig. S-31B, compiled for 3 specimens) is attributable to extensive microcracking and crack branching. Fractography indicates purely intergranular cracks as shown in Fig. S-32 for P2A. Activation of these additional energy sinks changes with crack front position and from specimen to specimen. R_e values vary around 40 J/m^2 and R_n around 30 J/m^2.

Clearly, the fracture of stabilized zirconia-hafnia solid solutions is closely related to the content of monoclinic phase and thus to the method of material fabrication and HfO_2 concentration. There is no single resistance-to-fracture value for these materials. The crack may propagate stably for a wide range of driving forces, the fracture mode differing along the crack front and with crack extension. Microscopic analysis of arrested cracks and fracture surfaces undermine the single mode stress intensity factor approach of linear elastic fracture mechanics to ceramic fracture.

Significant amounts of M phase in the stabilized ZrO_2-HfO_2 solid solutions is the result of the increased driving force for the T→M transformation of HfO_2. The development of a successful material fabrication technique (i.e., one that retards the T→M transformation to below room temperature) will result in larger constraint stresses on the resultant tetragonal grains than in the pure ZrO_2 based systems. One approach would be to reduce the grain size to < 0.5 μm, i.e., by an order of magnitude compared with the presently-synthesized materials. These contained an excessively large amount of monoclinic phase. Accordingly it is recommended that only POA-type materials be utilised for further room-temperature load relaxation (LR) studies as their analysis assumes perfect elastic behaviour, i.e., no permanent deformation. Similarly, POA and P1A-type materials should be utilised for high-temperature studies as the high M-phase content of the other

types rendered them sensitive to thermal shock cracking on heating.

5.2.2 Zirconia-Beta-Alumina Composites

These composites were based on commercial zirconia powders partially stabilized with 4.5 mole % Y_2O_3 (the Z4-series materials) or fully with 6.9 mole % Y_2O_3 (the Z8 series materials). Fracture tests were performed on the compo sites and pure matrix samples. A typical LFU-CA record for partially stabilized zirconia PSZ (coded as Z4) is shown in Fig. 5-33A and the resistance to fracture results for four specimens are compiled in Fig. 5-33B. The permanent deformation was 2 μm, a portion of which is attributable to the crushing of the specimen surface by the sapphire knife edges. The linear loading plots indicate the insignificant role of microcracking. Initially R_e varies around 50 J/m^2 and drops to 30 J/m^2 as full fracture is approached. R_n varies around 5 J/m^2 and vanishes as full fracture is approached. The crack opening displacement is less than 1 μm (Fig. 5-34A). Fracture is transgranular through the large cubic grains and mixed-mode through the mixture of smaller tetragonal and monoclinic grains (Fig. 5-34B).

The introduction of β-Al_2O_3 into the PSZ matrix gives the microstructures discussed previously (Fig.5-18). It was expected that the β-Al_2O_3 inclusions would provide effective fracture initiation sites at the tip of the chevron notches

in the initial LFU-CA experiments with the composites. The specimens were therefore not HF etched. However, only partial fracture stabilization was thus achieved. The load-displacement diagram for composite Z4A50 is shown in Fig. 5-35A. The high fracture initiation load (> 80 N) suggests the presence of compressive surface stresses and results in a partial loss of stability in the second cycle. As the cross-head was stopped at point S, the crack propagated unstably under fixed grips conditions finally arresting at point M (such conditions were numerically modelled in Section 3.2 and the load-relaxation experiments will be discussed further in Section 5.3). LFU cycles are performed after the arrest point M to a total permanent deformation of 8 μm. Micro-cracking is suggested by curved loading plots.

R_e and R_n values were compiled for two type Z4A50 specimens and are summarized in Fig. 5-35B. The initial R_e is similar for both specimens (80 J/m^2) but deviations occur after A=40%. The scatter of results for different specimens is characteristic of the PSZ-β-Al_2O_3 composites and the scatter scales with the size of the inhomogeneities (compare with the uniform R_e and R_n bands for the four specimens of pure matrix material, Z4, Fig. 5-33B). The increase of R_e above 100 J/m^2 (specimen Z4A53) suggests crack branching and tilting, a function of the local fracture conditions. The crack tip bifurcated into branches as shown on the polished section, Fig. 5-36A. The β-Al_2O_3 particles (average size 50

μm) are generally traversed by the propagating crack but pull-out and tilt/twist is recognizable on the fracture surface, Fig. 5-36B. The frictional pull-out accumulation is responsible for the R-curve behaviour (rising R_n) in the latter stages of the experiment.

Increase of the average β-Al_2O_3 inclusion size to 90 μm produces a dramatic increase in the permanent deformation of the composite (Fig. 5-37A) and the nonelastic energy dissipation rate increases to 300 J/m^2 (Fig. 5-37B, for two specimens). This phenomenon is related to a network of macrocracks linking the β-Al_2O_3 particles (Fig. 5-19) and also modifying the propagation of the main crack (Fig. 5-38A). The crack follows the particle-matrix interfaces and accordingly is tilted and twisted. The particle pull-out (see fracture surface, Fig. 5-38B) accumulates far back from the crack front due to the large particle size. The net effect is the material's R-curve behaviour (Fig. 5-37B).

This phenomenon is further magnified in the 20 vol. % 120 μm average size β-Al_2O_3 composite. The two-stage loading compliance and noncoincident loading and unloading paths of the full load-displacement record (Fig. 5-39A) indirectly demonstrate intensive microcracking in the material. The fracture record is reminiscent of that for a metal or plastic rather than a brittle ceramic. As the crack extends, an increasing share of the energy input is dissipated non-elastically and the total permanent deformation reaches 170

μm. The total energy consumption as the crack drives through the composite increases with crack length and reaches a value an order of magnitude larger than that for pure PSZ. The resistance to fracture, R_e, exceeds 200 J/m^2 whilst R_n increases to 600 J/m^2 (Fig.5-39B). The tortuous path of the crack through the composite (Fig.5-40A) is enhanced by the pull-out of the β-Al_2O_3 particles from their keying α-Al_2O_3 interfacial reaction product (Fig. 5-40B). Multiple fracture accompanies the propagation of the main crack, the R-curve mechanism being similar to that of the Z4A90 composites.

To identify the individual roles of the matrix and inclusions in the fracture behaviour of the ZrO_2-β-Al_2O_3 composites, similar materials were prepared based of fully stabilized (with 6.9 mole % Y_2O_3) cubic ZrO_2. The load-deflection curve of the pure matrix material (coded Z8) is shown in Fig.5-41 and the microstructure in Fig.5-42. The loading paths (Fig.5-41A) do not suggest microcracking and the total permanent deformation is probably the result of indentation of the soft surface by the sapphire knife edges. Accordingly no R_n values can be determined. The R_e values varied around 11 J/m^2 (Fig. 5-41B). The crack opens to 8 μm (Fig. 5-42A) and fracture is predominantly trans-granular (Fig. 5-42B). The addition of 20 vol % β-Al_2O_3 of 50 μm average size results in extensive nonelastic deformation (up to 50 μm in Fig. 5-43A). The R_e values vs. crack length are initially dispersed around 20 J/m^2 and increase to 40 J/m^2

during the final stages of fracture (Fig. S-43B for three specimens). The value of R_n is widely scattered between 10 and 40 J/m^2 being higher in general than that for similar composites based on a partially stabilized zirconia matrix (compare Fig. S-35B and S-43B). The crack is twisted by the β-Al_2O_3 inclusions, some of which are traversed and some pulled-out (Fig. S-44).

The network of macrocracks that develops and links the 90 μm β-Al_2O_3 particles in the FSZ matrix results in a significant drop of the maximum load maintainable by the specimen, Fig. S-45A. Other fracture features are similar to those of previous materials. R_e increases from 20 J/m^2 to 30 J/m^2 and R_n scatters between 20 and 40 J/m^2 (Fig. S-45B). The main crack follows the existing macrocrack network and thus is subject to sudden tilt (Fig. S-46).

The fracture behaviour of composite type Z8A120 (20 vol. % of particles 120 μm average size) is similar. The low fracture initiation load, the microcracking and the large nonelastic deformation are observed on the load-displacement record, Fig.S-47A. The resistance to fracture is similar to that of the previous two composites (20 to 40 J/m^2, Fig. S-47B for two specimens). The nonelastic energy dissipation rate, R_n, increases with crack extension to 80 J/m^2. This increase is caused by crack branching (in fact, several cracks are being driven simultaneously through the specimen as shown in Fig. S-48A). The β-Al_2O_3 inclusions serve to

arrest and tilt the crack, Fig. S-48A, B.

Summarizing the experimental results presented, R_e values are comparable for most investigated β-Al_2O_3/ZrO_2 materials (with the possible exception of the strong R-curve behaviour of type Z4A120). The term "brittle fracture" seems inadequate to describe these ceramics which exhibit strong crack-microstructure interactions. These interactions determine the nonelastic energy dissipation rate input into the fracture toughness and result in R-curve behaviour. The value of the resistance to fracture characterizes the combined effect of the local conditions of fracture, which vary along the crack front, and the changes that occur with crack extension. The less homogenous the material, the less meaningful is an averaged, single material parameter conventionally termed the "fracture toughness".

As additional fracture energy sinks accumulate behind and/or ahead of the main crack front (i.e., frictional particle pull-out, microcracking, branching, etc.), the total resistance to fracture increases. The crack growth kinetics for such a material cannot be described by a single intrinsic parameter but rather depend on the local balance between the driving force and the accumulating resistance to fracture. To address this problem in more detail, a series of experiments were performed in which the time variable was monitored together with crack length and crack driving force. These involved load-relaxation tests, the results of which will now

be discussed.

5.3 Resistance-to-Fracture at Room Temperature Determined Via Load-Relaxation Techniques

The basic assumption in the analysis of the load relaxation (LR) experiments is the ideal elastic behaviour of the tested material (Section 3.2, Fig. 3-10A). If a certain amount of nonelastic behaviour is present, i.e. there is some permanent deformation at zero load on the load-displacement record, the true crack length and crack driving force are smaller, than calculated in the LR analysis. LR experiments were therefore performed with samples of type POA and Z4 (i.e.; pure PSZ). Some results will be also presented for the ZrO_2/β-Al_2O_3 composites to illustrate the nature of crack-particle interactions in this system. The errors resulting from the assumption of ideal elasticity are discussed. Since LEFM techniques are employed, the crack driving force, R_e, is equivalent to the strain energy release rate, G_I, and R_n=0. The relative slope of the G_I and resistance-to-fracture curves vs. crack extension determine the crack propagation stability (Section 2.1.3).

The results for five LR experiments on POA-type ceramics are compiled in Fig. 5-49A as G_I (or K_I, obtained through eq. 2.12) vs. % fracture area, A. In Fig. 5-49B these results are repeated as the crack velocity v vs. A. The characteristic shape of the G_I curves (discussed in Section 3.2) depends on the load at the moment of fracture initiation

and the initial specimen compliance vs. that of the machine (this ratio can be increased in favour of stable crack growth by extending the initial notch length, x_0, or increasing the bending span ratio S_1/S_2). For the specimen coded P0A2, large initial G_I and dG_I/dA values (perhaps due to the notch bluntness) caused temporary loss of stability and crack acceleration at G_I=104 J/m^2. This value should be taken as the "fracture-toughness" of the material. Stability is subsequently regained at G_I=94 J/m^2, suggesting increasing inertia of the propagating crack as discussed previously. The error in the G_I determination via the LR test leads to an overestimation of G_I and this error increases with the crack length; therefore, the crack inertia effect must be significant).

A sharp drop of the crack velocity is observed for all specimens at G_I=65±5 J/m^2. This heralds the approach of fracture arrest or the threshold value of G, i.e. G_t. The two limiting values of 65 and 104 J/m^2 agree with the results of LFU-CA experiments (in Fig. 5-29B the calculated values of R_e are between 50 and 90 J/m^2). The crack propagates with an approximately constant velocity of 20 µm/sec for A=20 to 40% for all the specimens tested (Fig. 5-49B).

Similar results for the commercial PSZ ceramic (sample type Z4, i.e. the matrix material of the ZrO_2/β-Al_2O_3 composites) are plotted in Fig. 5-50. The crack accelerates beyond G_I=40 J/m^2 reaching a critical velocity at G_I=60 J/m^2 (=G_{IC}), Fig. 5-50A. The Z4-material had a lower fracture toughness

(compared with POA) so it was more difficult to perform a complete LR test (i.e., up to the fracture arrest point). A modified LR test was therefore developed which facilitated estimation of the threshold (G_t) and critical fracture (G_{IC}) conditions. The results of this test are shown in Fig.5-50B. After the conventional load-relaxation period (path IU), the specimen was quickly unloaded (at point U). Subsequently another LR tests is performed on the same specimen, the crack growth velocity and G_I being monitored from the start point S until the catastrophic fracture at point C. The strain energy release rate at the fracture re-initiation point (S) can be obtained from the loading compliance and it is not "infinite" as per a virgin CN specimen at the chevron tip. The sample is effectively precracked so overcoming fracture initiation difficulties. G_I at the point S approaches the threshold value, G_t, and the critical value, G_{IC}, is approached at the point C. Values of 30 J/m^2 and 64 J/m^2 were thus obtained and are in good agreement with the results of the continuous LR test (Fig. 5-50A) and the LFU-CA analysis (Fig. 5-33B).

A series of LR experiments were performed to monitor the kinetics of crack-particle interactions in ZrO_2/β-Al_2O_3 composites. The nonelastic behaviour of these materials leads to an overestimation of the crack length and driving force so the results, especially of the G_I calculations, should be treated as qualitative or upper limits. As the results of the crack velocity calculations are plotted on a logarithmic

scale, the discrepancy between the true and calculated values is less apparent. Moreover, for long cracks even large errors in the compliance measurements result in negligible errors in the crack length calculations (but not negligible in the crack driving force G_I calculations, as discussed in Section 4.8).

The normalized load-relaxation records are compared for PSZ and the three ZrO_2/β-Al_2O_3 composites in Fig. 5-51. The variability of the record and the tendency for the crack to arrest is proportional to the inhomogeneity of the material. PSZ fractures catastrophically when half the load has been relaxed. The crack arrests at $P/P_{max} \simeq 0.25$ for Z4A120 and at $P/P_{max} \simeq 0.05$ for Z4A50 (Fig. 5-51A). A similar graph for Z4A90 (Fig. 5-51B) has the crack velocity v results also plotted. As expected, the variation of v follows that of the load within at least two orders of magnitude due to the proportionality between the crack velocity and slope of the P vs. time curve (equation 4.3).

The tortuous velocity curve demonstrates the crack-particle interactions which result in repeated acceleration, decceleration and finally arrest. This point is further illustrated if the crack velocity is plotted with the driving force (taking into account the precautions previously discussed) vs. crack extension, Fig. 5-52A. The characteristic shape of the G_I curve (i.e., the externally applied crack driving force) determines the different ranges of crack-par-

ticle interaction. In the vicinity of the minimum G_I, the crack is likely to oscillate between arrest and an average velocity of 30 μm/s. Near maximum G_I the trend reverses and the crack accelerates from the average towards the critical velocity. It finally arrests as full fracture is approached. This example clearly excludes the application of a single kinetic power law for crack growth (similar to eq. 2.4) for a material exhibiting strong crack-microstucture interactions. The acceleration-decceleration events scale approximately with the particle size, Fig. S-52B. The crack path between arrest points is 240, 160 and 270 μm for the β-Al_2O_3 particle size (Z4A20 composite) between 106 and 150 μm.

Although quantitative analysis of the LR results requires the assumption of ideal elasticity, qualitative observation provides insight into crack-microstructure interactions unavailable by other testing techniques. This proved particulary useful for the ZrO_2/β-Al_2O_3 composites. The quantitative results of the LR tests agree well with the data generated by the LFU-CA technique at room temperature for the reference materials, POA and Z4. At elevated temperatures neither technique can be employed with sufficient accuracy. The concept of the strain energy release rate as the crack driving force is invalid if fracture is accompanied by large-scale nonelastic deformation. The crack length calculations via the compliance measurement are inadequate for similar reasons. Therefore, load-fracture-unload and electri-

cal potential drop analyses (LFU-PD) were conducted, as will now be discussed.

5.4 The Resistance-to-Fracture at Elevated Temperatures

Loading-fracture-unloading tests combined with potential drop analysis (LFU-PD) allow exclusive determination of that part of the total fracture energy responsible for the effective crack extension, i.e. R_e, at elevated temperatures. The value of R_e may be much smaller than the nonelastic energy dissipation rate R_n, at high temperatures. The crack can extend at a variable velocity under the influence of a variable driving force R_e. The smallest recorded R_e value that can drive the crack is defined as the resistance to fracture initiation. The analysis pattern used hitherto is maintained in this section. The variation of R_e with fracture area is correlated with the microstructural interactions of arrested cracks.

5.4.1 Zirconia-Hafnia Solid Solutions

The LFU-PD load (P) vs. potential drop (U_2) across a crack in a POA ceramics at 1000 and 1300°C is shown in Fig. 5-53A and Fig. 5-53B respectively. Crack closure and partial reestablishment of electrical contact is responsible for the potential drop decrease in the last stages of unloading. This effect is more pronounced at 1000°C (compare to 1300°C) due to the higher elasticity of the material at 1000°C. The reopening of partially closed cracks requires a higher load, eg. by increment MN in the sixth cycle shown in Fig. 5-

53A. This observation is similar to that for room temperature experiments and suggests that fracture energy is frictionally dissipated in the closing and opening of microcracks. Moreover, the shifting the meniscus of liquid grain boundary phases (known to be present in ZrO_2 ceramics) provides additional energy dissipation. The high-temperature crack closure effects in aluminas containing glassy second phase were reported by Kromp and Pabst [61].

The unloading and reloading paths deviate from each other (for example the paths TS and UW respectively in Fig. 5-53A) as the crack grows longer. The origin of this effect is not clear at present. The period of crack reopening (path VW) can be easily differentiated from the period of loading at constant crack length (path WU). The fracture re-initiation point is U. In subsequent calculations, the potential drop at the moment of unloading start (point T) has been taken as indicative of the crack length. As the temperature is increased to 1300°C (Fig. 5-53B), the effects of crack closure and deviating loading-unloading paths are suppressed.

At intermediate temperatures (1000°C) and longer cracks (for example cycles # 6 to 9 in Fig. 5-53A) the period of loading with a stationary crack is sharply distinct from the period of crack movement. This is in contrast to the pattern for shorter cracks (cycles # 2 to 4) or higher temperatures (the first ten cycles in Fig. 5-53B), where the start of crack motion is accompanied by a further load

increase. This jump-like manner of the crack propagation in a viscoelastic body was theoretically predicted by Nikitin and Krayanov [170], for specific values of externally applied load. However, the effect was not observed experimentally so far. It seems that the potential drop technique utilised in this thesis enables observation of phenomena difficult to record by other techniques.

The resistance-to-fracture results (R_e) for the two specimens are presented in Fig. S-53C. At 1000°C R_e decreases towards 6 J/m^2 and at 1300°C towards 2 J/m^2. If the error bands are imposed on these results, the resistance-to-fracture-initiation at 1000°C is between 4 and 8 J/m^2 and at 1300°C between 1 and 3 J/m^2 for the POA ceramics. Microstructural examination of the arrested crack at 1300°C reveals an accumulation of creep-like damage in the vicinity of the fracture, Fig. S-54A. The change of fracture mechanism between room and elevated temperatures, from mixed mode to pure intergranular, is illustrated by comparison of Figs. S-30A and S-54A, B. This change is accompanied by a 25 times decrease of the resistance-to-fracture (from 50 J/m^2 to 2 J/m^2).

The presence of the monoclinic phase in the P1A type ceramics increases the probability of microcracking and crack branching (the creation of multiple fracture zones). The M→T transformation during heating makes high-temperature experimentation with this material more difficult. An LFU-PD record

taken at 1300°C is shown in Fig. S-55A. The unexpected increase of transmitted load (and thus the work of fracture) during the fifth and subsequent cycles suggests that the crack is twisting and/or branching. This appears as a temporary increase of the calculated resistance-to-fracture, R_e, from 3 J/m^2 to $6J/m^2$, Fig. S-54B. As the notch is further extended, R_e falls again towards 2 J/m^2.

Similar results were obtained for the test conducted at 1000°C, i.e. R_e decreases towards 2 J/m^2. It appears that the grain boundaries which have been weakened by the monoclinic-to-tetragonal phase transformation, determine the low resistance-to-fracture of the P1A type ceramics in the range 1000 to 1300°C. This value of R_e is still an order of magnitude lower than that at room temperature (Figs. S-29B and S-54B). The mixed fracture mode is maintained up to 1000°C, Fig. S-56A. The purely intergranular fracture mode is evident at 1300°C, Fig. S-56B. The rounded grains, visible on the 1300°C fracture surface, suggest that the low viscosity amorphous grain boundary layer is also playing a role in the material's resistance-to-fracture.

The fabrication techniques employed for the preparation of the ZrO_2-HfO_2 solid solutions proved ineffective in retarding the devastating tetragonal-to-monoclinic phase transformation in the HfO_2-rich materials. This is not surprising as the driving force for this transformation is much larger in ZrO_2-HfO_2 than for pure ZrO_2. Accordingly,

the effect of HfO_2 content on the high-temperature fracture characteristics could not be determined.

The spray-freezing freeze-drying of the stabilized ZrO_2 powders (POA materials) gave ceramics with a resistance to fracture 2x that of the commercial powder, Z4, at room as well as elevated temperatures. At 1300°C the low viscosity amorphous grain boundary phase still determines the resistance to fracture initiation ($\sim$2 J/m^2). This result stimulated an alternative approach to improving the high-temperature fracture properties of ZrO_2 ceramics. This involved the dispersion of a non-deformable second phase of β-Al_2O_3 refractory particles. The results of the investigation of this composite at elevated temperatures are now presented.

5.4.2 Zirconia-Beta-Alumina Composites

The ZrO_2/β-Al_2O_3 composites (ZBA) are based on the yttria partially (Z4-series) or fully (Z8-series) stabilized commercial zirconium oxide. The fracture properties of the PSZ matrix (i.e., pure Z4 material) were investigated between 800°C and 1300°C.

It proved impossible to stabilize the fracture process between 800 and 1000°C and so no R_e data were gathered in this range. The tetragonal phase of the yttria stabilized zirconia is stable above 500°C and thus the transformation toughening (which predominantly determines the materials resistance to fracture) is no longer active. Since the fracture stability at a given crack-driving-force is determined by the overall material toughness (i.e., $R_e + R_n$), it is the increasing nonelastic energy dissipation rate that restores crack stability above 1000°C.

The load vs. electrical potential drop curves Z4 and ZOA are qualitatively similar for between 1100 and 1300°C (compare Figs. S-S38 and S-S7C). The R_e results are summarized in Fig. S-S7 A, B, D (at 1100°C, 2 specimens; 1200°C, 2 specimens and 1300°C, 4 specimens). The minimum values of R_e vary between 1 and 6 J/m^2 but no significant correlation with test temperature was observed. It was concluded that the resistance to crack propagation for Z4 (i.e., the yttria-partially stabilized zirconia) is 2 J/m^2 between 1100 and

1300°C (note this value does not include the larger non-elastic energy dissipation rate, R_n. This contribution will be discussed in subsequent parts of this section).

The associated fractographs are compiled in Fig. S-58A to G. At 800°C fracture is predominantly transgranular, even for the mixture of small tetragonal and monoclinic grains, Fig. S-58A. As the test temperature increased, intergranular fracture increased. Initially it occured between the tetragonal grains exclusively (Fig. S-58B, at 1000°C) but for the whole structure between 1100 to 1200°C (Figs. S-58C, D). Viscoelastic deformation at 1300°C caused cavity coalescence in the crack plane, Fig. S-58F (the crack arrested after the last LFU-PD cycle). Again the rounded grain surfaces are evidence of this phenomenon (Fig. S-58E). Crack arrest at 1100°C (Fig. S-58G) involved branching and multiple fracture but no viscoelastic deformation.

Dispersion of 20 vol.%, 50 μm average-size β-Al_2O_3 particles throughout the PSZ matrix improved the fracture stability and facilitated performance of the LFU-PD experiments between 1000°C and 1300°C. The 1000°C load vs. potential drop record for the Z4A50 type ceramics is shown in Fig. S-59A. Fracture initiation was noted at point S and the system quickly unloaded thereafter. The elastic energy stored in the machine and the specimen was suffi ciently large however to drive the crack at a velocity close to the critical value through most of the cross-section in 1 second,

giving apparent arrest at Z. Effectively the test was one of load-relaxation with the strain-energy-release-rate changing up to the arrest point as predicted in Fig. 3-11.

This observation was further verified by the resistance-to-fracture results, Fig. 5-59B. It was assumed in the numerical analysis that the potential drop value at any point along the SZ curve represents the crack length (as would the unload curve at that point). The R_e results are plotted in Fig. 5-59B for two specimens (triangles and circles). The arrest point, Z, is reached at R_e=2 J/m^2 for both samples. Large values of R_e before the arrest point are responsible for the loss of stability and initial crack acceleration.

It must be emphasized that, although R_e is defined as the "resistance to fracture", it is actually the energy released from the testing system and the specimen per unit area of the created fracture surface. Large values of R_e indicate, that there is rapid energy release rate and this is not necessarily equivalent to a large material toughness. Only consideration of the crack velocity at given R_e values allows one to draw conclusions about the material toughness. Consequently, in the present thesis the values of R_e are investigated whereat the crack is being arrested. For the composite Z4A50 at 1000°C, R_e in the range of 50 J/m^2 causes near-catastrophic failure (i.e., the fracture-toughness is being approached) whilst R_e in the range of 2J/m^2 causes crack arrest (i.e., the resistance-to-fracture-initiation is approached).

A fractograph of the Z4A50 composite tested at 1000°C is shown in Fig. 5-60A. The PSZ matrix exhibits the characteristic mixed-mode fracture (cf. Fig. 5-58B). Most of the β-Al_2O_3 particles are crossed by the propagating crack, suggesting the presence of a strong α-Al_2O_3 interface between the β-Al_2O_3 and the matrix. As the test temperature increased to 1300°C, the interface weakened and complete β-Al_2O_3 particle pull-out takes place. The cavity left by one such pull-out is shown in figure 5-60B. The residue of β-Al_2O_3 grains can be clearly seen at the bottom of the cavity. Fig. 5-60C shows the pull-out site left by the β-Al_2O_3 particle after complete pull out from its "coat" of α-Al_2O_3.

Examination of the surface normal to the arrested crack plane (Fig. 5-60D) shows that the β-Al_2O_3 particles provide sites of main crack deflection and branching. The occurence of these phenomena are reflected in the 1300°C load vs. potential drop record, Fig. 5-61A. The drop of maximum load in each cycle vs. crack extension is slower than that for pure PSZ at 1300°C or Z4A90 at 1000°C (and, as will be seen later, for the larger-β-Al_2O_3-particle composite Z4A120). The unexpected increase in the maximum load transmitted in the 9th cycle is the result of crack branching and this occurence is quantitatively reflected by an increase of the calculated R_e values from the expected 4 J/m^2 to 8 J/m^2 (Fig. 5-61B, open circles). The R_e values obtained for two other specimens of the same material gave 2 to 4 J/m^2, as per

pure PSZ. It is therefore the nonelastic energy dissipation rate, R_n, which is affected by the dispersion of refractory particles in a viscoelastic matrix and not the value of R_e.

The composites containing β-Al_2O_3 particles of average size 120 μm (i.e., the Z4A120 series) were tough enough to assure fracture stability at temperatures as low as 700°C, i.e., the temperature limit of applicability of the potential drop technique for ZrO_2 ceramics. The 700°C load vs. potential drop record shows partial instability followed by fracture arrest (point A, Fig. 5-62A). Several subsequent LFU-PD cycles demonstrate the tendency for crack closure upon unloading indicative of elastic behaviour of the specimen. Since crack closure does not continue with time for a completely unloaded specimen, no viscoelastic strain component is involved. R_e tends to 4 J/m^2 as full fracture is approached, Fig. 5-62B (two samples).

The dramatic decrease of the resistance to fracture between room temperature and 700°C (from 200 J/m^2 to 4 J/m^2, cf. Fig.5-39B) is attributable to the loss of the transformation toughening and a change in the crack-particle interaction mechanism. Fractography shows a well-developed α-Al_2O_3 interface on the large β-Al_2O_3 particles. The crack traverses most of the particles, the rest are pulled out (Fig.5-63A,B).

Tested at 1000°C, Z4A120 (Fig. 5-64) exhibits a lower tendency for crack closure but the viscoelastic strain component induces closure at zero load (for example path YZ in

Fig. 5-64A represents a crack closure of 50 μm over three minutes). The viscoelastic deformation component improves fracture stability and so influences the resistance-to-fracture. R_e values for Z4A120 tested at 1000°C range between 5 and 12 J/m^2, Fig. 5-64B (two specimens). Micrographs of arrested cracks and fracture surfaces (Fig. 5-65) show that most β-Al_2O_3 particles are traversed. The crack opening displacement is uniform and ≃ 40 μm.

Increase of the test temperature to 1300°C eliminates crack closure, i.e., the strain is now time independent and irrecoverable (plastic), Fig. 5-66A. Calculated values of R_e decrease to 2 to 6 J/m^2, Fig. 5-67B. Large discrepancies between the curves for three samples reflect the inhomogeneity of the Z4A120 composites (cf. similar curves for the more homogenous Z4A50, Fig. 5-61B, and the pure PSZ, Fig. 5-57D).

Figure 5-67A is a polished section micrograph of a Z4A120 sample cut normal to the crack plane wherein the crack was arrested after the last unloading cycle. The fracture predominantly follows the interfaces between the PSZ and Na-β-Al_2O_3 and the network of macrocracks linking the particles. Examination of a fracture surface, Fig. 5-67B, revealed the crack-interface interactions. A β-Al_2O_3 particle has pulled out, leaving a sheared-off α-Al_2O_3 layer. It is characteristic that the α-Al_2O_3 appears mainly at the bottom of the original β-Al_2O_3 site. This indicates that this particular Na-β-Al_2O_3 particle was oriented with its fast-diffusion

planes perpendicular to the fracture surface. α-Al_2O_3 will only form at the edge of these planes as the Na^+ is immobile through the spinel blocks of the β-Al_2O_3 structure.

From the results presented, the resistance to fracture, R_e, of the ZBA ceramics changes little with temperature and composition above 500°C (2 to 10 J/m^2). It is clear however, that the presence of the β-Al_2O_3 particles influences the overall toughness of the composite materials (i.e., $R_t = R_e + R_n$). Therefore R_n was estimated for a limited number of PSZ, Z4A50 and Z4A120 specimens at 1300°C.

The nonelastic energy dissipation rate, R_n, resulting in permanent deformation of the specimen, can be calculated only if the load-application point displacement is simultaneously recorded. For plastically deforming ceramics at high temperatures, $R_n \gg R_e$, so R_n approximates the total input of work to break unit area of the specimen. At 1300°C the creep deformation of the testing system (alumina tubes and plates of the smallest cross-section 3 cm^2) under the applied loads and time of test was insignificant compared with the specimen deformation. Therefore the total input of work in each cycle, ΔW, corresponds to the area under the load-displacement curve. The displacement was measured outside the furnace. Since the fracture area increment, ΔA, was calculated from the potential drop, R_n for each cycle is obtained as $\Delta W/\Delta A$.

The load against displacement plots for PSZ and the two β-Al_2O_3 composites are shown in Figs. 5-68A to C (Figs.

S-68B, S-61A; S-68C, S-66A and S-68A, S-57C are in pairs, i.e., they are simultaneous records for the same samples). The drop of load in consecutive cycles was fast for Z4A120 and PSZ; the permanent deformation reached 200 μm for PSZ and 400 μm for Z4A120. A slower drop of maximum load was observed for the Z4A50 (demonstrated already in Fig. S-61A) and this is accompanied by a total permanent deformation of 600 μm. The R_n results are compiled in Fig. S-68D. The values for PSZ or Z4A120 (closed symbols) tend to ~300 J/m^2 (i.e., the range between 200 to 400 J/m^2 allowing for the estimated error) whilst the values for Z4A50 (open symbols) tend to ~700 J/m^2 (i.e., 400 to 1000 J/m^2).

As shown above and in the discussion of the room temperature results, the incorporation of β-Al_2O_3 particles into a PSZ matrix creates additional modes of fracture energy dissipation at high and low temperatures. The fracture modes change with temperature however. Strong R-curve behaviour at room temperature is attributed to the matrix/β-Al_2O_3 interfacial microcracking and frictional pull-out of the β-Al_2O_3 particles. The small opening displacement of the crack at room temperature keeps these mechanisms active far back from the crack tip and causes an increase of R_n with crack extension. The reduction of the Na-β-Al_2O_3 particle size to 50 μm or less prevents the matrix spontaneously cracking and improves the strength and continuity of the α-Al_2O_3 at the interface. Consequently, the presence of the particles is ignored by a

crack running at room temperature and the strength is improved whilst the toughness deteriorates.

An increase of temperature to 1300°C causes softening of the amorphous grain-boundary phase. Viscous flow of the PSZ matrix thus results in a large crack opening displacement soon after fracture initiation. Therefore, even large particle pull-out can only take place close to the crack tip and this is now facilitated by the weaker interface (especially in the case of Z4A12O). This eliminates the R-curve mechanisms of room temperature. Instead viscous flow close to and ahead of the crack tip provides the predominant portion of the fracture energy. The presence of 50 μm β-Al_2O_3 particles in the viscous zone appears to provide sites for crack arrest, branching, microcracking close to the fracture surface and particle pull-out close to the crack tip. Effectively the particles "harden" the viscously deforming matrix especially if the interfacial product α-Al_2O_3 separates from the β-Al_2O_3 during deformation.

It is expected that control of the Na-β-Al_2O_3 particle size is as important as control of the particle-matrix interface reactivity. With respect to the latter, the system is very flexible due to the easy ion exchange of the Na-β-Al_2O_3 particles at any stage of the processing and the possibility of matching the properties of the particles and interfaces to those of the matrix (not necessarily PSZ).

It has been suggested [110] that the high-temperature

fracture of PSZ monocrystals is influenced by the presence of finely dispersed tetragonal (T) phase precipiates. The T-phase in polycrystalline PSZ is present not only as individual grains 1 to 3 μm large, Fig. S-34B, but also as fine inclusions precipitated within larger cubic grains during the cooling of the ceramics from sintering temperatures [82, 83]. It is interesting therefore to compare the energy for the high-temperature fracture of PSZ and that for fully stabilized zirconia FSZ (i.e., that with no tetragonal phase, type Z8) and the respective β-Al_2O_3 composites (Z8-series).

The 1000°C results for Z8 and the Z8A50 composite are compared in Fig. S-69A, B. The 1300°C results are compared in Fig. S-70A, B. The initial unstable fracture of the Z8 ceramics at 1000°C (discussed already for Z4-ceramics) is characteristic of homogenous stabilized zirconium oxide at temperatures between the transformation toughening range (< 500°C) and the plastic deformation range (> 1100°C). The dispersion of β-Al_2O_3 particles improves the overall toughness of the composite sufficiently to control crack propagation (Fig. S-70B). The maximum load transmitted through the specimen at 1300°C (Fig. S-70) is only half of that at 1000°C, for both Z8 and the β-Al_2O_3 composite. A period of accelerated fracture still occurs in the Z8-material (Fig. S-70A), although it is limited to shorter crack lengths and slower propagation velocities.

Such instability was not observed in the partially

stabilized zirconia tested at 1300°C (Fig. S-57C). This suggests some interaction between the crack and the stable tetragonal precipitates during the high-temperature fracture of ZrO_2 ceramics. The higher composite toughness enables control of the high-temperature fracture (Fig.S-70B). The resistance to fracture data from Figs. S-69 and S-70 quantitatively prove these conclusions. The R_e value of Z8 drops to fractions of J/m^2 at temperatures ≥ 1000°C (Fig. S-71A) whilst that of the composite (20 vol.% of β-Al_2O_3 particles of 50 μm average size) is an order of magnitude higher (2 and 4 J/m^2 at 1300 and 1000°C respectively, Fig. S-71B).

Fractography of the pure matrix, Z8, (Fig. S-72) shows that the large-grained (40 μm average grain size) fully stablized zirconia fractures by grain separation at 1000°C and 1300°C. High temperature grain-boundary cavitation (especially visible on comparison of Figs. S-72A and S-42B) is a characteristic failure mechanism. It seems that the resistance to fracture of the Z8-ceramics at 1300°C is determined by the surface tension of the liquid grain boundary phase therein. Accordingly, the cracking of the β-Al_2O_3 particles at 1000°C (Fig. S-73A) or their cracking and pull-out at 1300°C (Fig. S-73B) provides a relatively large increase of material toughness. The result is therefore, that the dispersion of β-Al_2O_3 particles is more effective in increasing the toughness of fully rather than partially stabilized zirconia at high temperatures.

Generally, any zirconium oxide ceramics are damaged at high temperatures by cracks propagating under driving forces of the order of 1 J/m^2. The failure mechanism and partition of the total fracture energy into crack extension and non-elastic deformation is a strong function of the microstructure. Grain-boundary cavitation and coalescence seems to be the primary high-temperature failure mechanism of materials based on fully stablized zirconia. The continuous film of amorphous grain boundary phase controls the fracture of ceramics based on partially stabilized zirconia. Thus crack advance is dictated by the liquid properties and the balance between the applied driving force and the liquid/solid meniscus curvature.

This effect appears responsible for the discontinuous crack propagation in the POA type ceramics under small applied forces (Figs. S-53 A to C). The sharp, discontinuous crack advance observed at point U (Fig. S-53A) suggests liquid meniscus breakage (i.e., an unbalancing of the equilibrium between the surface tension and the externally applied driving force). Beyond this critical point, fast crack penetration of the intergranular layer takes place. This effect (predicted theoretically [170]) is less pronounced at high temperatures (Fig. S-53B) as the liquid viscosity is lower. Similar discontinuous crack extension has been observed in MgO/CaO-stabilized-ZrO_2 at 900°C [163]. The effect was not explained as the true resistance-to-fracture

(i.e., the energy input to extend the fracture surface by unit area) and the total "fracture toughness" (i.e., in practice, the nonelastic energy dissipation rate) were not differentiated.

The high-temperature slow crack propagation is accompanied by damage accumulation. The damage zone extends further from the crack plane as the threshold value of the crack driving force is approached. This side damage and the cavitation lend to crack blunting and arrest (for example, consider Fig. 5-54A).

The results of the present study of the high-temperature resistance-to-fracture of ZrO_2 ceramics is difficult to compare with literature data as there is little of the latter (limited results have been reported for MgO/ZrO_2 in terms of the total work-of-fracture up to 900°C [163] or as the "standard" K_{IC} test up to 1300°C [165]). The general trend of decreasing total work-of-fracture (i.e. in terms of this thesis, R_e+R_n) with the crack extension for Mg-PSZ was observed by Swain and Hannink [171]. If the 1300°C properties of zirconias are controlled by an amorphous grain-boundary phase, the order of magnitude of the resistance-to-fracture should be similar to that of glass-containing α-Al_2O_3 at 1400°C, Fig. 2.68 [164]. In fact, a threshold crack driving force value of 1 to 7 J/m^2 was obtained for these materials [164]. These values are in agreement with the data of the present thesis.

CHAPTER 6

CONCLUSIONS AND RECOMMENDATIONS FOR FUTURE WORK

The fracture properties of pure and composite zirconium oxide ceramics were studied. Chevron-notched (CN), four-point bend specimen geometry was utilised. The behaviour of the CN specimen was numerically simulated and guidelines were developed for its use in the testing of brittle materials exhibiting subcritical crack growth. If the CN specimen is to be utilised for K_{IC} determinations, crack instability must follow stable crack initiation and must coincide with the maximum load on the load-displacement (or time) curve. Crack instability at any other load (or catastrophic failure without a stable crack growth period) will underestimate the value of fracture toughness unless the precise length of the crack at the onset of instability is known.

If the coincidence of K_{IC} and the maximum load is unknown for given experimental conditions (loading rate, machine stiffness, etc.), the fracture toughness test should be performed in steps as follows: (a) perform initial tests on a series of CN samples utilising a machine cross-head

displacement rate such that instability occurs after the maximum load is reached ; (b) increase the displacement rate such that instability occurs at the maximum load. Now the standard LEFM formulae for K_{IC} can be utilised.

The work-of-fracture (or effective fracture energy) is a function of the notch depth in CN samples due to sub-critical crack growth. As the crack extends (or the specimen is notched deeper) a smaller portion of the input energy is utilised to accelerate the crack or is dissipated as heat. The work-of-fracture in multiple loading-unloading experiments approaches the threshold crack driving force (or the resistance-to-fracture-initiation) as the cracked area approaches 100% of the specimen cross-section.

The kinetics of crack-microstructure interactions were best observed via load-relaxation (LR) experiments. Numerical study of CN specimen testing via LR experiments resulted in G_I curves as a function of specimen geometry and parameters of the testing system. Stable crack extension at the beginning of the LR test (due to the negative slope of the G_I vs. crack extension curve) is followed by periods of crack acceleration and deceleration. The LR experiment allows determination of the crack driving force at arrest or critical fracture and generation of full K_I-velocity curves.

A semiempirical approach was proposed for the determination of the crack length in a CN specimen utilising an electrical potential drop method. The technique is appli-

cable to any crack-front shape of known curvature. The formulation of the crack length as a function of the potential drop was successfully verified at room temperature for model graphite specimens and at elevated temperatures for stabilized zirconia specimens (ionic conductors).

The experimental part of the thesis led to the following conclusions:

1. The alloying of stabilized zirconia with hafnia causes extensive microstructural damage via the detrimental transformation from the high-temperature tetragonal phase to the low temperature monoclinic phase as the material is cooled from sintering temperatures. The transformation-generated microcracking resulted in a decrease of material elasticity and an increased ability to nonelastically dissipate fracture energy.

Successful hafnia alloying must be accompanied by imposition of more severe (compare to partially stabilized ZrO_2) transformation constraints. Submicron grain size seems a necessary condition for the proper synthesis of zirconia-hafnia ceramics. In this respect an effective processing route was spray-freeze, freeze-drying.

2. The dispersion of β-Al_2O_3 particles in a partially

stabilized zirconia matrix did not significantly affect the level of monoclinic phase therein. The elastic properties of the material dropped due to the network of microcracks present in composites with > 50 μm β-Al_2O_3 average particle size or with a fully stabilized zirconia matrix. Depletion of Na^+ from the periphery of the β-Al_2O_3 particles led to precipitation of α-Al_2O_3 at the interface between the particles and the zirconia matrix. This interface plays a decisive role in the fracture properties of the composites.

3. Damage in the zirconia-hafnia solid solutions (due to the tetragonal to monoclinic phase transformation) resulted in large nonelastic energy dissipation rates, 10 to 60 J/m^2. Fracture is arrested when the crack driving force, R_e, equals 10 to 20 J/m^2 for materials obtained by oxide mixing and at 20 to 40 J/m^2 for materials obtained by spray-freeze/freeze-drying.

4. Zirconia-β-alumina composites exhibit strong R-curve behaviour at room temperature. The nonelastic energy dissipation rate reaches 700 J/m^2 for a composite with 120 μm β-Al_2O_3 particles in a partially stabilized zirconia matrix. The accumulated frictional β-Al_2O_3 particle pull-out far back from the crack front is the source of the R-curve behaviour. These ceramics are expected to exhibit superior thermal shock resistance.

5. The load-relaxation experiments resulted in the predicted variation of the strain-energy-release-rate. The crack-arrest point for PSZ was G_I=30 J/m^2 and this result agrees well with those of the room-temperature loading-fracture-unloading technique. The load relaxation vs. time records revealed periodic crack acceleration and deceleration in scale with the size of the major microstructural obstacles (eq. β-Al_2O_3 particles in the composite).

6. The minimum crack driving force at arrest for ZrO_2 ceramics drops by an order of magnitude between room temperature and 1000°C (for example from 40 J/m^2 to 5 J/m^2 for PDA). It drops further at 1300°C to about 1 J/m^2. The load vs. potential drop record at high temperatures suggests a viscoelastic process of crack initiation, propagation and closure in ZrO_2 ceramics. The materials crack intergranulary above 1000°C. High-temperature fracture is accompanied by damage zone accumulation and intergranular cavitation.

7. The presence of β-Al_2O_3 particles in partially stabilized zirconia (PSZ) does not significantly influence the resistance to fracture R_e (i.e., the elastically dissipated fracture energy) at elevated temperatures. However, the frictional particle pull-out from the β-Al_2O_3 interface, the crack tilt and branching and the plastic deformation of

the matrix increase the nonelastic energy dissipation rate, R_n. At 1300°C crack arrest corresponds to an R_n value of 700 J/m^2 for the Z4A50 composite.. $R_n \simeq 300$ J/m^2 at 1300°C crack arrests for PSZ and the Z4A120 composite.

8. At elevated temperatures, fully stabilized zirconia exhibits an exceptionally low resistance to fracture at the crack arrest point (0.5 and 0.1 J/m^2 at 1000 and 1300°C respectively). Consequently, dispersion of β-Al_2O_3 particles results in a significant increase in the crack driving force at arrest (4 and 2 J/m^2 respectively).

Stable, slow crack growth was achieved over a wide range of applied driving forces in the ZrO_2 ceramics investigated. The loading-fracture-unloading cycles repeated on one specimen revealed the response of the material to externally applied stress as a function of the crack extension and the materials microstructure and homogeneity. The globally measured response is an average of local conditions which vary along the crack front in proportion to the inhomogeneity of the material. Since the measurement of the local resistance to fracture is experimentally impossible at present, efforts were concentrated on determination of the minimum force capable of driving the crack front. Consequently less attention was paid to the intermediate and critical values of the crack driving forces. The theoretical and experimental studies

undertaken suggest a range of new directions for future research:

1. Experimental verification of the numerical simulation of the fracture toughness test utilising CN specimens.

2. Extension of the solutions of the potential drop technique obtained for the not-straight-through crack to curved crack fronts of arbitrary shape. This research area bridges the achievements of the present thesis (devoted mainly to ceramic materials) with other areas of materials science (eg. fatigue of metals, fracture of conducting polymers, etc.).

3. Processing of fine-grained zirconia-hafnia solid solutions to synthesise ceramics composed of single tetragonal phase at room temperature.

4. Investigation of the thermal shock resistance and reliability of the ZrO_2/β-Al_2O_3 composites. Also the possible extension of the β-Al_2O_3 dispersion technique to other ceramic matrices.

5. The strengthening of ceramic composites containing dispersed β-Al_2O_3 by ion exchange of the β-Al_2O_3 in ionic melts. The Na^+ residing on the fast-conduction planes of the

β-Al_2O_3 can be relatively easily exchanged with other ions (K^+, Li^+, Sr^{2+}, etc.) and the reactivity and physical properties of the particles can be controlled. The ion exchange $Na^+ \rightarrow K^+$ results in a volume increase of the β-Al_2O_3. The ion-exchange of constrained, surface β-Al_2O_3 particles will thus induce compressive stresses in the composite. This is an original method of inducing compressive surface stresses in brittle materials and it is presently being studied.

APPENDIX 1

Numerical Techniques for Compliance Analysis

Subroutine XCOM(S_1, S_2, B, W, E, V, x_0, x_1, N, Z, x)

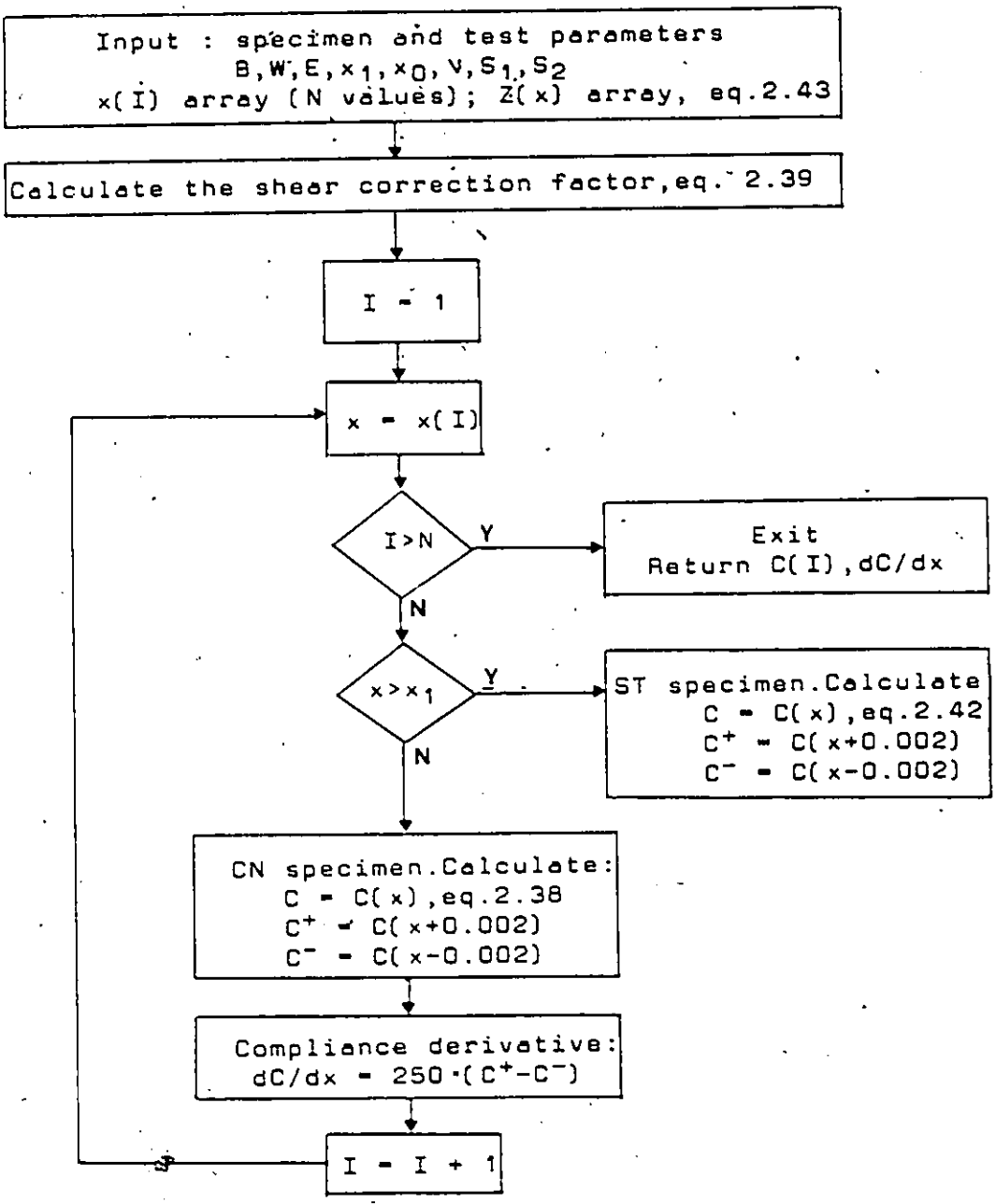

Subroutine COMX(S_1,S_2,B,W,E,V,x_0,x_1,N,Z,C1)

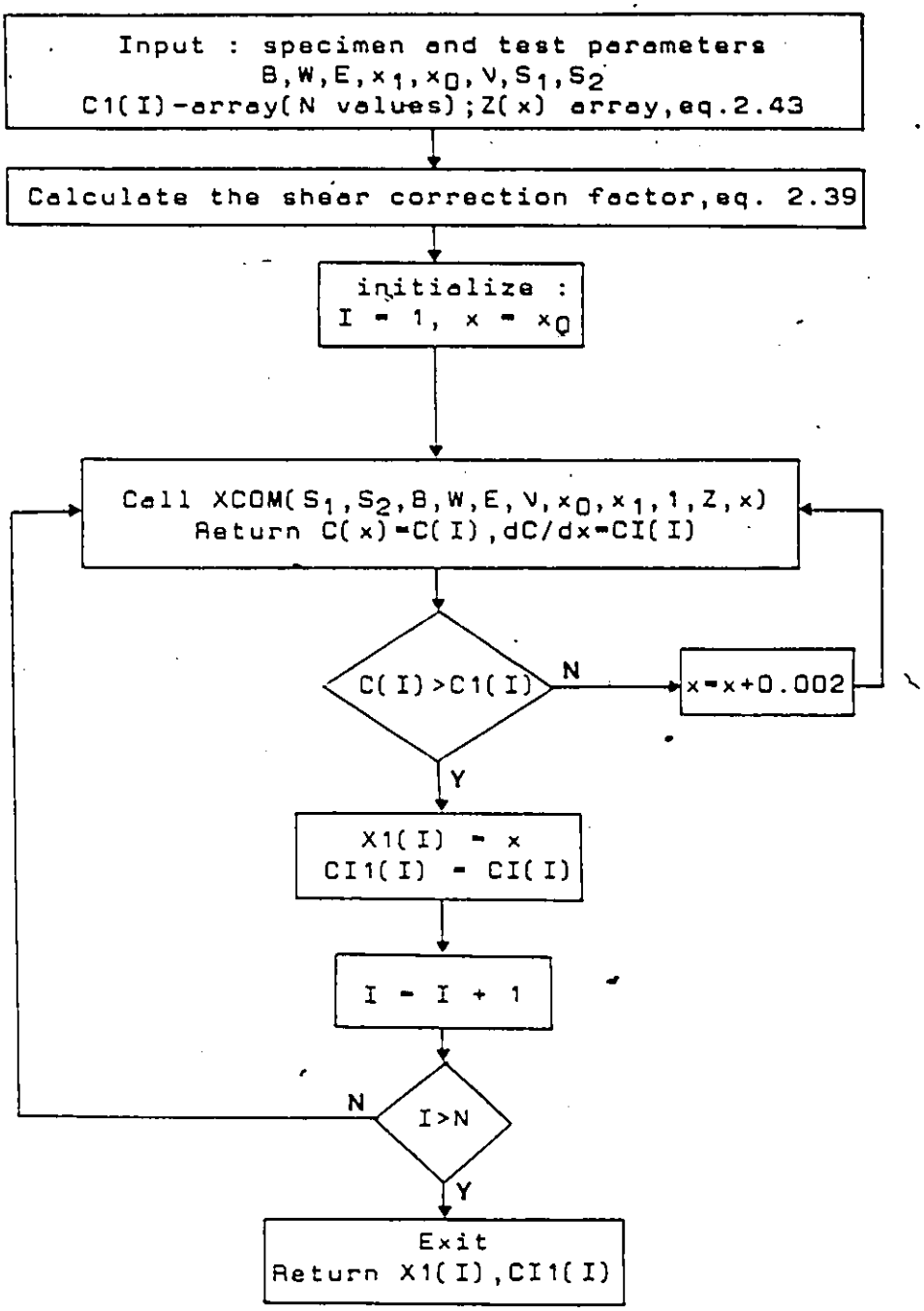

APPENDIX 2

Numerical Techniques for Potential Drop Analysis

Subroutine XDOP(C1,C2,C3,x_0,x_1,N,x)

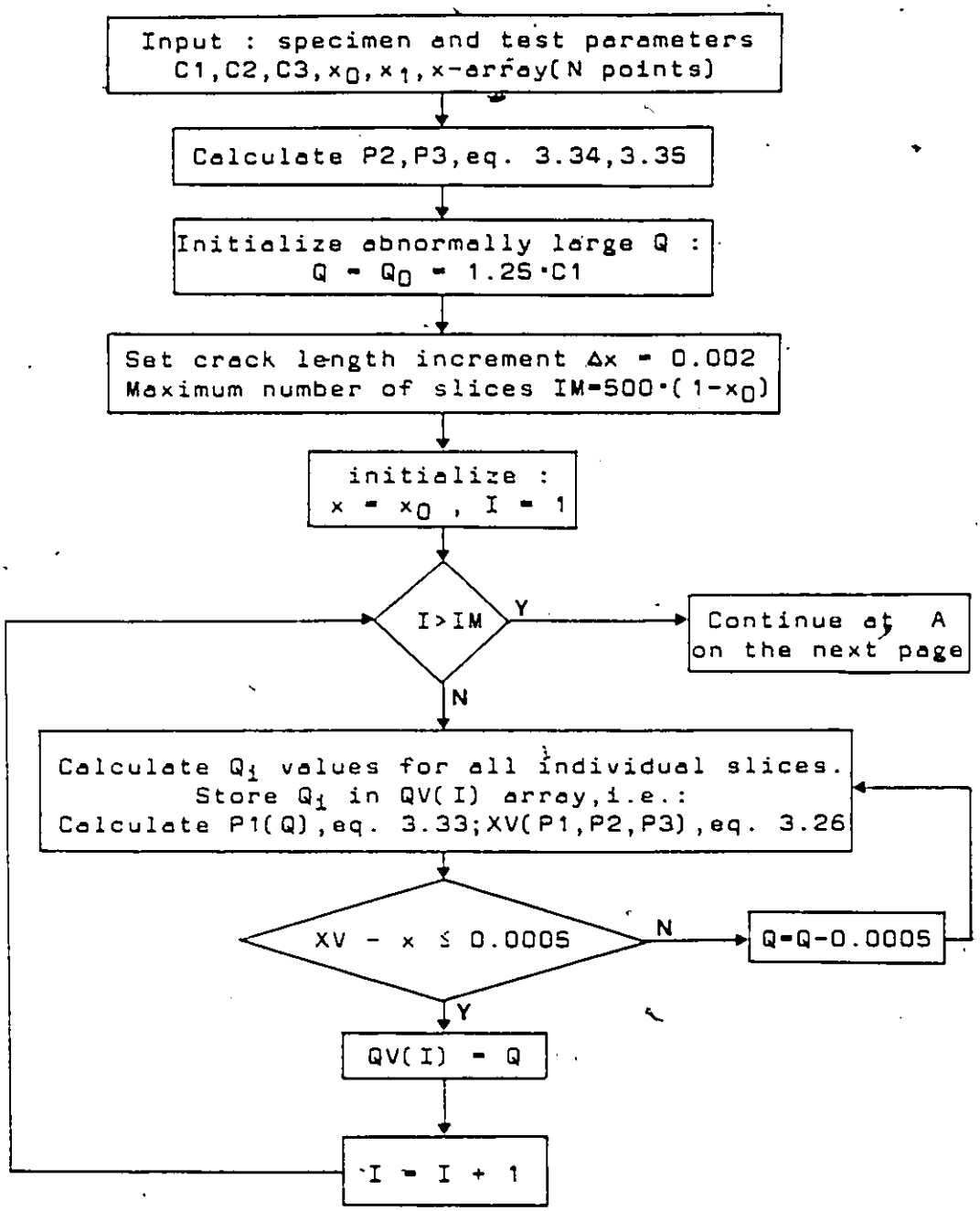

Subroutine XDOP continued :

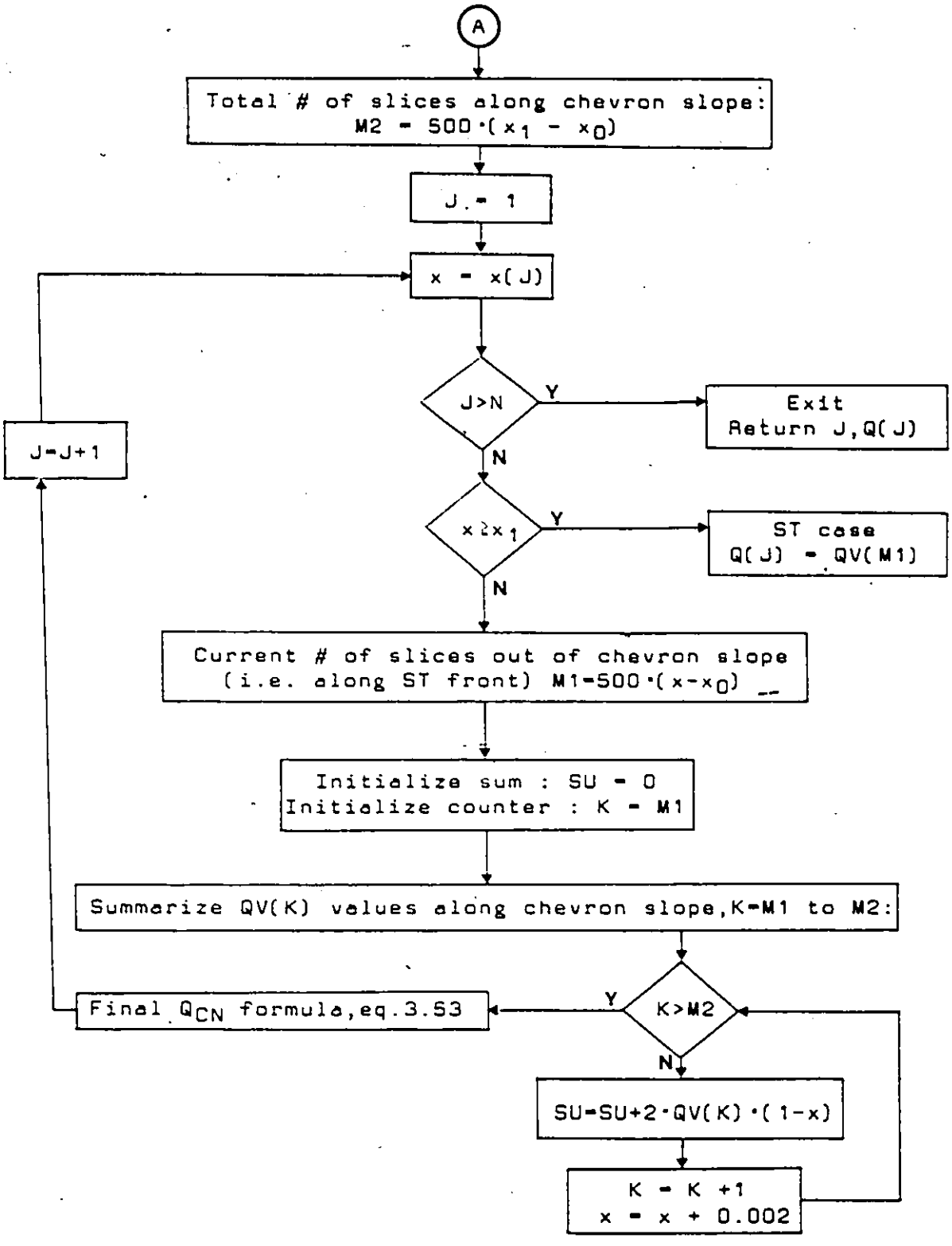

Subroutine DOPX(C1,C2,C3,x_0,x_1,N,Q)

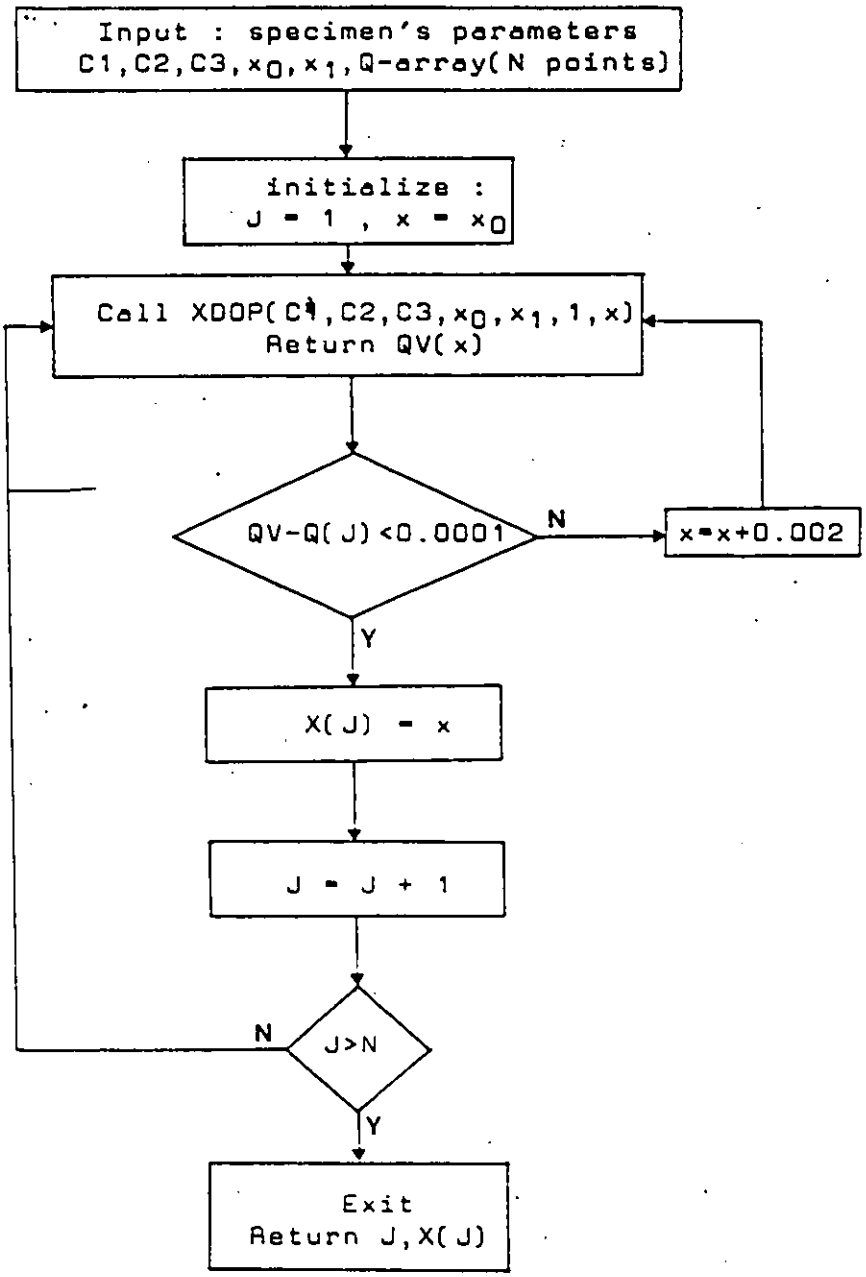

APPENDIX 3

Numerical Techniques for Room Temperature Fracture Tests

Program LR (Load Relaxation)

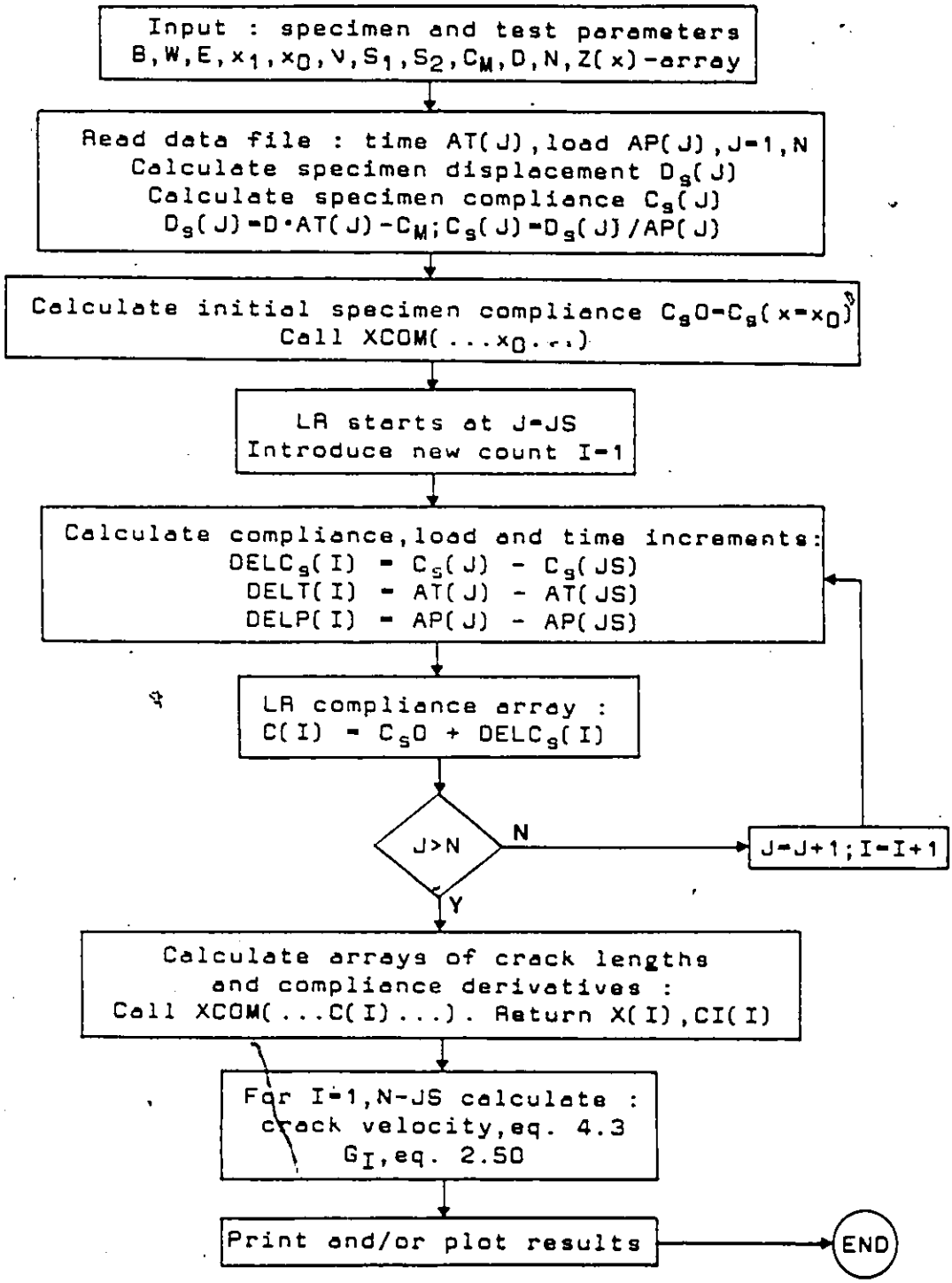

Program LFURT
(Loading-Fracture-Unloading at Room Temperature)

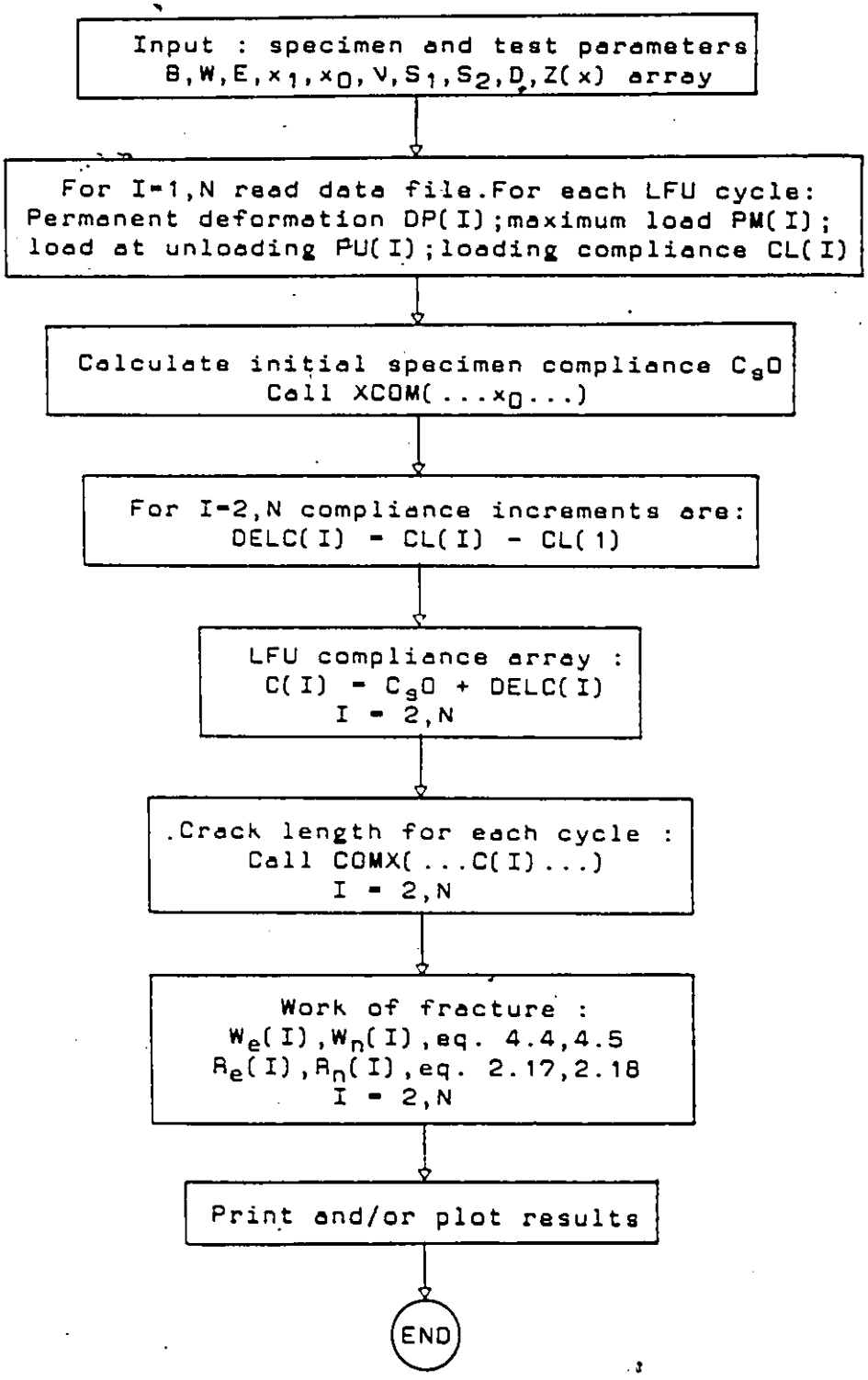

APPENDIX 4

Numerical Techniques for Elevated Temperatures Fracture Tests

Program LFUHT
(Loading-Fracture-Unloading at High Temperatures)

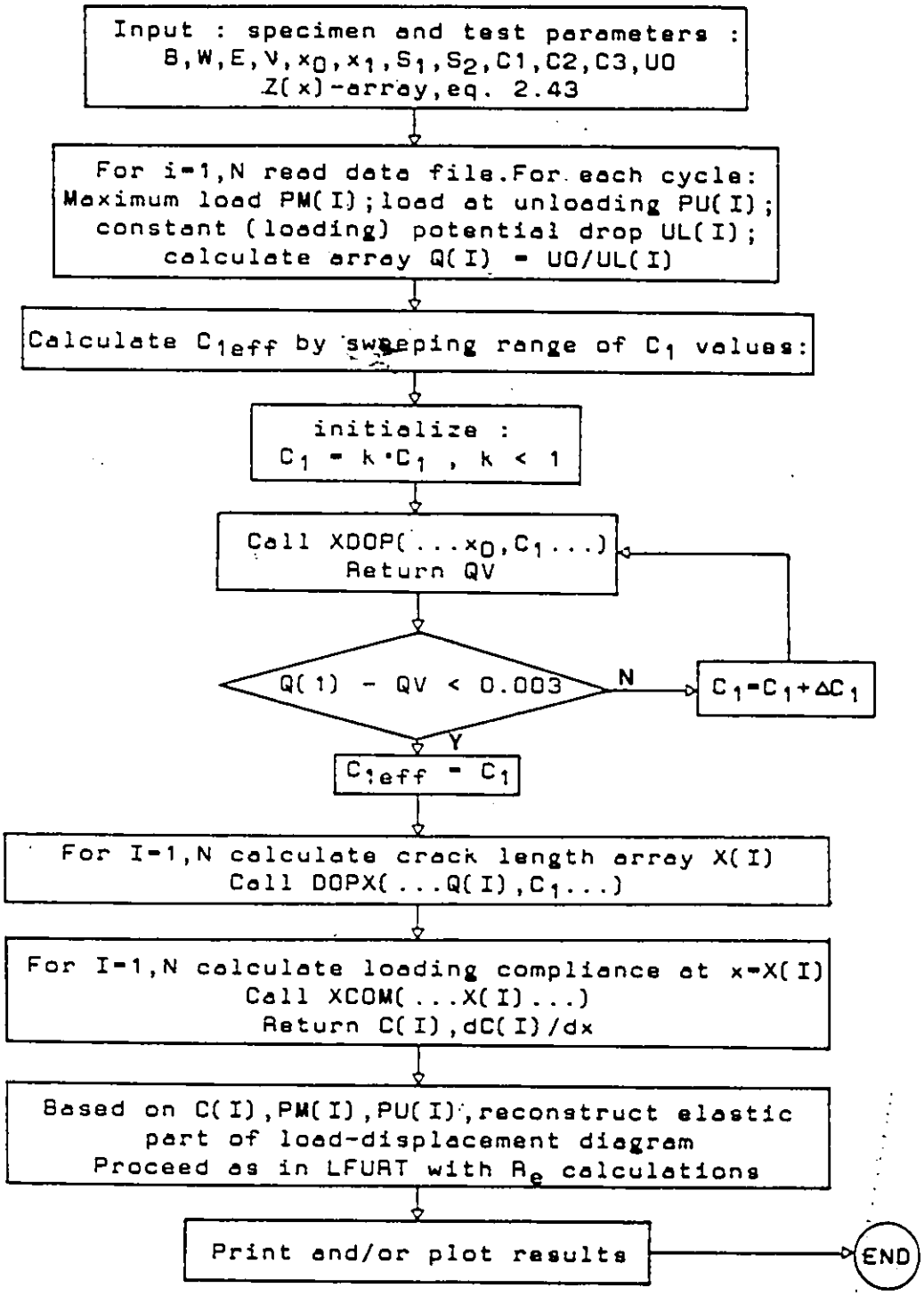

APPENDIX 5

Symbolic Names of the Synthesized Materials

Zirconia - Hafnia Solid Solutions

Preparation Method	Mole % of zirconia replaced by hafnia: 0	10	20	30	100
Mixed Oxides (OM) stabilized by 4.5 m% Y_2O_3	P0	P1	P2	P3	PSH
6.9 m% Y_2O_3	F0	F1	F2	F3	FSH
Spray-Freeze Freeze-Dry (SFFD)	P0A	P1A	P2A	-	-

Zirconia - β-Alumina Composites (ZBA)

m% Y_2O_3 in solid solution	Average size of 20 vol.% β-Al_2O_3 particles [μm]: 0 (pure matrix)	50	90	120
4.5	Z4 (PSZ)	Z4A50	Z4A90	Z4A120
6.9	Z8 (FSZ)	Z8A50	Z8A90	Z8A120

REFERENCES

1. B.J.Hockey and B.R.Lawn,J.Mat.Sci 10,1275,1975

2. B.R.Lawn,B.J.Hockey and S.M.Wiederhorn,J.Mat.Sci 15, 1207,1980

3. E.Orowan,Trans.Inst.Eng.Shipbldrs.Scotl. 89,95,1952

4. A.A.Griffith,Phil.Trans.R.Soc. A221,163,1921

5. J.Plateau,Int.J.Fract.Mech. 4,35,1968

6. D.P.H.Hasselman,D.A.Krohn,R.C.Bradt and J.A.Coppola,pp 749-45 in Fracture Mechanics of Ceramics,vol.2,ed R.C.Bradt,D.P.H.Hasselman and F.F.Lange,Plenum Press,New York,1974

7. H.Doremus,J.Appl.Phys. 42,1833,1976

8. E.M.Fuller,Jr. and R.M.Thomson,pp 507-48 in Fracture Mechanics of Ceramics,vol.4,ed. R.C.Bradt, D.P.H.Hasselman and F.F.Lange,Plenum Press,New York,1978

9. S.N.Zhurkov,Int.J.Fract.Mech. 1,311,1965

10. S.M.Wiederhorn,pp. 613-46 in ref. 6.

11. S.M.Wiederhorn,pp. 549-80 in ref. 8.

12. B.J.Pletka and S.M.Wiederhorn,pp. 745-60 in ref. 8.

13. E.R.Fuller,Jr.,B.R.Lawn and R.M.Thomson,Acta Metall 28,1407,1980

14. S.M.Wiederhorn,E.R.Fuller,Jr.,and R.M.Thomson,Metals Sci. Aug-Sept 1980,pp. 450-58

15. D.Maugis,J.Mat.Sci. 20,3041,1985

16. G.R.Irwin and J.A.Kies,Weld.J.Res.Suppl.31,95,1952

17. G.R.Irwin and J.A.Kies,ibid. 33,193,1954

18. H.H.Westergaard,Trans. ASME 61,A49,1939

19. B.R.Lawn and T.R.Wilshaw,"Fracture of Brittle Solids",Cambridge University Press,1975

20. B.R.Lawn,D.B.Marshall and A.H.Heuer,J.Am.Ceram.Soc.67 C-253,1984

21. N.H.Macmillan,J.Am.Ceram.Soc.68,C-288,1985

22. G.R.Irwin,J.Appl.Mech. 24,361,1957

23. J.E.Srawley and W.F.Brown,ASTM STP 381,"Fracture Toughness Testing and its Application",Philadelphia 1965

24. G.R.Irwin and P.C.Paris,pp. 1-46 in "Fracture",vol.3, ed.H.Liebowitz,Academic Press,New York,1971

25. A.S.Kobayashi,pp.456-68 in Experimental Mech.,Dec 1979

26. F.A.Nichols,Eng.Fr.Mech.12,307,1979

27. E.Orowan,Trans.Inst.Shipb.Scot.89,165,1945

28. J.Eftis and H.Libowitz,Eng.Fr.Mech. 2,101,1975

29. A.G.Evans,A.H.Heuer and D.L.Porter,pp.529-56 in Fracture 1977,vol.1,ICF4,Waterloo,Canada,1977

30. H.A.Shimmoeller,Int.J.Fract.12,481,1976

31. M.Sakai and R.C.Bradt,pp. 127-42 in Fracture Mechanics of Ceramics,vol. 7,ed. R.C.Bradt, D.P.H.Hasselman,A.G.Evans and F.F.Lange,Plenum Press,New York,1986

32. M.Sakai,K.Urashima and M.Inagaki,J.Am.Ceram.Soc. 66,868,1983

33. A.V.Virkar and R.S.Gordon,J.Am.Ceram.Soc.59,68,1976

34. C.C.Wu,S.W.Freiman,R.W.Rice and J.J.Mecholsky, J.Mat.Sci.13,2659,1978

35. R.W.Rice,pp.5-103 in "Fractography of Ceramic and Metal Failures",ASTM STP 827,ed.J.J.Mecholsky and S.R.Powell, ASTM,1984

36. P.L.Pratt,Metals Sci,Aug-Sept 1980,pp.363-73

37. S.M.Wiederhorn,J.Am.Ceram.Soc.52,485,1969

38. S.M.Wiederhorn,Ann.Rev.Mat.Sci. 14,373,1984

39. R.W.Rice,S.W.Freiman and J.J.Mecholsky,J.Am.Ceram.Soc. 63,129,1980

40. A.J.Gesing,PhD Thesis,The Pennsylvania State University,1982

41. R.W.Rice,R.C.Pohanka and W.J.McDonough,J.Am.Ceram.Soc. 63,703,1980

42. R.F.Cook,B.R.Lawn and C.J.Fairbanks,J.Am.Ceram.Soc. 68,604,1985

43. J.A.Kuszyk and R.C.Bradt,J.Am.Ceram.Soc.56,420,1973

44. N.Claussen,J.Steeb and R.F.Pabst,Am.Ceram.Soc.Bull. 56,559,1977

45. R.G.Hoagland,J.D.Embury and D.J.Green,Scripta Metall. 9,907,1975

46. R.G.Hoagland and D.J.Embury,J.Am.Ceram.Soc.63,404,1980

47. D.P.H.Hasselman and J.P.Singh,Am.Ceram.Soc.Bull. 58,856,1979

48. R.M.McMeeking and A.G.Evans,J.Am.Ceram.Soc.65,242,1982

49. R.W.Rice,pp. 199-381 in "Treatise on Materials Science and Technology",vol.11,ed.R.K.McCrone,Academic Press, New York 1977

50. Y.Fu and A.G.Evans,Acta Metall.33,1525,1985

51. R.W.Davidge and T.J.Green,J.Mat.Sci.3,629,1968

52. A.G.Evans and K.T.Faber,J.Am.Ceram.Soc.64,394,1981

53. N.E.Claussen,J.Am.Ceram.Soc.59,49,1976

54. D.J.Green,J.Am.Ceram.Soc.65,610,1982

55. D.J.Green,J.Am.Ceram.Soc.64,138,1981

56. D.J.Green,F.F.Lange and M.R,James,pp.240-50 in "Advances in Ceramics",vol.12,ed.N.Claussen,M.Ruhle and A.H.Heuer, Am.Ceram.Soc.Inc.,Columbus,OH,1984

57. K.T.Faber and A.G.Evans,Acta.Metall.31,565,1983

58. K.T.Faber and A.G.Evans,Acta.Metall.31,577,1983

59. K.T.Faber and A.G.Evans,J.Am.Ceram.Soc.66,C94,1983

60. A.G.Evans and W.Blumenthal,pp.423-48 in "Fracture Mechanics of Ceramics",vol.6,ed.R.C.Bradt,D.P.H.Hasselman, A.G.Evans and F.F.Lange,Plenum Press,New York,1983

61. K.Kromp and R.F.Pabst,pp.449-61 in ref.60

62. E.C.Subbarao,pp.1-24 in "Advances in Ceramics",vol.3,ed. A.H.Heuer and L.W.Hobbs,Am.Ceram.Soc.Inc.,Columbus,OH,1981

63. G.M.Wolten,J.Am.Ceram.Soc.46,418,1963

64. G.K.Bansal and A.H.Heuer,Acta Metall.20,1281,1972

65. G.K.Bansal and A.H.Heuer,Acta Metall.22,409,1974

66. A.H.Heuer and M.Ruhle,pp.1-13 in "Advances in Ceramics", vol.12,ed.N.Claussen,M.Ruhle and A.H.Heuer,Am.Ceram.Soc. Inc.,Columbus,OH,1984

67. R.Ruh and H.J.Garret,J.Am.Ceram.Soc.50,257,1967

68. R.C.Garvie and P.S.Nicholson,J.Am.Ceram.Soc. 55,152,1972

69. R.C.Garvie,R.H.Hannink and R.T.Pascoe,Nature 258,703,1975

70. G.K.Bansal and A.H.Heuer,J.Am.Ceram.Soc.58,235,1975

71. D.L.Porter and A.H.Heuer,J.Am.Ceram.Soc.62,298,1979

72. R.H.Hannink,J.Mat.Sci.18,457,1983

73. M.V.Swain and R.H.Hannink;pp. 225-39 in ref. 66

74. D.J.Green,P.S.Nicholson and J.D.Embury,J.Am.Ceram.Soc. 56,619,1973

75. R.H.Hannink,K.A.Johnston,R.T.Pascoe and R.C.Garvie, pp. 116-36 in ref. 62

76. R.H.Hannink,J.Mat.Sci13,2487,1978

77. R.A.Miller,J.L.Smialek and R.G.Garlick,pp. 241-53 in ref. 62

78. M.Ruhle,N.Claussen and A.H.Heuer,pp. 352-70 in ref. 66

79. T.K.Gupta,pp. 877-89 in ref. 8

80. N.Claussen,pp. 325-51 in ref. 66

81. T.H.Etsell and S.N.Flengas,Chem.Rev.70,339,1970

82. M.Matsui,T.Soma and I.Oda,pp. 371-81 in ref. 66

83. M.Watanabe,S.Ito and I.Fukunura,pp. 391-98 in ref. 66

84. N.Caussen and J.Jahn,J.Am.Ceram.Soc.61,94,1978

85. F.F.Lange and D.J.Green,pp.217-25 in ref. 62

86. D.J.Green,F.F.Lange and M.R.James,pp. 240-50 in ref. 66

87. S.Hori,M.Yoshimura,S.Somija and R.Takahashi,pp. 794-805 in ref. 66

88. D.W.Stacy and D.R.Wilder,J.Am.Ceram.Soc.58,285,1975

89. R.Ruh,H.J.Garret,R.F.Domagala and N.M.Tallan, J.Am.Ceram.Soc.51,23,1968

90. C.E.Curtis,L.M.Doney and J.R.Johnson,J.Am.Ceram.Soc. 37,458,1954

91. A.G.Karaulov and N.M.Taranukha,Refractories 20,241,1971

92. JANAF Termochemical Tables,NSRDS-NBS 37,ed.D.R.Stull and H.Prophet,Washington,1971

93. J.Cook and J.E.Gordon,Proc.Roy.Soc.A282,508,1964

94. S.J.Glass,P.S.Nicholson and C.B.Clark, J.Am.Ceram.Soc.68,C176,1985

95. T.B.Troczynski and P.S.Nicholson, pp. 199-201 in "Fracture Mechanics of Ceramics",vol.8,ed.R.C.Bradt, D.P.H.Hasselman,A.G.Evans and F.F.Lange,Plenum Press, New York,1986

96. T.B.Troczynski and P.S.Nicholson, ibid., pp. 187-98

97. T.B.Troczynski and P.S.Nicholson,J.Am.Ceram.Soc. 68,C277,1985

98. T.B.Troczynski and P.S.Nicholson, J.Am.Ceram.Soc. 70,February,1987

99. M.Ruhle,B.Krauss,A.Strecker and D.Waidelich, pp. 256-74 in ref. 66

100. E.H.Schoenlein,M.Ruhle and A.H.Heuer,pp. 257-82 in ref. 66

101. D.L.Porter,A.G.Evans and A.H.Heuer,Acta Metall. 27,1649,1979

102. A.G.Evans and A.H.Heuer,J.Am.Ceram.Soc.63,241,1980

103. A.G.Evans,N.Burlingame,M.Drory and W.M.Kriven,Acta Metall.29,447,1981

104. T.B.Troczynski and P.S.Nicholson,Am.Ceram.Soc.Bull. 65,772,1986

105. B.Budiansky,J.W.Hutchinson and J.C.Lambropoulos, Int.J.Sol.Struct.19,337,1983

106. A.G.Evans,pp. 193-212 in ref. 66

107. N.Claussen,R.L.Cox and J.S.Wallace,J.Am.Ceram.Soc. 65,c190,1982

108. K.T.Faber,pp. 293-305 in ref. 66

109. H.Ruf and A.G.Evans,J.Am.Ceram.Soc.66,328,1983

110. R.P.Ingel,D.Lewis,B.A.Bender and R.W.Rice,J.Am.Ceram.Soc. 65,C150,1982

111. J.Nakayama,J.Am.Ceram.Soc.43,583,1965

112. T.B.Troczynski and P.S.Nicholson,J.Am.Ceram.Soc. 68,439,1985

113. L.P.Pook,Int.J.Fract.Mech.8,103,1972

114. H.G.Tattersall and G.Tappin,J.Mat.Sci.1,296,1966

115. J.I.Bluhm,Eng.Fract.Mech.7,593,1975

116. H.Hubner and H.Schuhbauer,Eng.Fract.Mech.9,403,1977

117. R.J.Fields,E.R.Fuller,Jr.,T.J.Chuang and L.Chuck,pp. 463-73 in "Fracture Mechanics of Ceramics",vol.6,ed. R.C.Bradt,D.P.H.Hasselman,A.G.Evans and F.F.Lange, Plenum Press,New York,1983

118. H.Tada,P.Paris and G.Irwin,"The Sress Analysis of Cracks Handbook",Del Research Corp.,Hellertown,Pa,1973

119. J.I.Bluhm,pp. 409-17 in Fracture,vol. 3,ed. D.M.R.Taplin, University of Waterloo Press,Waterloo,Ont,Canada,1977

120. M.Sakai and K.Yamasaki,J.Am.Ceram.Soc.66,371,1983

121. J.C.Newman,Jr.,pp. S-31 in "Chevron Notched Specimens : Testing and Stress Analysis",ASTM STP 855, Philadelphia 1984

122. D.Munz,R.T.Bubsey and J.E.Srawley,Int.J.Fract. 16,359,1980

123. P.R.Bevington,"Data Reduction And Error Analysis for the Physical Sciences",McGraw-Hill Book Comp. New York 1980

124. Wu Shang Xian,Int.J.Fract.19,R27,1982

125. L.Chuck,E.R.Fuller,Jr.,and S.W.Freiman, pp. 167-75 in ref. 121

126. D.Munz,R.T.Bubsey and J.L.Shannon,Jr.,J.Am.Ceram.Soc. 63,300,1980

127. D.Munz,G.Himsolt and J.Eschweiler,J.Am.Ceram.Soc. 63,314,1980

128. P.F.Becher,J.Mat.Sci.21,297,1986

129. Li-Shing-Li and R.F.Pabst,J.Mat.Sci.15,2861,1980

130. M.Inagaki,K.Urashima,S.Toyomasu,Y.Goto and M.Sakai,J.Am.Ceram.Soc.68,704,1985

131. T.B.Troczynski,internal report,McMaster University,1983

132. F.F.Lange,J.MAt.Sci.17,225,1982

133. J.Glass,internal report,McMaster University,1985

134. J.Adam and B.Cox,J.Nucl.Eng. A2,31,1959

135. E.D.Whitney,Trans.Farad.Soc.61,1191,1965

136. P.A.Evans,R.Stevens and J.G.P.Binner,Br.Cer.Trans.J. 83,39,1984

137. H.Toraya,M.Yoshimura and S.Somija,J.Am.Ceram.Soc. 67,C119,1984

138. J.Krautkrammer and H.Krautkrammer,"Ultrasonic Testing of Materials",Springer-Verlag,New York,1977

139. J.D.Ferry,"Viscoelastic Properties of Polymers",John Wiley & Sons Inc.,New York,1980

140. J.B.Watchman,Jr.,and D.G.Lam,Jr.,J.Am.Ceram.Soc. 42,254,1959

141. J.D.Buckley and D.N.Braski,J.Am.Ceram.Soc.50,220,1967

142. M.Shimada,K.Matsuchito,S.Kuratani,T.Okamoto,M.Koizumi, K.Tsukuma,T.Tsukidate,J.Am.Ceram.Soc.67,C23,1984

143. C.Gault,F.Platon and D.LeBras,Mat.Sci.Eng.74,105,1985

144. J.D.Buckley,PhD Thesis,Iowa State University,1968

145. T.J.Chuang,J.Chuck,R.J.Fields and E.R.Fuller,Jr., Eng.Fract.Mech.12,1099,1983

146. D.Munz,J.L.Shannon,Jr.,and R.T.Bubsey,Int.J.Fract. 16,R137,1980

147. F.I.Baratta,"Requirements for Flexure Testing of Brittle Materials",Final Report,Army Materials and Mechanics Center,Watertown,1982

148. A.J.A.Winnubst,K.Keizer and A.J.Burggraef,J.Mat.Sci. 18,1958,1983

149. A.A.Anctil,E.B.Kula and E.DiCesare,ASTM Proceedings 63,799,1963

150. H.H.Johnson,Mat.Res.Std.5,442,1965

151. D.M.Gilbey and S.Pearson,RAE Tech.Rep. No 66402, Farnborough,U.K.,1966

152. R.O.Richtie,G.G.Garret and J.F.Knott,Int.J.Fract. 7,462,1971

153. G.H.Aronson and R.O.Richtie,J.Test.Eval.7,208,1979

154. G.Cark and J.F.Knott,J.Mech.Phys.Sol.23,265,1975

155. J.F.Knott,pp. 113-35 in "The Measurment of Crack Length and Shape During Fracture and Fatigue",ed. C.J.Beevers, EMAS,U.K.,1980

156. S.G.Druce and G.S.Booth,pp. 136-63 in ref. 155

157. R.J.Cooke and J.L.Robinson,internal report,Dept. of Physical Metallurgy and Science of Materials,University of Birmingham,U.K.,1971

158. G.Baudin and H.Policella,pp. 159-74 in "Advances in Crack Length Measurment",ed. C.J.Beevers,EMAS,U.K.,1982

159. J.R.Whiteman and N.Papamichael,J.App.Math.Phys. 23,655,1972

160. N.Papamichael and J.R.Whiteman,J.Appl.Math.Phys. 24,305,1973

161. G.Baudin and H.Policella,Proceedings of the ICFS,vol.4, p. 1957,Cannes,1981

162. T.Haug,A.C.Bornhauser,H.G.Shmid,V.Gerold and R.F.Pabst, pp. 473-84 in "Proceedings of the Second International Conference on Creep and Fracture of Engineering Materials and Structures",Part 1,Pineridge Press, Swansea,UK,1984.

163. W.D.Vogel and R.F.Pabst,pp. 485-501 in ref. 162 .

164. A.G.Evans and W.Blumenthal,pp. 451-72 in ref. 162

165. Lishing Li and R.F.Pabst,pp. 371-81 in ref. 117

166. C.E.Turner,pp. 25-221 in "Post-yield Fracture Mechanics",2nd ed. by D.G.H.Latzko,C.E.Turner, J.D.Landes,D.E.McCabe and T.K.Hellen,Elsevier Appl.Sci.Publ.Co.,London,1984

167. V.Lauteri,T.E.Mitchell and A.H.Heuer,pp.118-30 in ref. 66

168. H.G.Scott,J.Mat.Sci 10,1527,1975

169. Subrata Mukherjee ,"Boundary Element Methods in Creep and Fracture",Appl.Sci.Publ.,London,1982

170. L.V.Nikitin and A.Y.Krayanov,pp.2579-86 in "Advances in Fracture Research (Fracture 84)",vol.4,Pergamon Press, Oxford,1986

171. M.V.Swain and R.H.J.Hannink,pp.2633-40 in ref. 170

172. T.B.Troczynski and P.S.Nicholson, Am.Ceram.Soc.Bull. 64,1272,1985

173. T.B.Troczynski and P.S.Nicholson, J.Am.Ceram.Soc. 69,C-136,1986

174. A.S. Krausz and H.Eyring, "Deformation Kinetics", J.Wiley & Sons, N.York, 1975

McMaster University Thesis

ENERGY ANALYSIS OF BRITTLE FRACTURE AND ITS APPLICATION TO ZIRCONIUM OXIDE CERAMICS

(ILLUSTRATIONS)

This report contains the illustrations

from the Ph.D. Thesis

ENERGY ANALYSIS OF BRITTLE FRACTURE AND ITS APPLICATION TO ZIRCONIUM OXIDE CERAMICS

By

Tomasz B. Troczynski, B. Eng., M. Sc.

The Thesis was submitted to the Faculty of Graduate Studies, McMaster University, in January, 1987

TABLE OF CONTENTS

Figure		Page
2-1	Quasi-one-dimensional lattice model	1
2-2	Crack modelling in LEFM	2
2-3	Crack velocity against driving force	3
2-4	Load-displacement diagram showing elastically (W_e) and nonelastically (W_n) dissipated fracture energy	4
2-5	Schematic load-displacement diagram for constant grips test, constant load test and intermediate cases	5
2-6	The role of an amorphous phase in the acceleration of intrinsic cracks and the growth rate of intrinsic and indentation induced cracks in alumina at 1400°C, [164]	6
2-7	Three polymorphs of ZrO_2:(A) C phase, (B) T phase, (C) M phase, [66]	7
2-8	Experimentally determined ZrO_2-rich portion of the phase diagram in the system Y_2O_3-ZrO_2, [66, 78, 167, 168]	8
2-9	Phase diagrams for hafnia solution with yttria and zirconia	9
2-10	Schematic illustrating the basis for crack shielding by a transformation zone [106]	10
2-11	Stress-strain curve for material subject to transformation and microcracking [106]	11
2-12	Geometry of the four-point-bend, chevron notched specimen	12
2-13	Universal four-point bend geometric factors I(x) and Y(x) as function of the normalized crack length x	13
2-14	CN specimen properties	14

2-15 (A) X-ray intensity ratio r_1 for HfO_2 and ZrO_2; (B) X-ray diffraction data for HfO_2 and ZrO_2.....15

2-16 Schematic spring-dashpot element and stress-strain relation for viscoelastic material.....16

2-17 Dependence of the Young's Modulus E of partially stabilized zirconia on temperature.....17

3-1 Schematic load-displacement diagram for stable fracture experiment.....18

3-2 Fracture characteristics of Type I material.....19

3-3 Stress intensity factor against percentage of fracture area, for Type II material.....20

3-4 Fracture characteristics of Type III material.....21

3-5 Stress intensity factor against percentage of fracture area for Type I material.....22

3-6 The relative error e in K_{IC} calculation from maximum load for CN specimen exhibiting subcritical crack growth, as function of the exponent N.....23

3-7 The relative error e in K_{IC} calculation from maximum load for CN specimen exhibiting subcritical crack growth, as function of the displacement rate....24

3-8 Crack driving force against percentage of fracture area for repeated loading-unloading experiments, Type I material(Al_2O_3, SiC).....25

3-9 Crack driving force against percentage of fracture area for repeated loading-unloading experiments, Type III material(graphite).....26

3-10 Schematic load-displacement (A) and load-time (B) diagrams for load-relaxation experiment.....27

3-11 G_I/R curves for changing: (A) Initiation load P_i; (B) Initiation load P_i and stiffer machine; (C) Crack initiation length, x_i;(D) Relative machine compliance,m, and short initial notch length, x_0.....29

3-12 G_I/R curves for changing: (A) Relative machine compliance, m, and deep initial notch length, x_0; (B) Bend spans at constant absolute machine compliance; (C) Side notch length, x_i.....30

3-13 Geometry and cross section of:(A) Straight-through notched specimen;(B)Chevron notched specimen.....31

3-14 Variation of the relative potential drop Q against the crack length x.....32

3-15 Sensitivity of the compliance and potential drop techniques.....35

4-1 Chevron notch positioning against the cutting blade.....36

4-2 Room temperature bending fixture.....37

4-3 Load-displacement records for the room temperature bending fixture alone.....38

4-4 Load-displacement records for the testing machine.....39

4-5 Compliance of the testing systems.....39

4-6 Comparison of measured and calculated compliance for two graphite CN specimens.....40

4-7 Calibration results of PD method for aluminum and graphite ST specimens.....41

4-8 Calibration results of PD method for four graphite CN specimens.....42

4-9 Attachement of the potential and current probes to the specimen's surface.....43

4-10 Reference potential drop (U_1) against temperature for materials based on partially and fully stabilized zirconia.....44

4-11 Working potential drop U_2 against inversed absolute temperature for PSZ and FSZ ceramics.....45

4-12 Experimental calibration and numerical results for PD method (PSZ-ST specimen at 700 °C).....46

4-13 Linear dependence of the potential drop U_2 against applied current for Z4A120 specimen.....47

4-14 Schematic loading-fracture-unloading (LFU) record and method of the fracture energy determination for general brittle nonelastic material.....48

4-15 High-temperature loading fixture.....49

4-16 Schematic load against potential drop record for LFU experiment.....50

4-17 Energy interchange for linear, fixed displacement unloading of an elastic-plastic elastic system, [166].....51

4-18 Schematic for the ultrasonic wave transit time t measurement.....52

4-19 Fracture testing results for graphite.....53

4-20 Simultaneous results of Potential Drop and Compliance Analysis for fracture testing of graphite specimen....54

4-21 Simulated error in the crack length determination by Compliance Analysis (A) and resulting relative error in the crack driving force (B).....56

4-22 Scatter of the crack length values calculated from PD at simulated error $\Delta C_2 = \pm 40\%$, plotted against true crack length x.....57

4-23 Relative error in the crack length calculation (A) and resulting relative error in the crack driving force, $\Delta G/G$ (B).....58

4-24 Maximum total error of the crack driving force calculation, $\Delta G/G$, at elevated temperatures by PD technique and at room temperature by CA technique.....59

4-25 Hypothetical calculated load-displacement graph for one LFU cycle at true (1) and underestimated (2) values of the Young's Modulus.....60

5-1 Monoclinic phase content in ZrO_2-HfO_2 solid solutions.....61

5-2 X-ray diffractograms for ZrO_2-HfO_2 solid solutions, obtained in LTC-OM route.....62

5-3 X-ray diffractogram records for ZrO_2-HfO_2 solid solutions, obtained in LTC-SFFD route.....63

5-4 Microstructures of zirconia-hafnia solid solutions:(A) P0 ;(B) P1 ;(C) P2 ;(D) P3.....64

5-5 HfO_2 stabilized with 4.5 mole % Y_2O_3: (A) Polished section; (B) Fracture surface.....66

5-6 HfO_2 stabilized with 6.9 mole % Y_2O_3: (A) Polished section; (B) Fracture surface.....67

5-7 Microstructures of zirconia-hafnia solid solutions: (A) P0A ;(B) P1A ;(C) P2A.....68

5-8 Elastic properties of HTQ-SFFD materials.....69

5-9 Relative density d[%] and Poisson's ratio ν, for SFFD materials.....69

5-10 Elastic properties of LTC-SFFD materials.....70

5-11 Static elastic modulus of LTC-SFFD materials against temperature.....70

5-12 Elastic properties of HTQ-OM materials against hafnia content.....71

5-13 Fraction of theoretical density of partially and fully stabilized OM zirconia-hafnia ceramics.....72

5-14 Elastic properties of OM-LTC zirconia-hafnia solid solutions.....73

5-15 Static elastic modulus of zirconia-hafnia ceramics against HfO_2 content.....73

5-16 X-ray diffraction records for partially stabilized zirconia-beta-alumina composites.....74

5-17 Static elastic modulus of PSZ-beta-alumina composites against temperature.....75

5-18 Microstructures of PSZ-beta-alumina composites.....76

5-19 Microstructures of FSZ-beta-alumina composites.....78

5-20 Properties of fully (Z8-series) and partially (Z4-series) stabilized zirconia-beta-alumina composites:(A) Dynamic elastic modulus and density against β-Al_2O_3 size; (B) Static elastic modulus against temperature.....80

5-21 Fracture testing results for P0 type ceramics.....81

5-22 Fractography of P0 type ceramics: (A) Arrested crack;(B) Fracture surface.....82

5-23 Fracture testing results for P1 type ceramics.....83

5-24 Fractography of P1 type ceramics: (A) Arrested crack;(B) Fracture surface.....84

5-25 Resistance to fracture of P2 type ceramics.....85

5-26 Resistance to fracture of P3 type ceramics.....85

5-27 Fractography of P2 type ceramics: (A) Arrested crack; (B) Fracture surface.....86

5-28 Fractography of P3 type ceramics: (A) Arrested crack; (B) Fracture surface.....87

5-29 Fracture testing results for SFFD type ceramics : (A) Load-displacement record for P0A ; (B) R_e compiled for two specimens of P0A and P1A.....88

5-30 Fractography of zirconia-hafnia solid solutions: (A) P0A type; (B) P1A type.....89

5-31 Fracture testing results for P2A type ceramics.....90

5-32 Fractography of P2A type ceramics: (A) Arrested crack; (B) Fracture surface.....91

5-33 Fracture testing results for PSZ.....92

5-34 Fractography of PSZ :(A) Arrested crack; (B) Fracture surface.....93

5-35 Fracture testing results for Z4A50 type ceramics.....94

5-36 Fractography of Z4A50 type ceramics: (A) Arrested crack; (B) Fracture surface.....95

5-37 Fracture testing results for Z4A90 type ceramics.....96

5-38 Fractography of Z4A90 type ceramics: (A) Arrested crack; (B) Fracture surface.....97

5-39 Fracture testing results for Z4A120 type ceramics.....98

5-40 Fractography of Z4A120 type ceramics: (A) Arrested crack; (B) Fracture surface.....99

5-41 Fracture testing results for FSZ.....100

5-42 Fractography of FSZ: (A) Arrested crack ; (B) Fracture surface.....101

5-43 Fracture testing results for Z8A50 type ceramics.....102

S-44 Fractography of Z8A50 type ceramics:
(A) Arrested crack ; (B) Fracture surface.....103

S-45 Fracture testing results for Z8A90 type ceramics.....104

S-46 Fractography of Z8A90 type ceramics:
(A) Arrested crack;(B) Fracture surface.....105

S-47 Fracture testing results for Z8A120 type ceramics....106

S-48 Fractography of Z4A120 type ceramics:
(A) Arrested crack; (B) Fracture surface.....107

S-49 Load-relaxation results for POA type ceramics:
(A) Crack driving force;(B) Crack velocity.....108

S-50 Load-relaxation results for commercial PSZ:
(A) Continuous test up to critical conditions;
(B) Specimen unloaded and reloaded.....109

S-51 Load-relaxation records for PSZ and PSZ-beta-alumina composites: (A) PSZ, Z4A50, Z4A120 ;
(B) Z4A90, with the crack velocity curve.....110

S-52 Crack velocity variation against fracture area, for PSZ-beta-alumina composites: Z4A50 (A) and Z4A120 (B).....111

S-53 Elevated temperature fracture testing results for POA type ceramics.....112

S-54 Fractography of POA type ceramics: (A) Arrested crack at 1300 °C; (B) Fracture surface at 1000°C.....114

S-55 Fracture testing results for P1A type ceramics.....115

S-56 Fracture surface of P1A type ceramics: (A) At 1000°C; (B) At 1300°C.....116

S-57 Elevated temperature fracture testing results for PSZ.....117

S-58 Elevated temperature fractography of PSZ.....119

S-59 Fracture testing results for Z4A50 type ceramics at 1000°C.....123

S-60 Fractography of Z4A50 composite: (A) Fracture surface at 1000°C ; (B,C) Particles pull-out at 1300°C ; (D) Crack-particle interaction at 1300°C....124

S-61 Fracture testing results for Z4A50 type ceramics at 1300°C.....126

S-62 Fracture testing results for Z4A120 type ceramics at 700°C.....127

S-63 (A,B) Fracture surface of Z4A120 composite at 700°C.....128

S-64 Fracture testing results for Z4A120 type ceramics at 1000°C.....129

S-65 Fractography of Z4A120 composite tested at 1000°C : (A) Arrested crack ; (B) Fracture surface.....130

S-66 Fracture testing results for Z4A50 type ceramics at 1300°C.....131

S-67 Fractography of Z4A120 composite tested at 1300°C.....132

S-68 Determination of the nonelastic energy dissipation rate, R_n, at 1300°C.....133

S-69 Load against potential drop at 1000°C for FSZ (A) and Z8A50 (B).....135

S-70 Load against potential drop at 1300°C for FSZ (A) and Z8A50 (B).....136

S-71 Resistance to fracture at 1000 and 1300°C of FSZ (A) and Z8A50 (B).....137

S-72 Fractography of FSZ at elevated temperatures: (A) Fracture surface at 1000°C ; (B) Crack arrested at 1300°C.....138

S-73 Fractography of Z8A50 at elevated temperatures: (A) Fracture surface at 1000°C ; (B) Crack arrested at 1300°C.....139

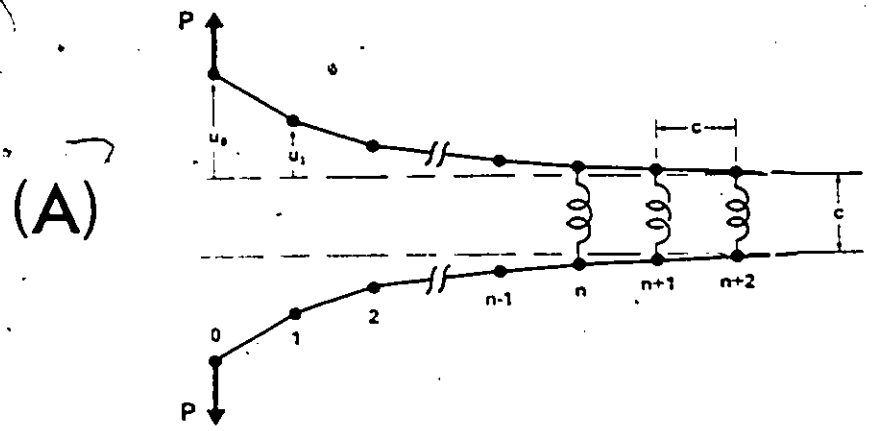

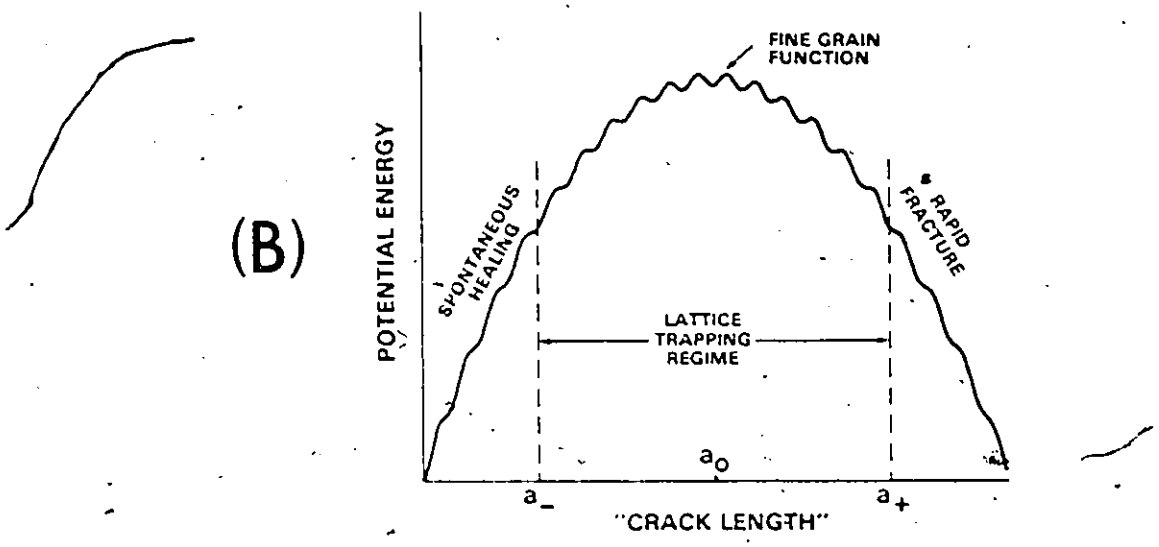

Fig. 2-1 Quasi-one-dimensional lattice model.(A) Crack subjected to an opening mode I of loading ; (B) Potential energy of a lattice as a function of reaction coordinate [8].

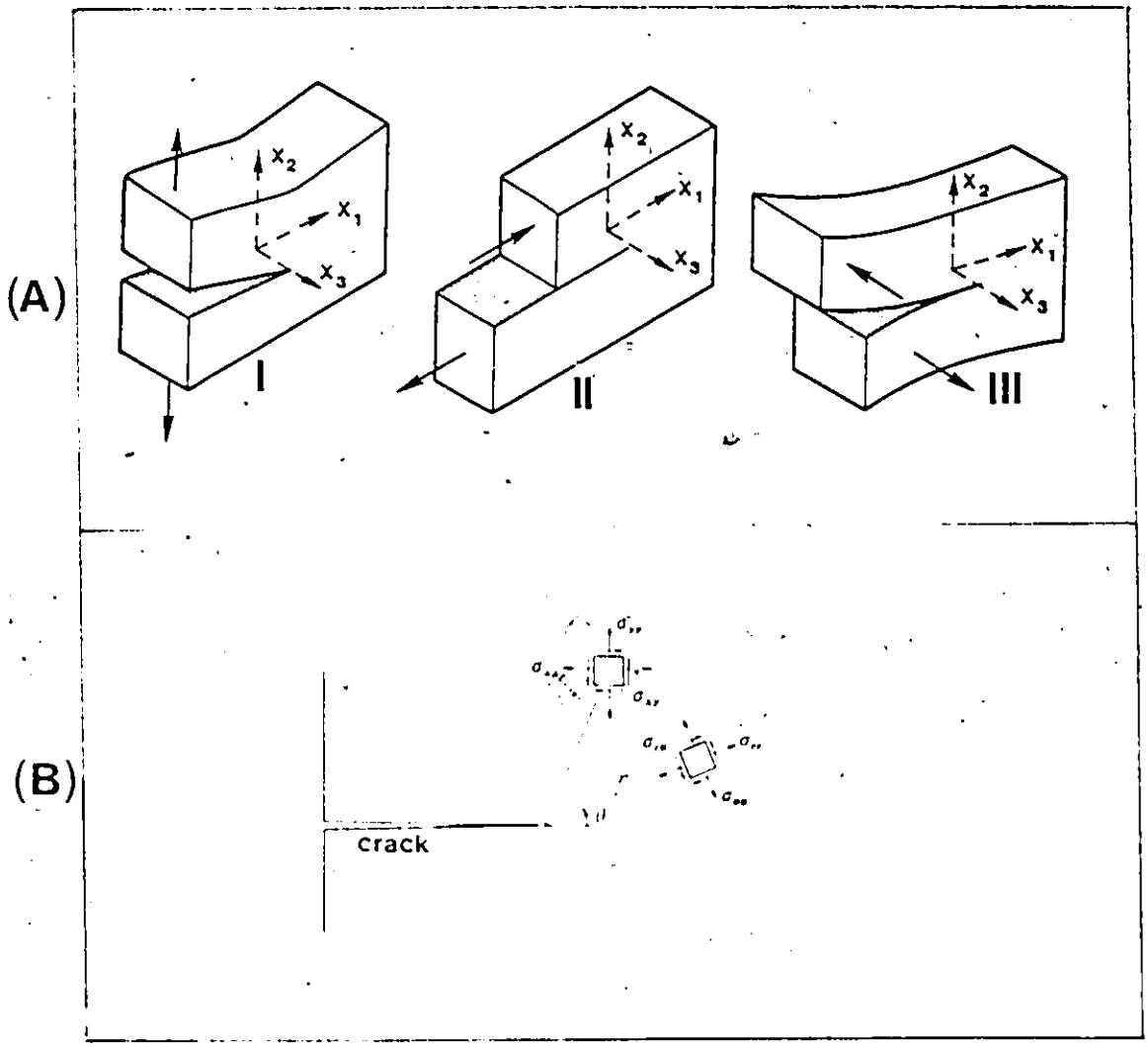

Fig. 2-2 Crack modelling in LEFM.(A) Three modes of fracture: opening (I), sliding (II), tearing (III). (B) Crack-tip stresses, showing rectangular and polar coordinate components.

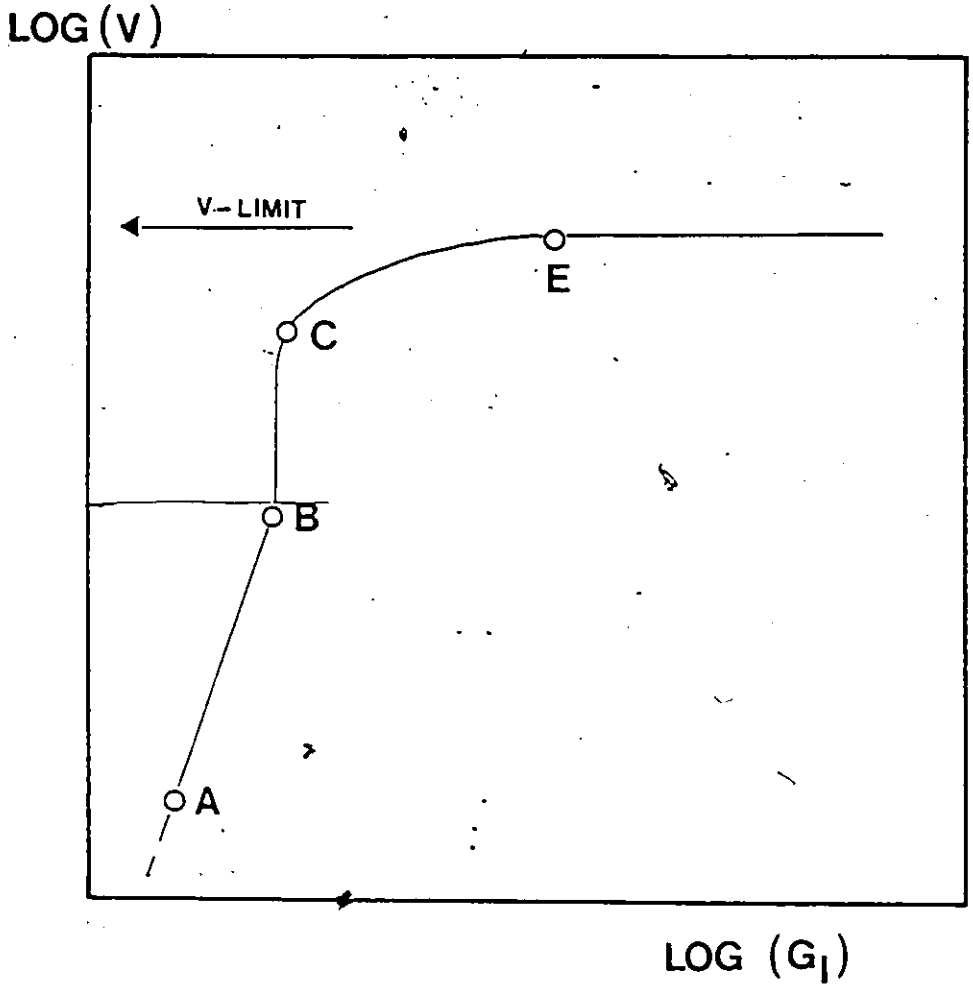

Fig. 2-3 Crack velocity against driving force. AB : slow stable growth ; BC : unstable growth ; CE:fast stable growth, [24].

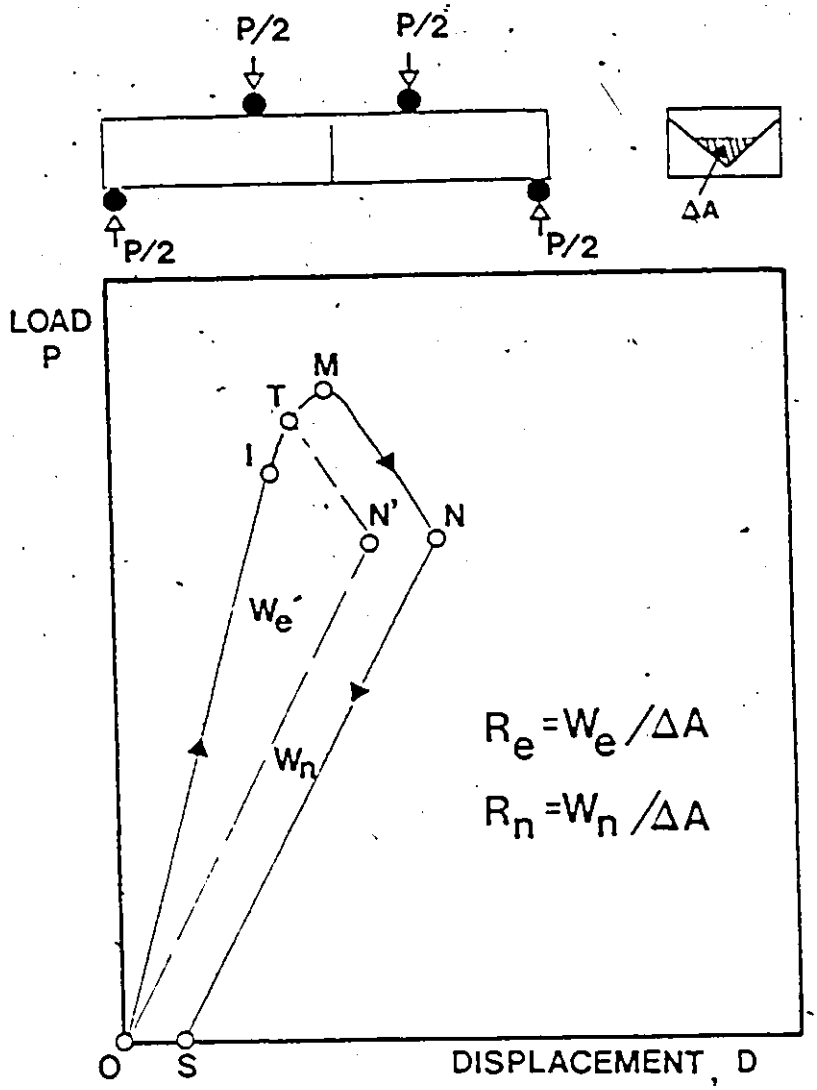

Fig. 2-4 Load vs. displacement diagram showing elastically (W_e) and nonelastically (W_n) dissipated fracture energy for partially cracked CN specimen.

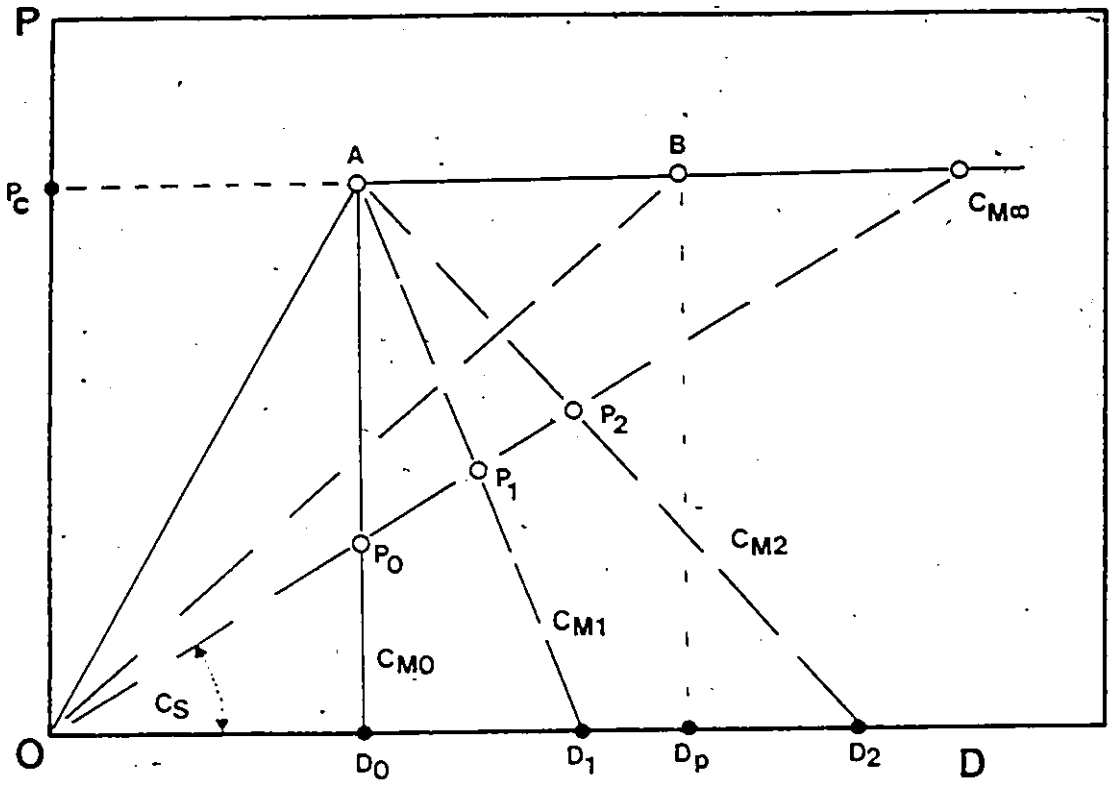

Fig. 2-5 Schematic load-displacement diagram for constant grips test (path OAD_0), constant load test (path OAB) and intermediate cases (OAD_1, OAD_2).

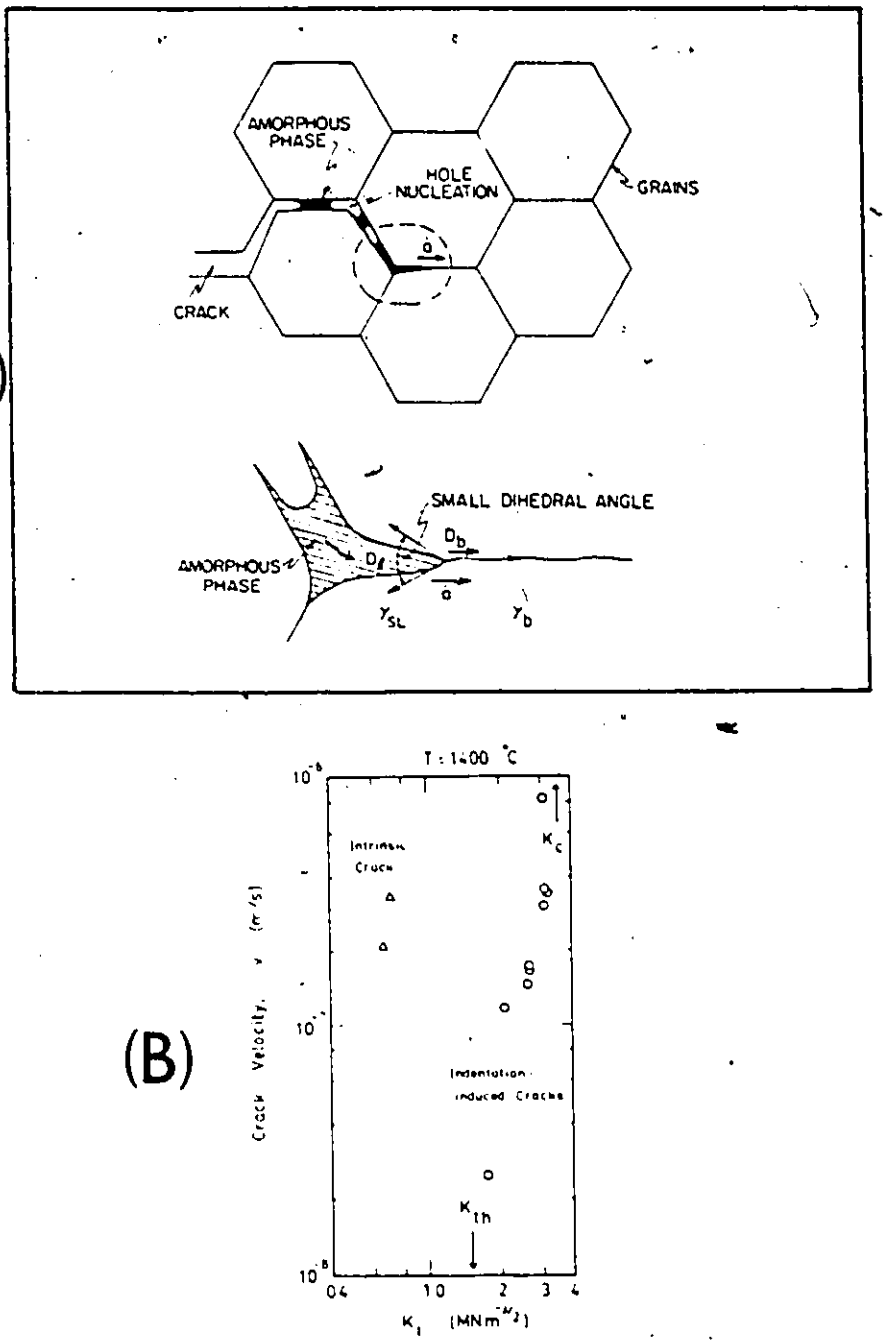

Fig. 2-6 The role of an amorphous phase in the acceleration of intrinsic cracks (A) ; The growth rate of intrinsic and indentation induced cracks in alumina at 1400°C (B), [164].

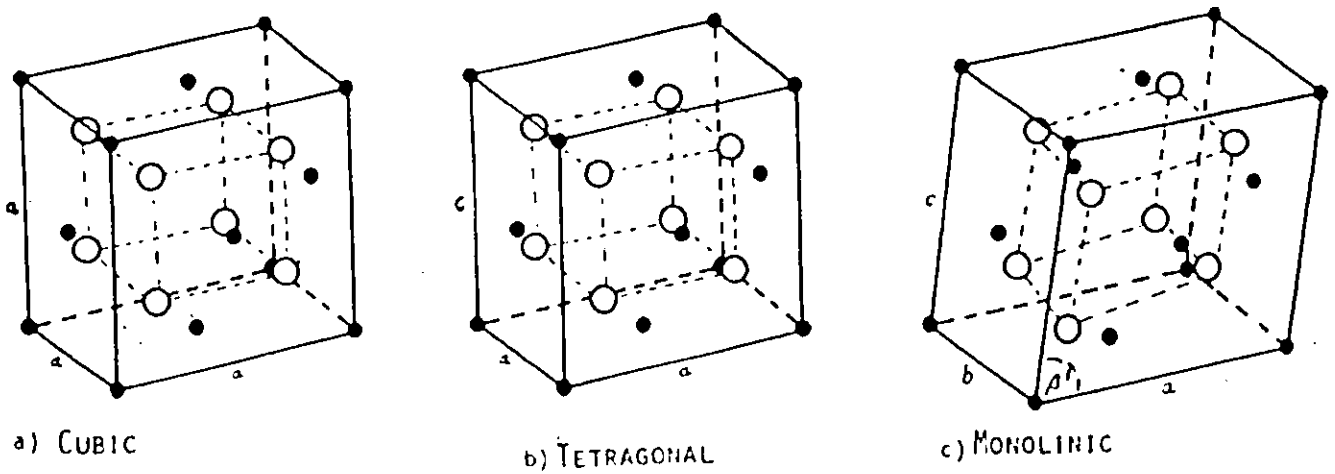

Fig. 2-7 Three polymorphs of ZrO_2 : (A) C phase, (B) T phase, (C) M phase, [66].

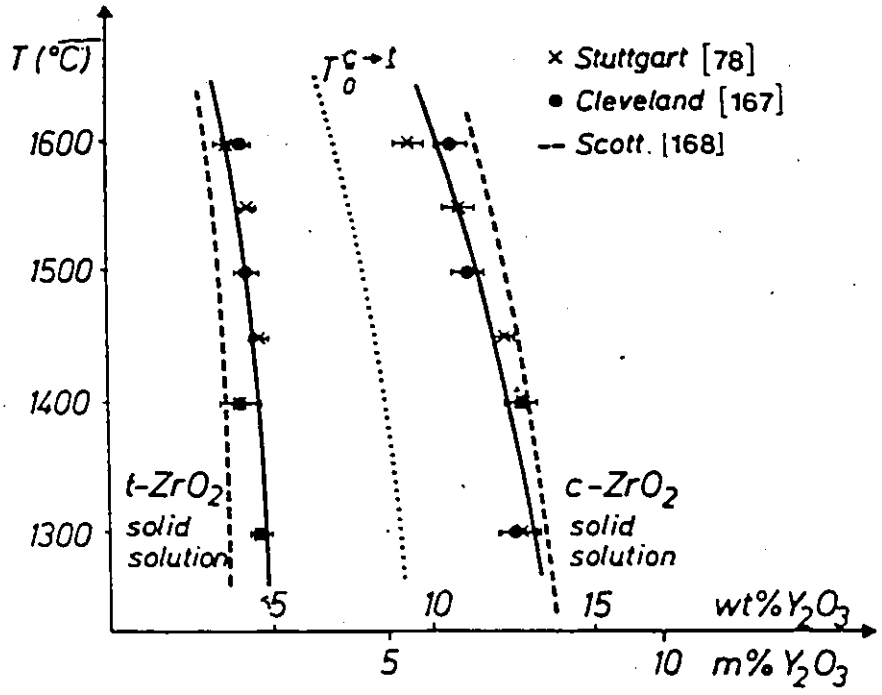

Fig. 2-8 Experimentally determined ZrO_2-rich portion of the phase diagram in the system Y_2O_3-ZrO_2, [66,78,167,168].

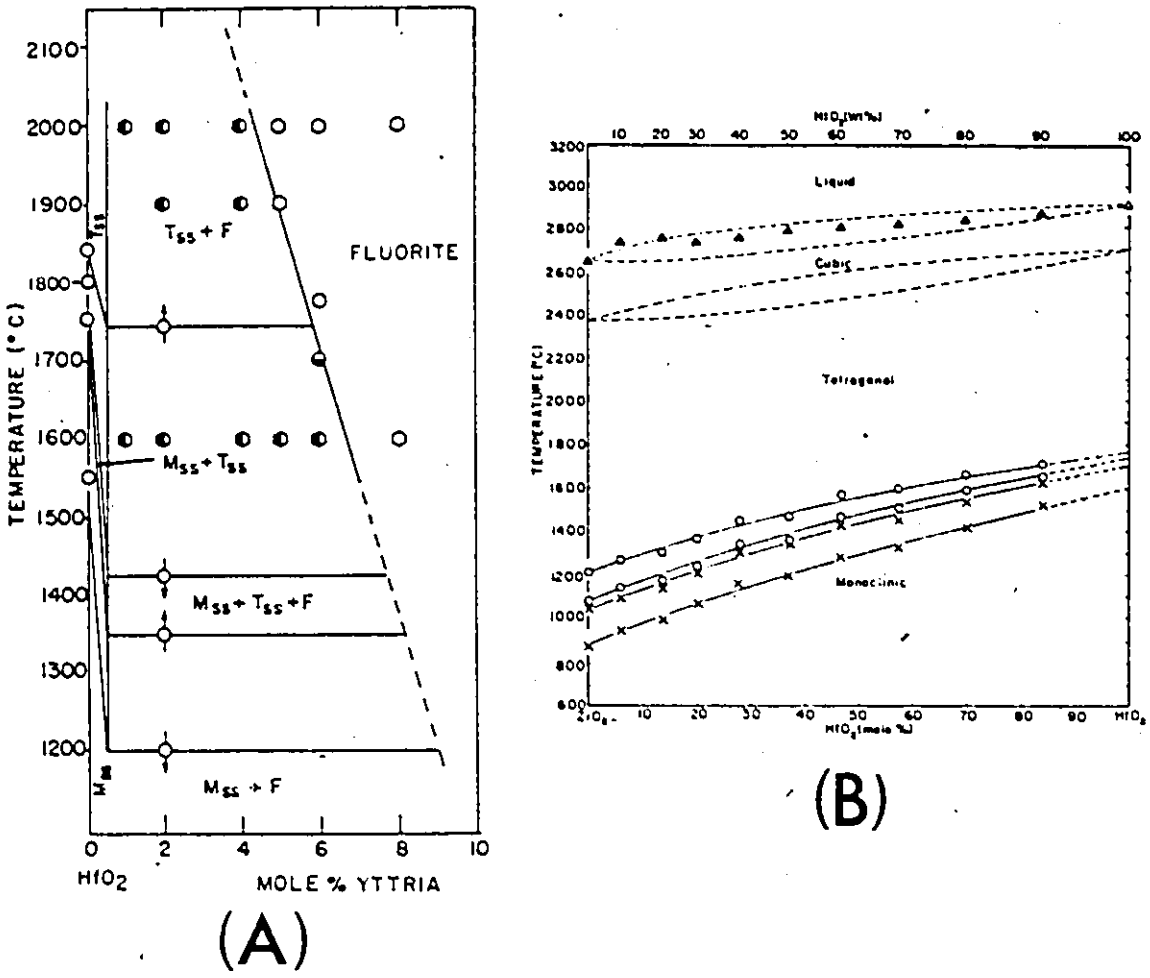

Fig. 2-9 Phase diagrams for hafnia solution with yttria (A, [88]) and zirconia (B, [89]).

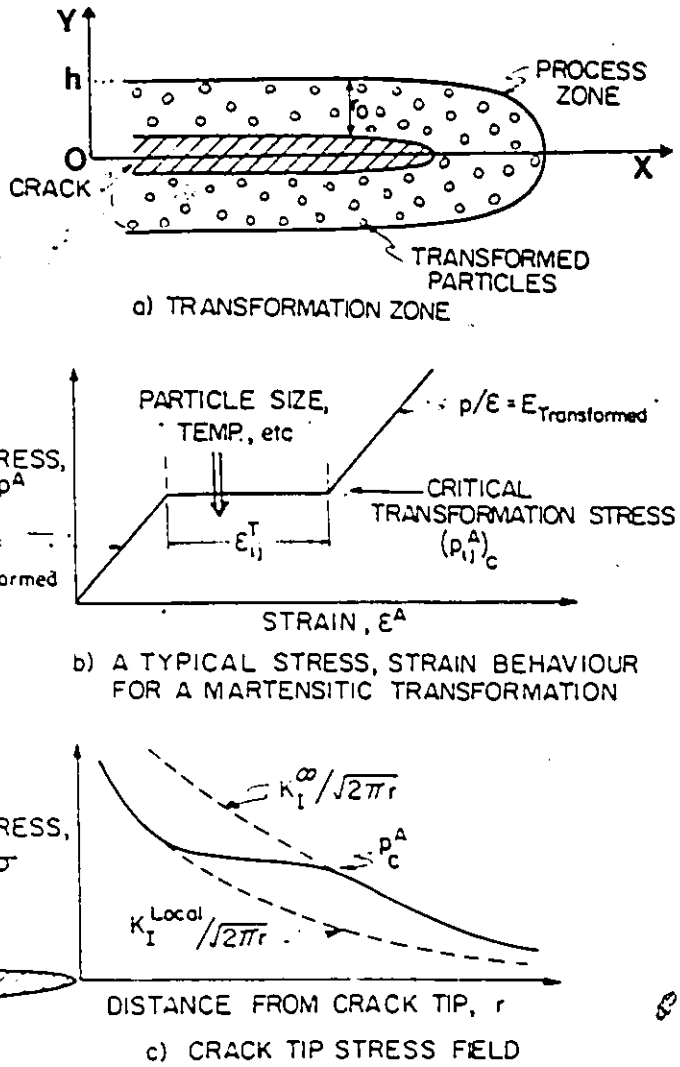

Fig. 2-10 Schematic illustrating the basis for crack shielding by a transformation zone: (A) The fully developed zone;(B) The stress-strain curve of the transforming material;(C) The modified stress field ahead of the crack tip, [106].

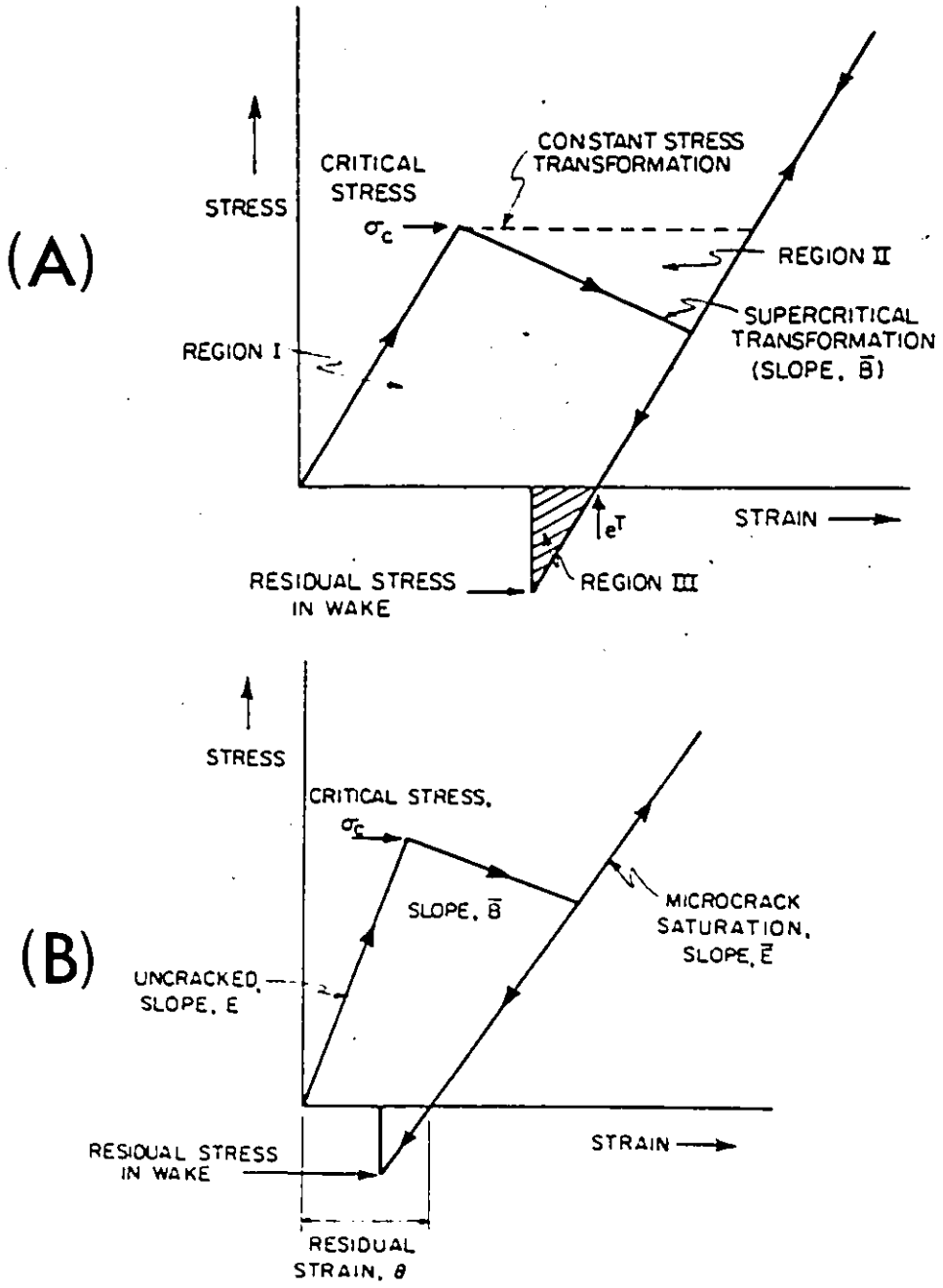

Fig. 2-11 Stress-strain curve for an element of material subject (A) to martensitic transformation (Region I is an area attributed to transformation at constant stress. Region II is an area that allows for the stress decrease due to supercritical transformation. Region III is the strain energy stored in the wake. (B) to microcracking, [106].

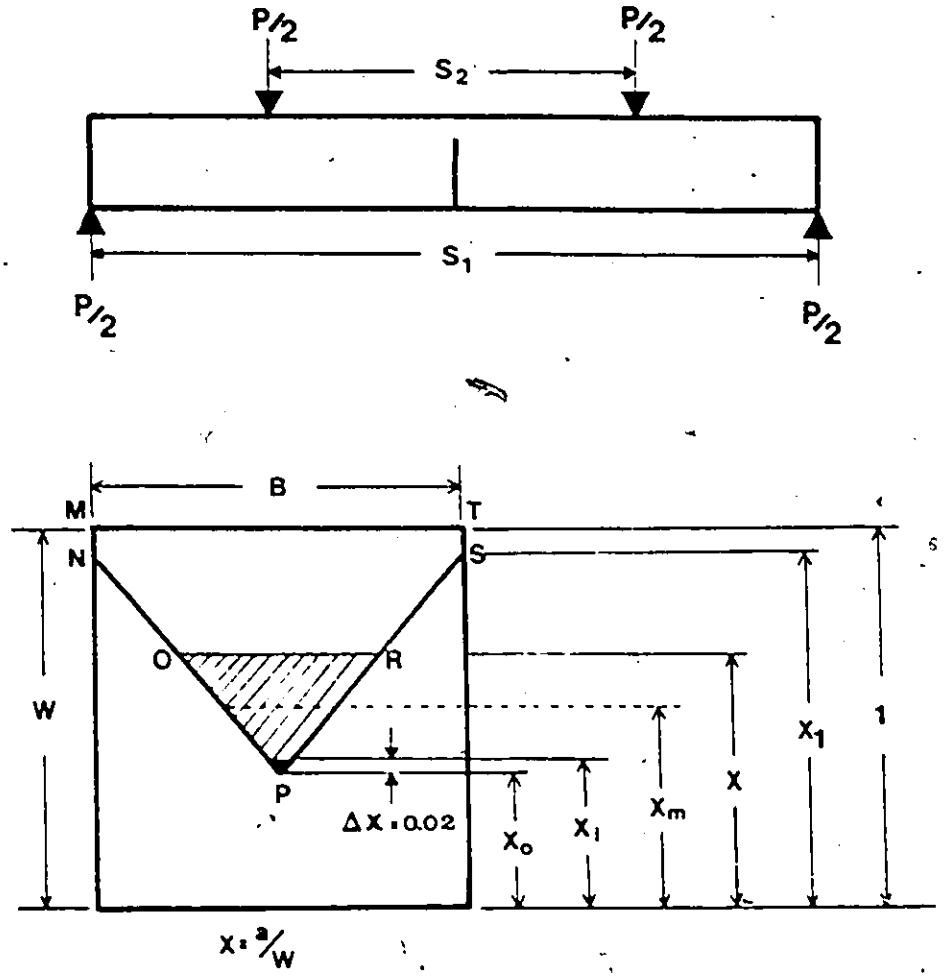

Fig. 2-12 Geometry of the four-point-bend, chevron notched specimen.

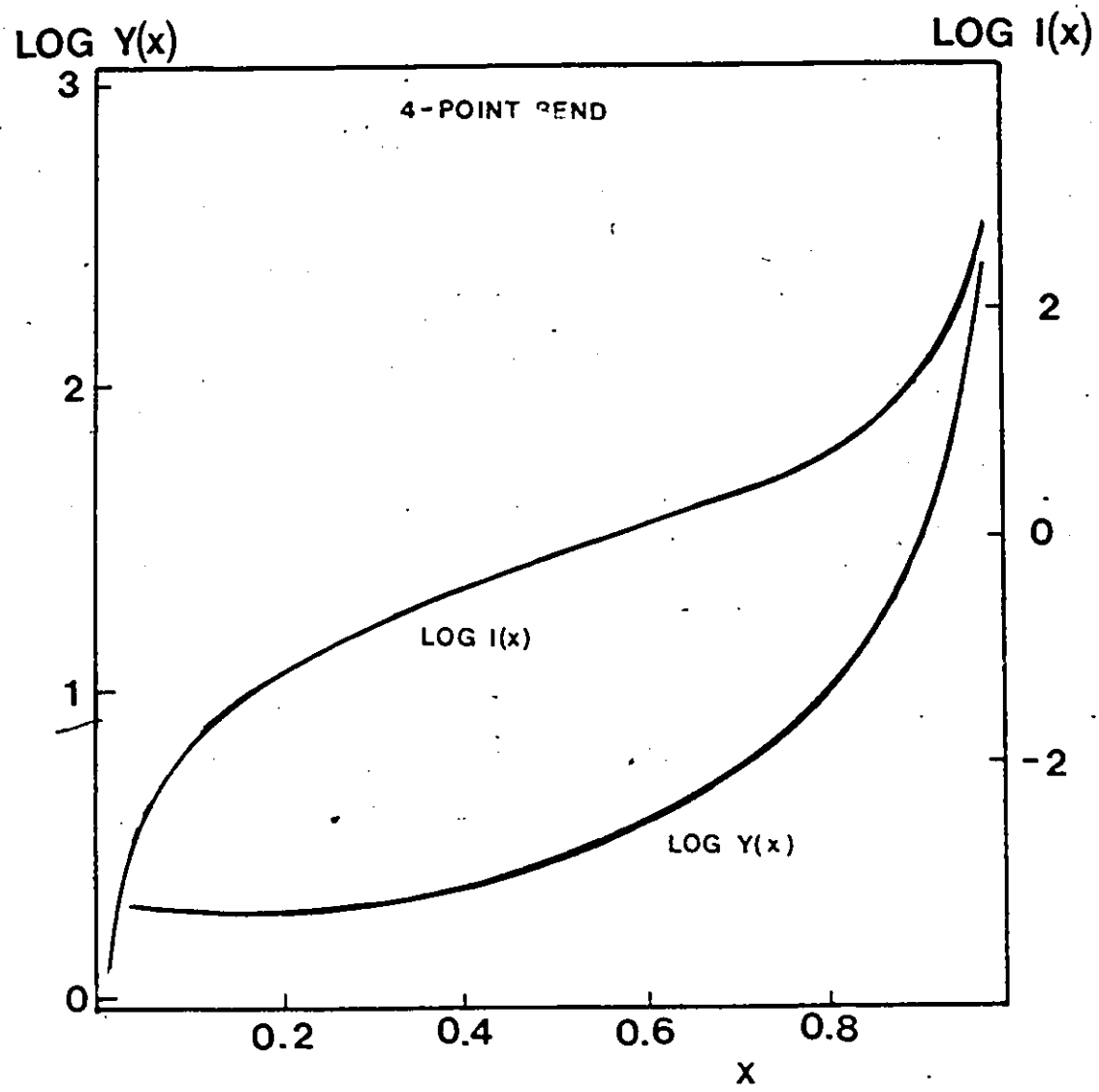

Fig. 2-13 Universal four-point bend geometric factors I(x), eq.2.43, and Y(x), eq.2.45, as function of the normalized crack length x.

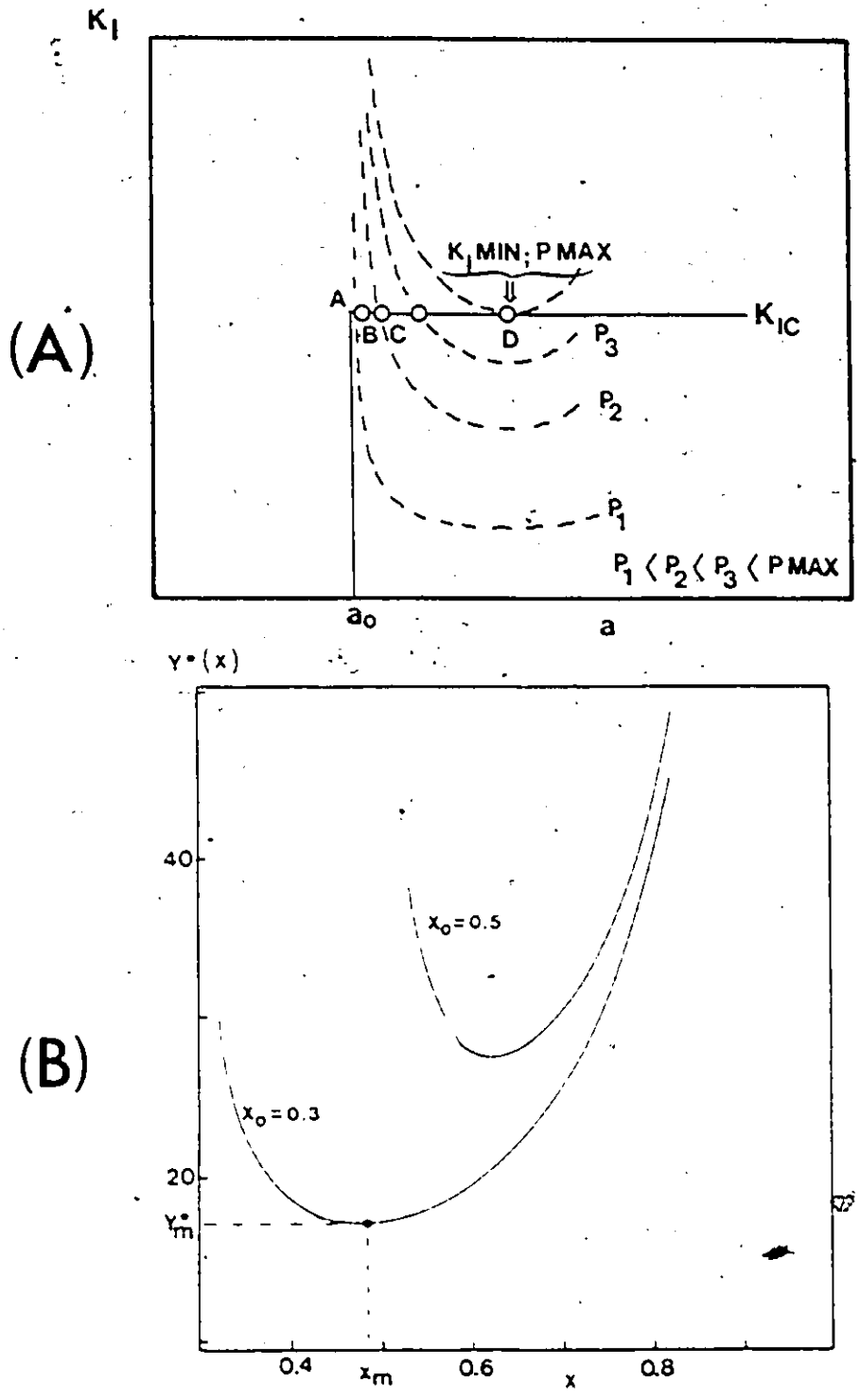

Fig. 2-14 CN specimen properties : (A) Variation of the stress intensity factor during fracture of the specimen made of material immune for subcritical crack growth; (B) Variation of the geometric factor $Y^*(x)$ for two specimens of the initial crack length x_0=0.3 and 0.5.

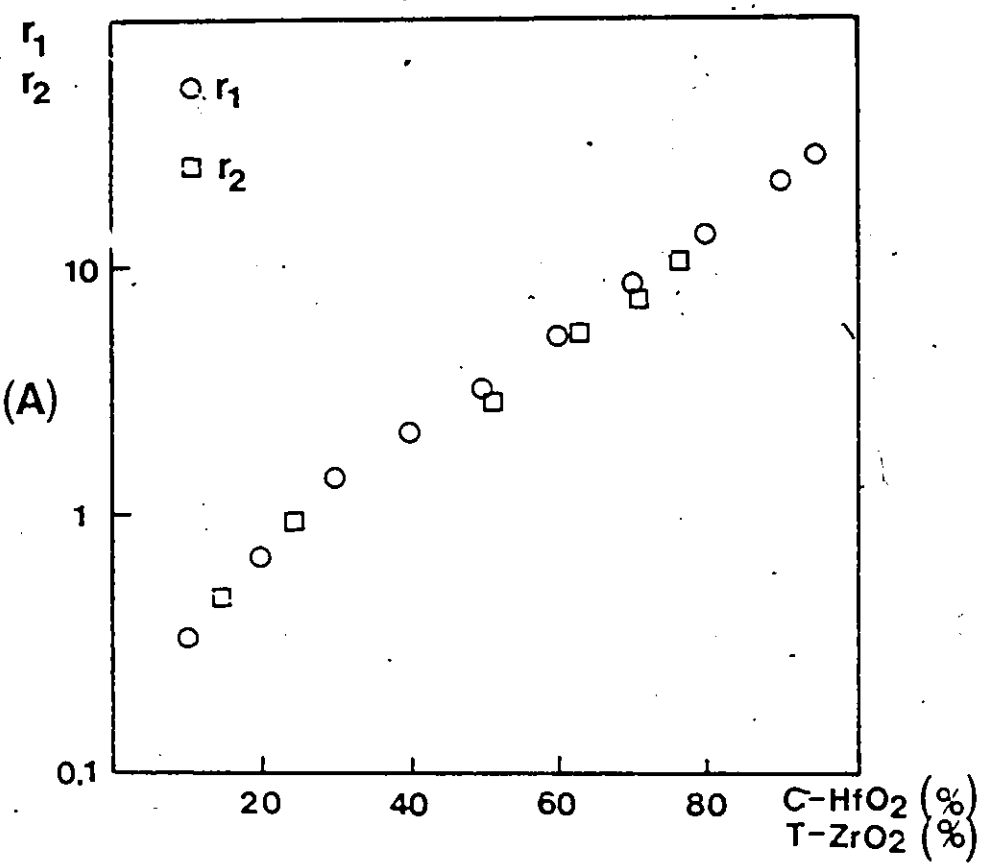

(B)

	tetragonal				cubic				monoclinic			
	hkl	I %	d[nm]	2θ°	hkl	I %	d[nm]	2θ°	hkl	I %	d[nm]	2θ°
ZrO_2												
	111	100	0.293	30.2	111	100	0.316	28.2				
									$11\bar{1}$	65	0.283	31.6
HfO_2												
	111	100	0.293	30.2	111	100	0.315	28.3				
									$11\bar{1}$	65	0.282	31.7

Fig. 2-15 (A) X-ray intensity ratio $r_1=(111)_C/(111)_M$ for HfO_2 as function of amount of cubic HfO_2, [144], and ratio $r_2=(111)_T/(111)_M$ for ZrO_2 as function of amount of tetragonal ZrO_2, eq.2.66. (B) X-ray diffraction data for the three polymorphs of ZrO_2 and HfO_2 in 2θ range 28 to 32° (λ=0.154 nm)

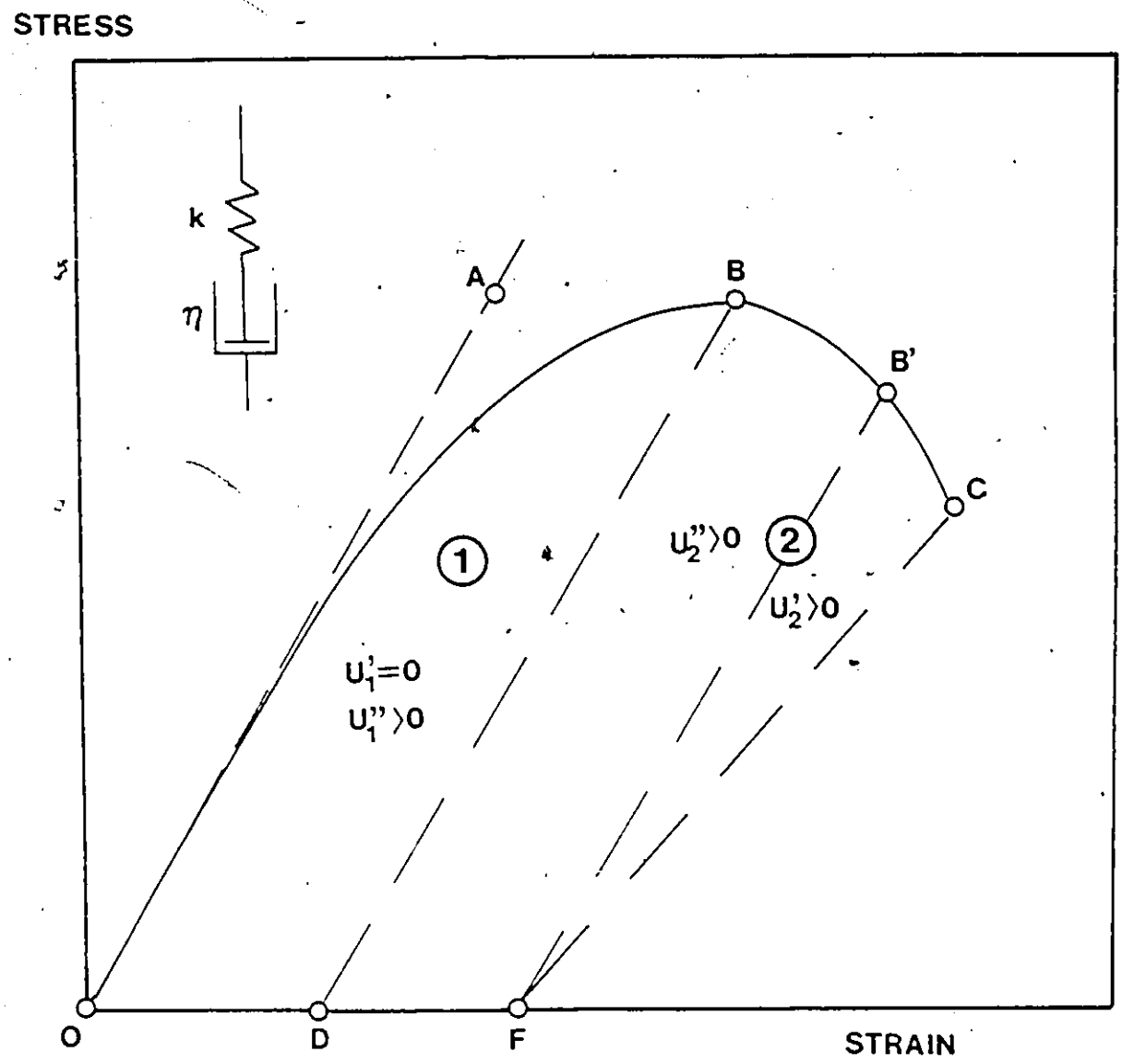

Fig. 2-16 Schematic spring-dashpot element and stress-strain relation for viscoelastic material.

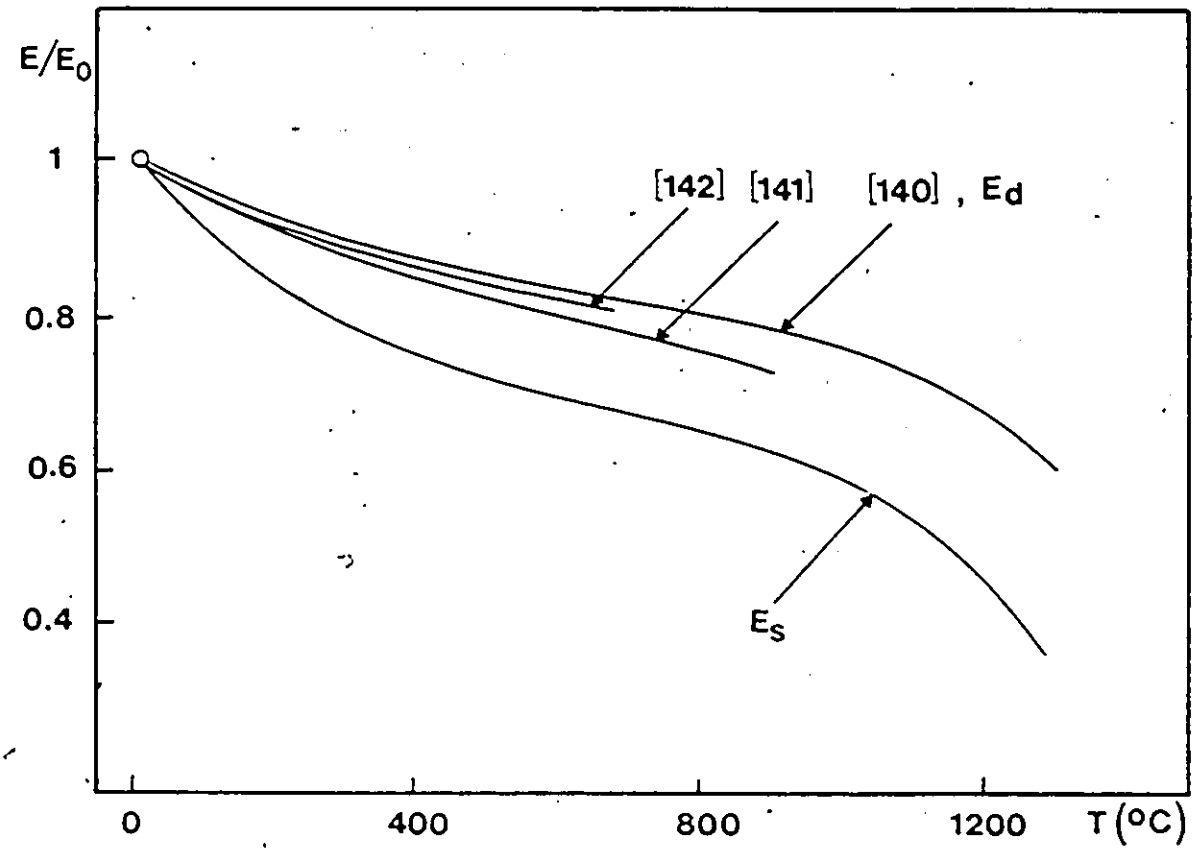

Fig. 2-17 Dependence of the Young's Modulus E of partially stabilized zirconia on temperature (E_0=E at 20°C)
E_d : dynamic measurement [140,141,142].
E_s : static measurement, this thesis.

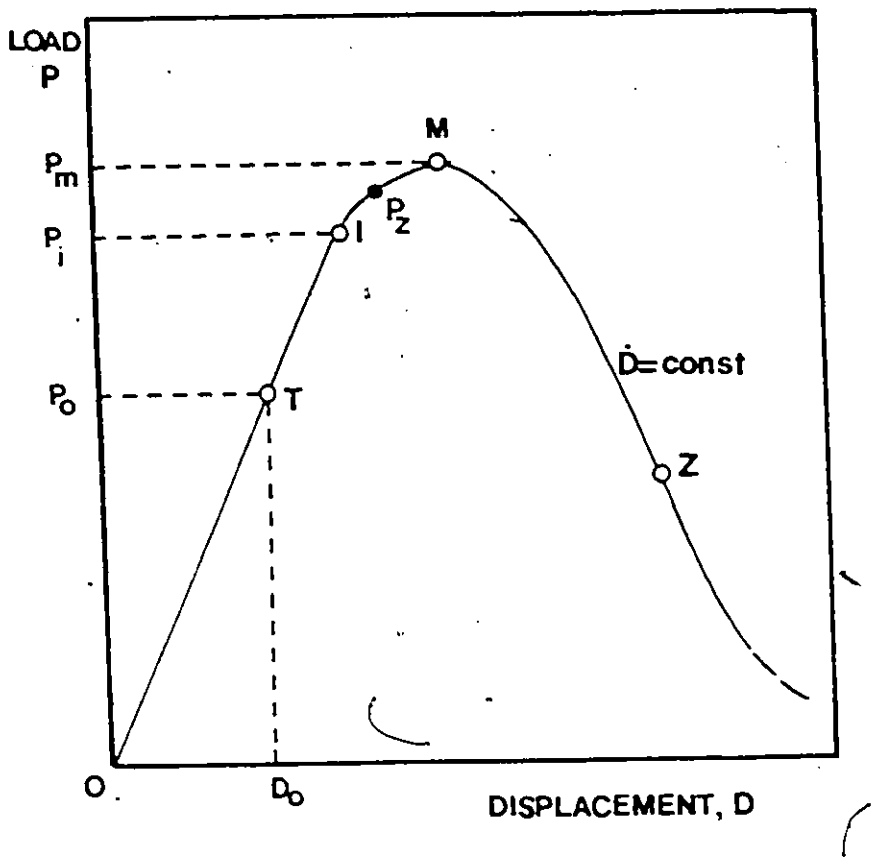

Fig. 3-1 Schematic load-displacement diagram for stable fracture experiment at constant displacement rate.

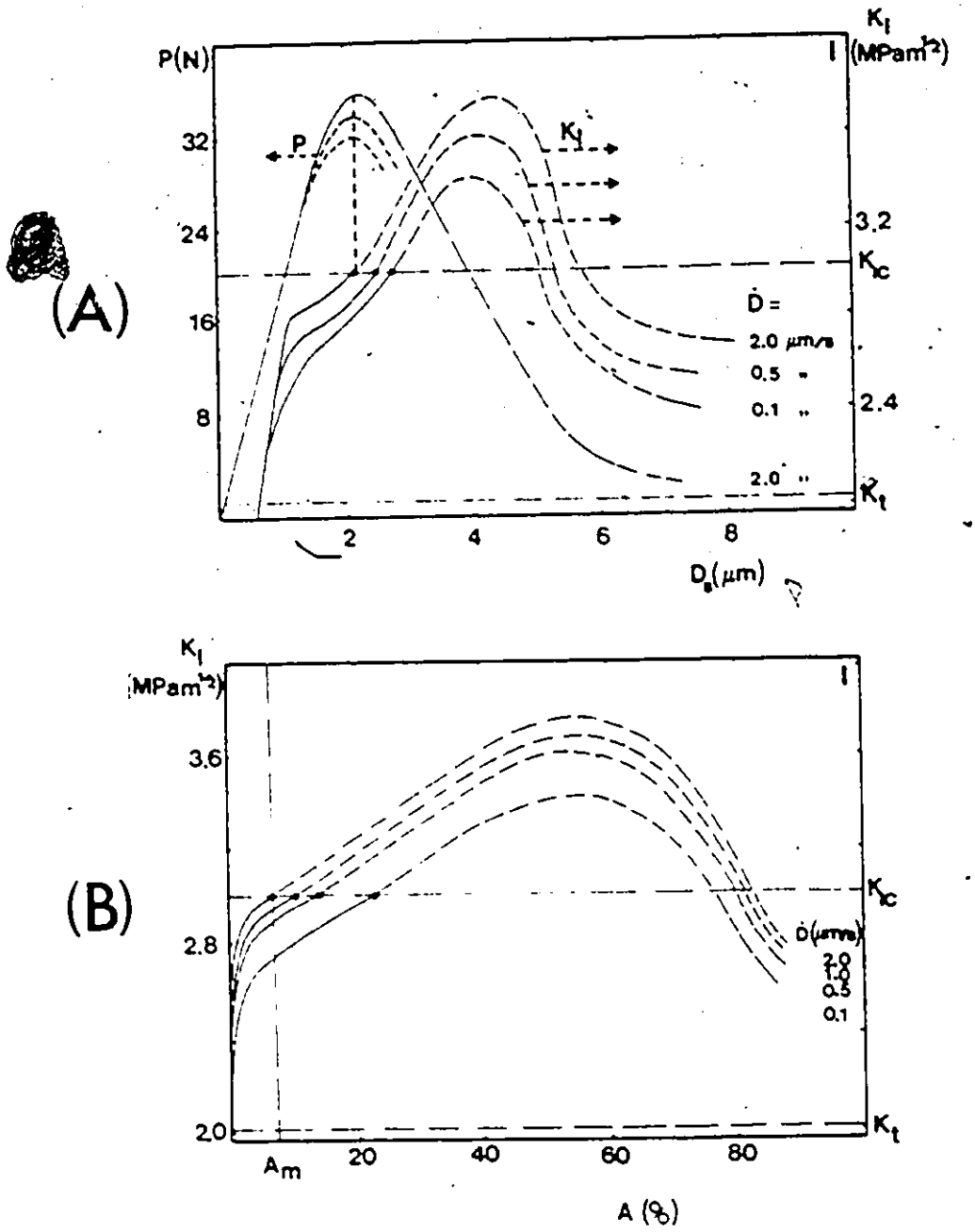

Fig. 3-2 Fracture characteristics of Type I material : (A) Load P and stress intensity factor K_I variations against load application point displacement. Crosshead velocity 0.1,0.5 and 2.0 μm/s ; (B) Stress intensity factor against percentage of fracture area. $A=A_m$ represents the area at minimum value of the chevron specimen geometric factor $Y^*=Y^*_m$.

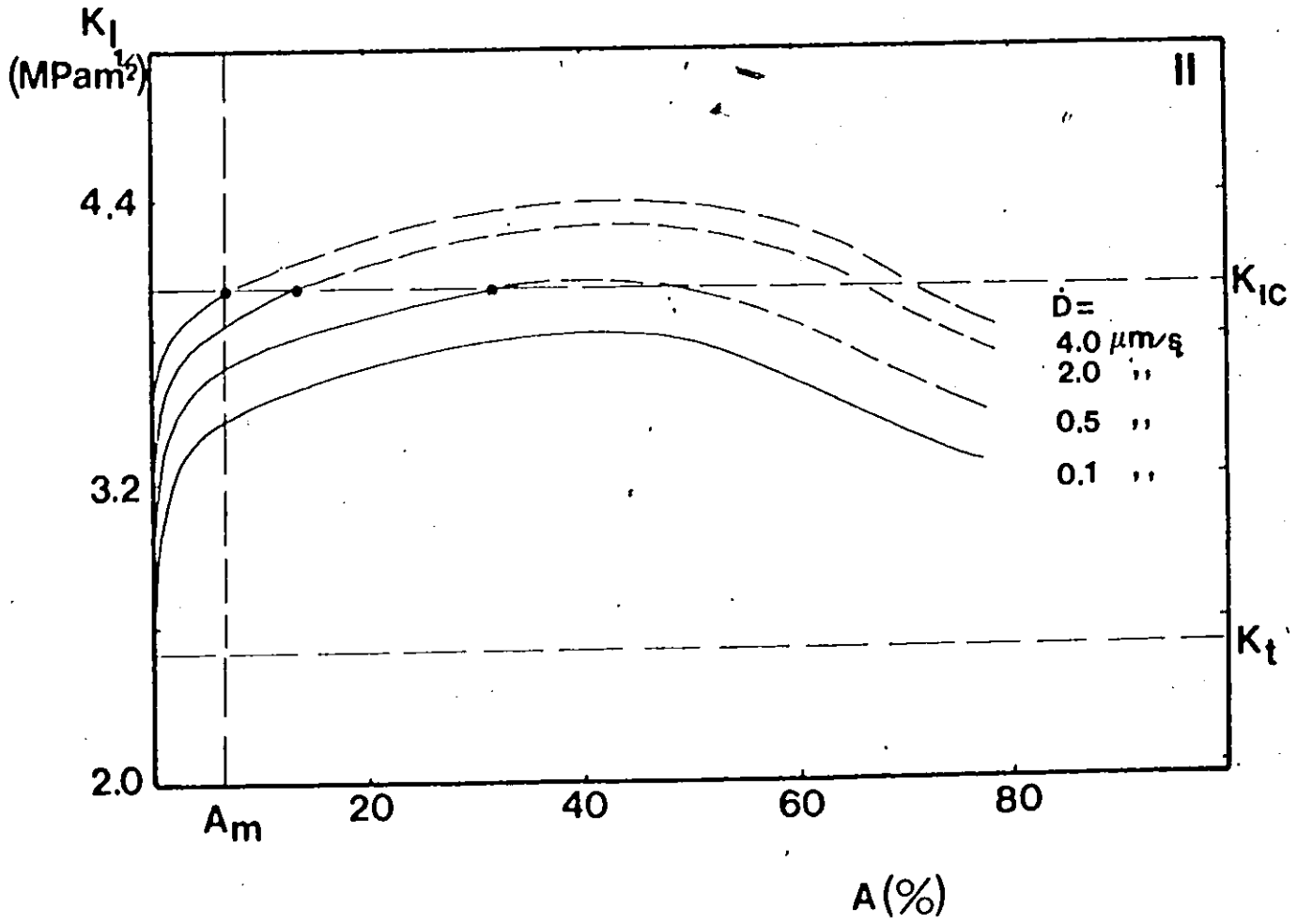

Fig. 3-3 Stress intensity factor against percentage of fracture area, for Type II material. Crosshead velocity 0.1, 0.5, 2.0, 4.0 μm/s..

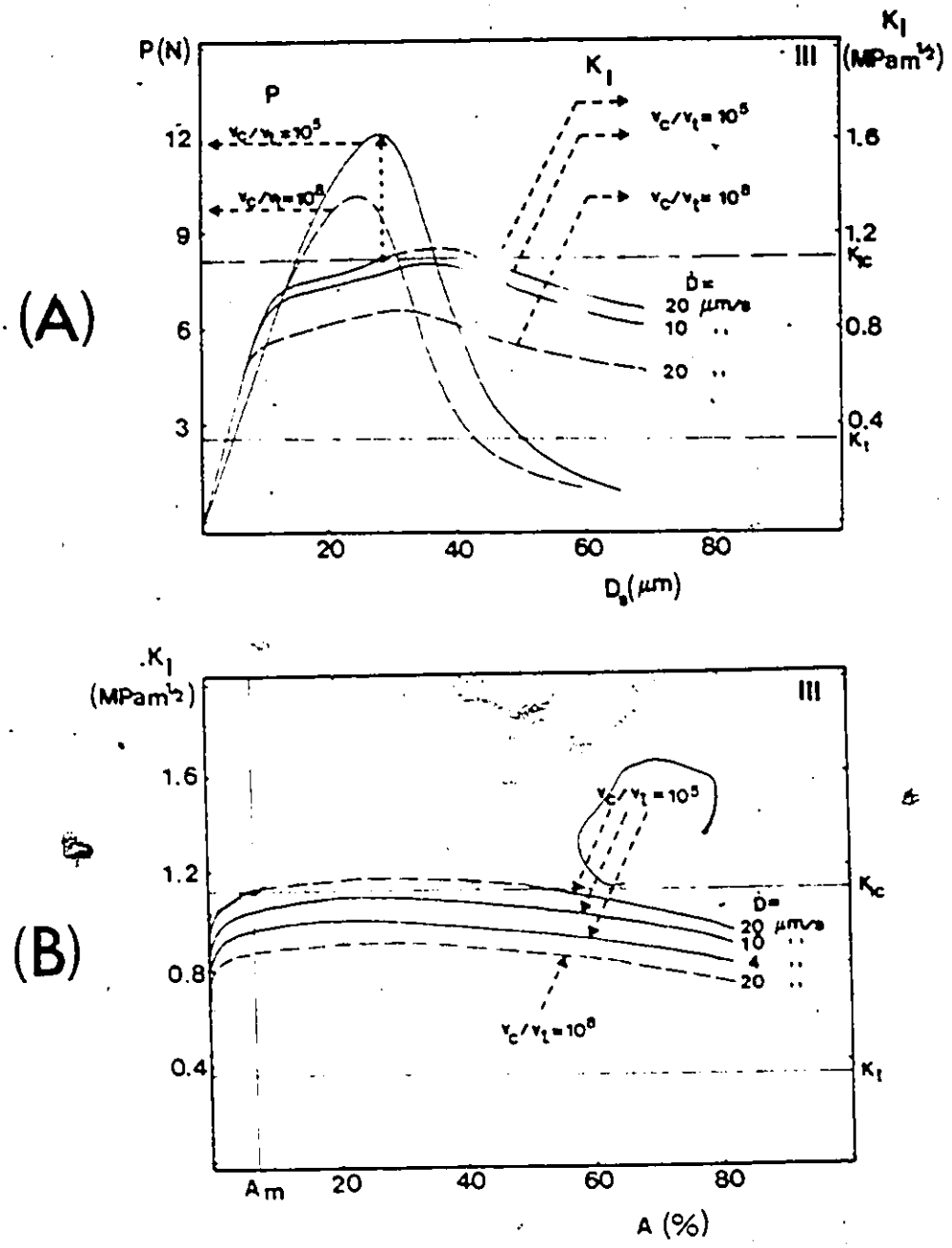

Fig. 3-4 Fracture characteristics of Type III material : (A) Load P and stress intensity factor K_I against load application point displacement; (B) Stress intensity factor against percentage of fracture area.

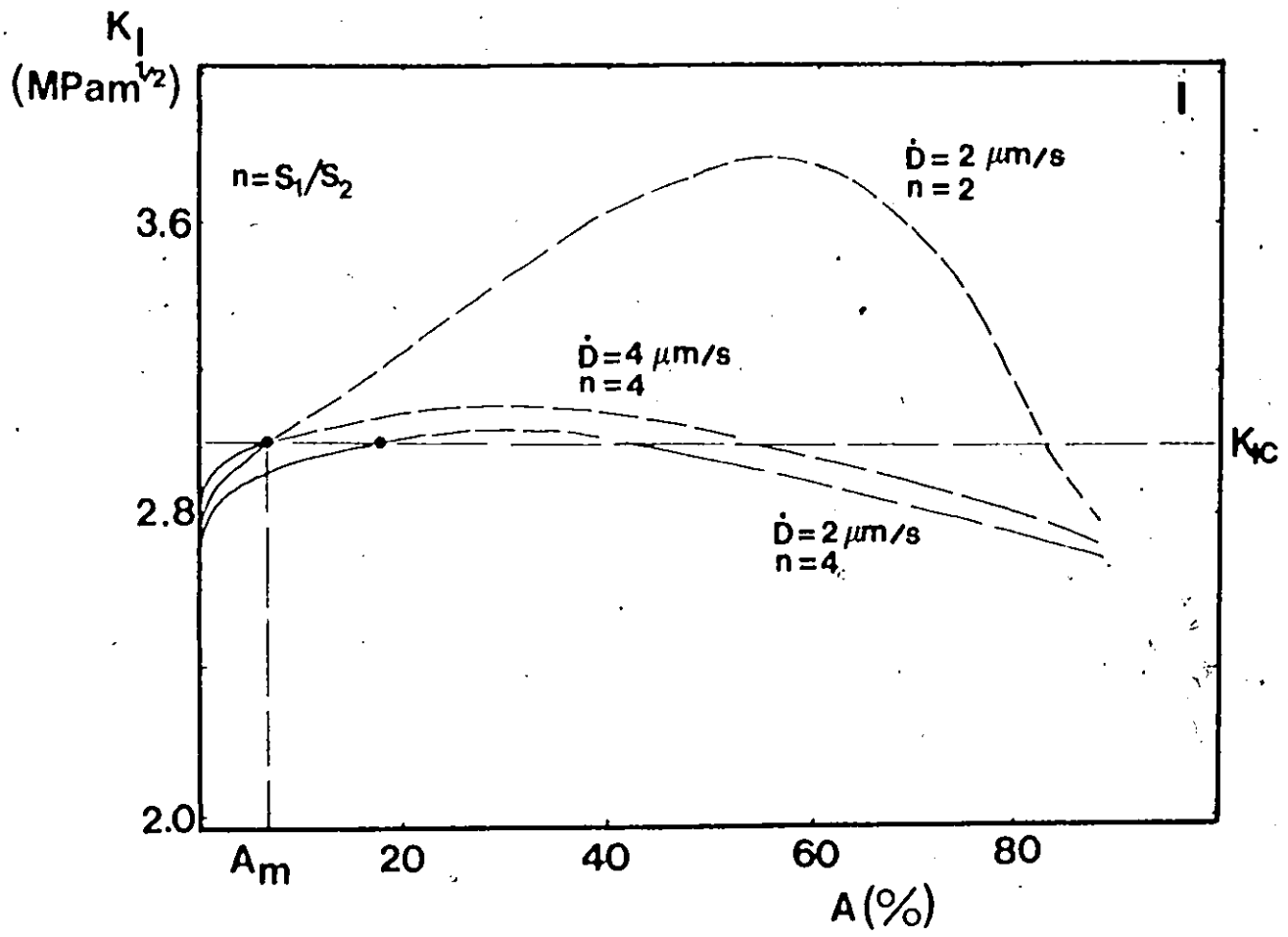

Fig. 3-5 Stress intensity factor against percentage of fracture area for Type I material. Bending span ratio n=2.0 and 4.0, crosshead velocity equal 2.0 and 4.0 μm/s.

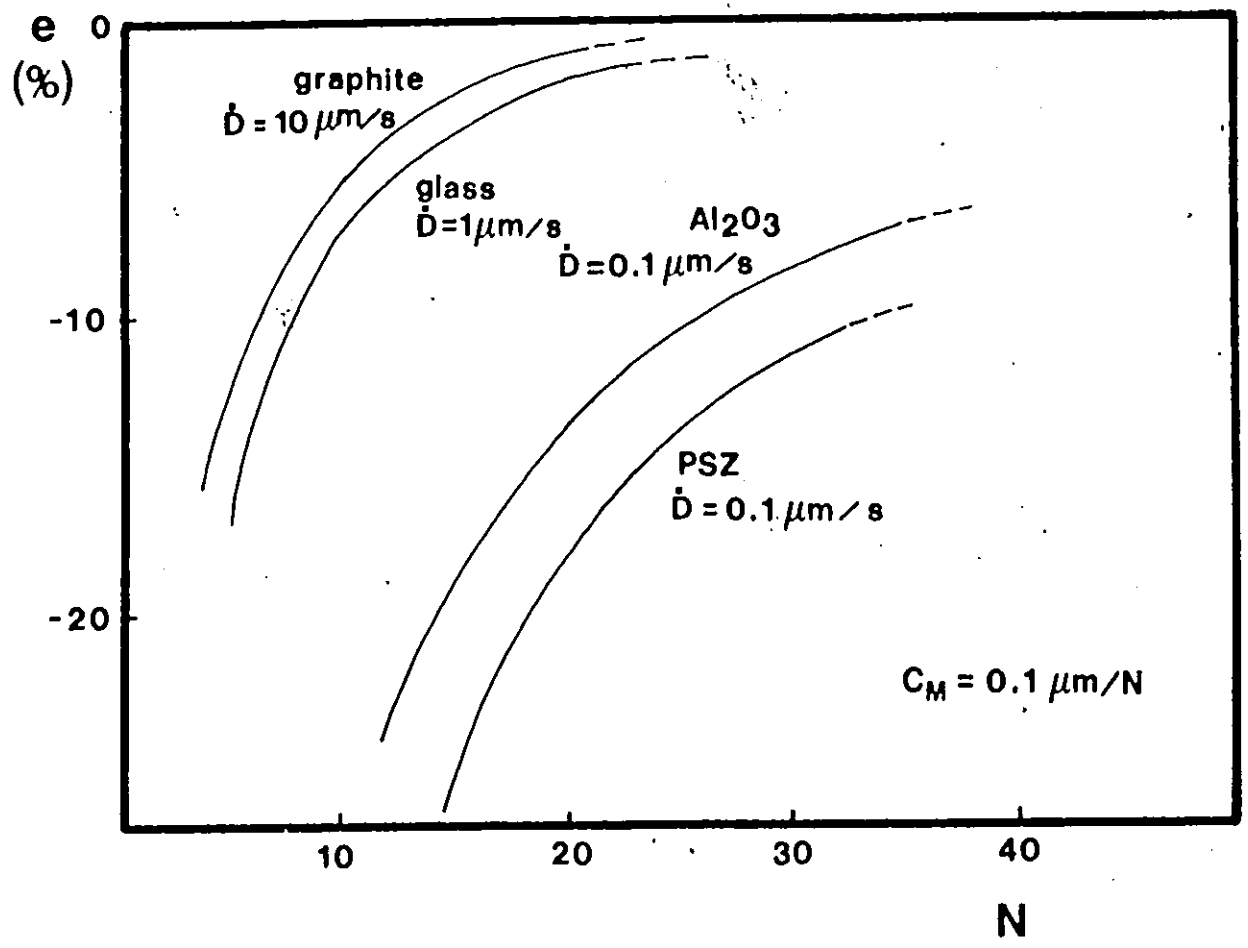

Fig. 3-6 The relative error e in K_{IC} calculation from maximum load for CN specimen exhibiting subcritical crack growth, as function of the exponent N.

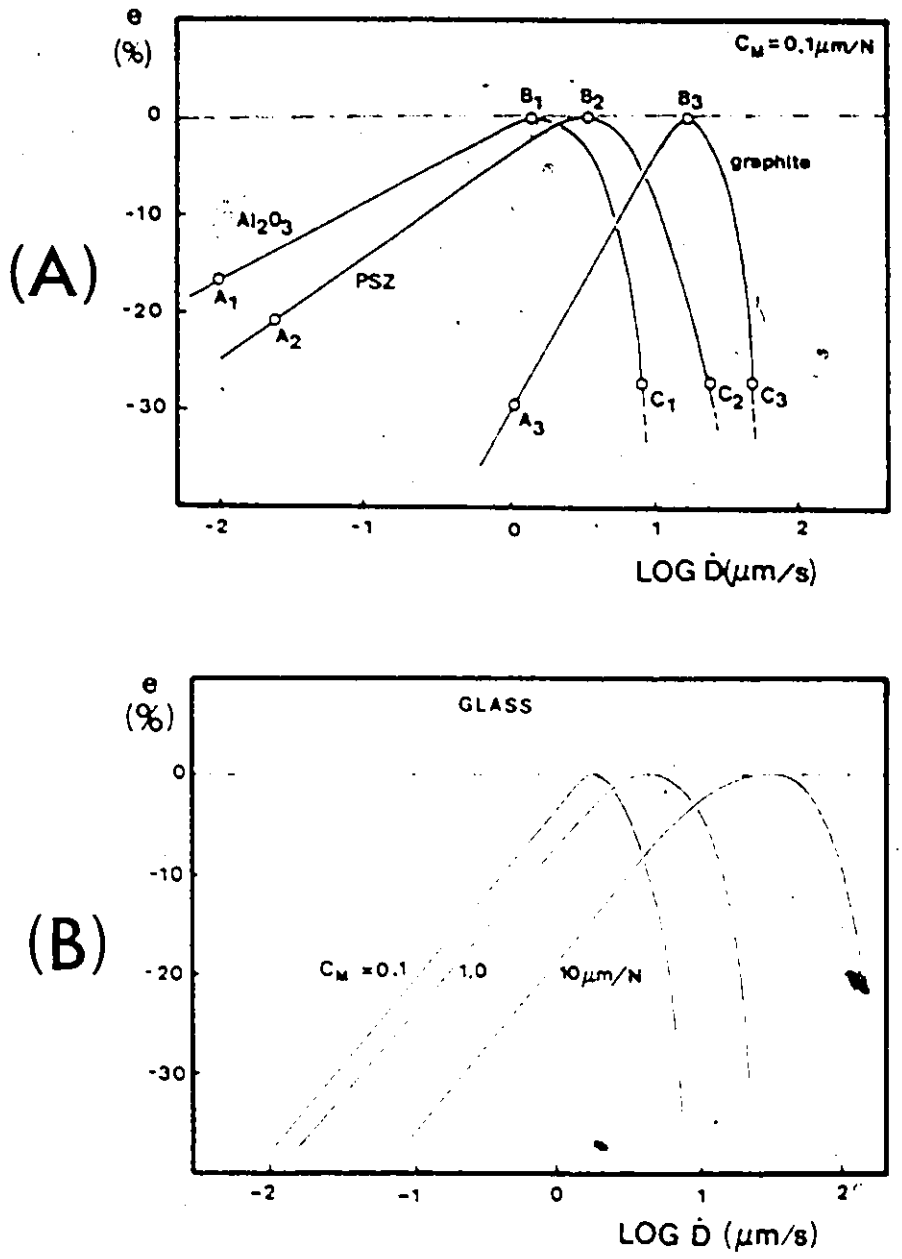

Fig. 3-7 The relative error e in K_{IC} calculation from maximum load for CN specimen exhibiting subcritical crack growth : (A) as function of the displacement rate at constant machine compliance C_M=0.1 μm/N, for materials Type I,II,III ; (B) As function of the displacement rate and machine compliance, for glass.

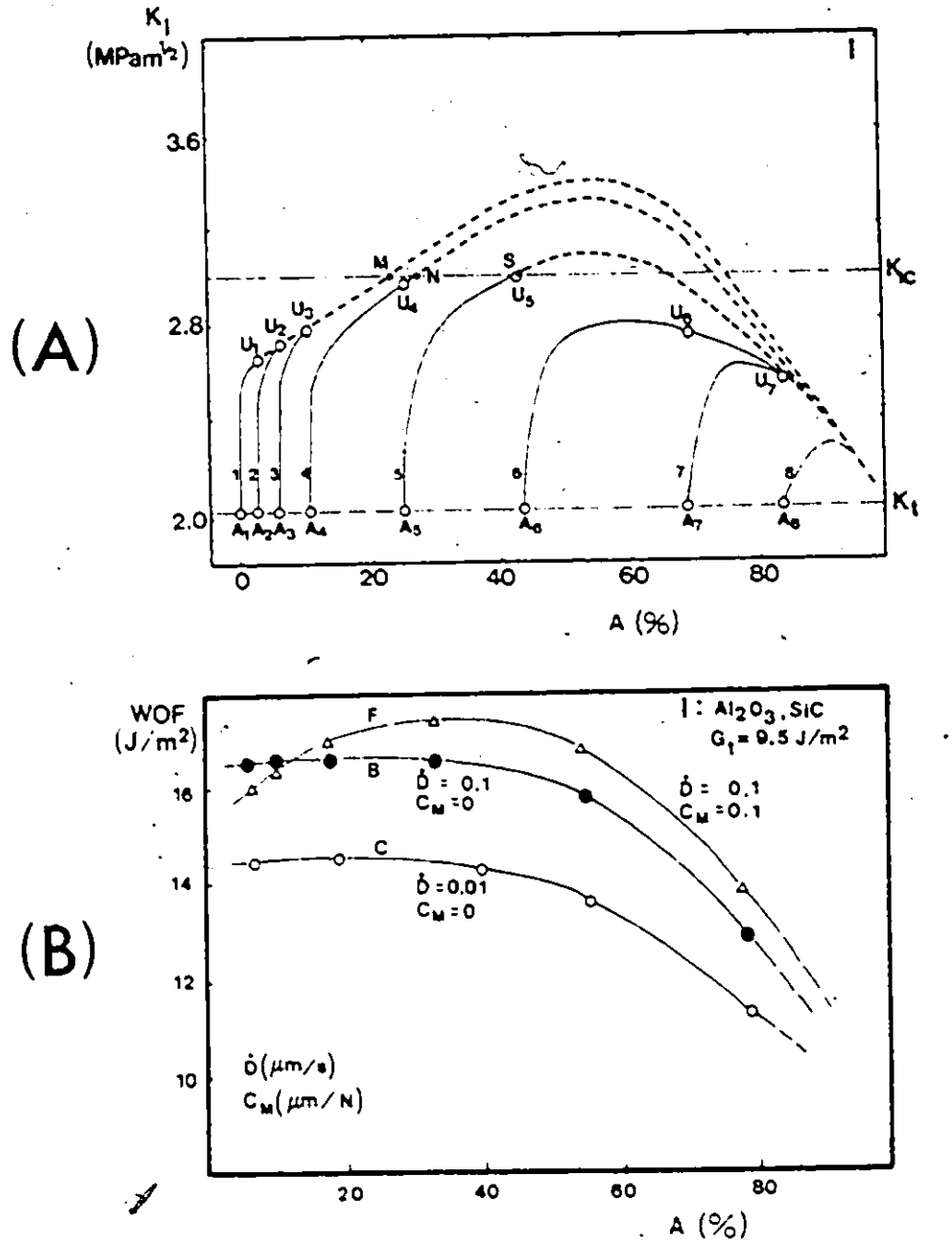

Fig. 3-8 Crack driving force against percentage of fracture area for repeated loading-unloading experiments, Type I material (Al_2O_3, SiC). C_M=0.1 μm/N, dD/dt = 0.1 μm/s : (A) Stress intensity factor ; (B) Partial work of fracture calculated as integrated G_I curves in loading-unloading experiments.

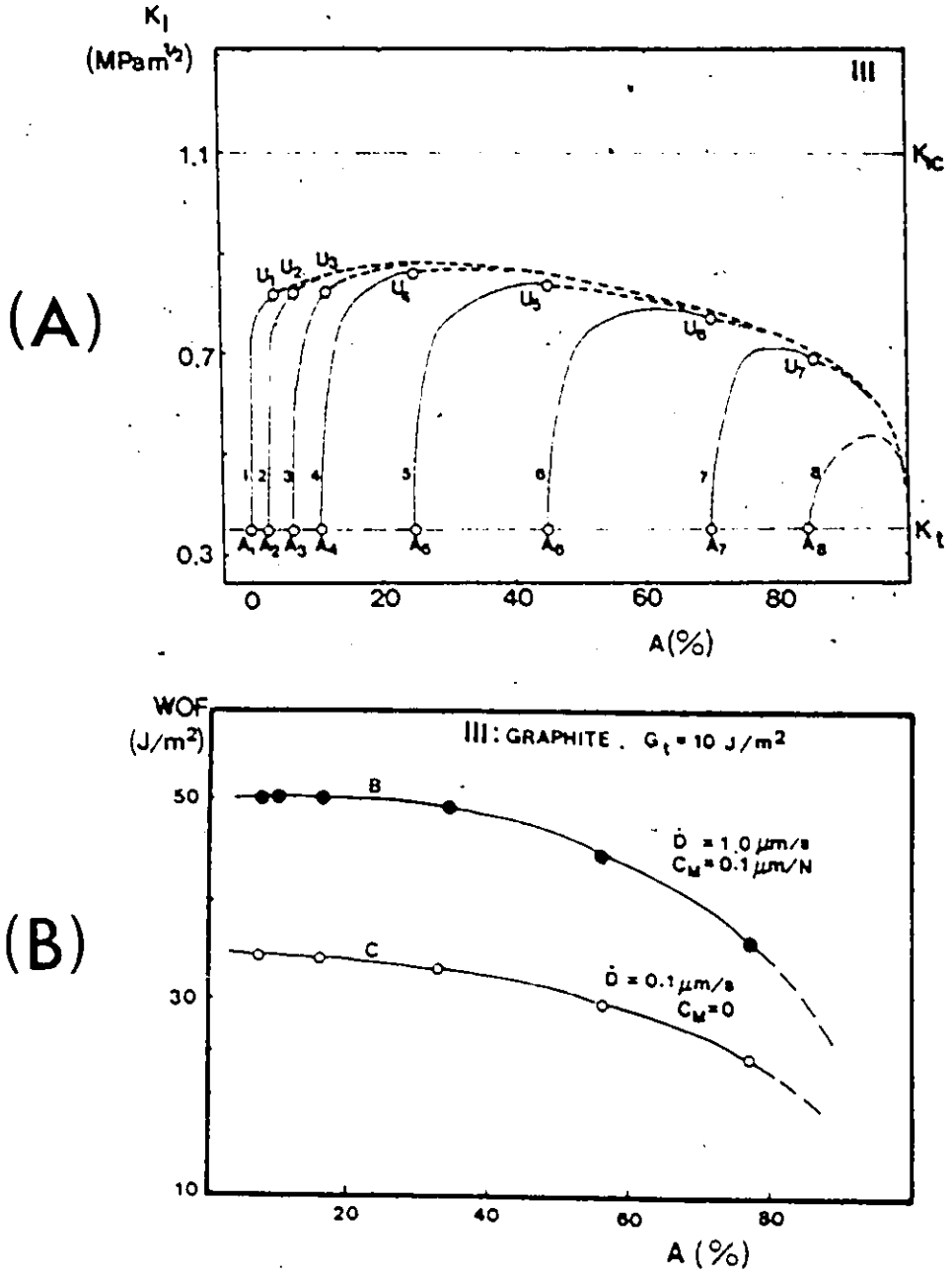

Fig. 3-9 Crack driving force against percentage of fracture area for repeated loading-unloading experiments, Type III material (graphite). C_M=0.1 μm/N, dD/dt = 1 μm/s : (A) Stress intensity factor; (B) Partial work of fracture, calculated as integrated G_I curves in loading-unloading experiments.

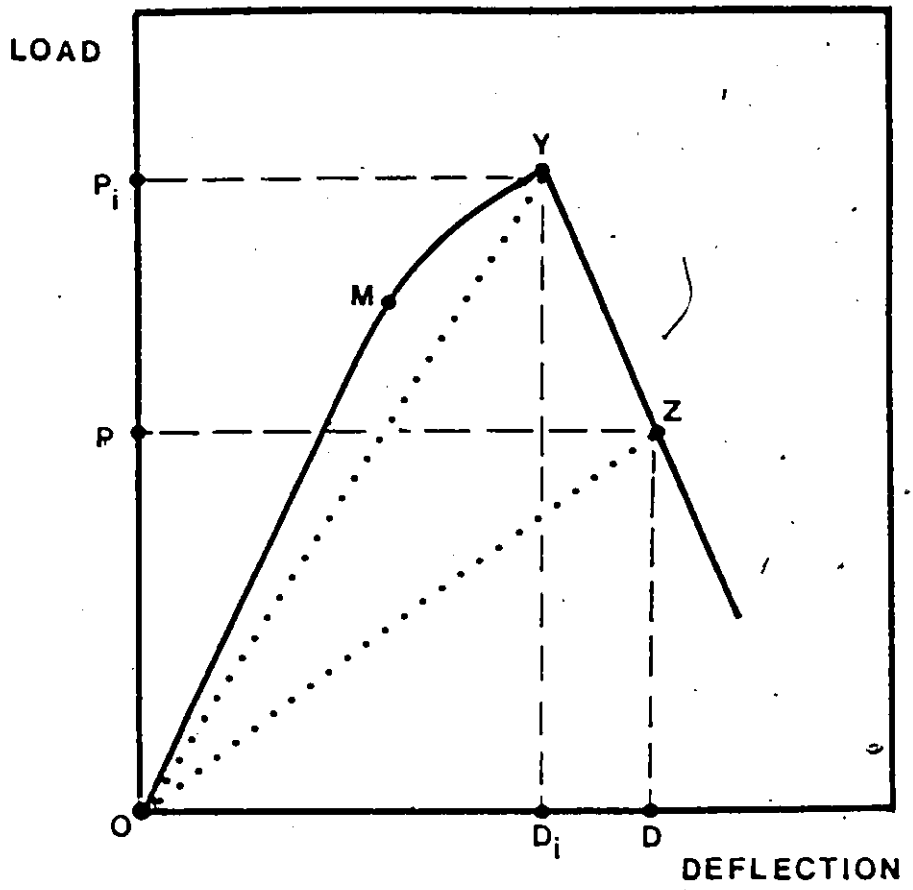

Fig. 3-10A Schematic load-displacement diagram for load-relaxation experiment.

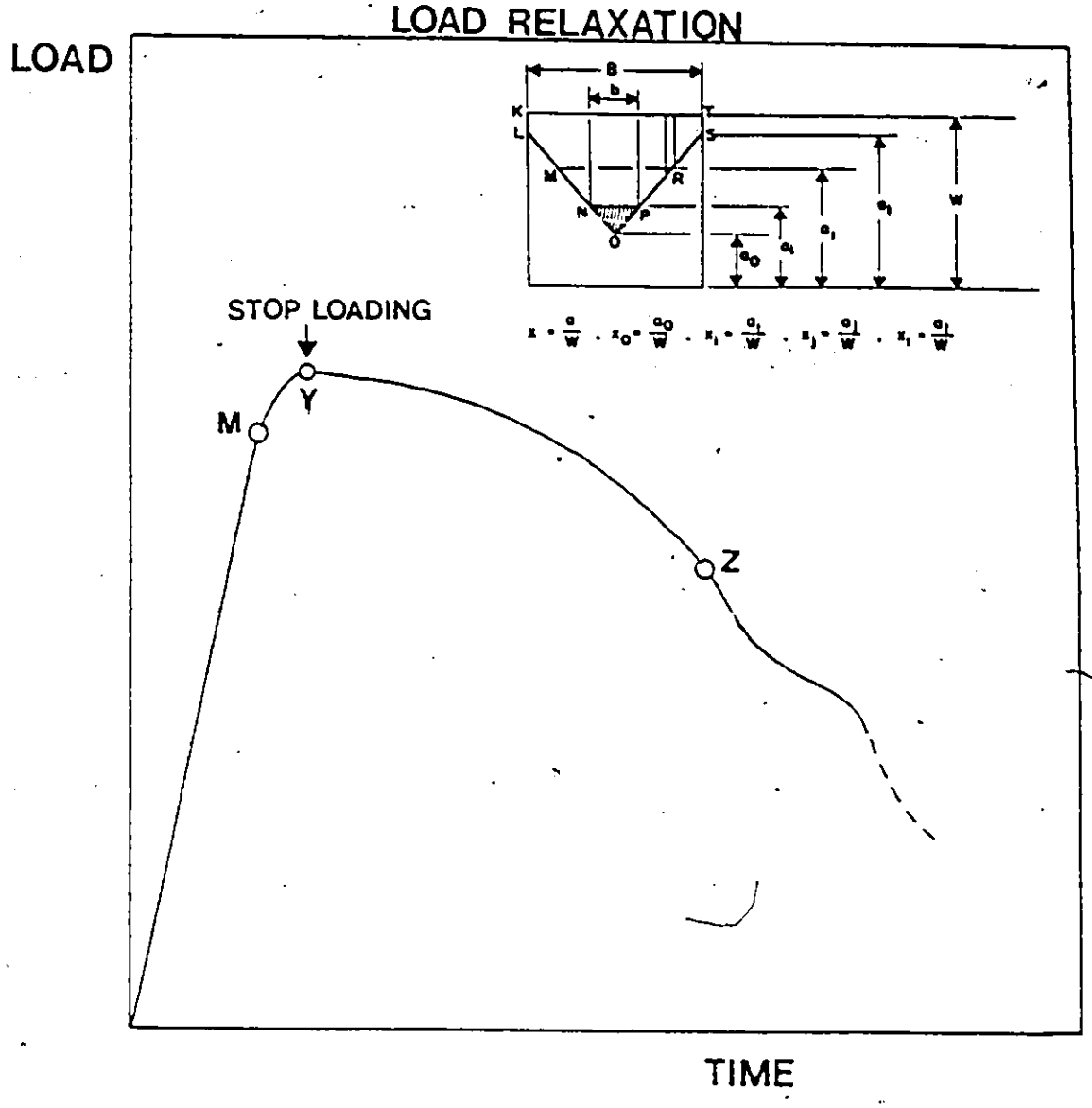

Fig. 3-108 Schematic load-time diagram for load-relaxation experiment.

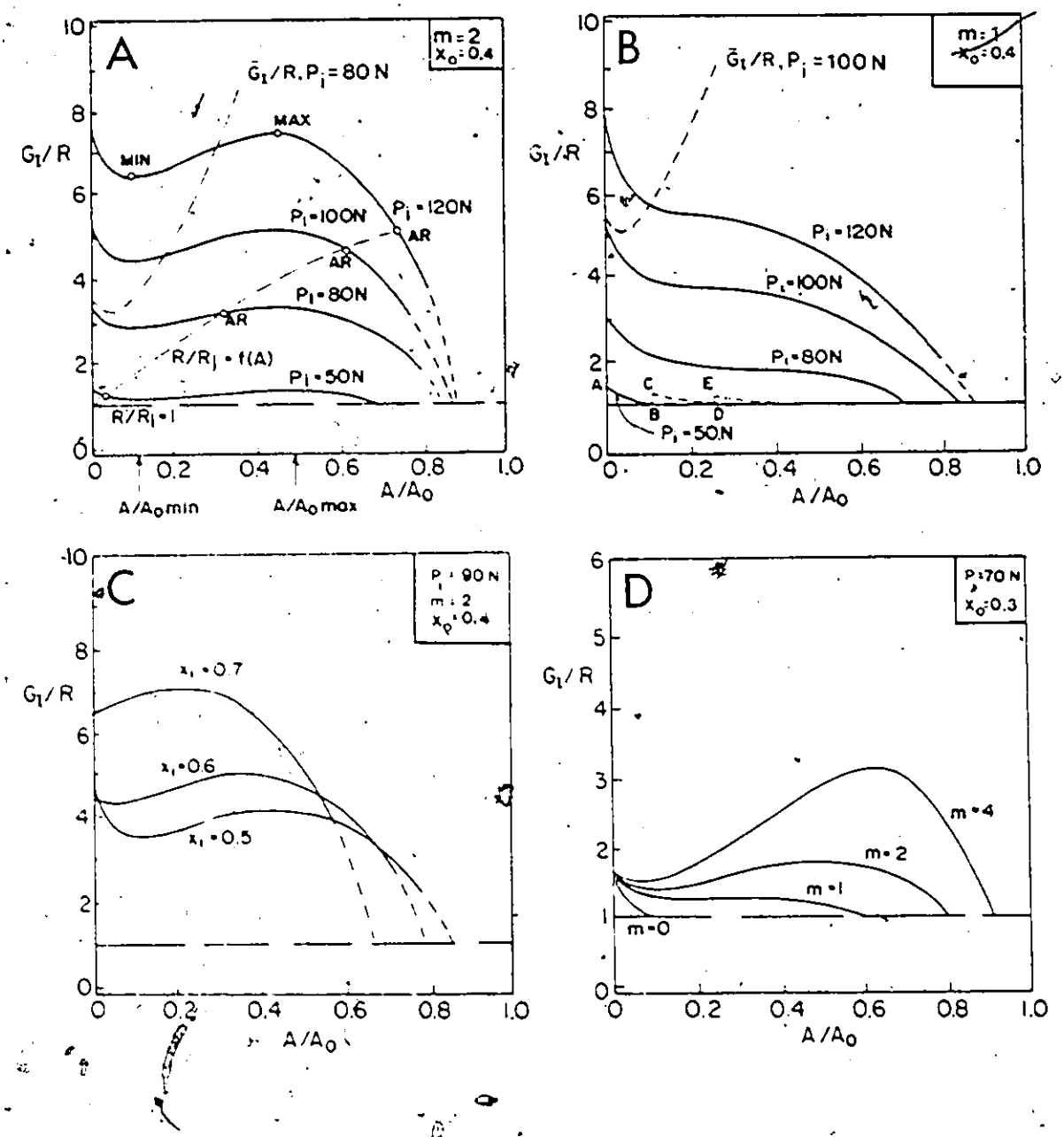

Fig. 3-11 G_I/R curves for changing:(A)Initiation load P_i ; (B) Initiation load P_i and stiffer machine ; (C) Crack initiation length, x_i ; (D) Relative machine compliance, m, and short initial notch length, x_0.

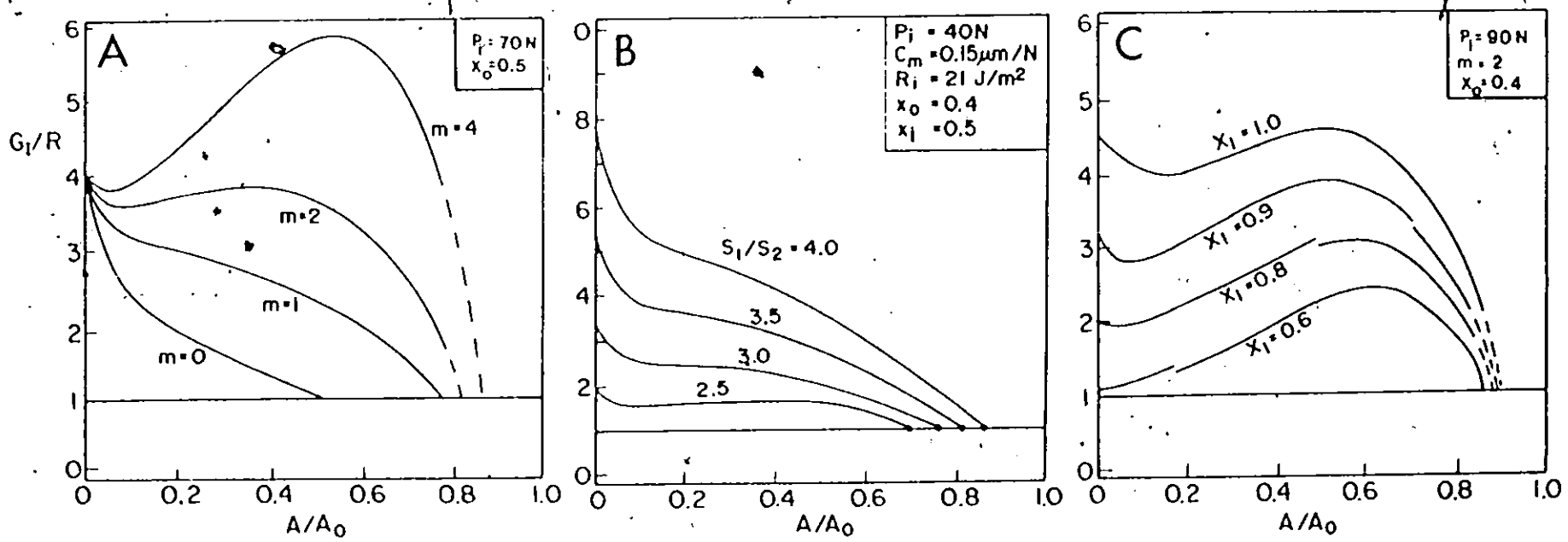

Fig. 3-12 G_I/R curves for changing : (A) Relative machine compliance, m, and deep initial notch length, x_0; (B) Bend spans at constant absolute machine compliance ; (C) Side notch length, x_1.

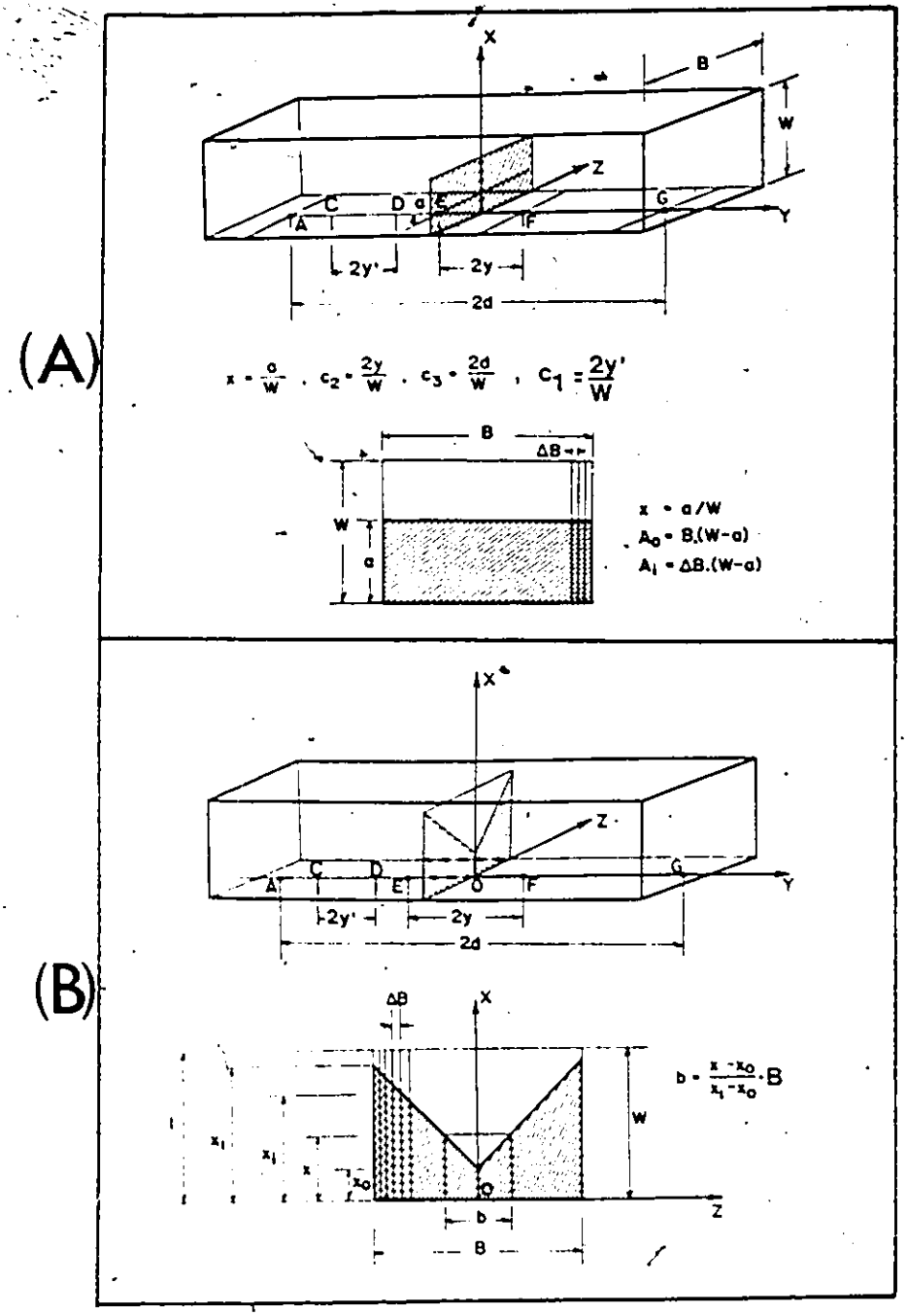

Fig. 3-13 Geometry and cross section of :(A) Straight-through notched specimen ; (B) Chevron notched specimen. The current probes are located at A, G ; voltage probes at E, F ; reference probes at C, D.

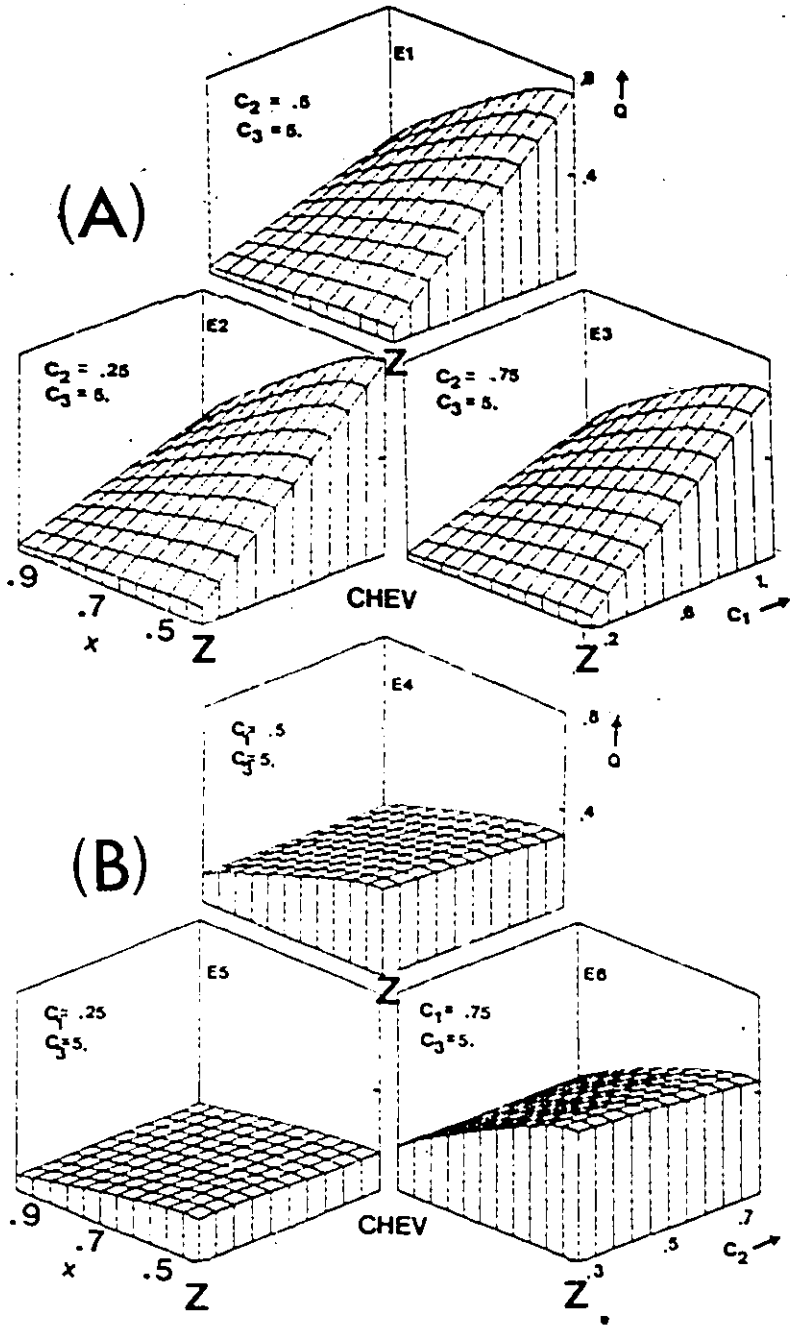

Fig. 3-14 Variation of the relative potential drop Q against the crack length x and : (A) The reference voltage probes distance C_1, for CN specimen ; (B) The working voltage probes distance C_2, for CN specimen ;

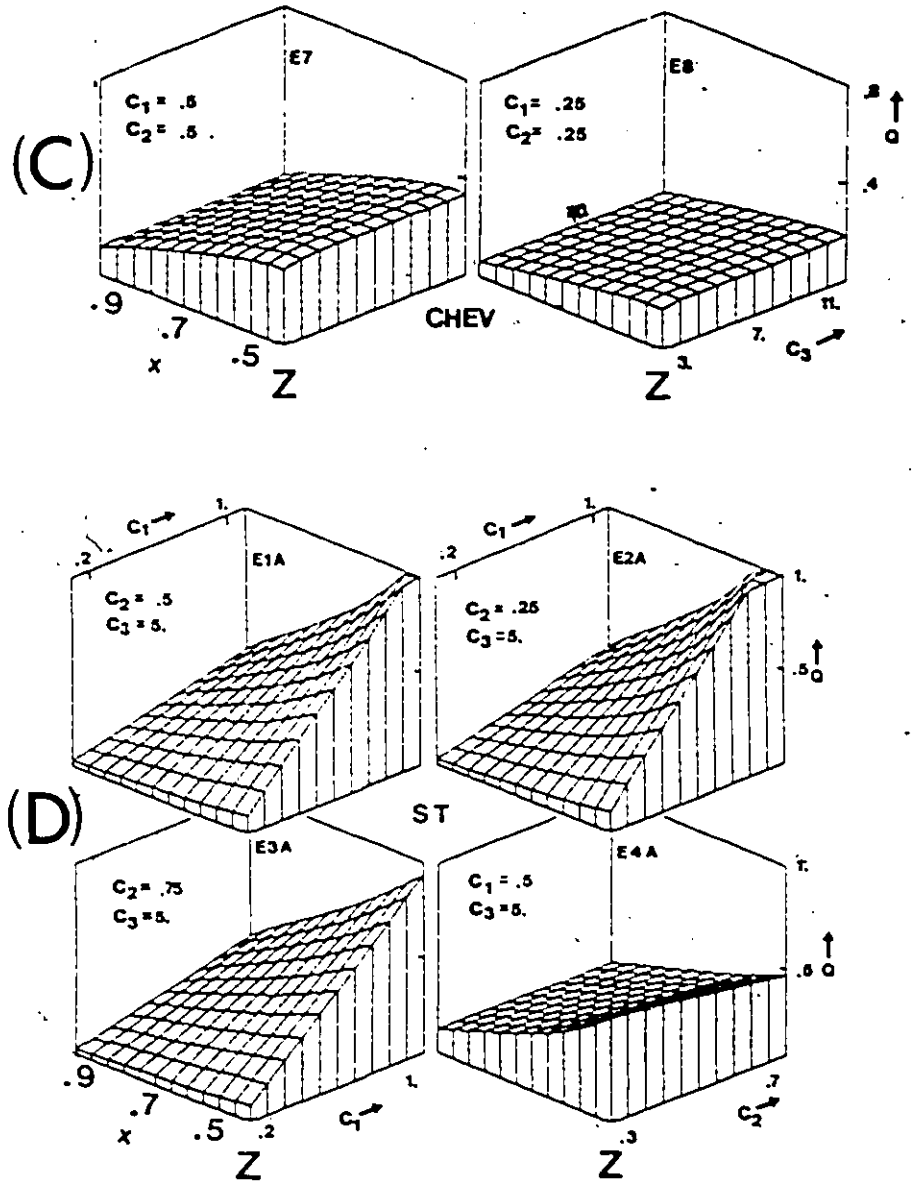

Fig. 3-14 Cont'd : Variation of the relative potential drop Q against the crack length x and : (C) The current probes distance C_3, for CN specimen ; (D) The reference voltage probes distance C_1 and the working voltage probes distance C_2 for ST specimen.

x 0.6 to 0.7

		CONSTANTS		VARIABLES	S - ΔQ/Δx			R - ΔQ/Q		
	FIGURE	↓C_3	↓C_2	→C_1	0.1	0.6	1.0	0.1	0.6	1.0
I	A/E2	5.0	0.25		0.09	0.56	0.91	0.153	0.156	0.156
	A/E1	5.0	0.50		0.08	0.50	0.83	0.143	0.147	0.146
	A/E3	5.0	0.75		0.08	0.42	0.71	0.145	0.133	0.145
	FIGURE #	↓C_3	↓C_1	→C_2	0.25	0.50	0.75	0.25	0.50	0.75
II	B/E5	5.0	0.25		0.23	0.21	0.18	0.154	0.148	0.136
	B/E4	5.0	0.50		0.47	0.42	0.35	0.157	0.148	0.133
	B/E6	5.0	0.75		0.70	0.62	0.53	0.156	0.146	0.134
	FIGURE #	↓C_1	↓C_2	→C_3	3.0	7.0	11.0	3.0	7.0	11.0
III	C/E7	0.5	0.5		0.41	0.42	0.42	0.158	0.160	0.160
	C/E8	0.25	0.25		0.22	0.23	0.23	0.161	0.168	0.168

Fig. 3-14 Cont'd : (E) Sensitivity S and error R parameters for the plots shown in Fig. 3-14 A to C.

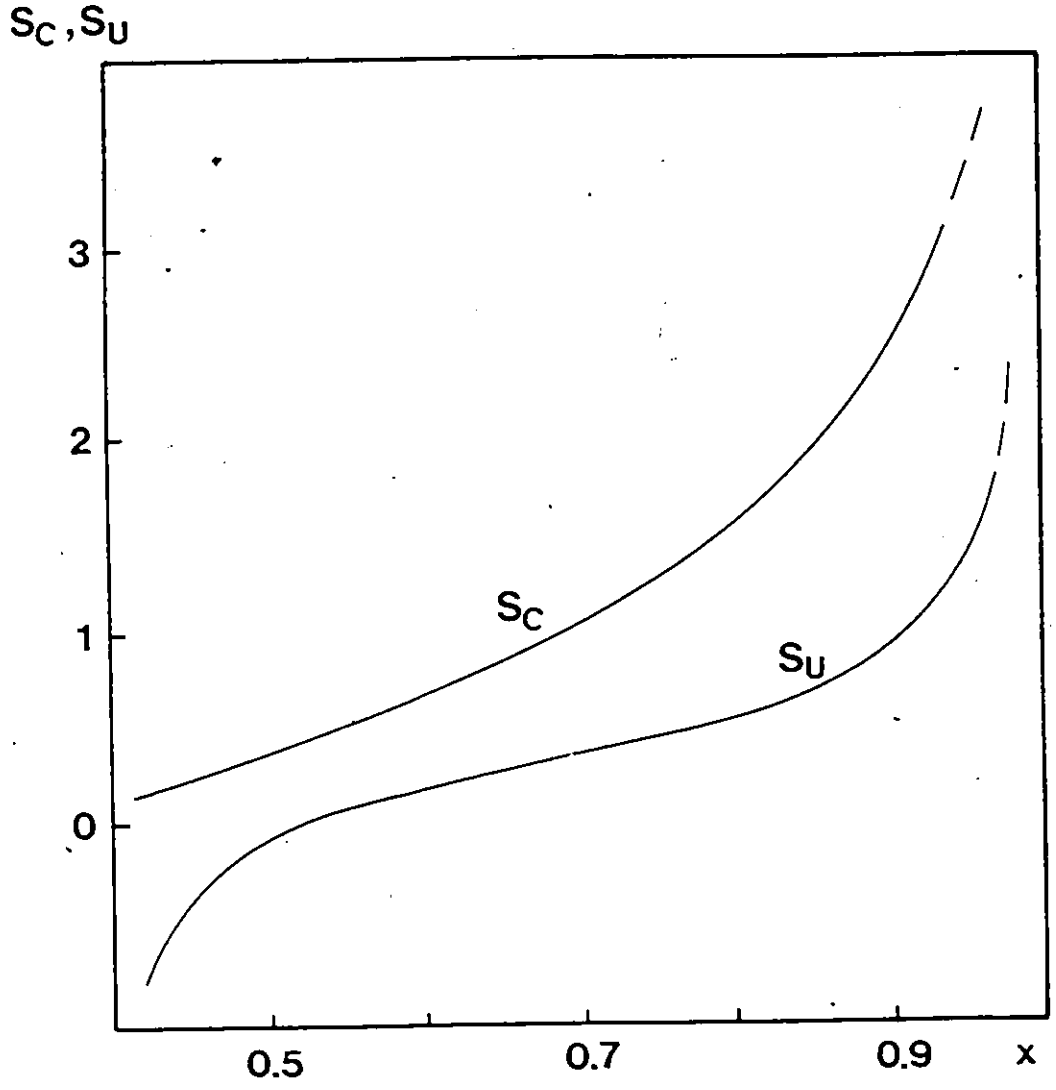

Fig. 3-15 Sensitivity of the compliance technique, S_C, eq.3.54, and the potential drop technique, S_U, eq.3.55, against the crack length, x.

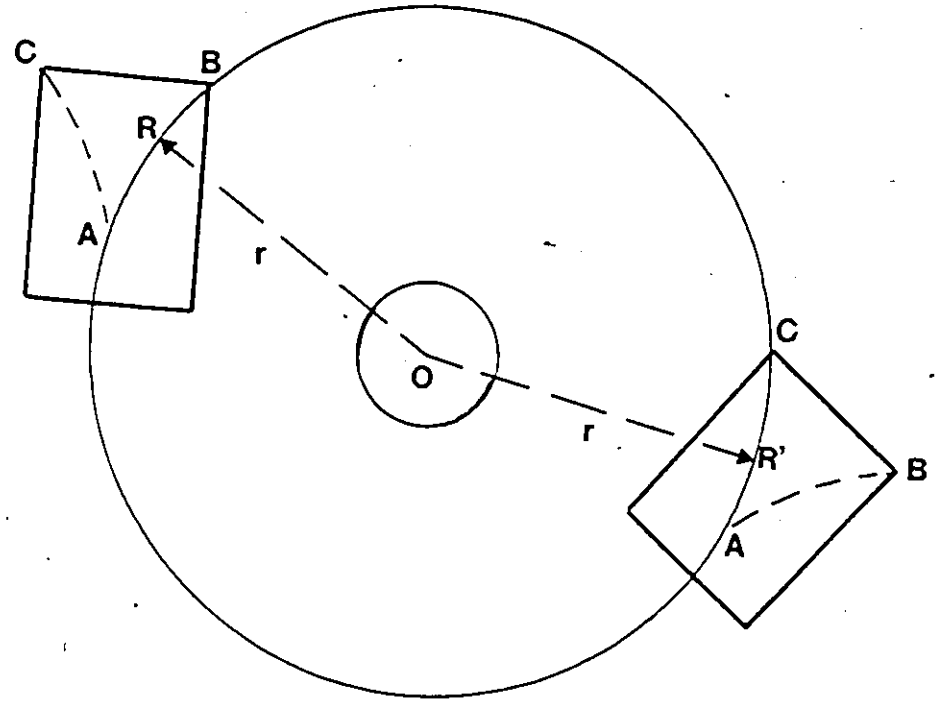

Fig. 4-1 Chevron notch positioning against the cutting blade.

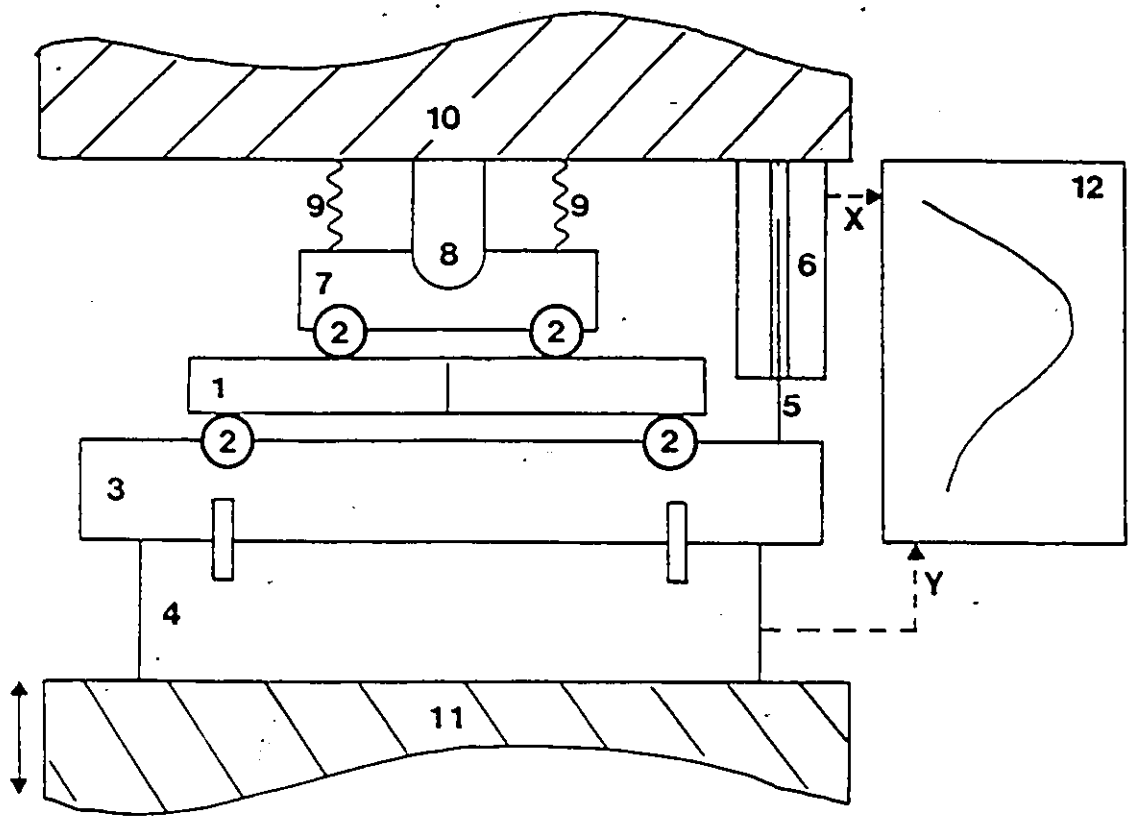

Fig. 4-2 Room temperature bending fixture.

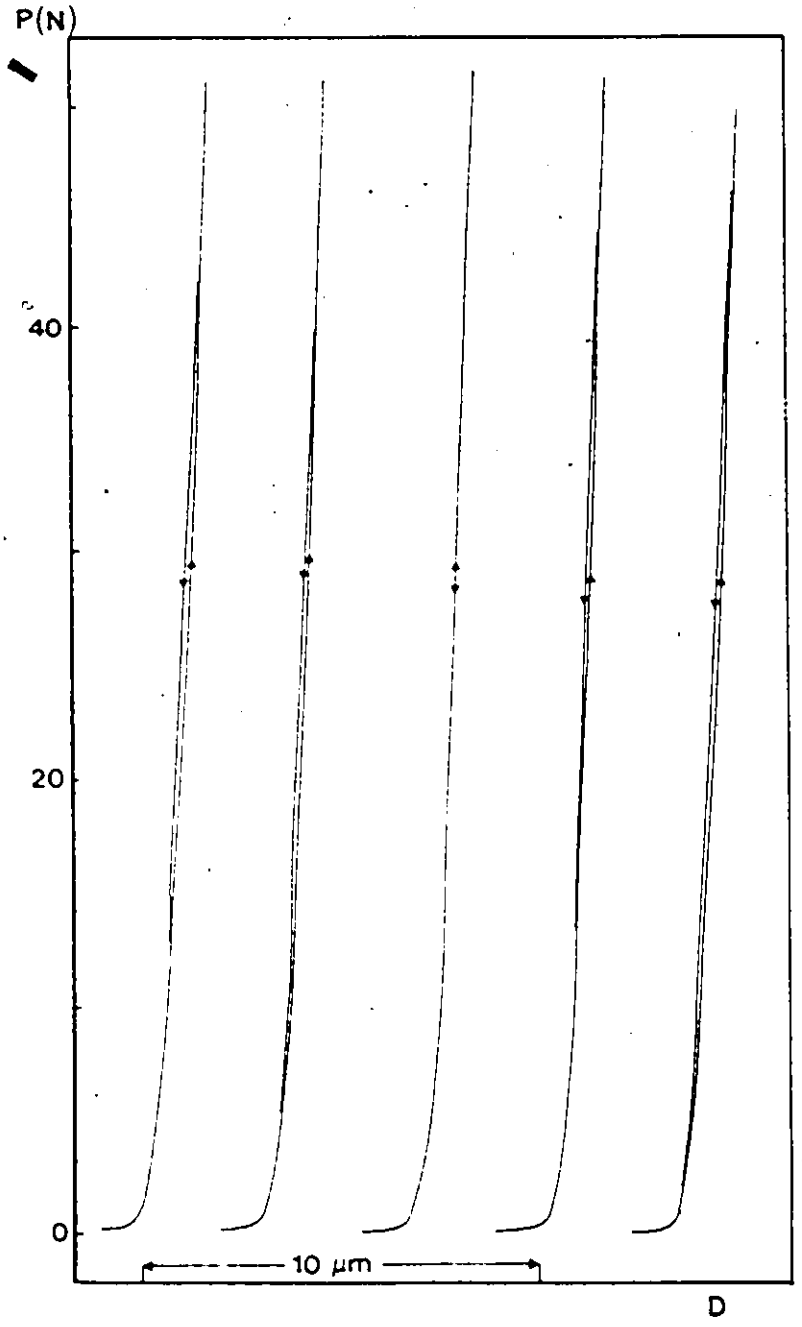

Fig. 4-3 Load-displacement records for the room temperature bending fixture alone.

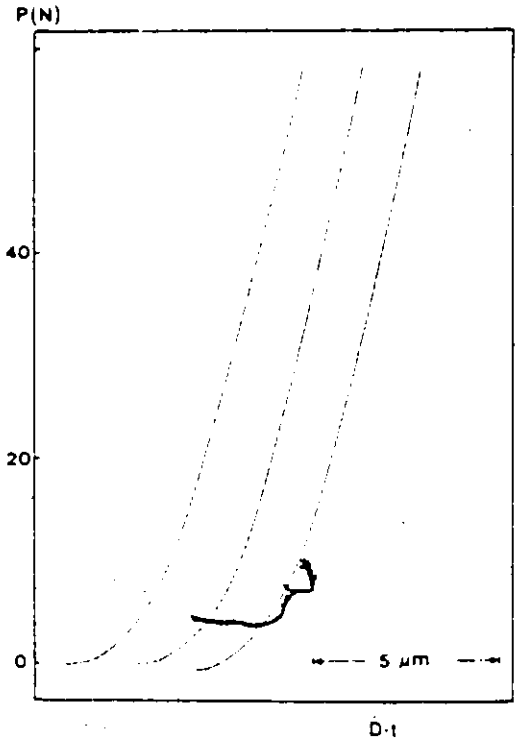

Fig. 4-4 Load-displacement records for the testing machine.

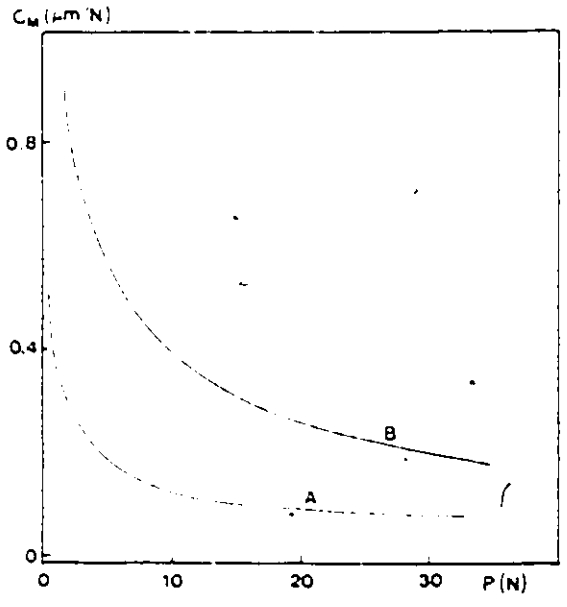

Fig. 4-5 Compliance of the testing systems : (A) Room temperature setup ; (B) Elevated temperature setup.

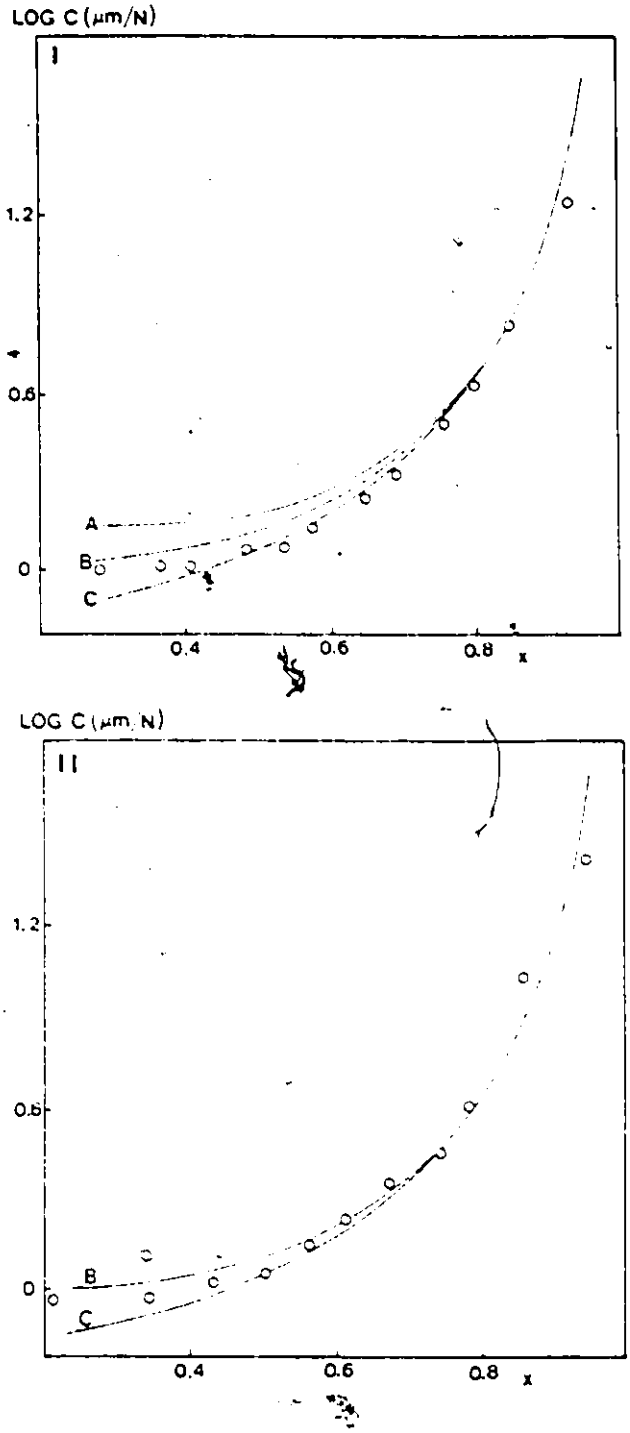

Fig. 4-6 Comparison of measured (dots) and calculated (lines A,B,C) compliance for two graphite CN specimens (I,II).

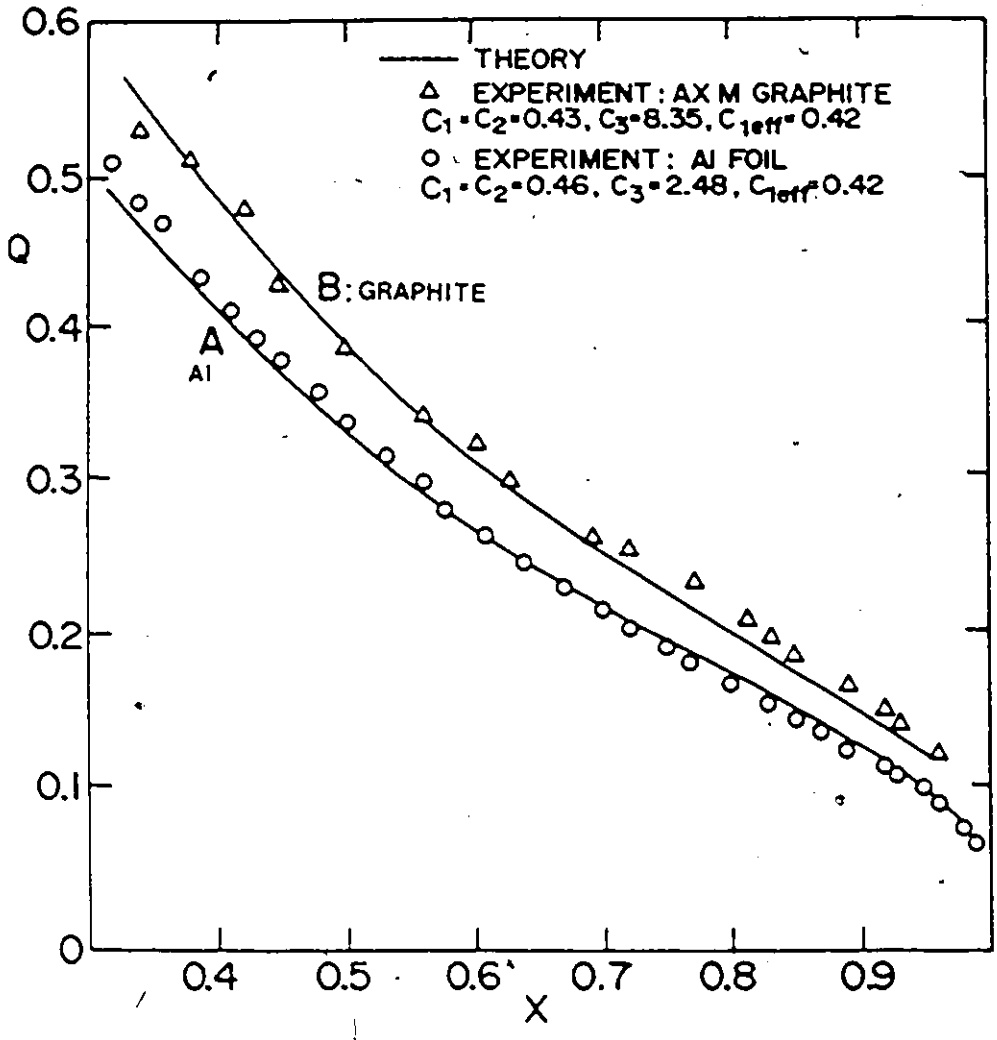

Fig. 4-7 Calibration results of PD method for aluminum and graphite ST specimens.

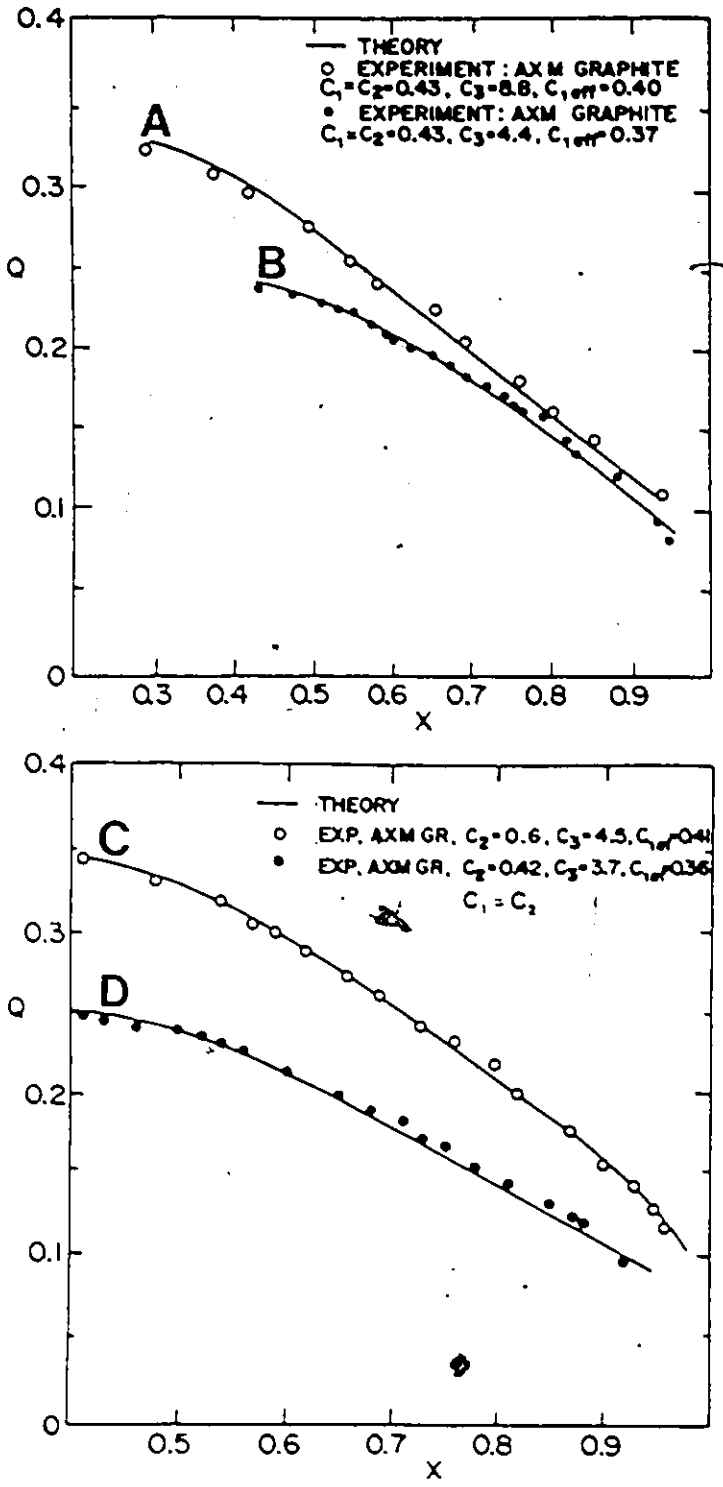

Fig. 4-8 Calibration results of PD method for four graphite CN specimens (A,B,C and D).

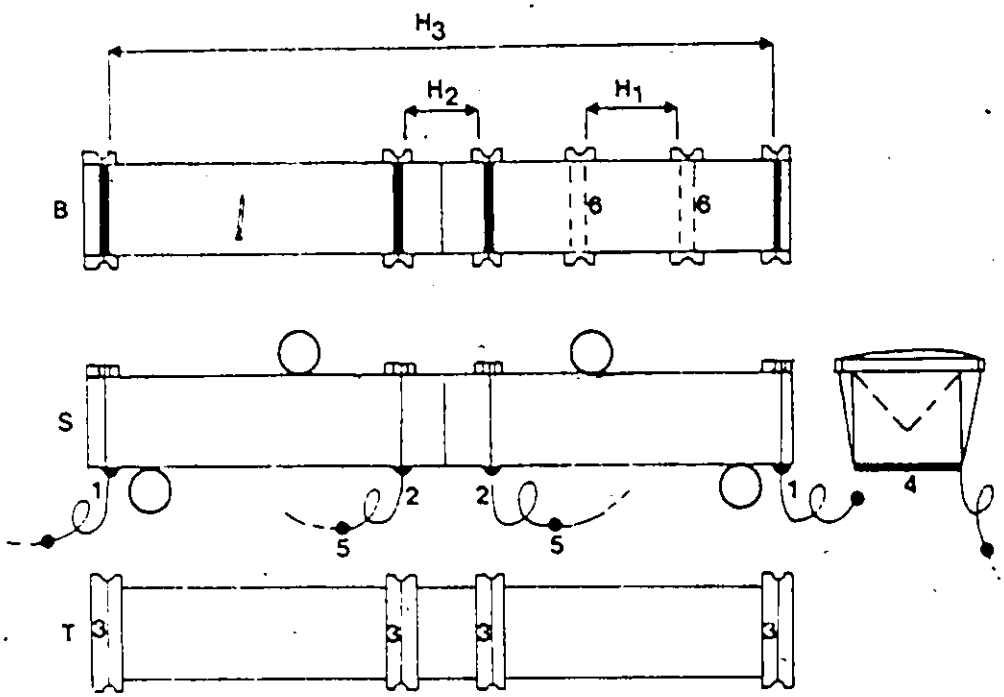

Fig. 4-9 Attachement of the potential and current probes to the specimen's surface.

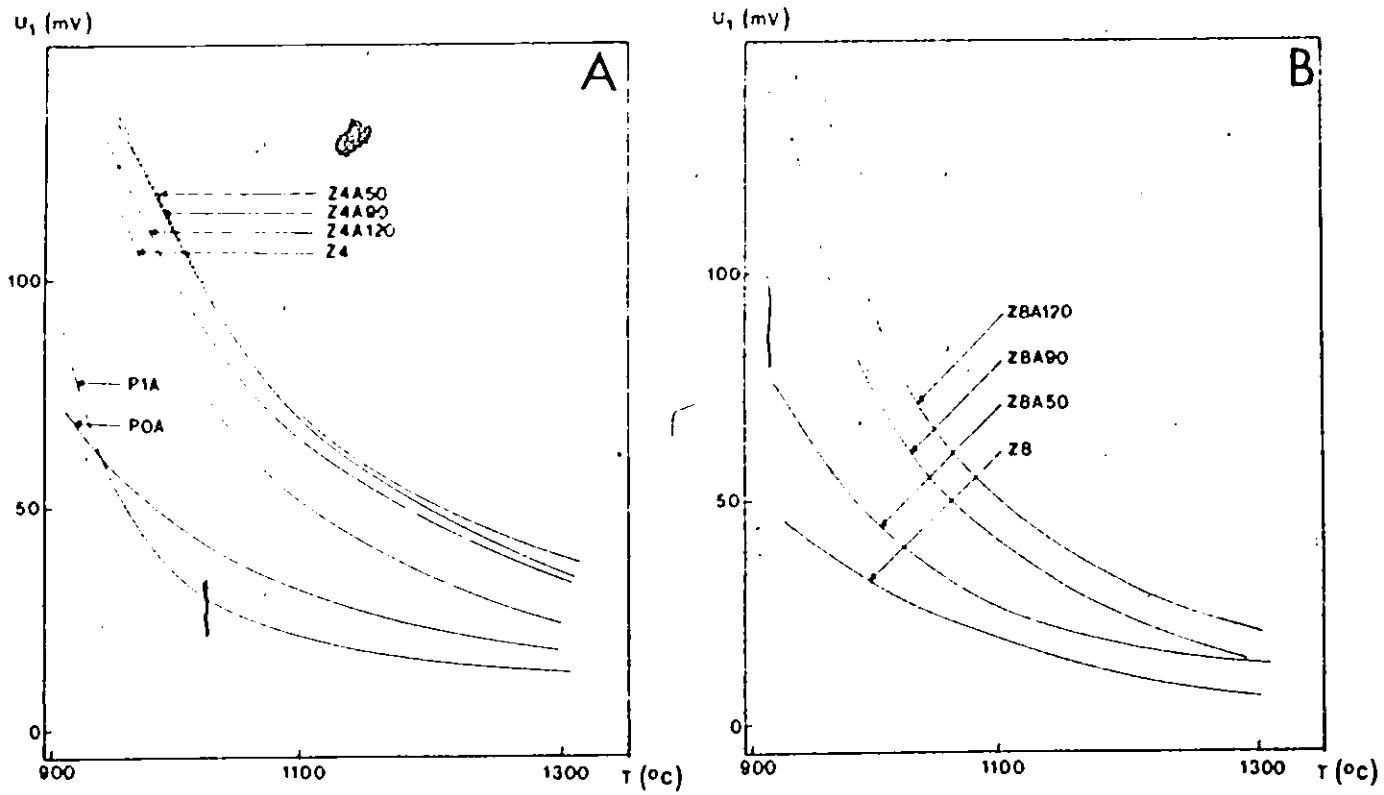

Fig. 4-10 Reference potential drop (U_1) against temperature for materials based on partially (A) and fully (B) stabilized zirconia. i=3mA, dT/dt = 5°C/min.

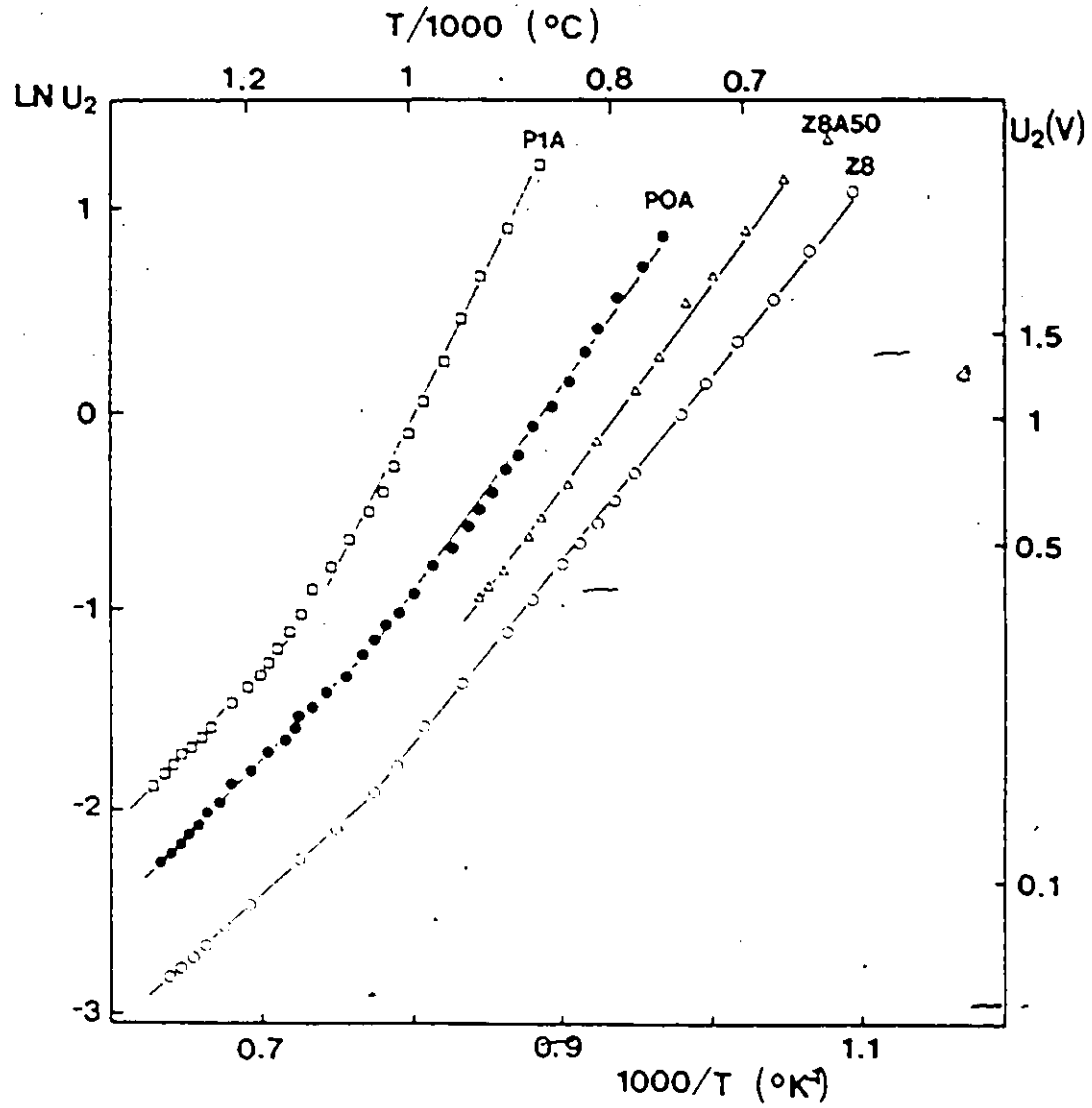

Fig. 4-11 Working potential drop U_2 against inversed absolute temperature for partially (P1A, POA) and fully (Z8, Z8A50) stabilized zirconia ceramics.

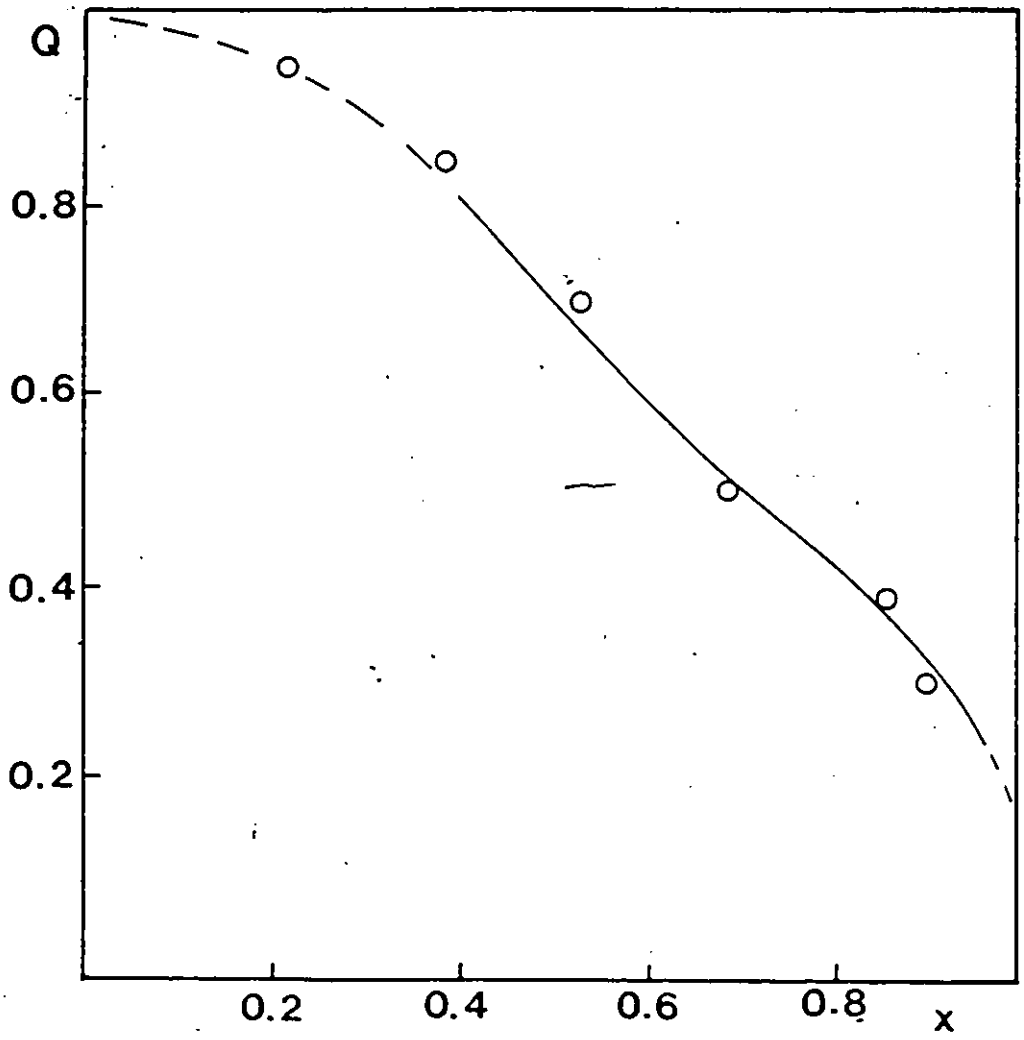

Fig. 4-12 Experimental calibration (dots) and numerical (line) results for PD method (PSZ-ST specimen at 700°C).

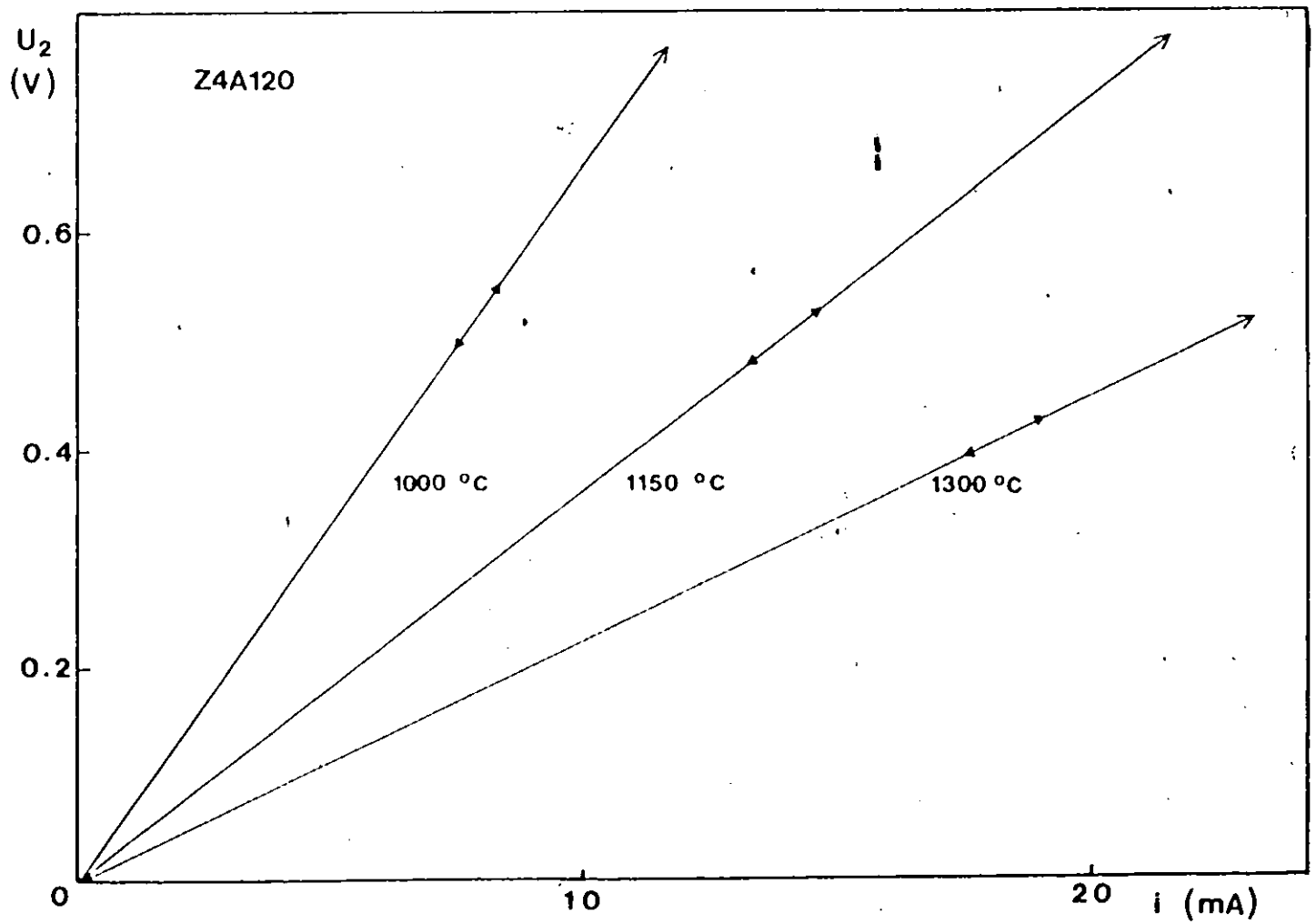

Fig. 4-13 Linear dependence of the potential drop U_2 against applied current for Z4A120 specimen (the linearity is maintained at least up to i=40 mA).

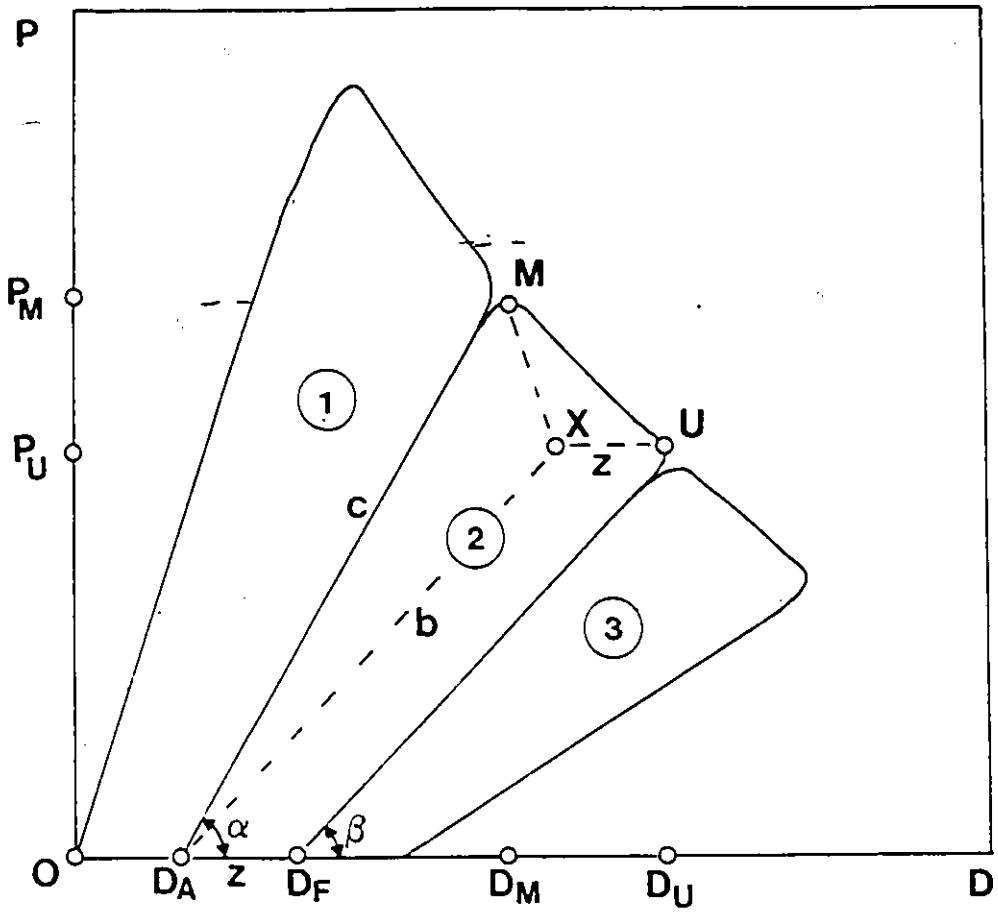

Fig. 4-14 Schematic loading-fracture-unloading (LFU) record and method of the fracture energy determination for general brittle nonelastic material.

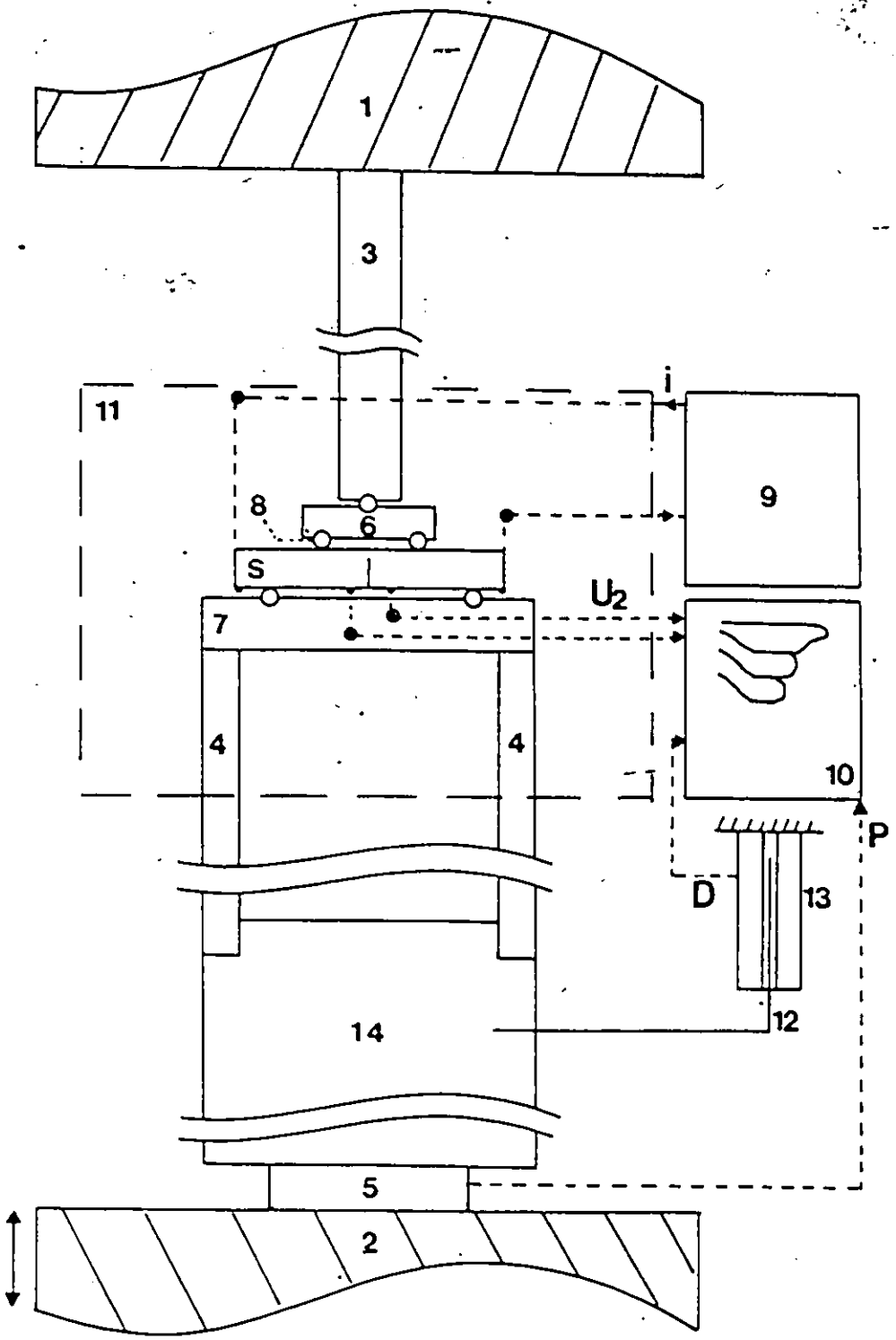

Fig. 4-15 High-temperature loading fixture.

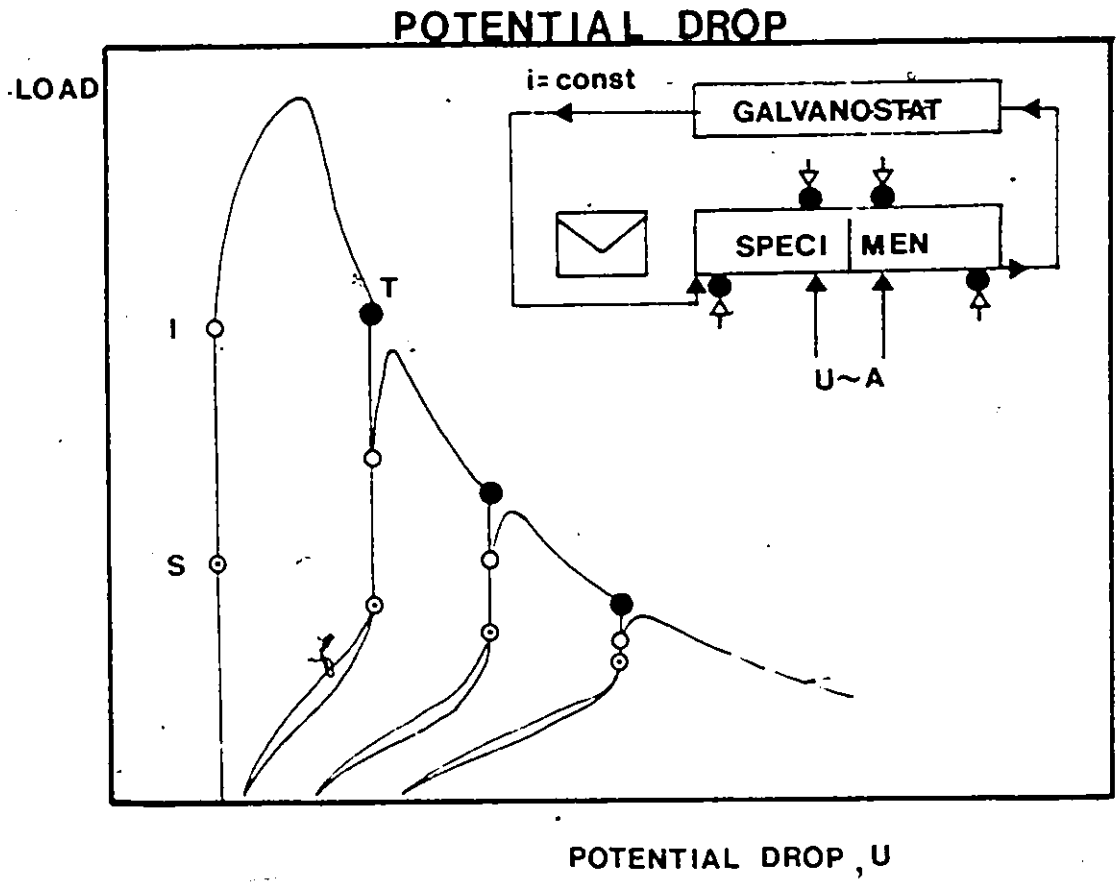

Fig. 4-16 Schematic load against potential drop record for LFU experiment.

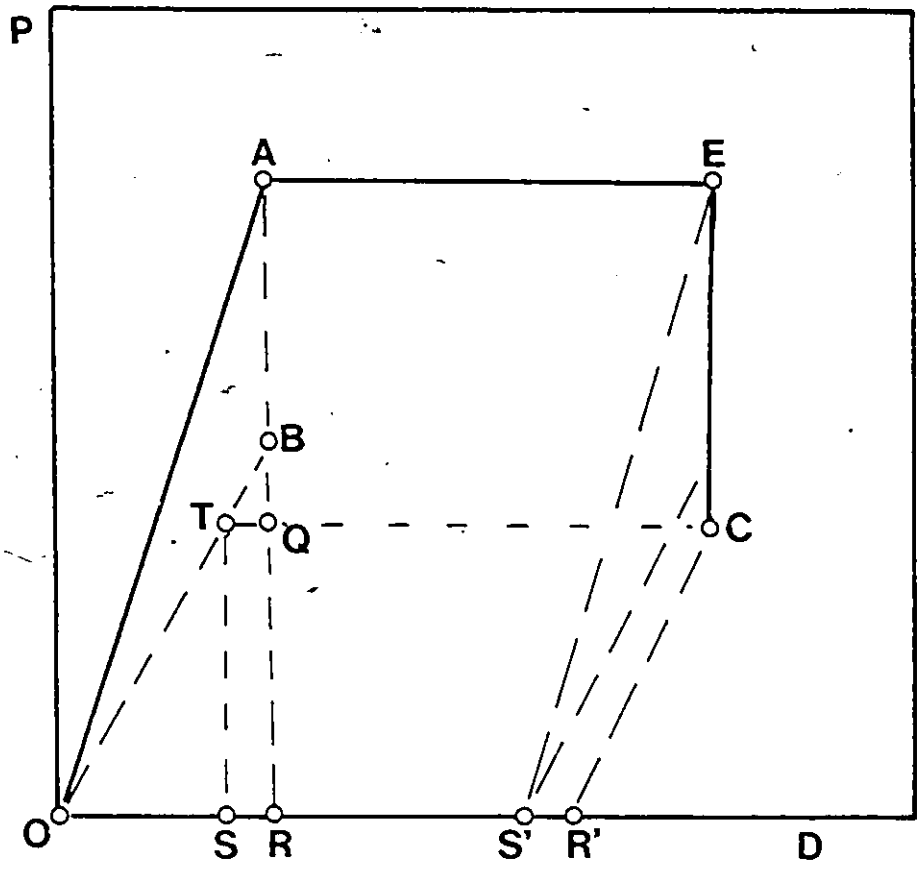

Fig. 4-17 Energy interchange for linear, fixed displacement unloading of an elastic-plastic elastic system, [166].

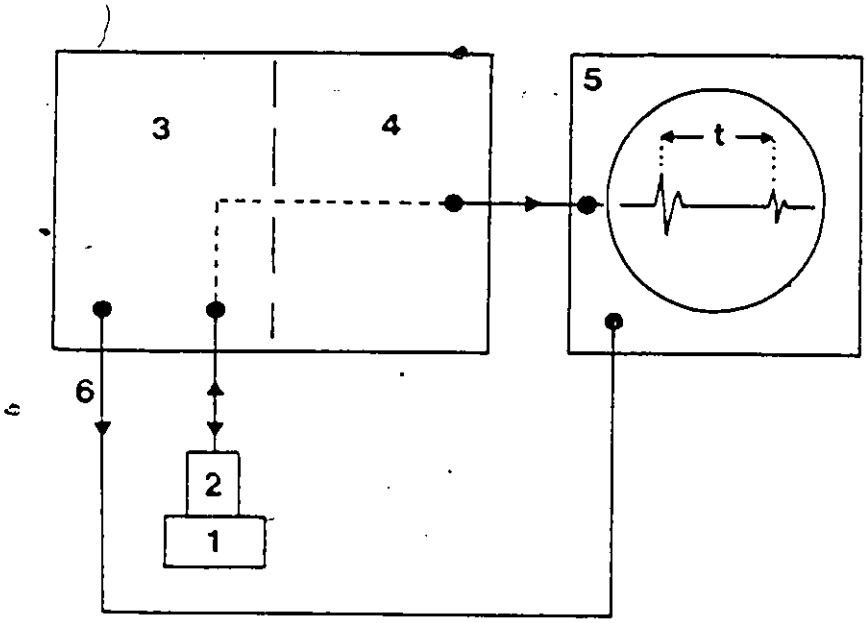

Fig. 4-18 Schematic for the ultrasonic wave transit time t measurement.

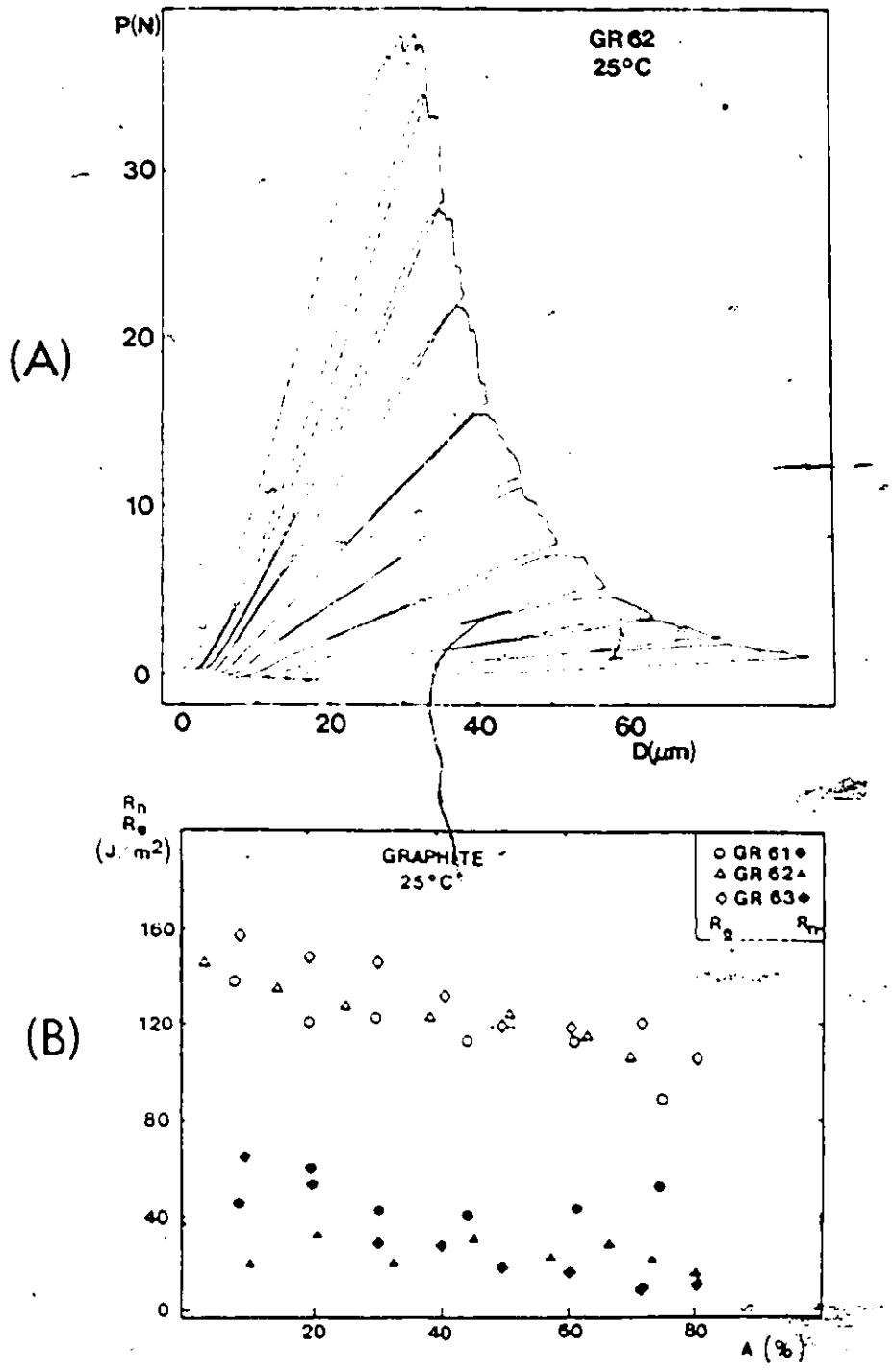

Fig. 4-19 Fracture testing results for graphite : (A) Load vs. displacement LFU diagram ; (B) Resistance to fracture R_e and R_n against fracture area.

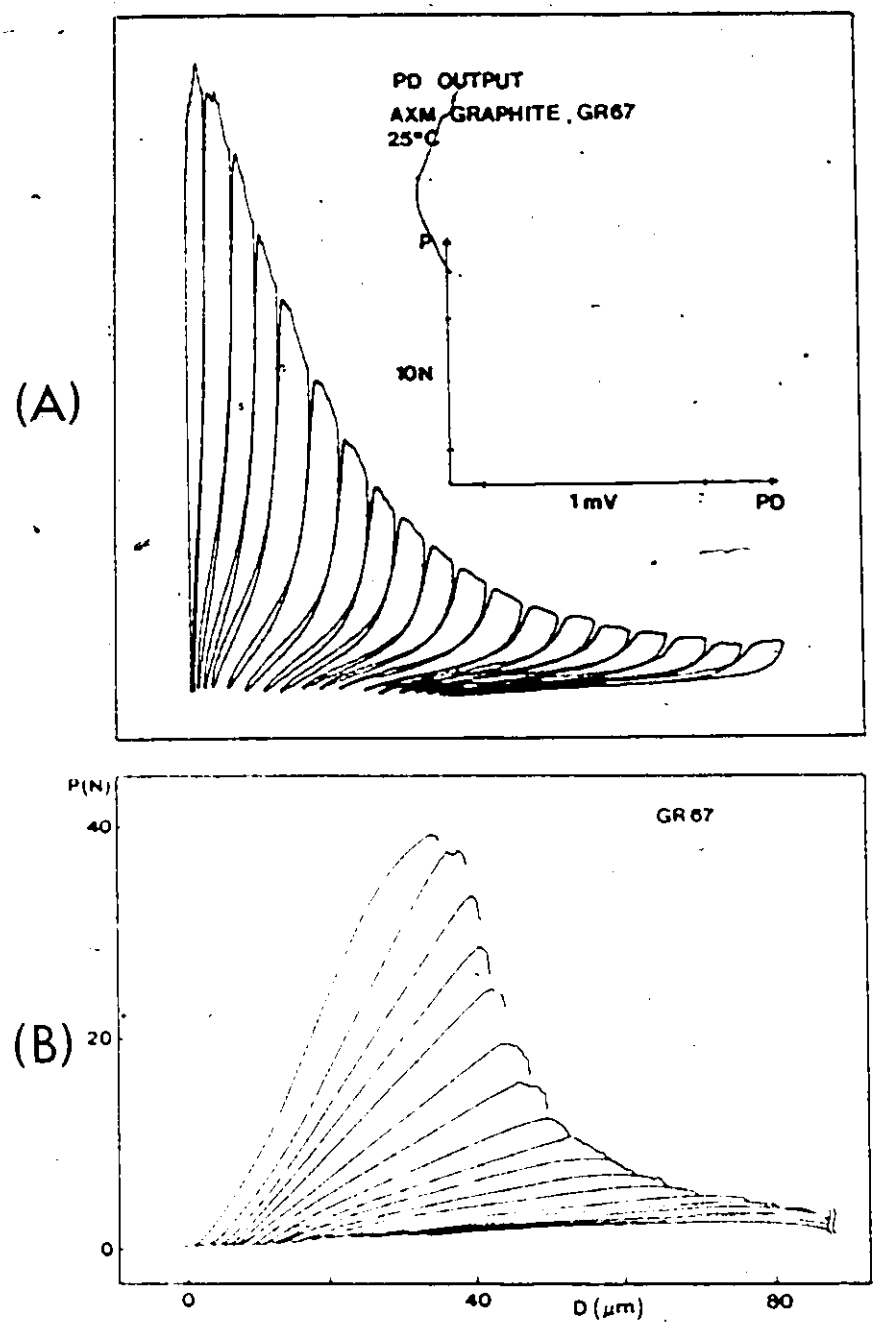

Fig. 4-20 Simultaneous results of Potential Drop and Compliance Analysis for fracture testing of graphite specimen #67, at i=200 mA :(A) Load vs. potential drop LFU diagram;(B) Load vs. displacement LFU diagram; (C) Crack length determined by PD (x_{PD}) against that determined by CA (x_{CA});(D) Resistance to fracture of graphite, determined simultaneously by PD (closed circles) and CA (open circles). Also are provided results at i=100 mA and i=0 mA, obtained by CA.

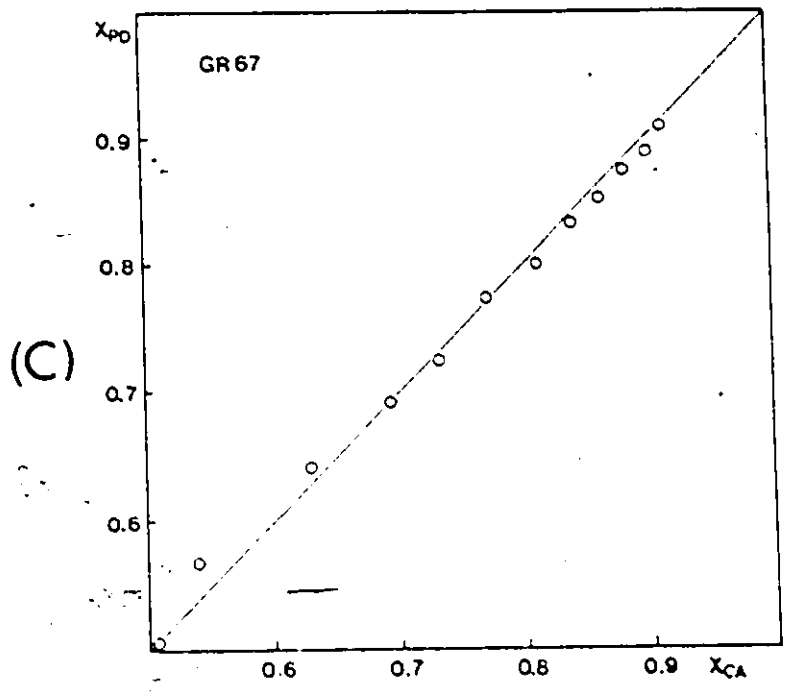

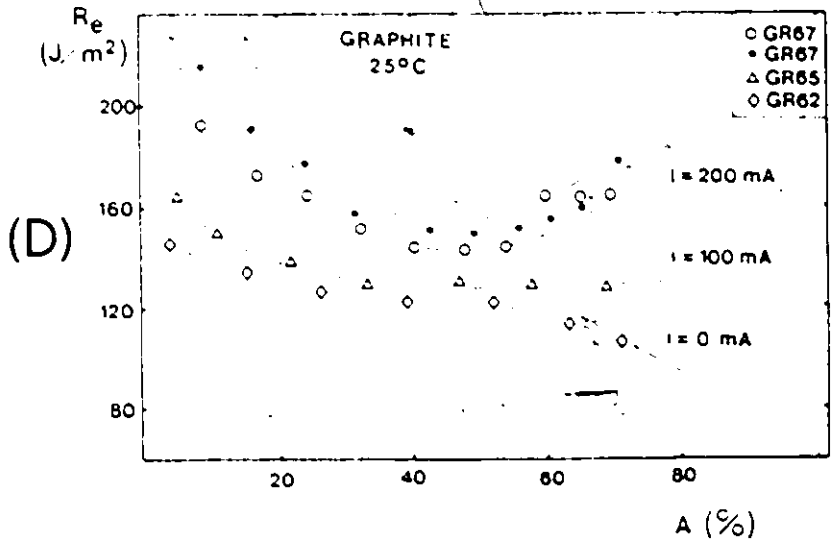

Fig. 4-20 Continued

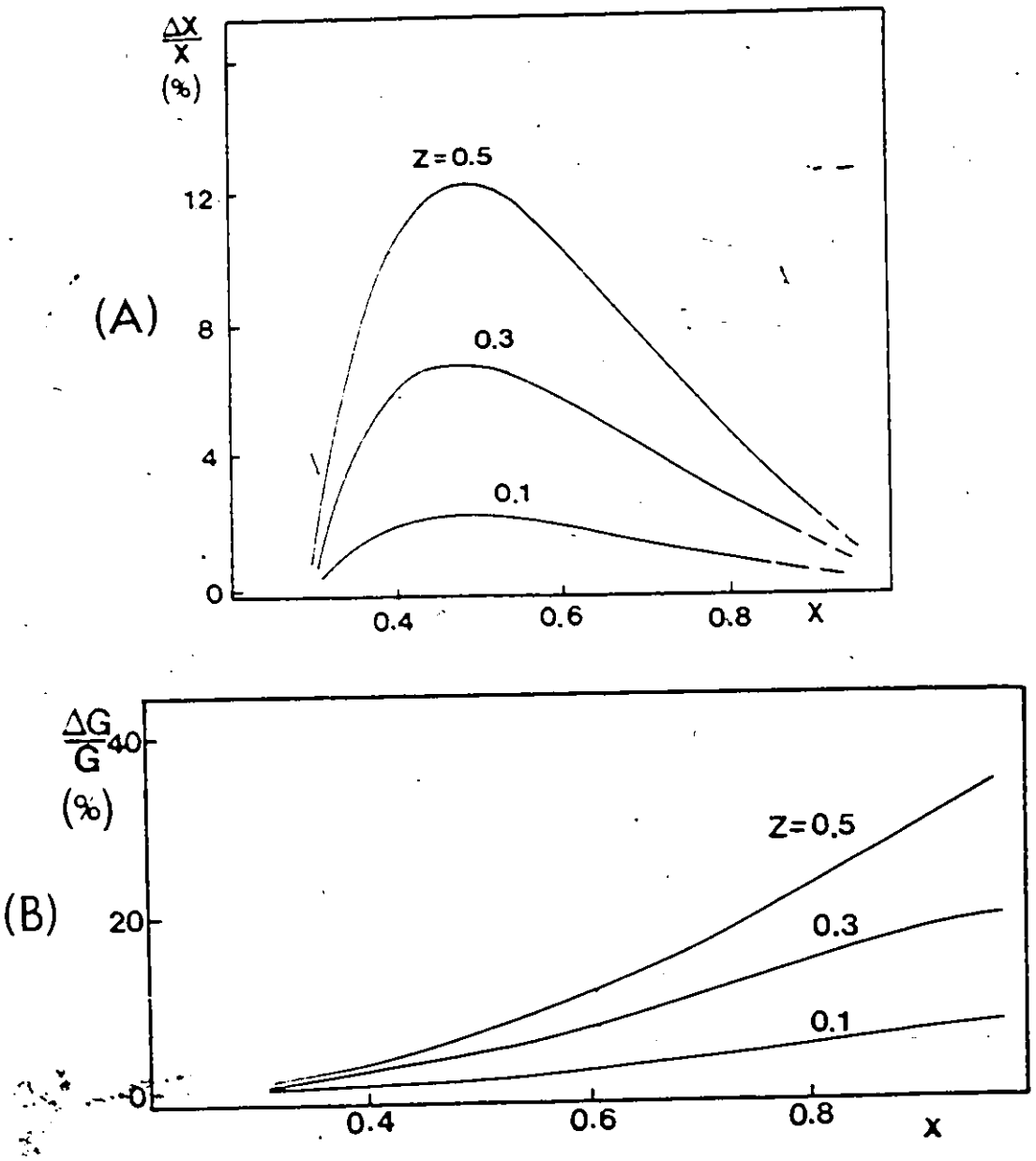

Fig. 4-21 Simulated error $\Delta x/x$ in the crack length determination by Compliance Analysis (A) and resulting relative error in the crack driving force, $\Delta G/G$ (B), at increasing error in the compliance reading $\Delta C/C = Z \cdot (x - x_0)$, $Z = 0.1$; 0.3 ; 0.5. The results are plotted against the crack length.

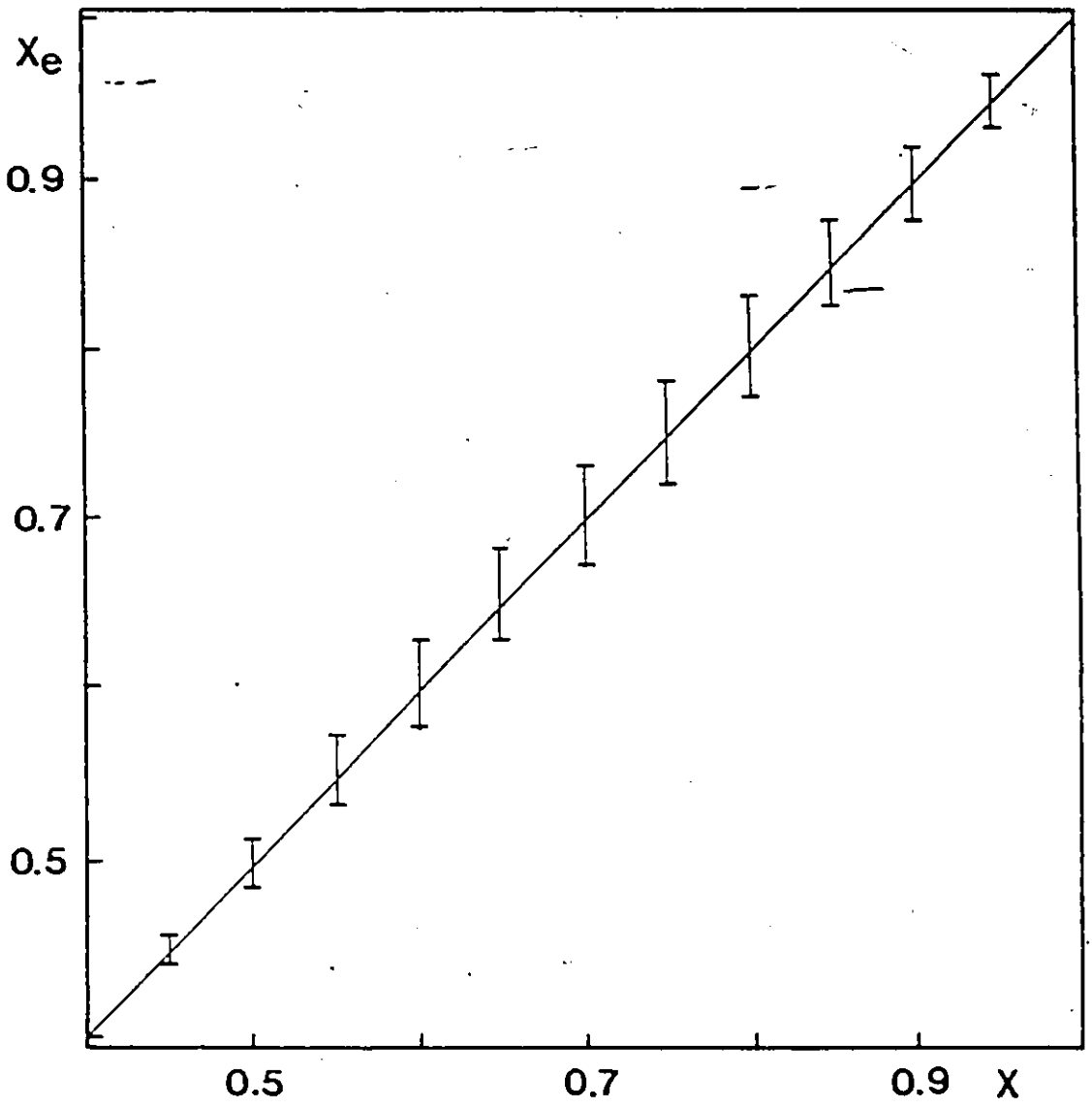

Fig. 4-22 Scatter of the crack length values calculated from PD, x_e, at simulated error $\Delta C_2 = \pm 40\%$, plotted against true crack length x.

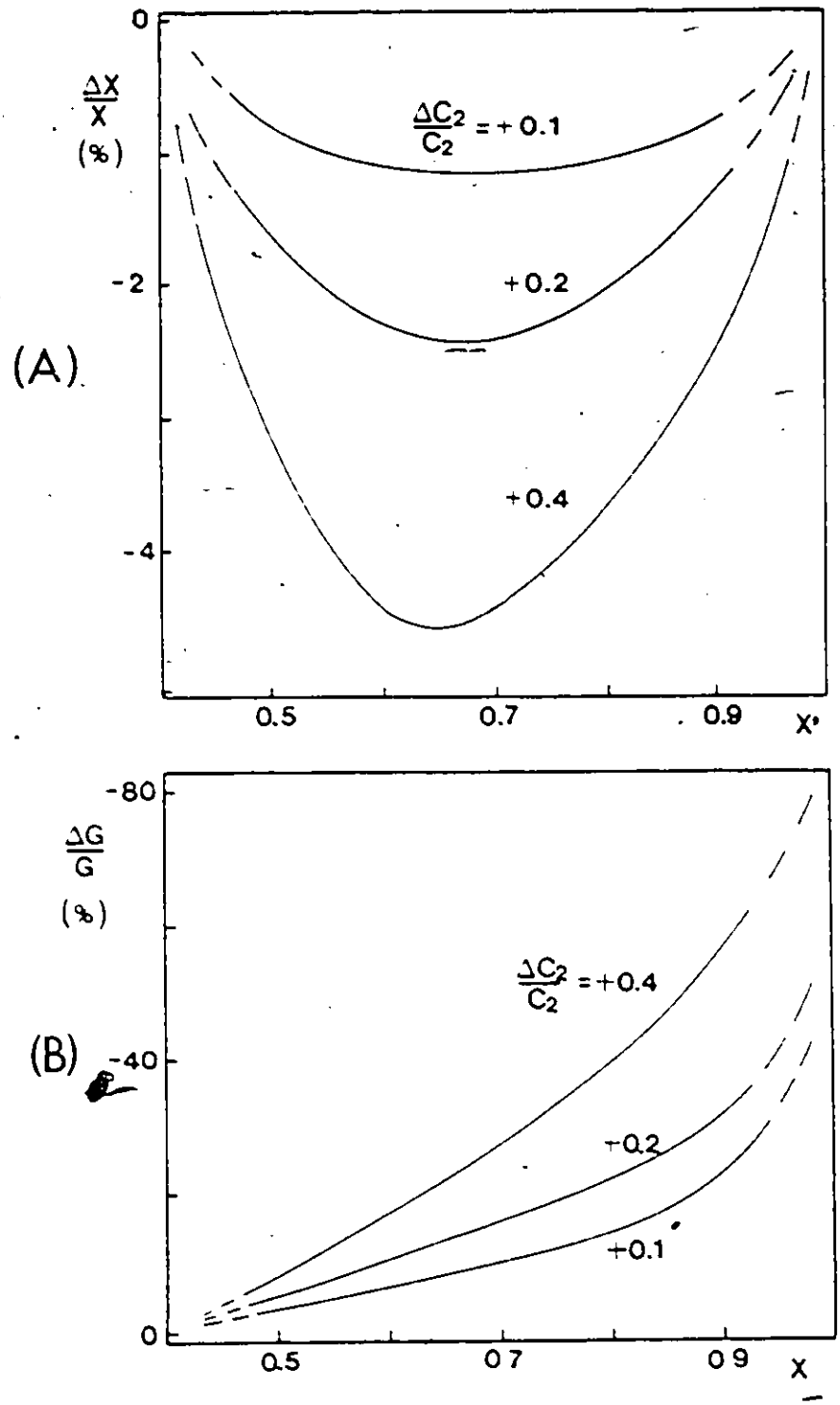

Fig. 4-23 Relative error in the crack length calculation (A) and resulting relative error in the crack driving force, $\Delta G/G$ (B) at uncertainity in the interprobe distance ΔC_2 = 0.1 ; 0.2 ; 0.4. The results are plotted against the crack length.

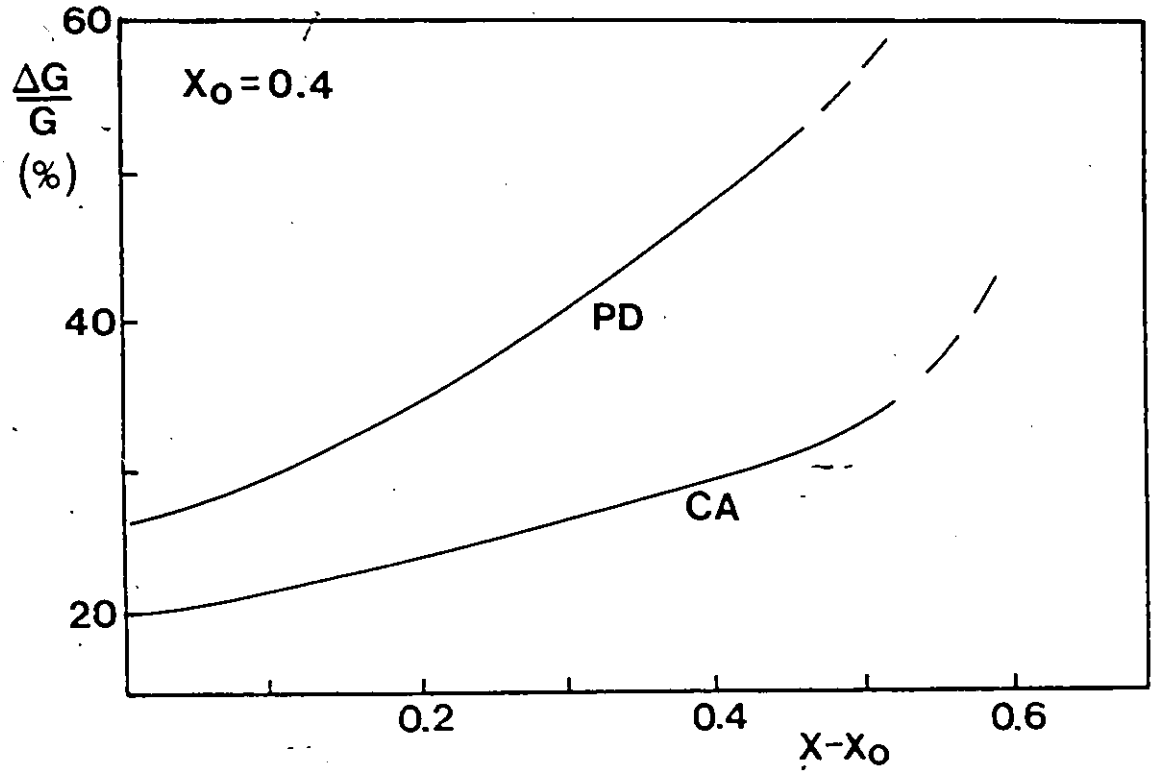

Fig. 4-24 Maximum total error of the crack driving force calculation, $\Delta G/G$, at elevated temperatures by PD technique and at room temperature by CA technique. The data are plotted against the crack length increment for typical specimen of x_o=0.4.

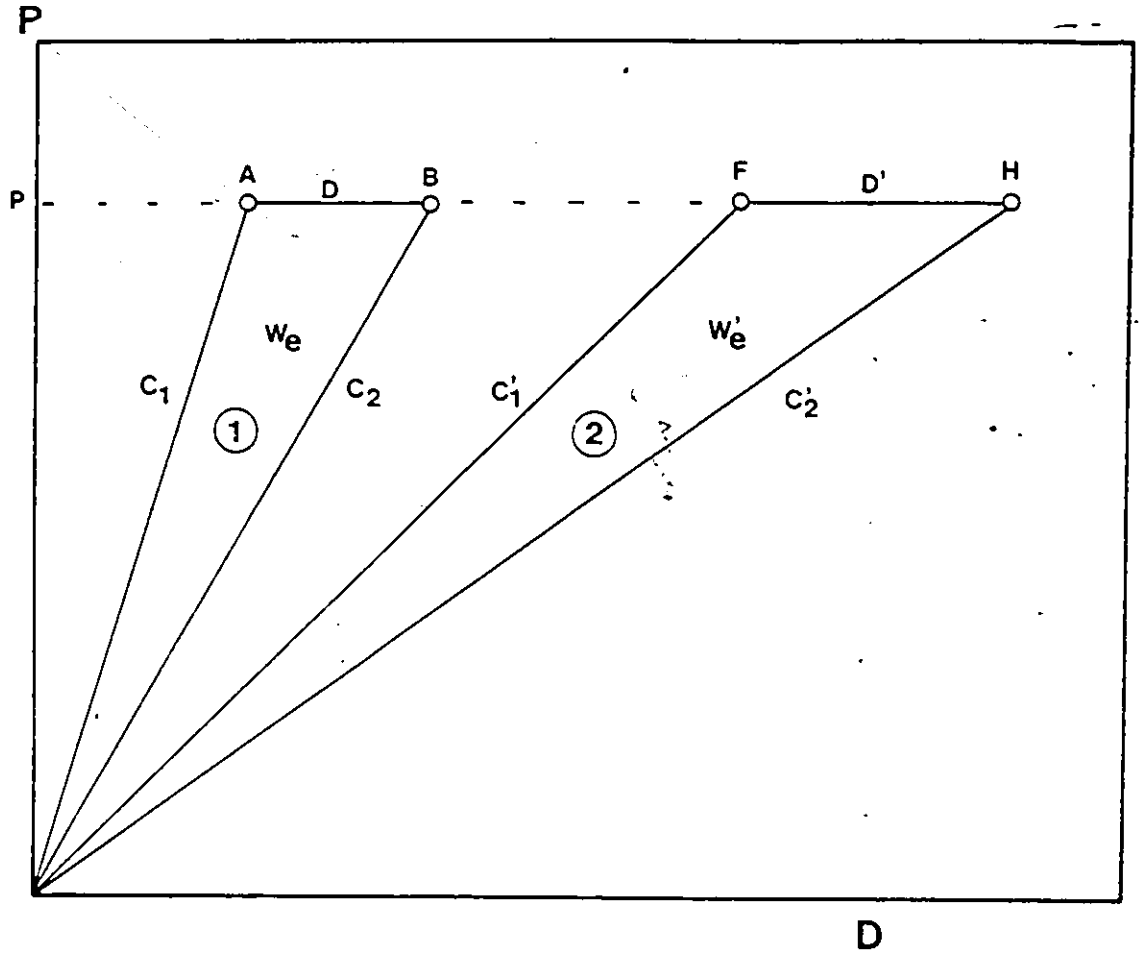

Fig. 4-25 Hypothetical calculated load-displacement graph for one LFU cycle at true (1) and underestimated (2) values of the Young's Modulus.

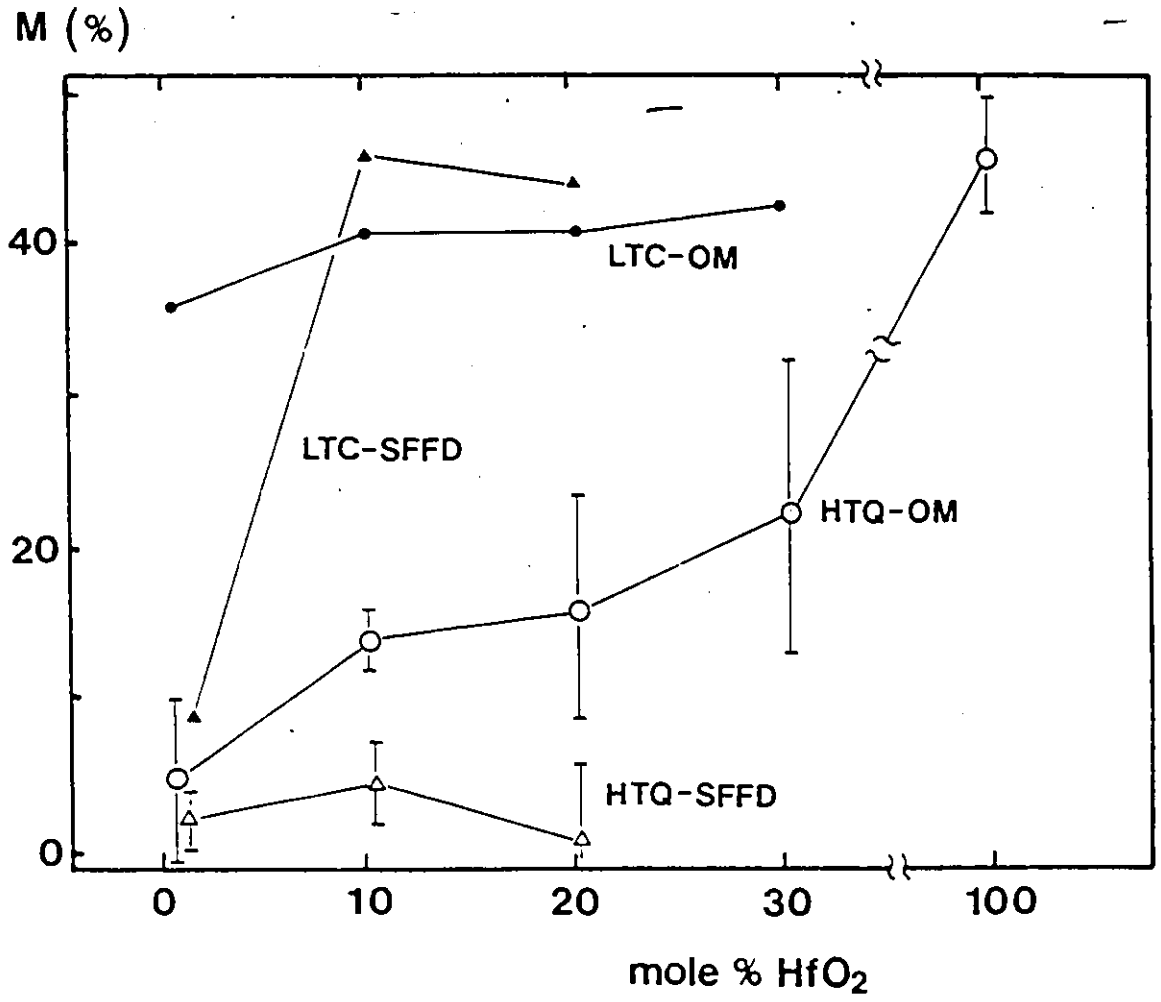

Fig. 5-1 Monoclinic phase content in ZrO_2-HfO_2 solid solutions.

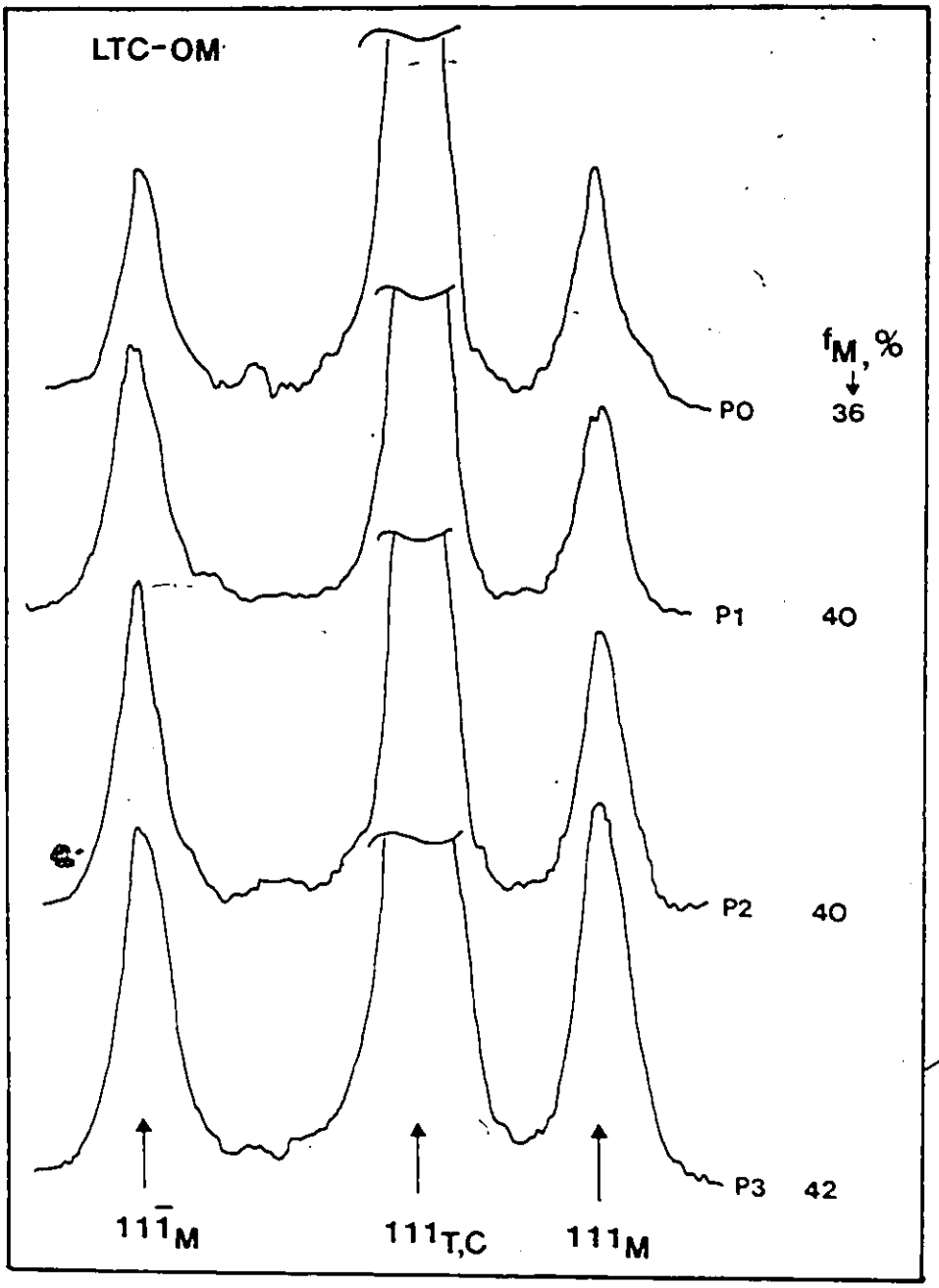

Fig. 5-2 X-ray diffractograms for ZrO_2-HfO_2 solid solutions, obtained in LTC-OM (mixed oxides) route.

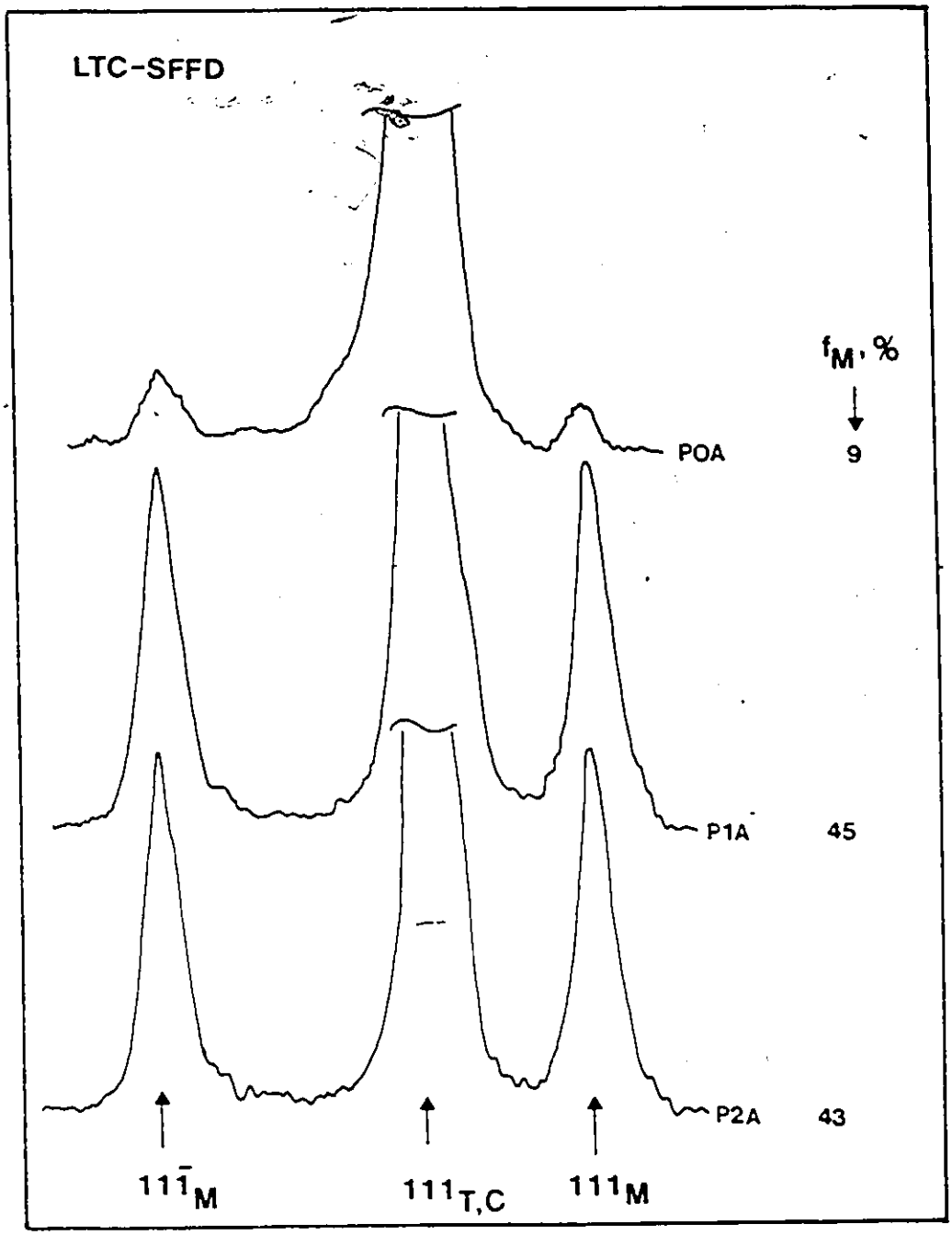

Fig. 5-3 X-ray diffractogram records for ZrO_2-HfO_2 solid solutions, obtained in LTC-SFFD (spray-freezed freeze-dried) route.

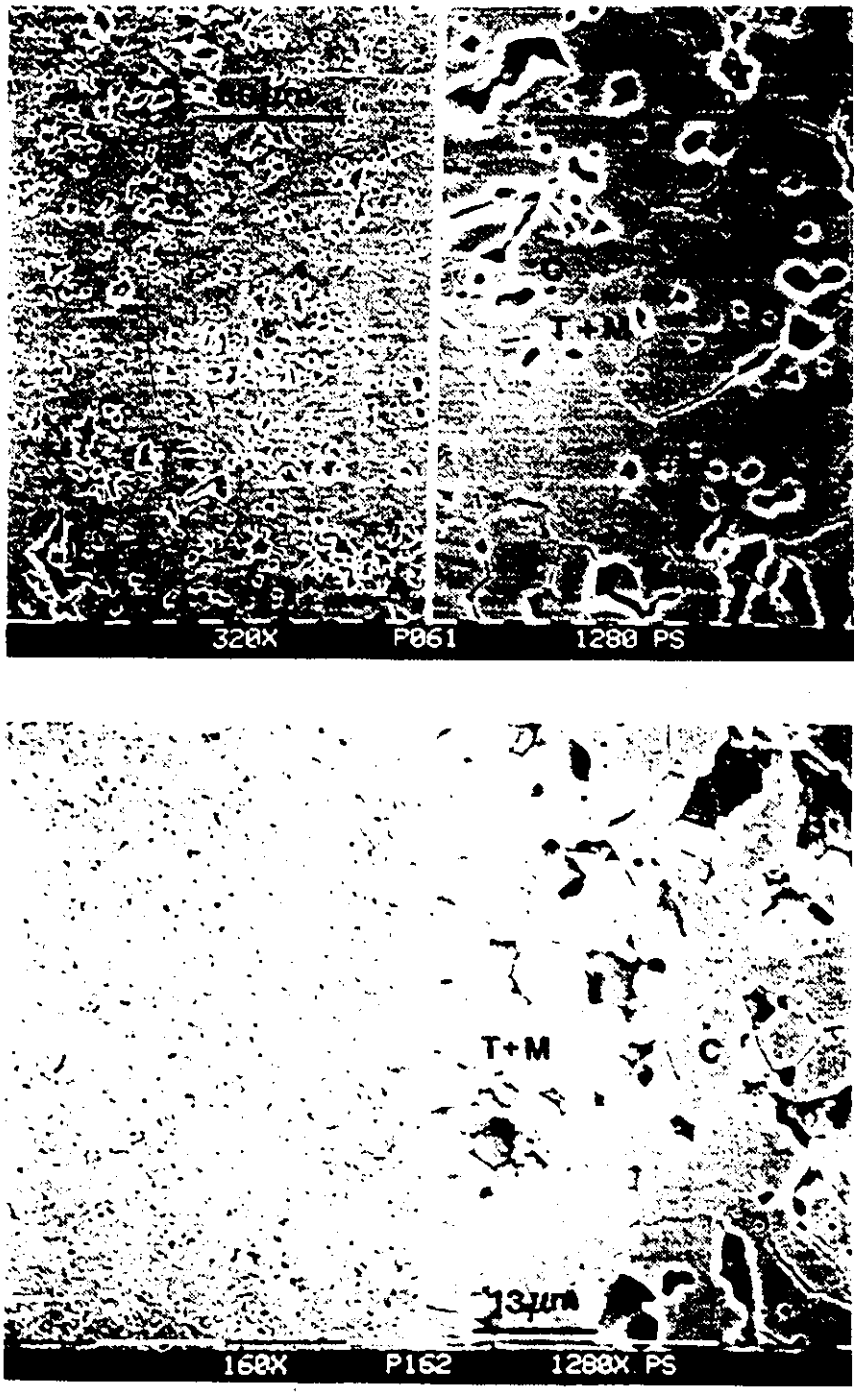

Fig. 5-4. Microstructures of zirconia-hafnia solid solutions:(A) P0 ;(B) P1 ;(C) P2 ;(D) P3.

(C)

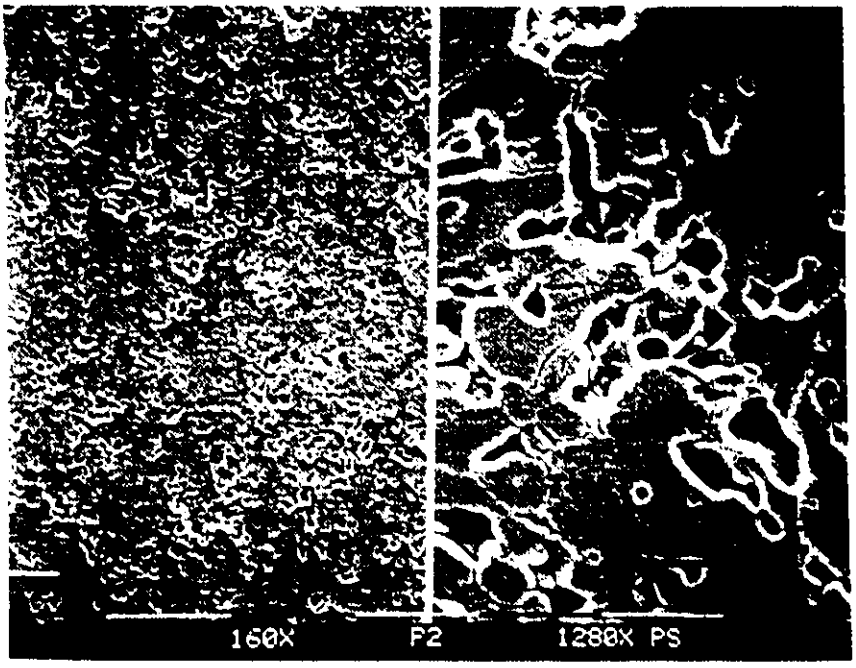

(D)

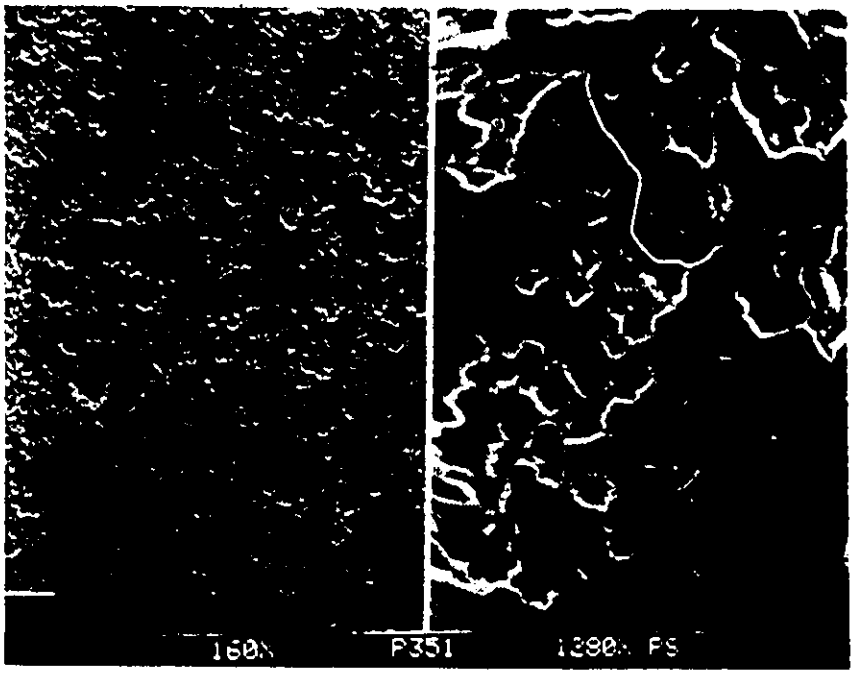

Fig. 5-4 Continued

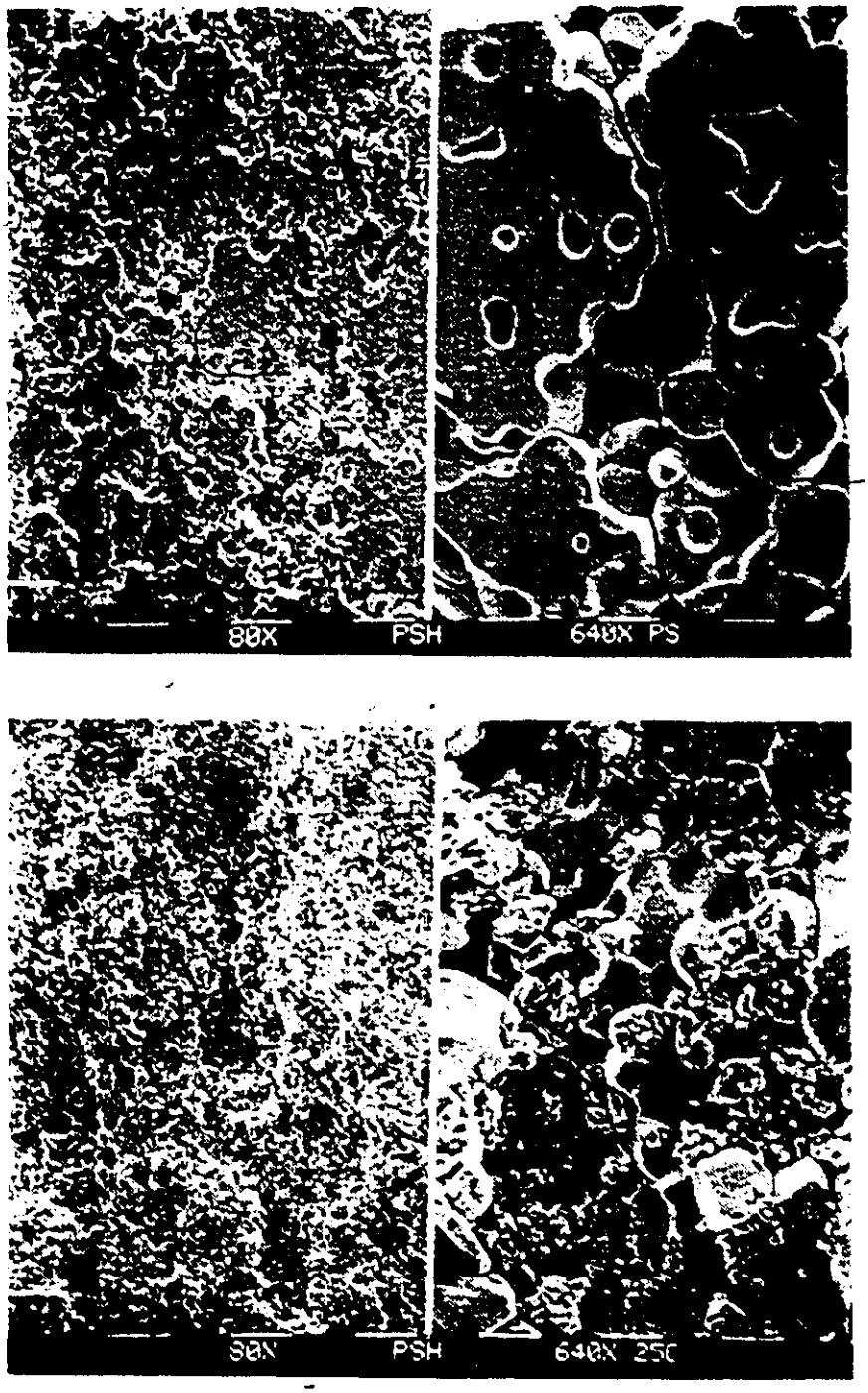

Fig. 5-5 HfO_2 stabilized with 4.5 mole % Y_2O_3 :
(A) Polished section ; (B) Fracture surface.

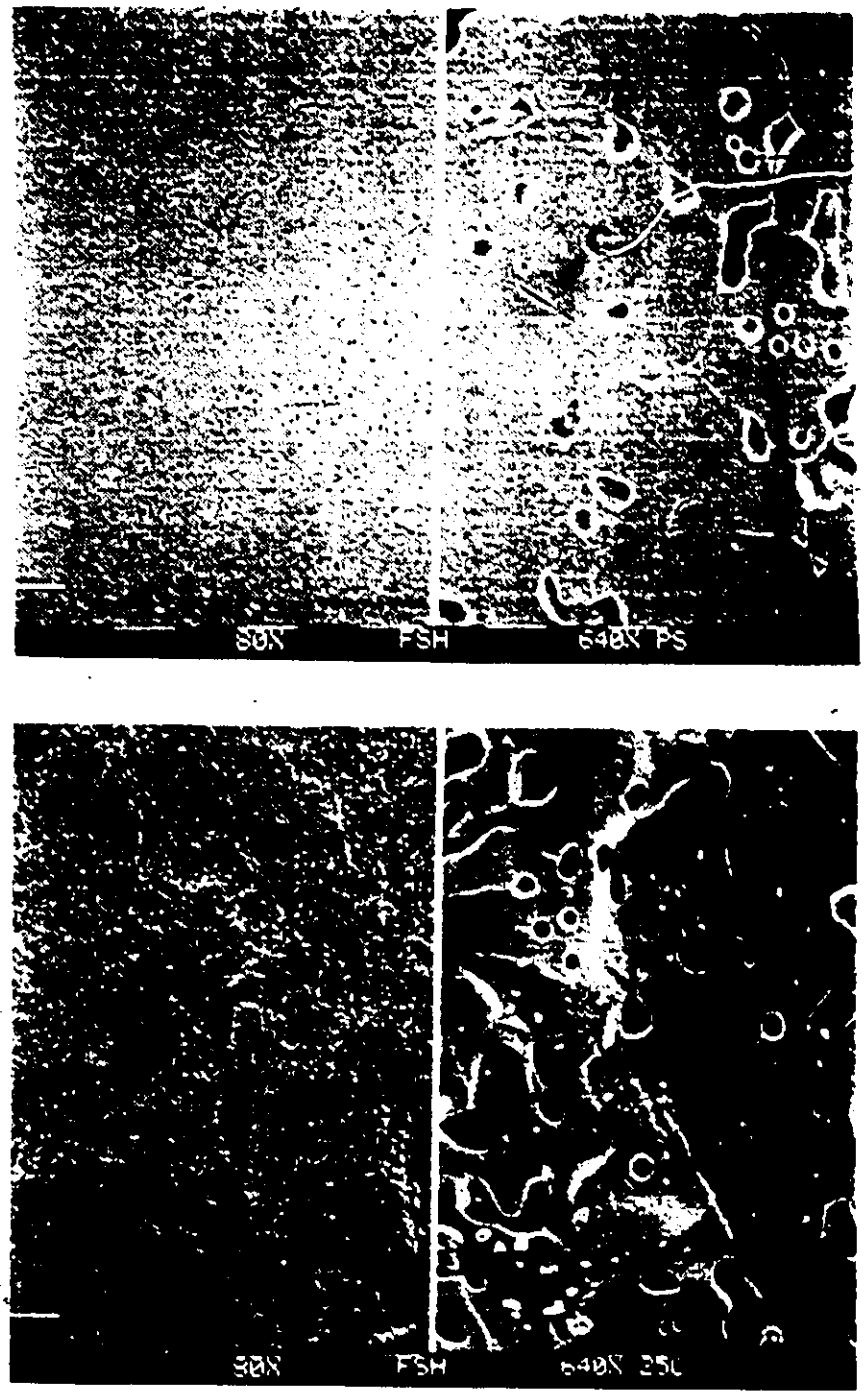

Fig. 5-6 HfO_2 stabilized with 6.9 mole % Y_2O_3 :
(A) Polished section;(B) Fracture surface.

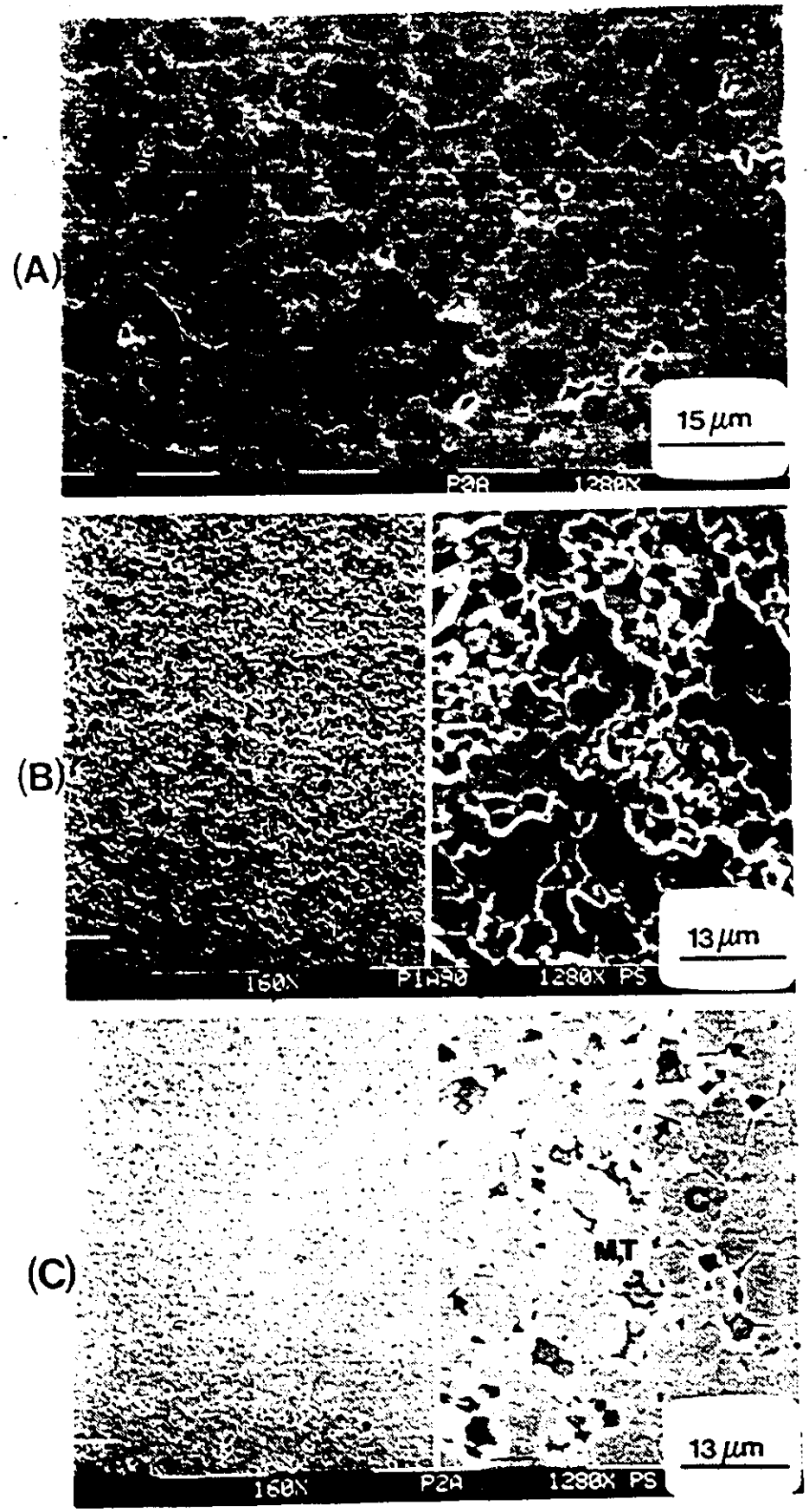

Fig. 5-7 Microstructures of zirconia-hafnia solid solutions: (A) P0A ;(B) P1A ;(C) P2A.

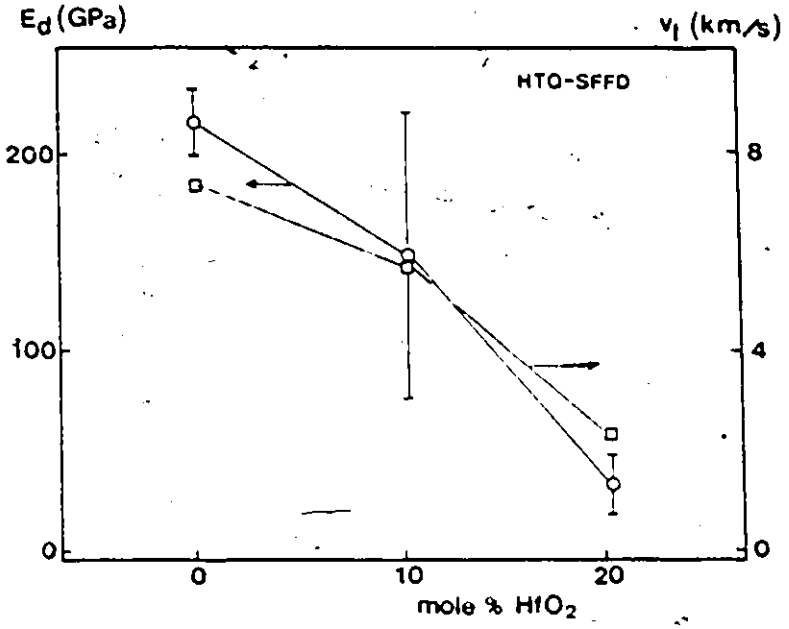

Fig. 5-8 Elastic properties of HTQ-SFFD materials.

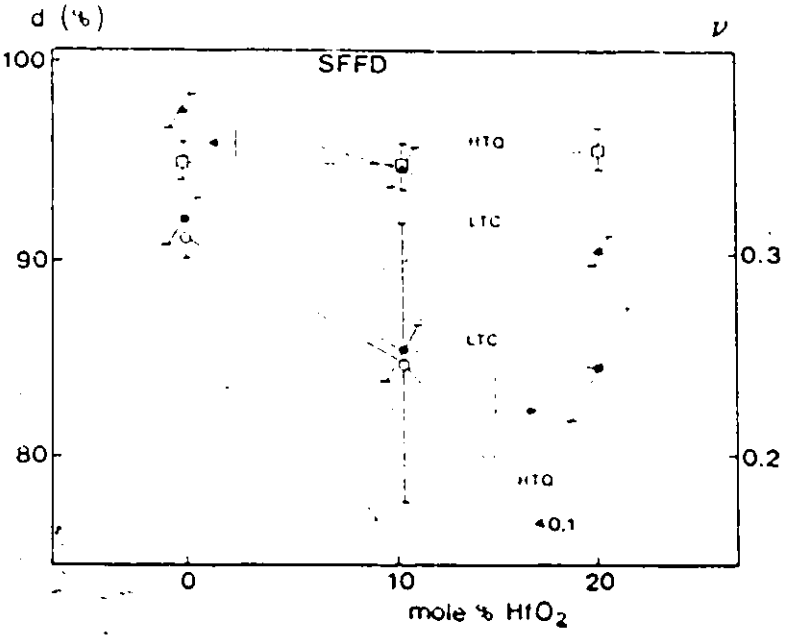

Fig. 5-9 Relative density d[%] and Poisson's ratio ν, for SFFD materials.

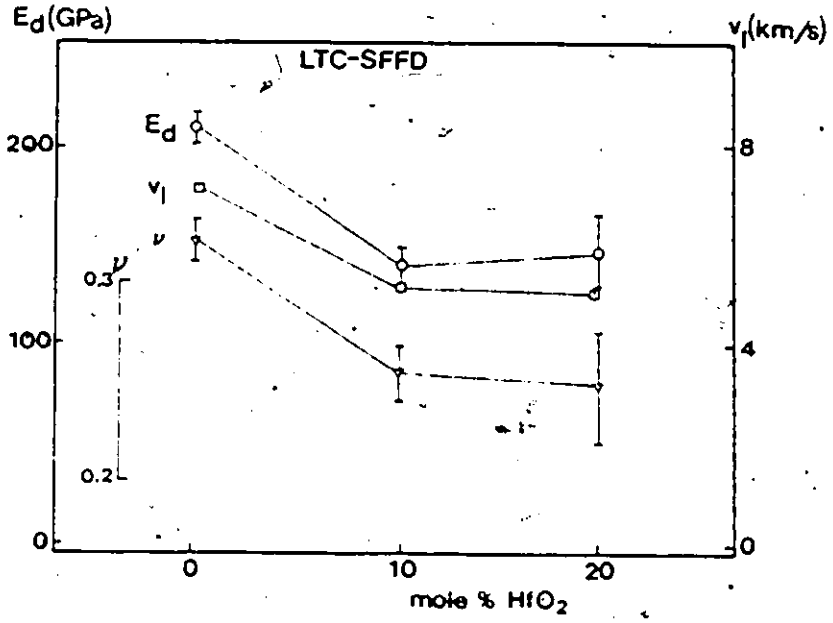

Fig. S-10 Elastic properties of LTC-SFFD materials.

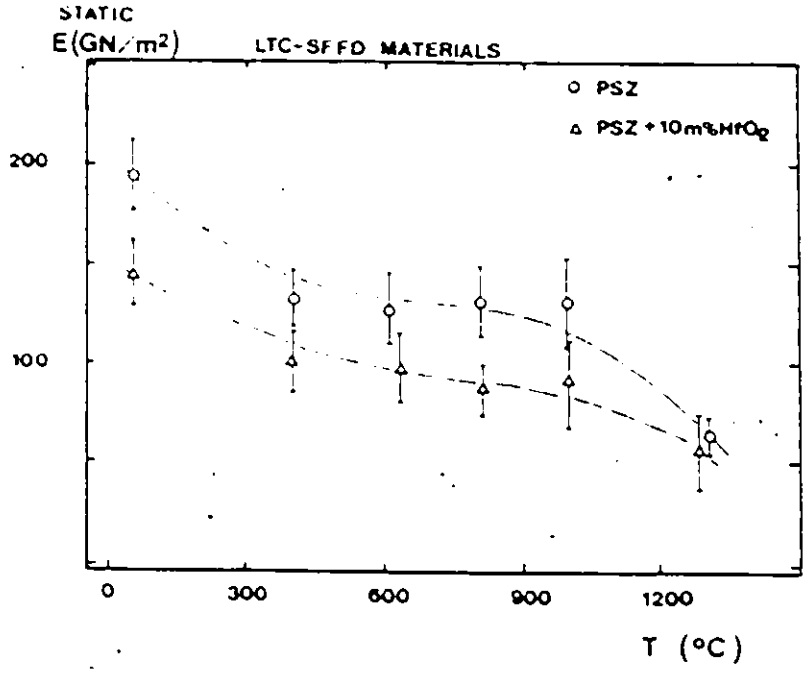

Fig. S-11 Static elastic modulus of LTC-SFFD materials against temperature.

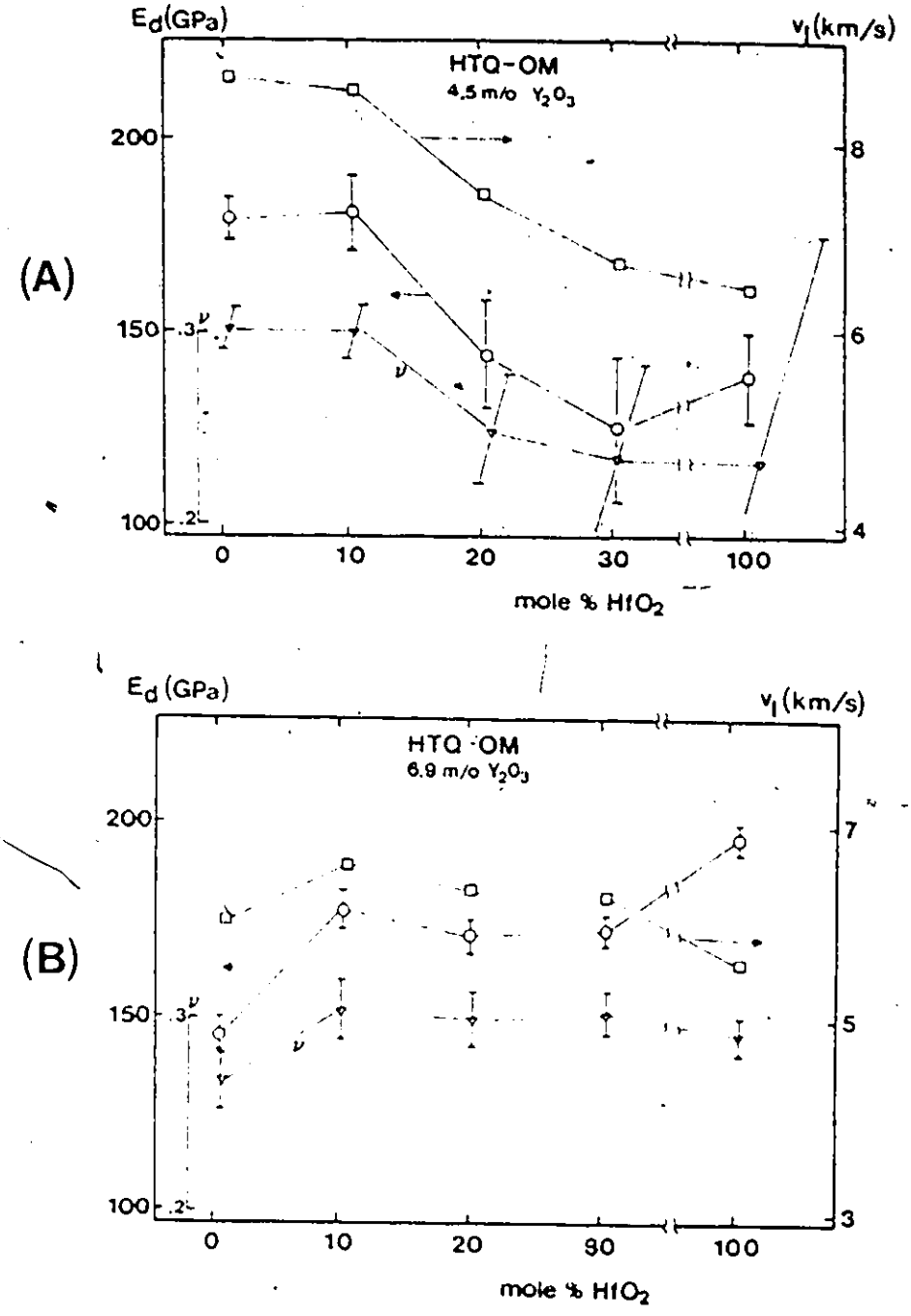

Fig. 5-12 Elastic properties of HTQ-OM materials against hafnia content : (A) partially stabilized with 4.5 mole % yttria ; (B) fully stabilized with 6.9 mole % yttria.

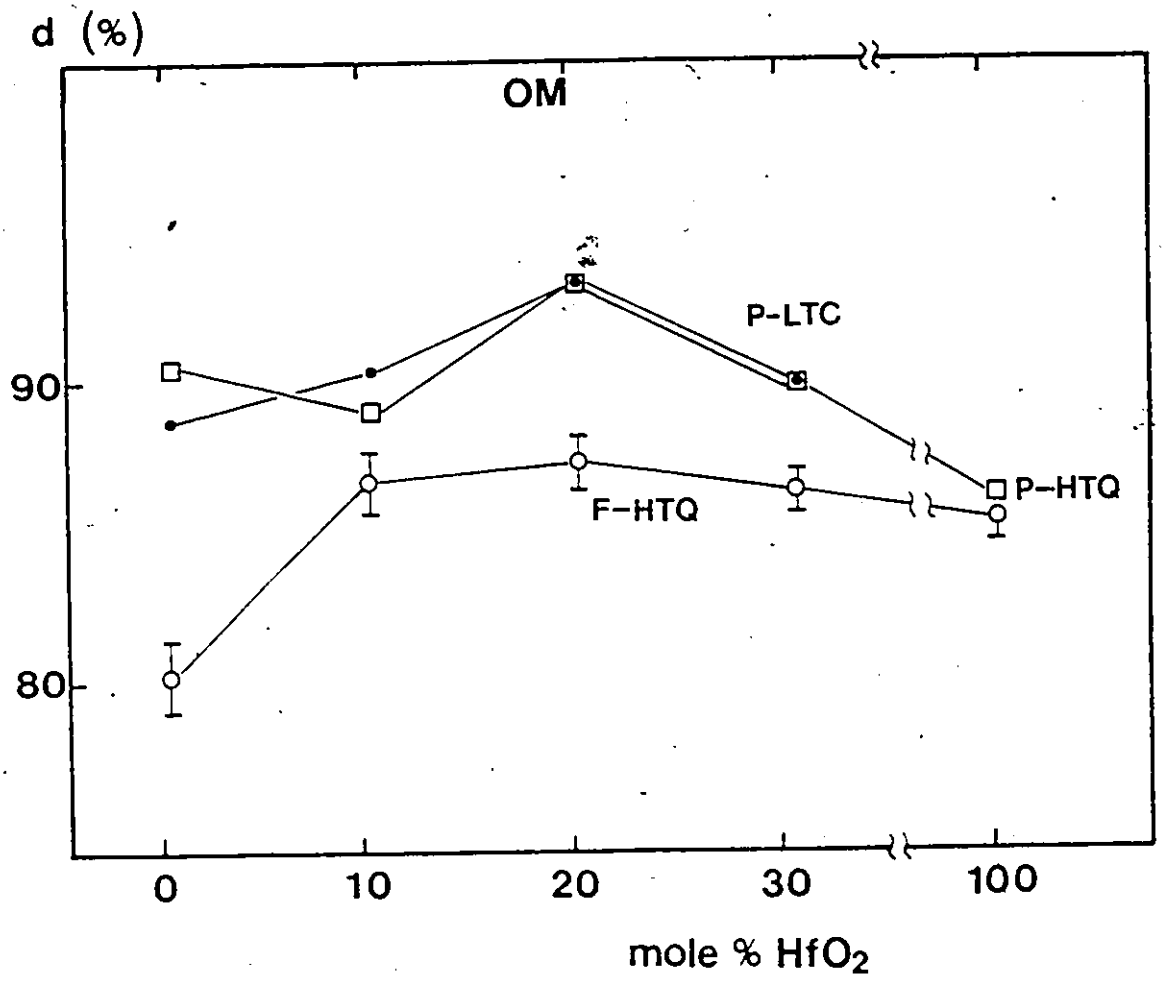

Fig. 5-13 Fraction of theoretical density of partially (P) and fully (F) stabilized OM zirconia-hafnia ceramics.

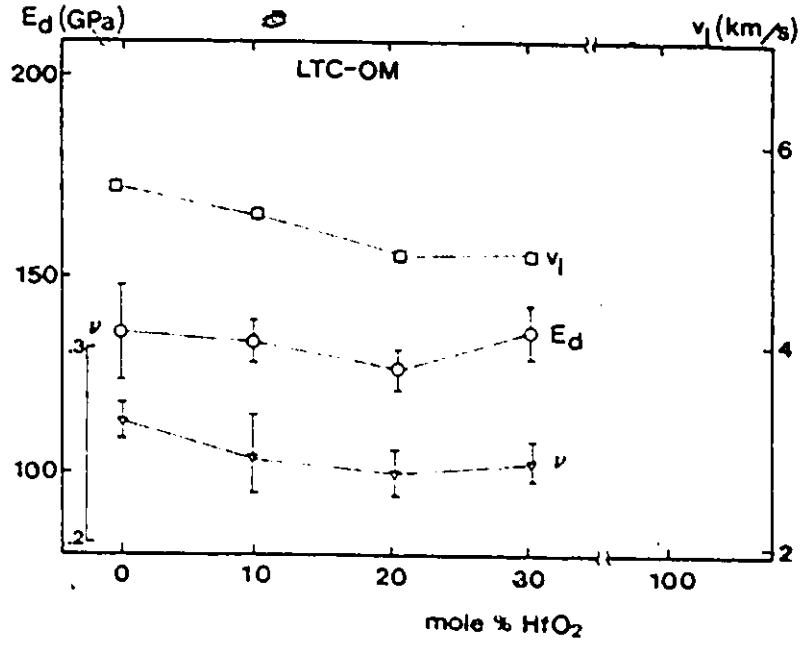

Fig. 5-14 Elastic properties of OM-LTC zirconia-hafnia solid solutions.

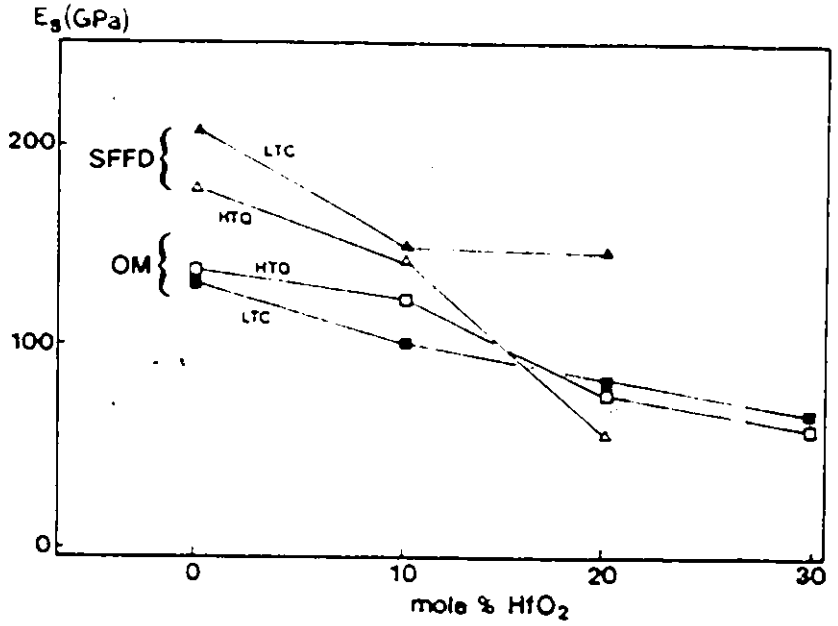

Fig. 5-15 Static elastic modulus of zirconia-hafnia ceramics against HfO_2 content.

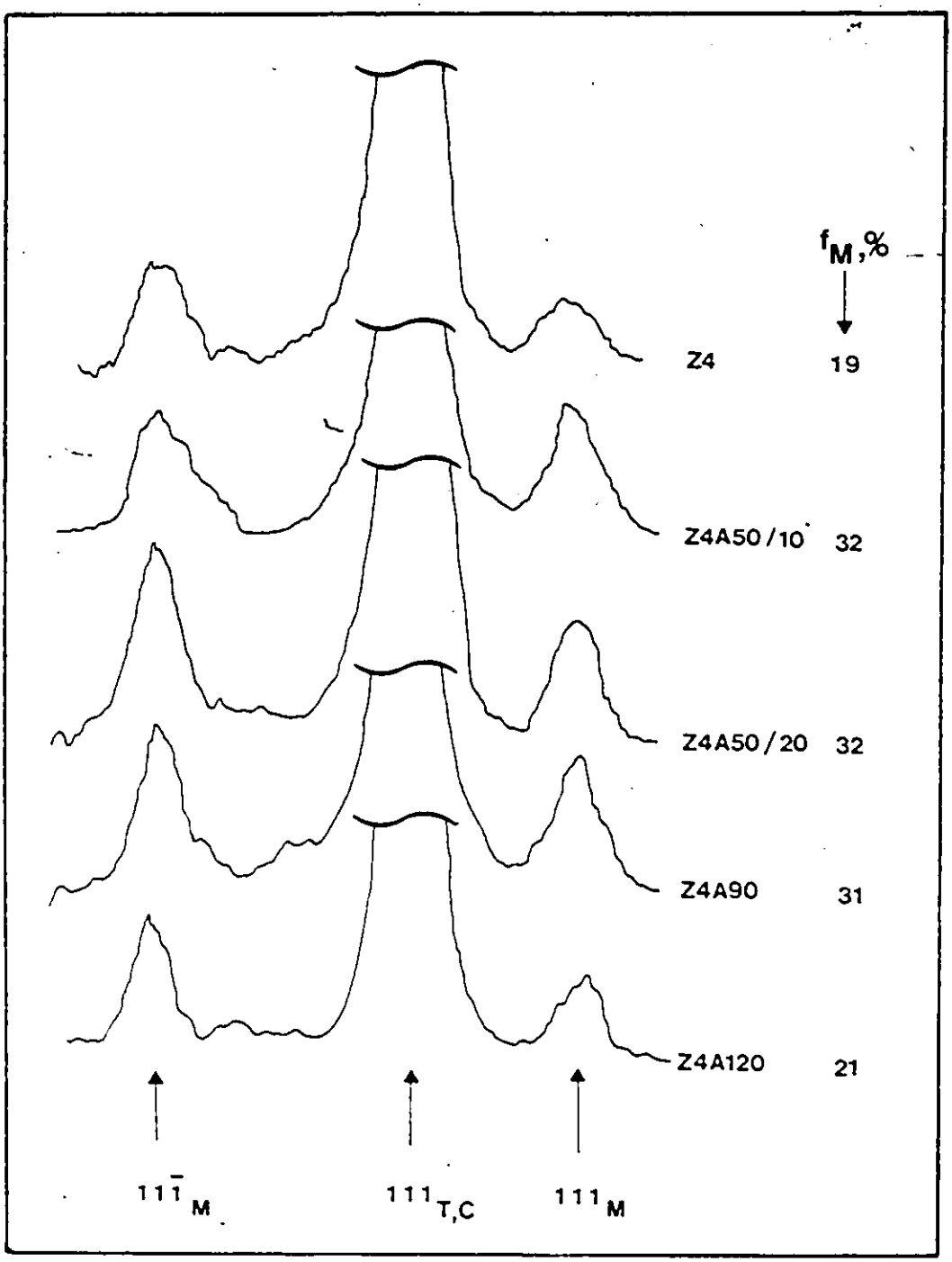

Fig. S-16 X-ray diffraction records for partially stabilized zirconia-beta-alumina composites.

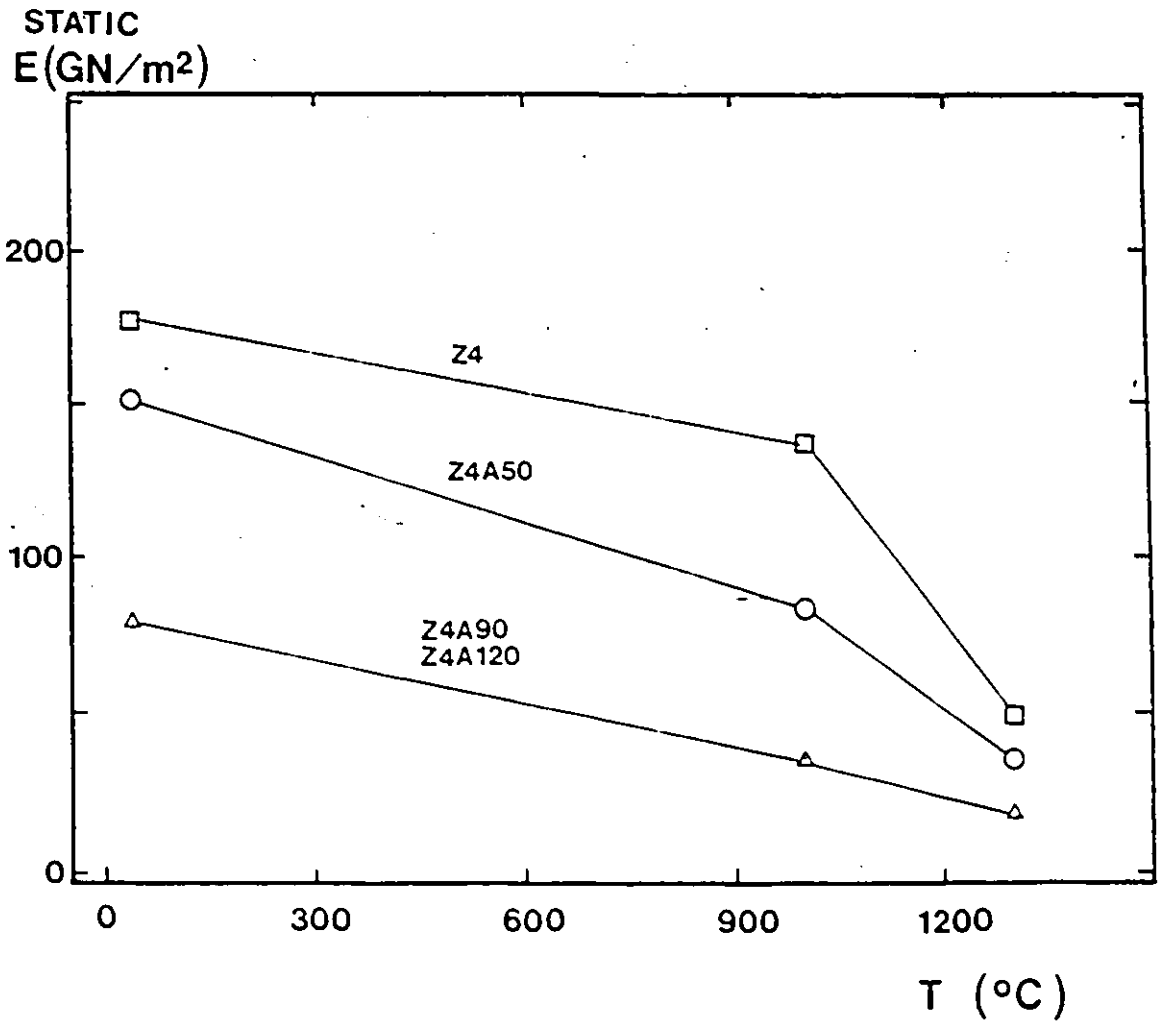

Fig. 5-17 Static elastic modulus of PSZ-beta-alumina composites against temperature.

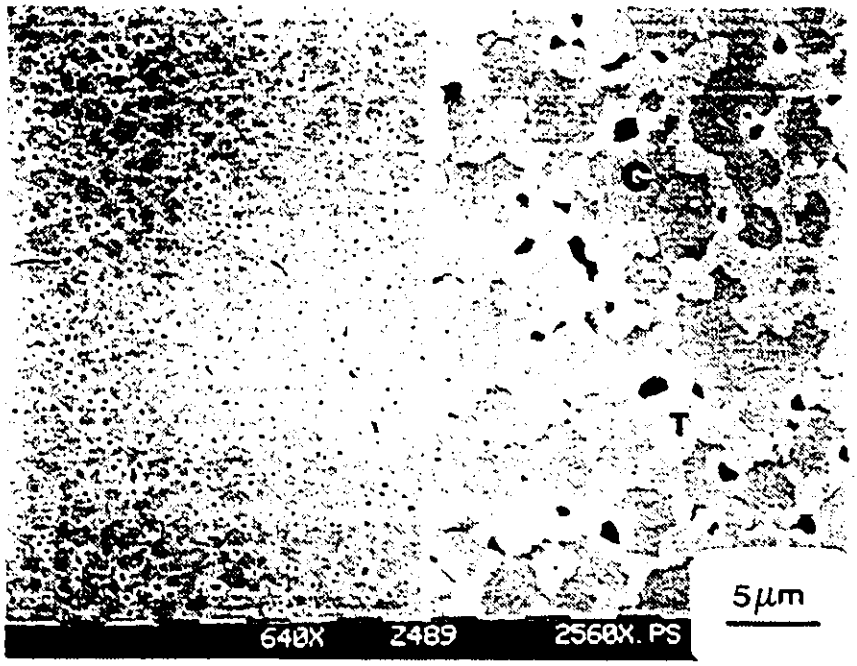

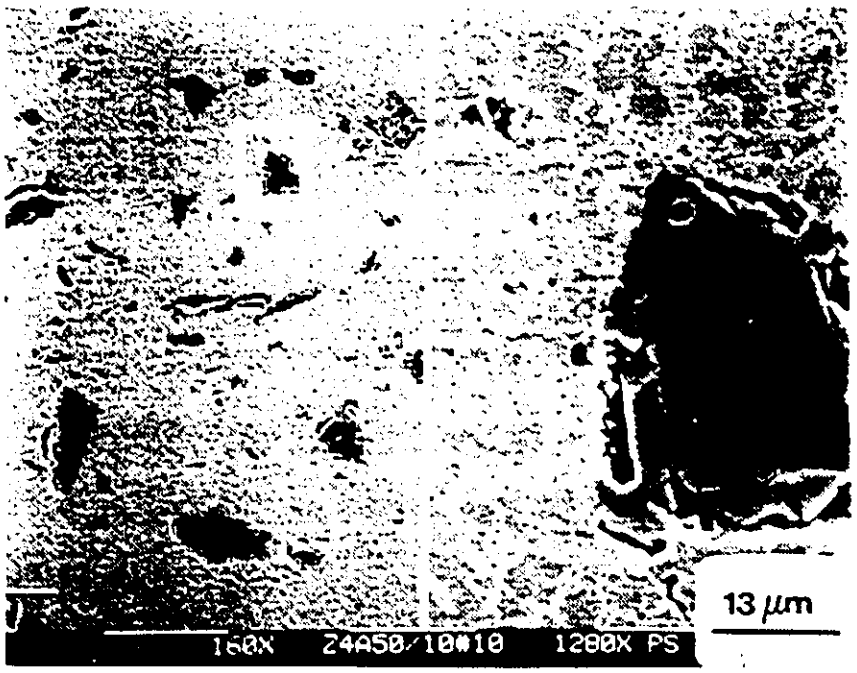

Fig. 5-18 Microstructures of PSZ-beta-alumina composites containing: (A) 0 vol.% βAl_2O_3 ; (B) 20 vol.% 50 μm large particles ; (C) 20 vol.% 90 μm large particles and (D) 20 vol.% 120 μm large particles.

(C)

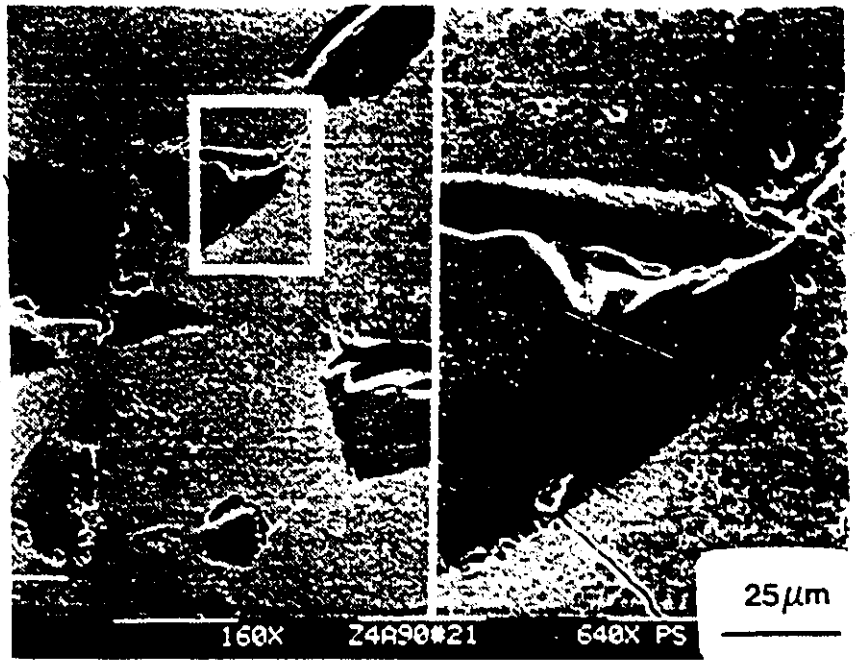

(D)

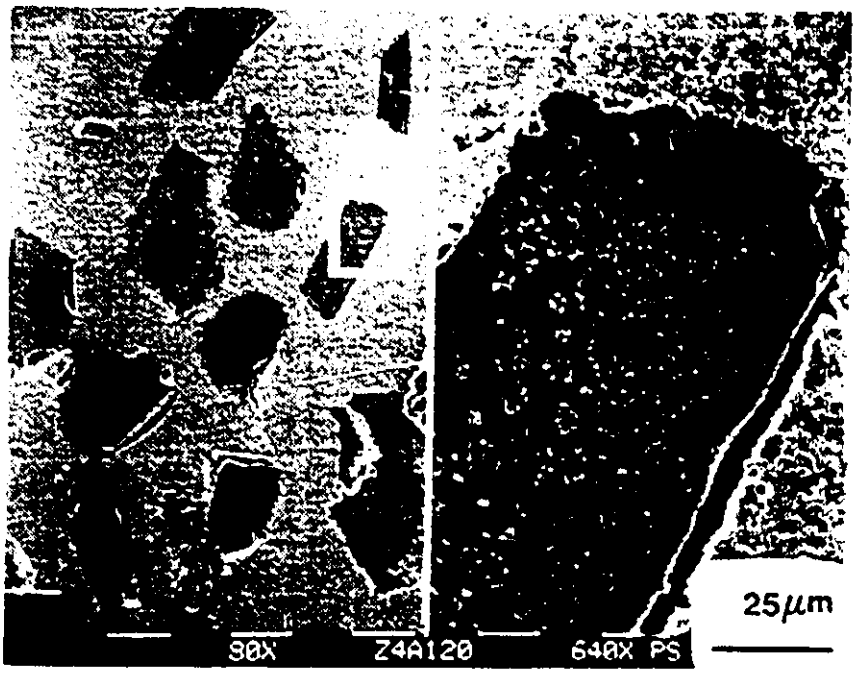

Fig. 5-18 Continued.

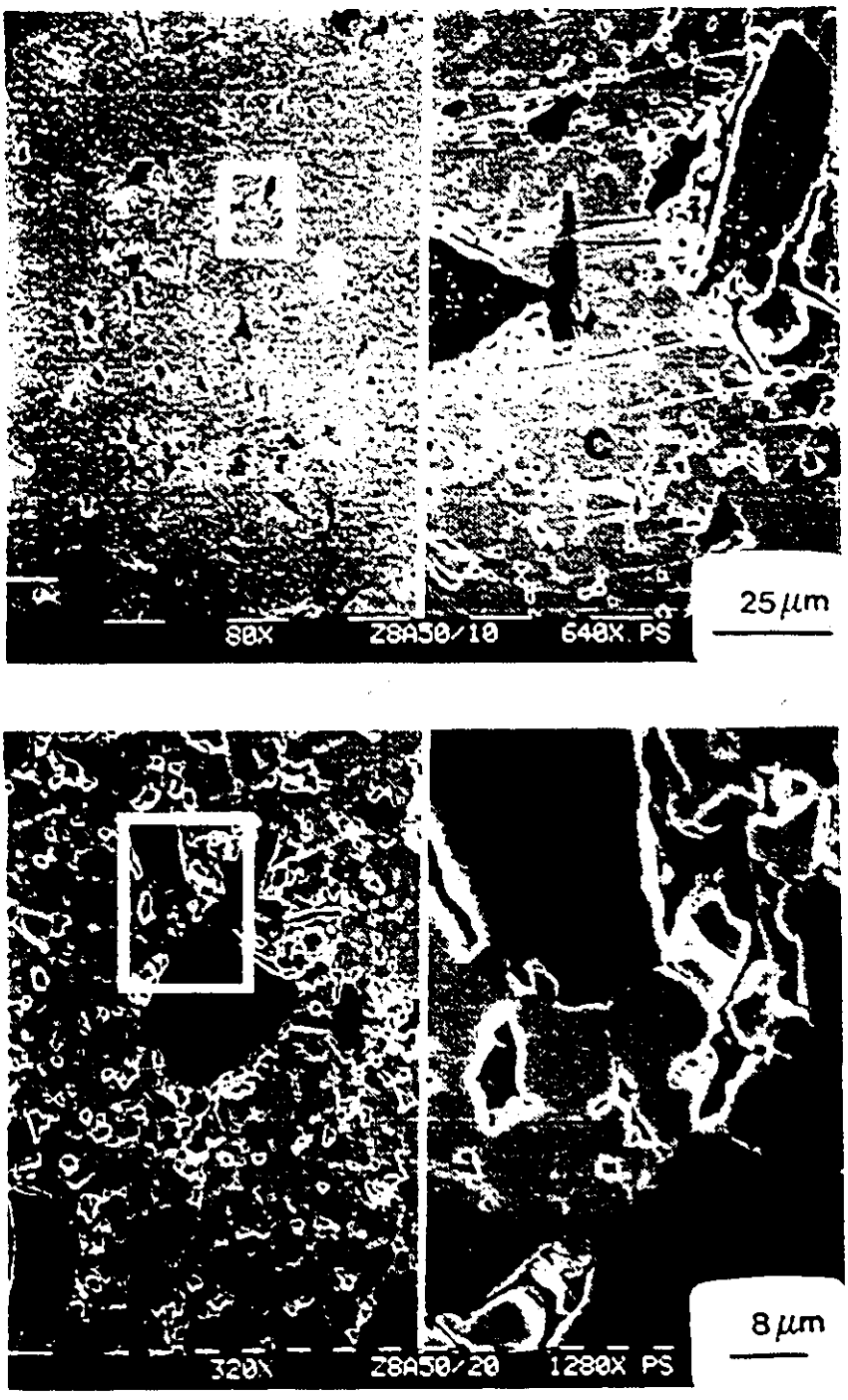

Fig. 5-19 Microstructures of FSZ-beta-alumina composites containing : (A) 0 vol.% βAl_2O_3 ; (B) 20 vol.% 50 µm large particles ; (C) 20 vol.% 90 µm large particles and (D) 20 vol.% 120 µm large particles.

(C)

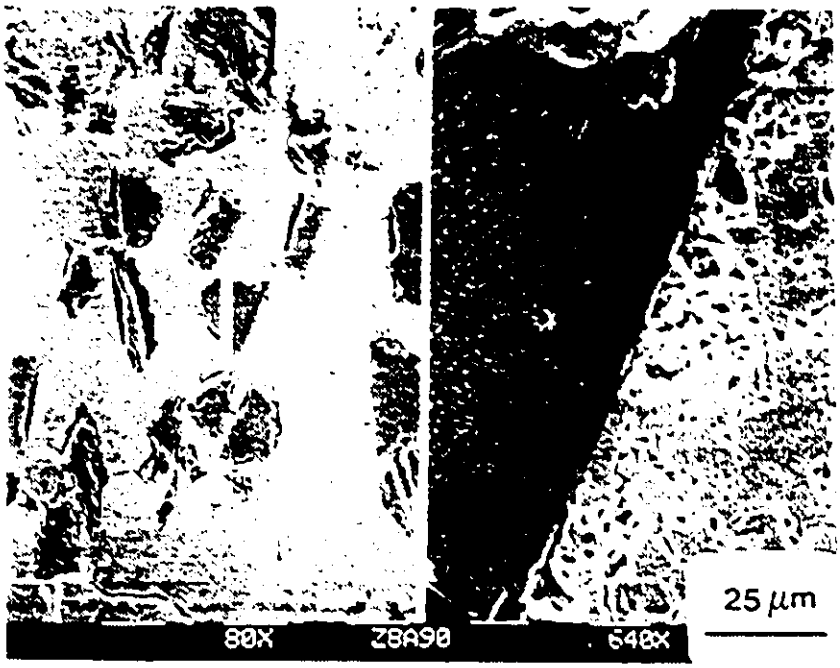

(D)

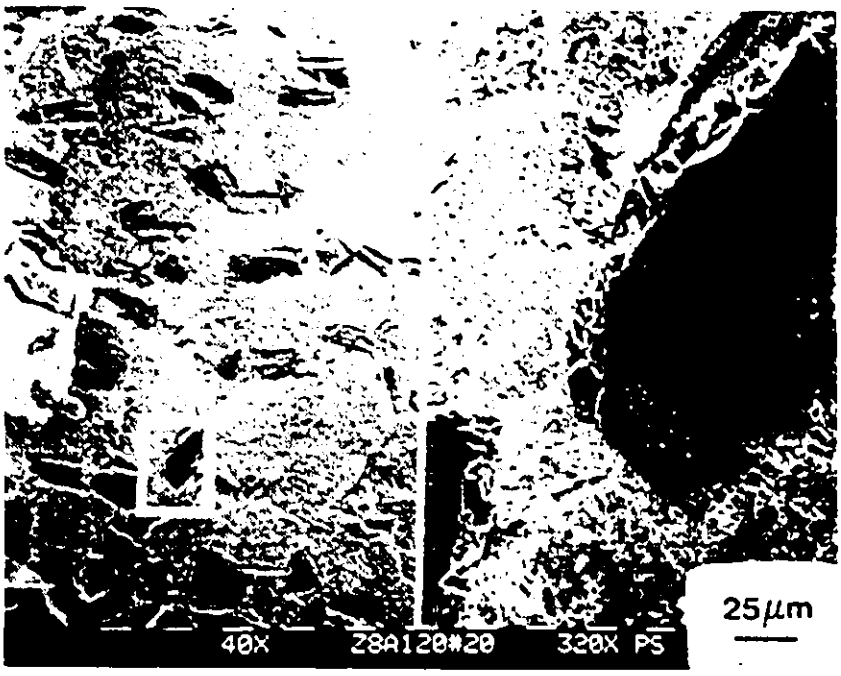

Fig. 5-19 Continued

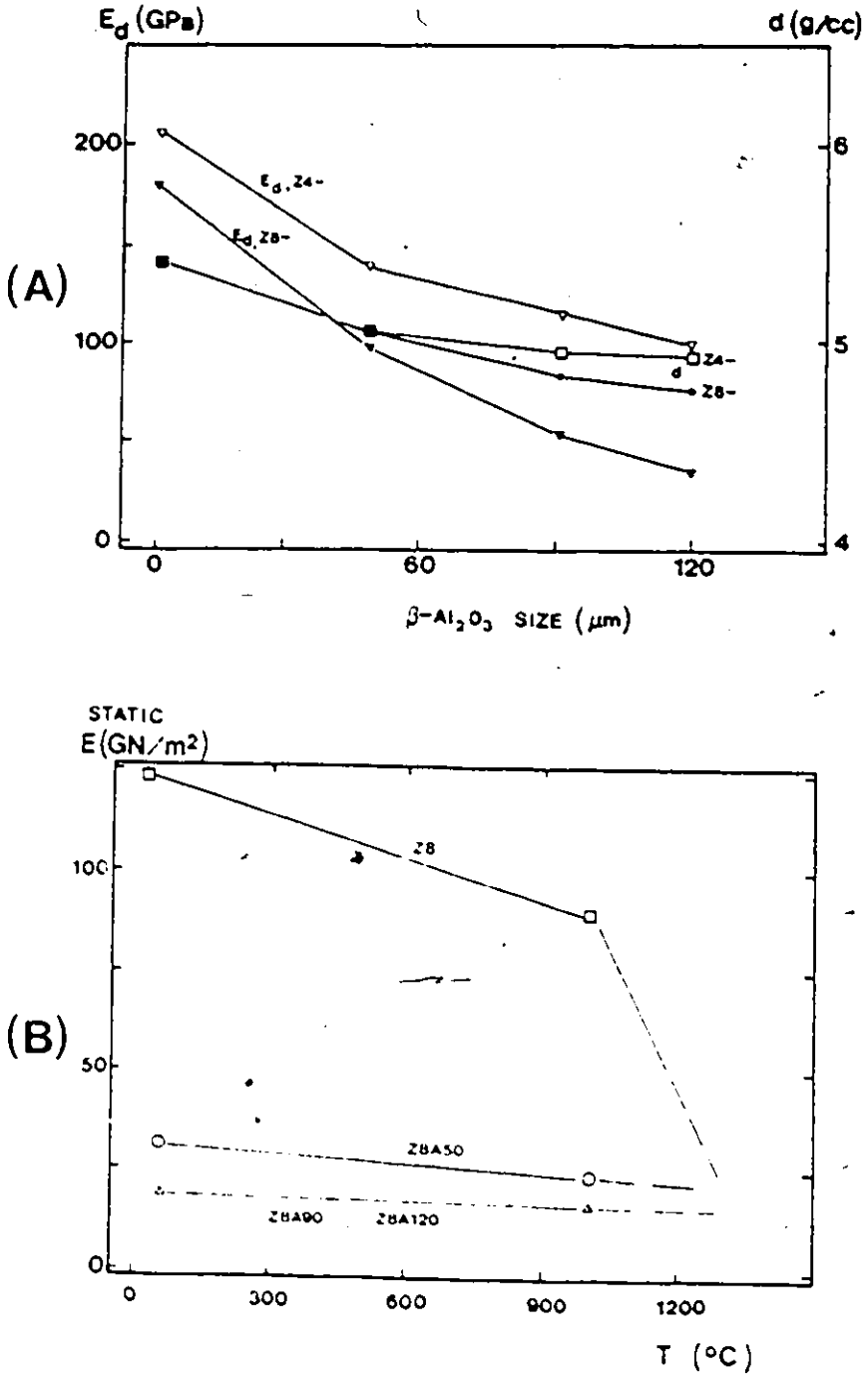

Fig. 5-20 Properties of fully (Z8-series) and partially (Z4-series) stabilized zirconia-beta-alumina composites : (A) Dynamic elastic modulus and density against β-Al_2O_3 size ; (B) Static elastic modulus against temperature.

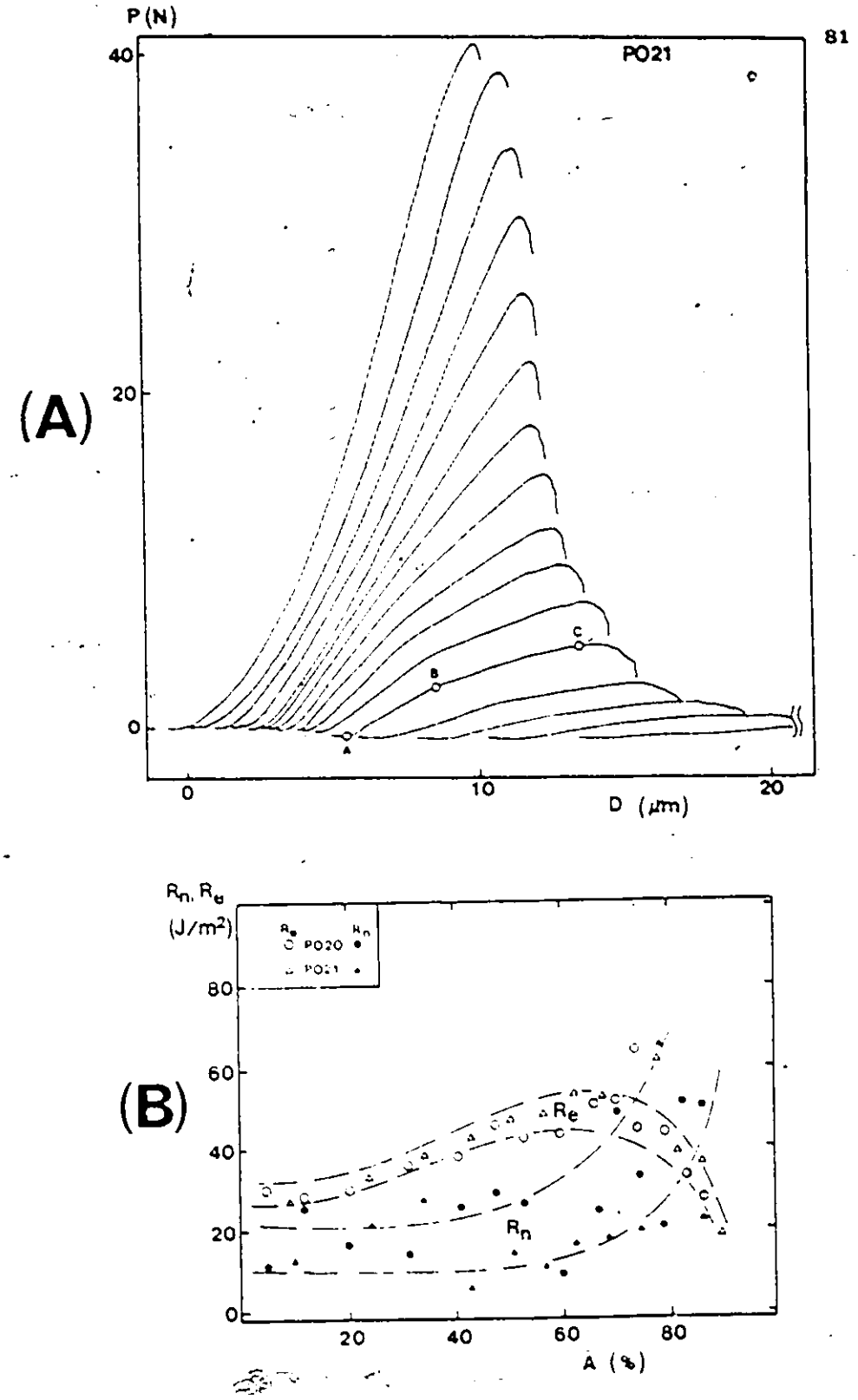

Fig. 5-21 Fracture testing results for PO type ceramics : (A) Load-displacement record ; (B) Resistance to fracture compiled for two specimens.

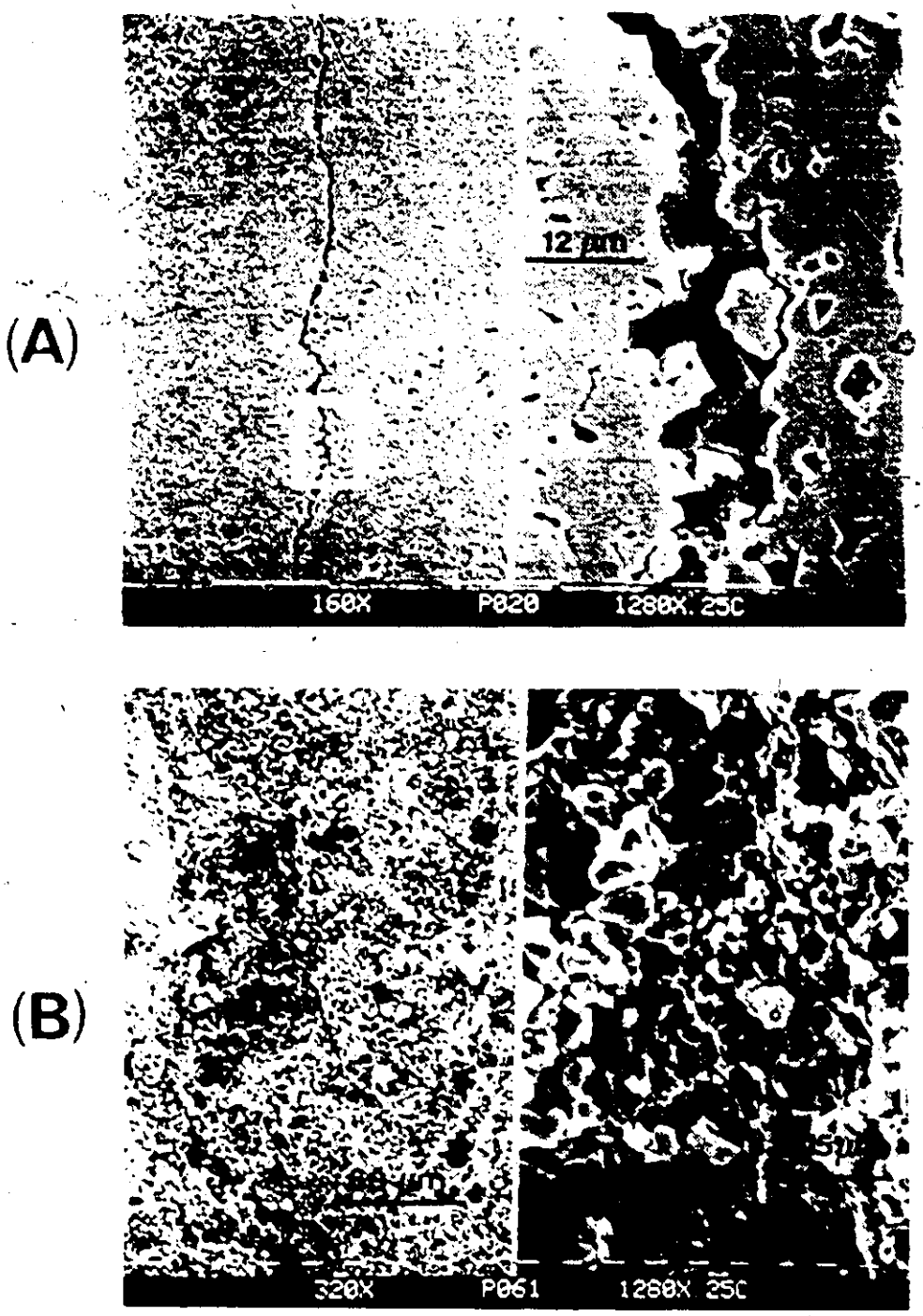

Fig. 5-22 Fractography of PO type ceramics : (A) Arrested crack ; (B) Fracture surface.

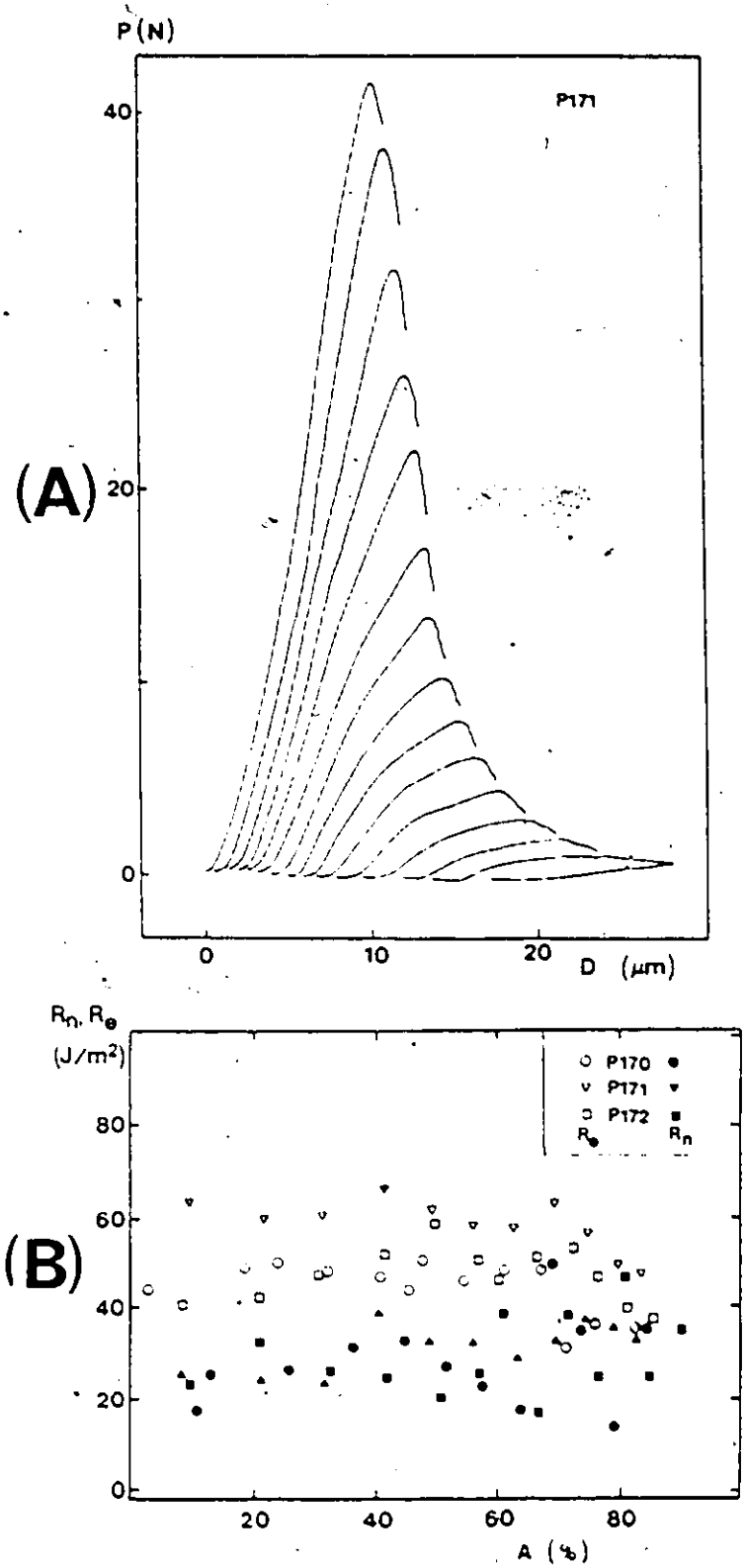

Fig. 5-23 Fracture testing results for P1 type ceramics : (A) Load-displacement record ; (B) Resistance to fracture compiled for three specimens.

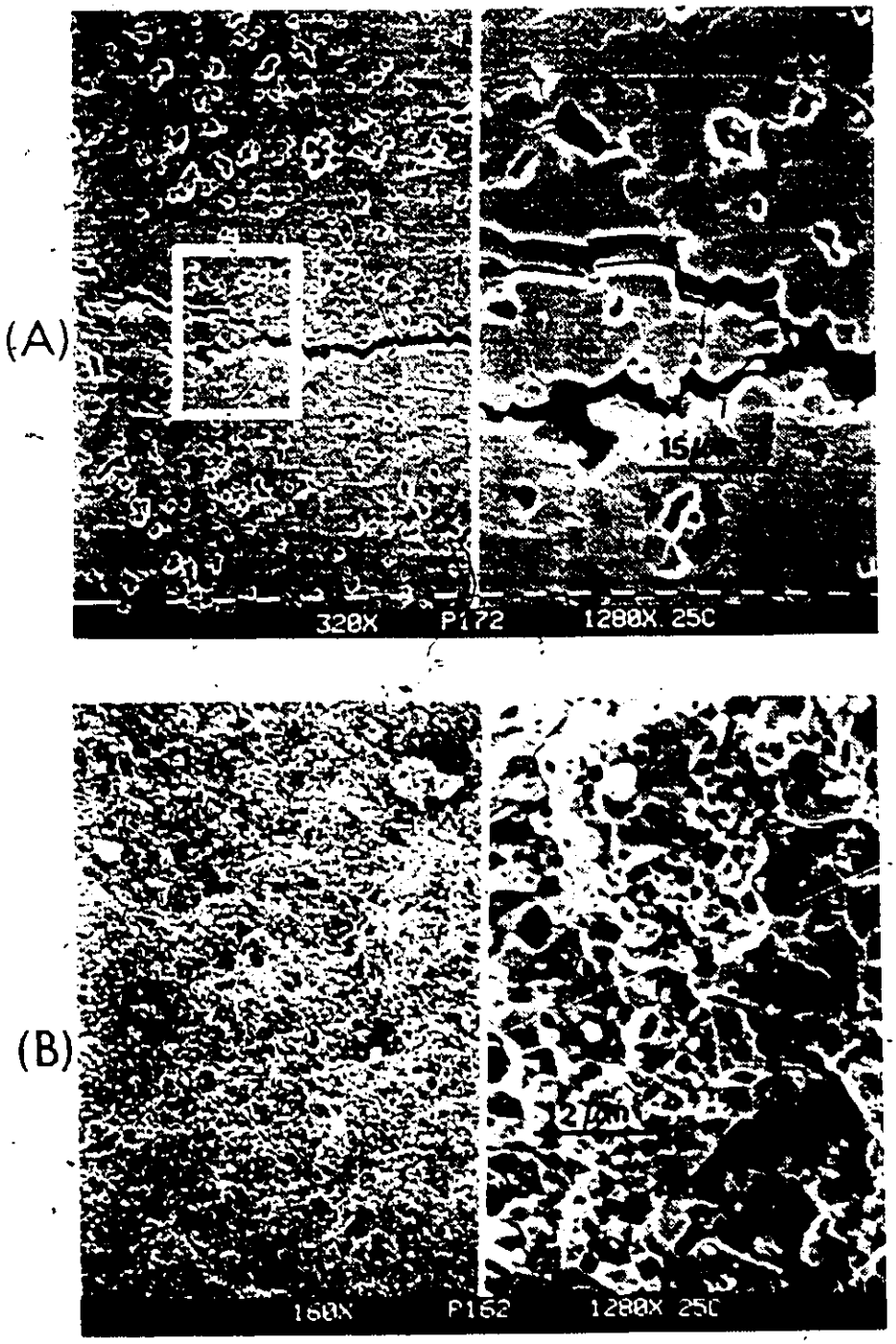

Fig. 5-24 Fractography of P1 type ceramics : (A) Arrested crack ; (B) Fracture surface.

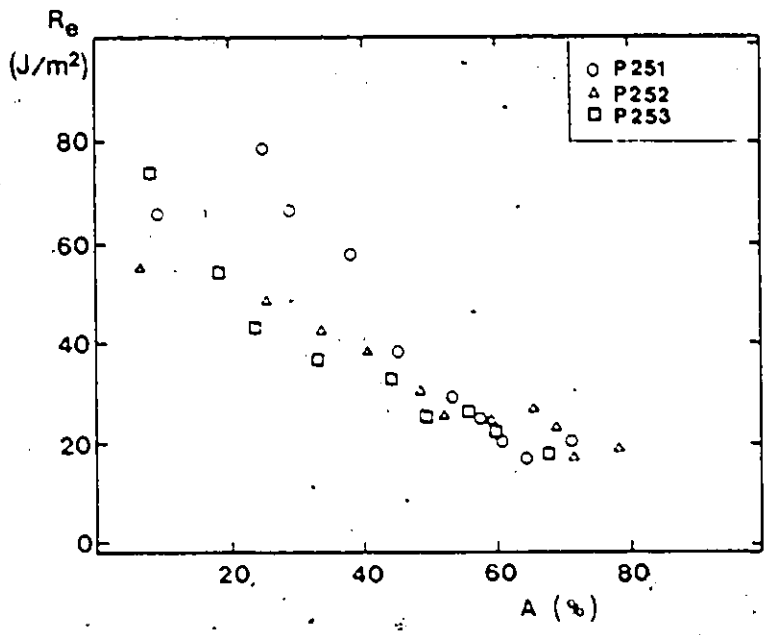

Fig. 5-25 Resistance to fracture of P2 type ceramics.

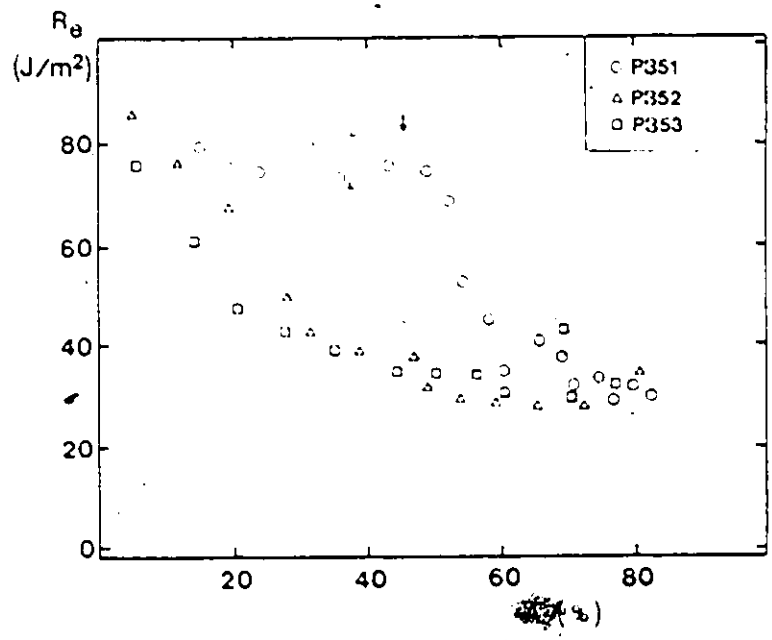

Fig. 5-26 Resistance to fracture of P3 type ceramics.

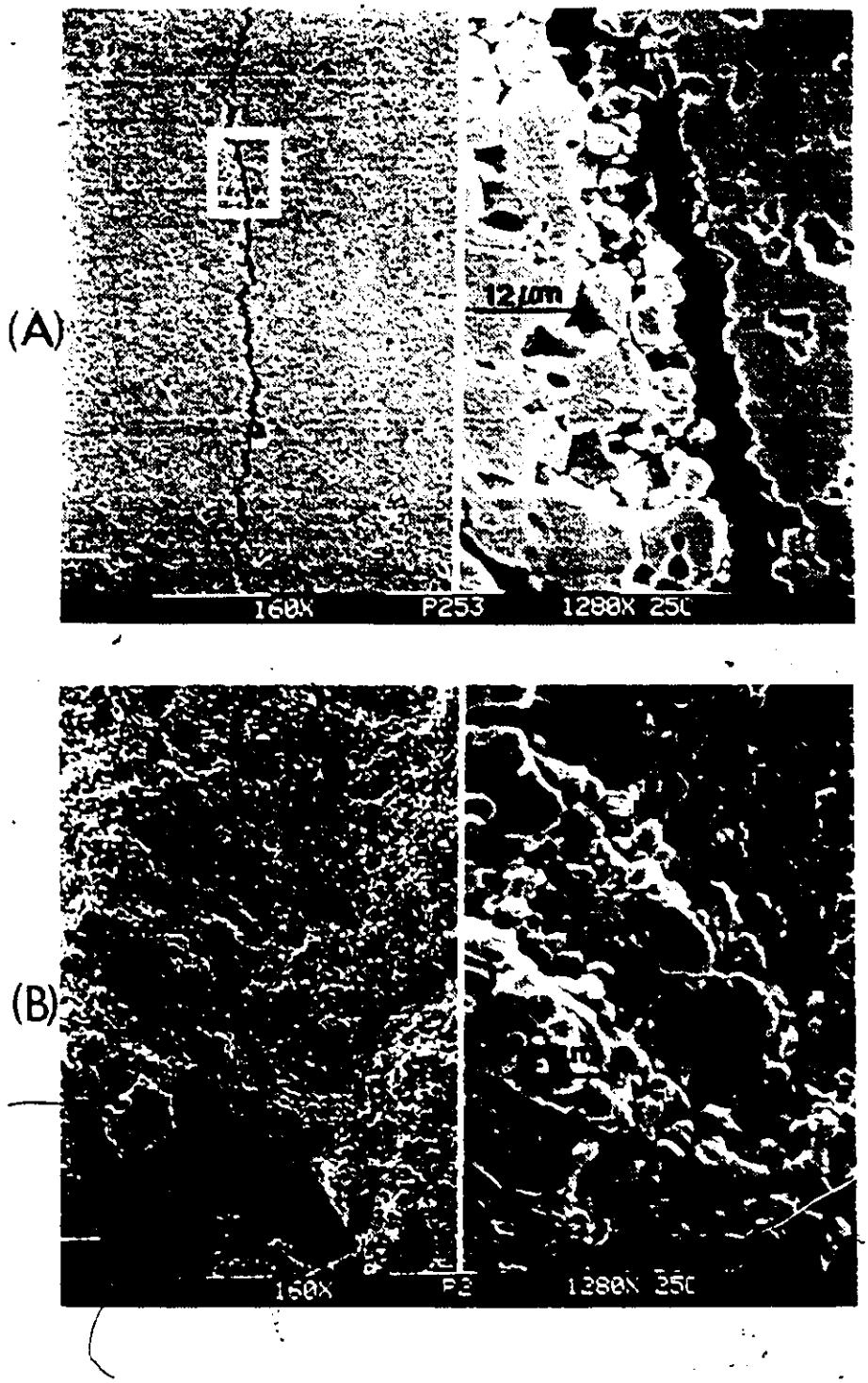

Fig. S-27 Fractography of P2 type ceramics : (A) Arrested crack ; (B) Fracture surface.

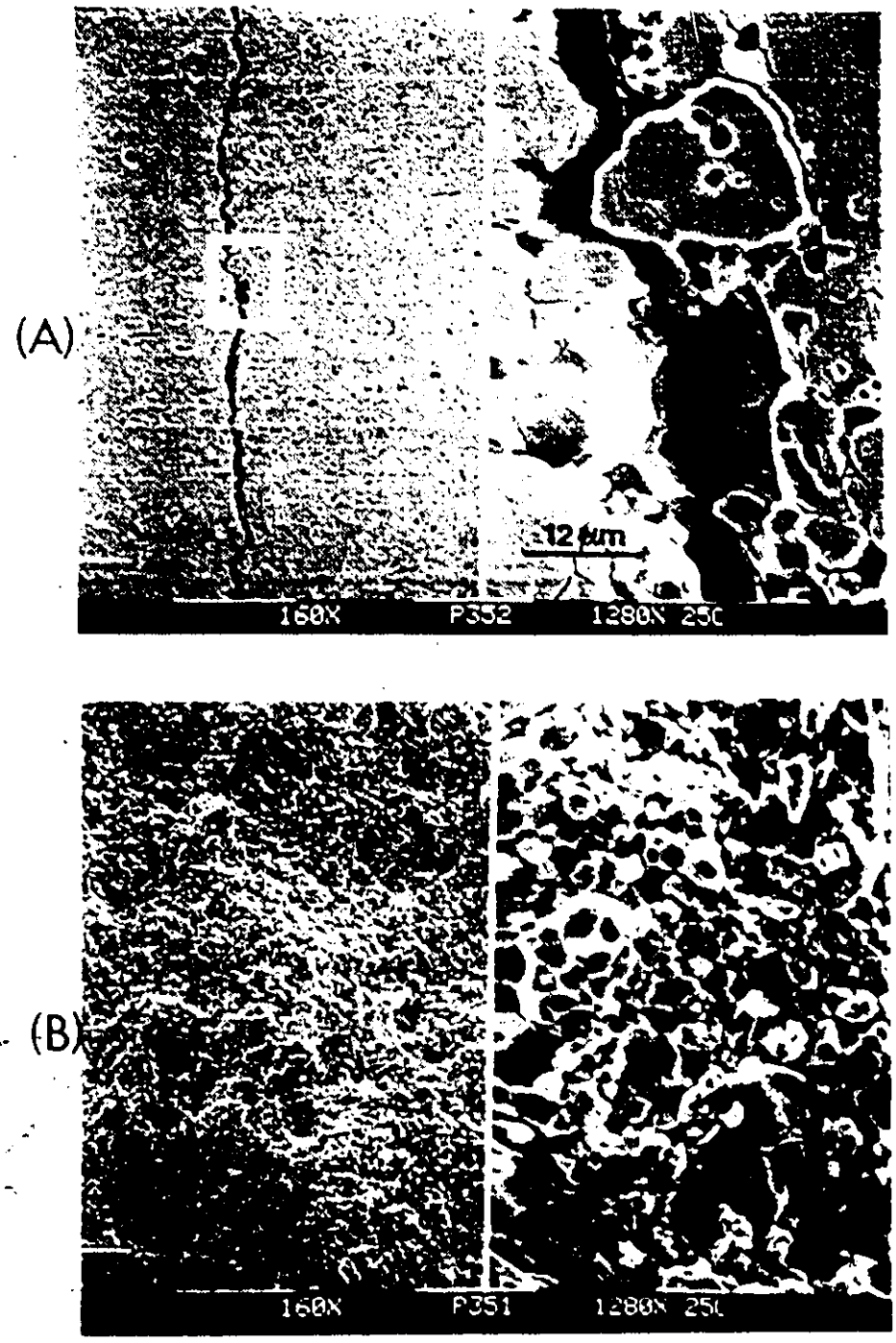

Fig. 5-28 Fractography of P3 type ceramics: (A) Arrested crack ; (B) Fracture surface.

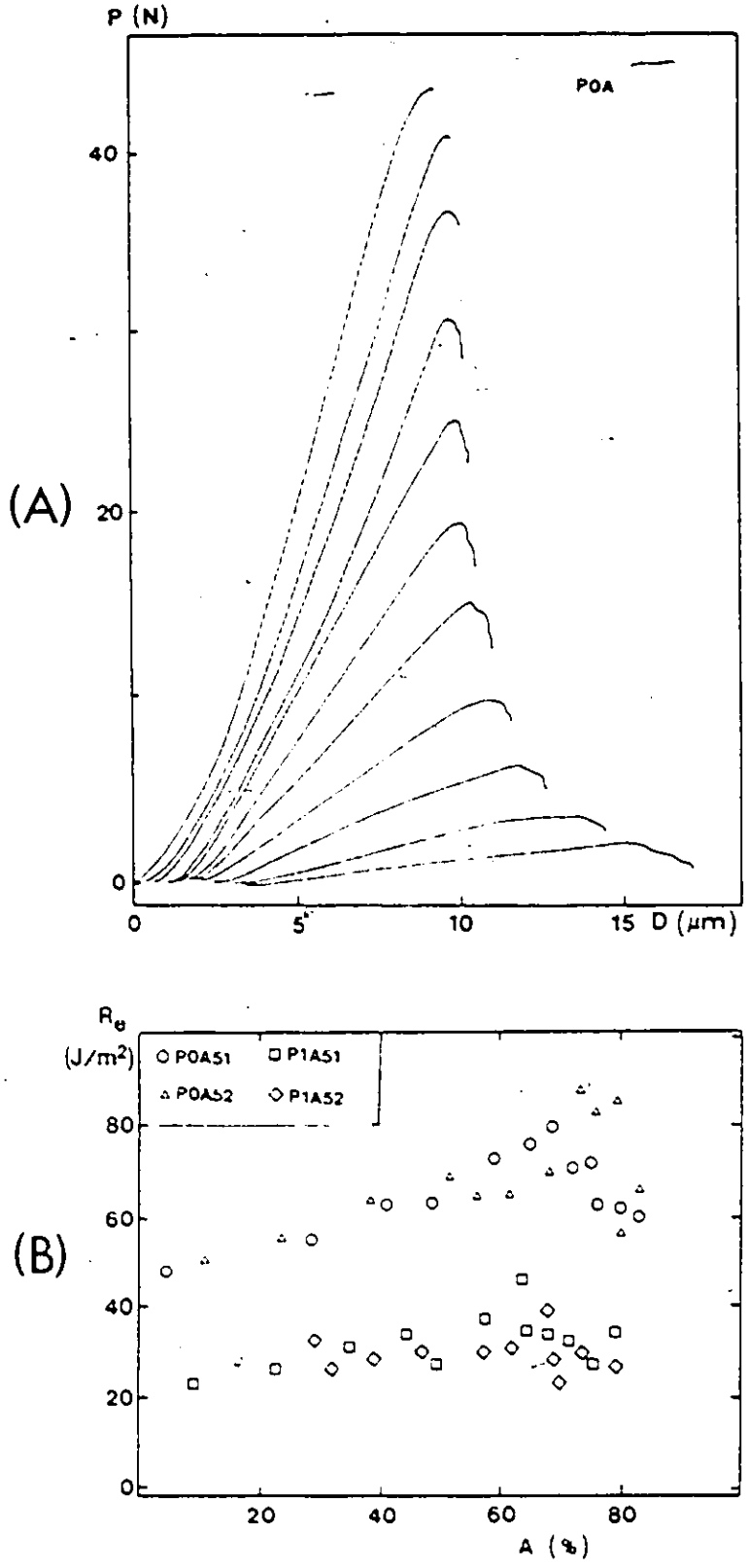

Fig. 5-29 Fracture testing results for SFFD type ceramics :
(A) Load-displacement record for P0A ;
(B) Resistance to fracture compiled for P0A and P1A

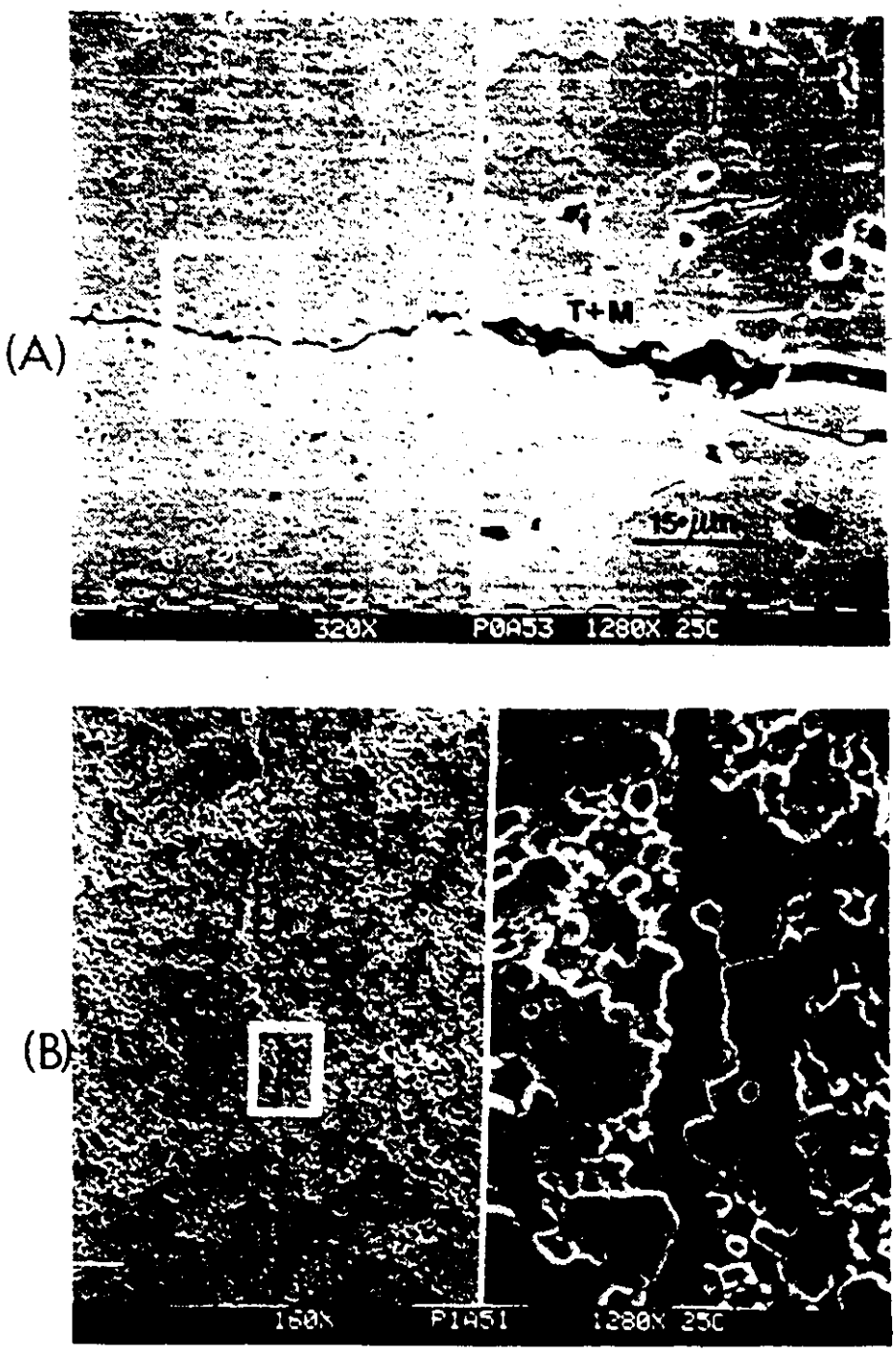

Fig. 5-30 Fractography of zirconia-hafnia solid solutions: (A) P0A type ; (B) P1A type.

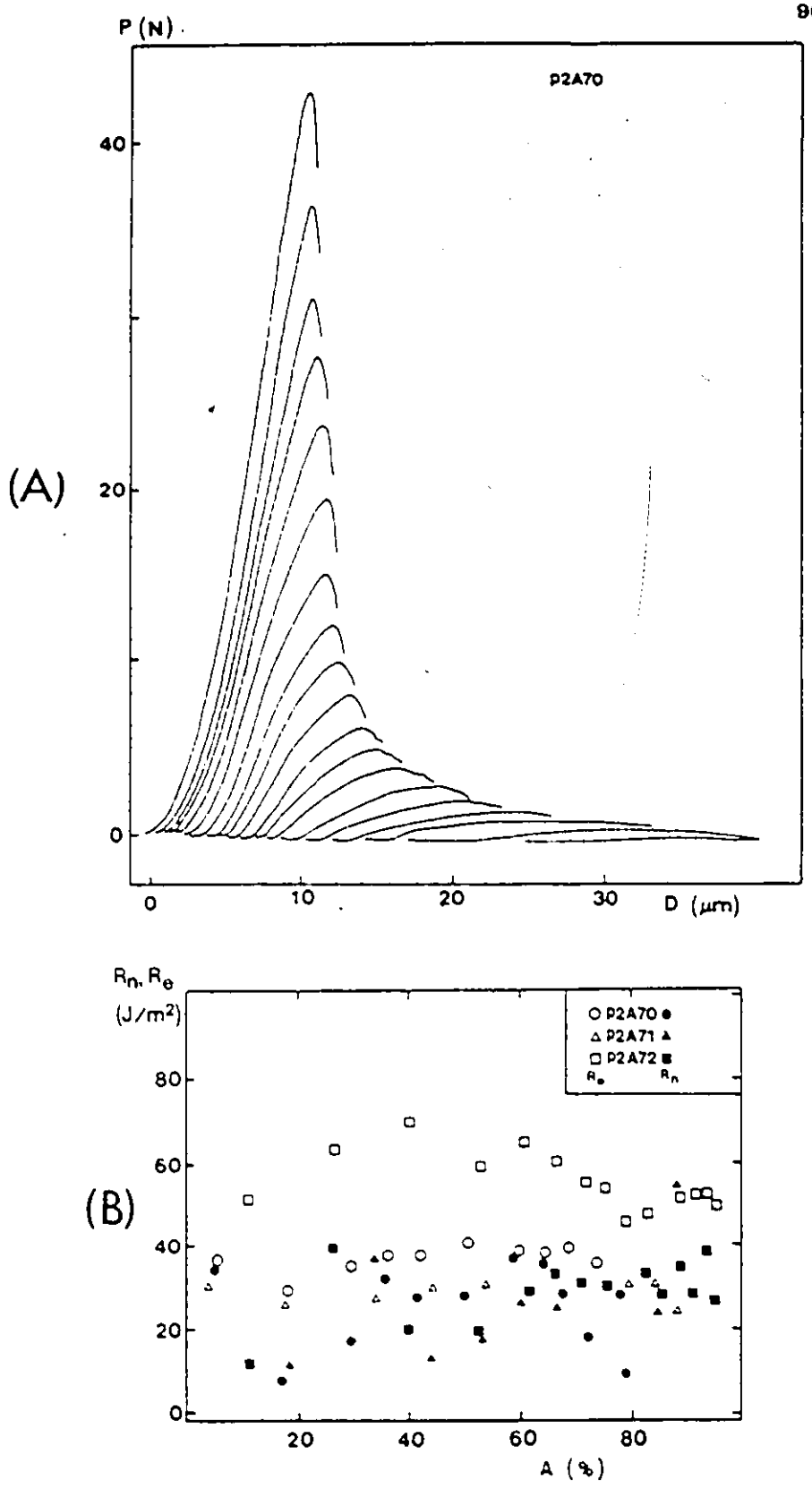

Fig. 5-31 Fracture testing results for P2A type ceramics : (A) Load-displacement record ; (B) Resistance to fracture compiled for three specimens.

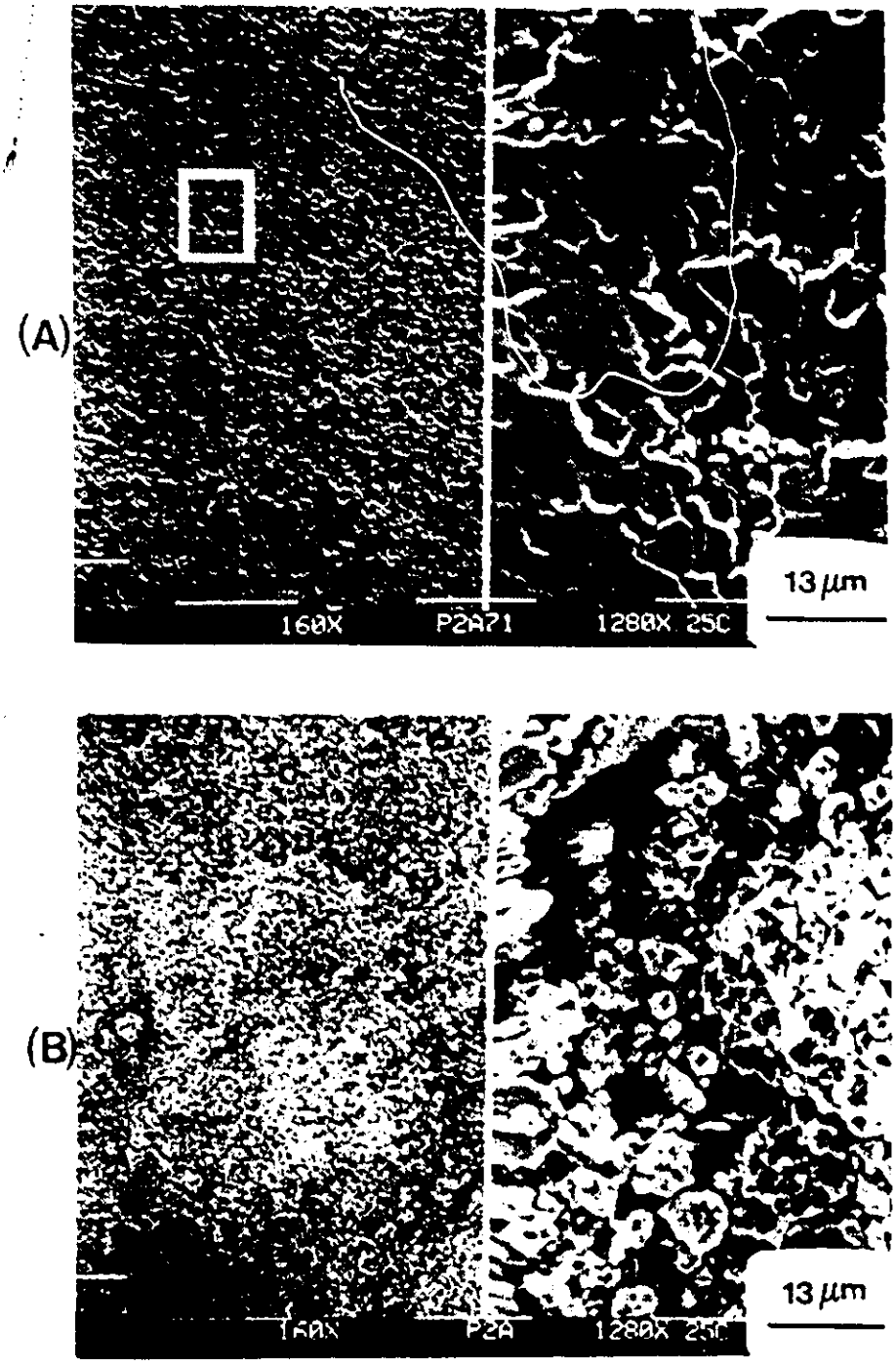

Fig. S-32 Fractography of P2A type ceramics : (A) Arrested crack ; (B) Fracture surface.

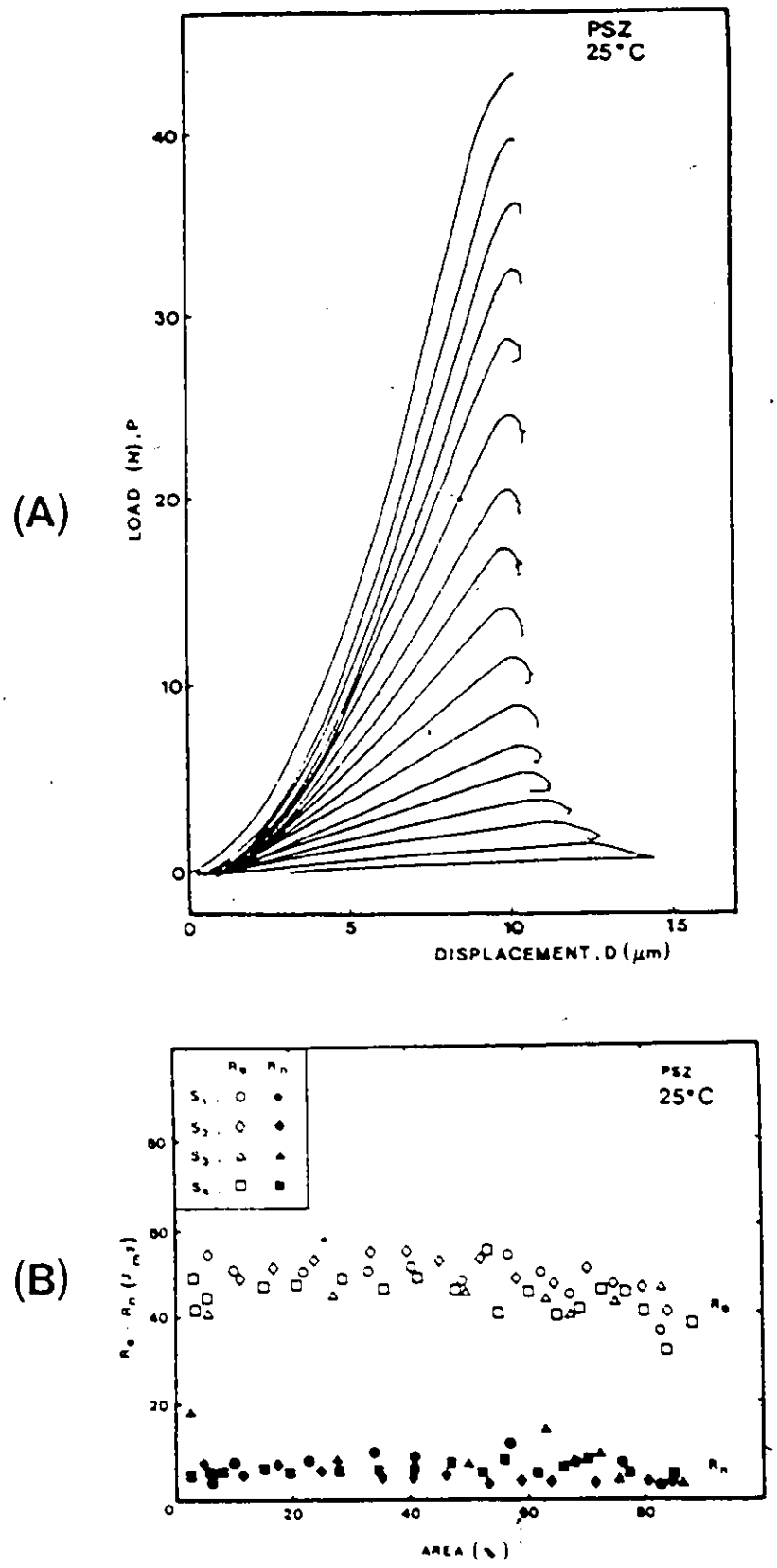

Fig. 5-33 Fracture testing results for PSZ :
(A) Load-displacement record ; (B) Resistance to fracture compiled for four specimens (S_1 to S_4).

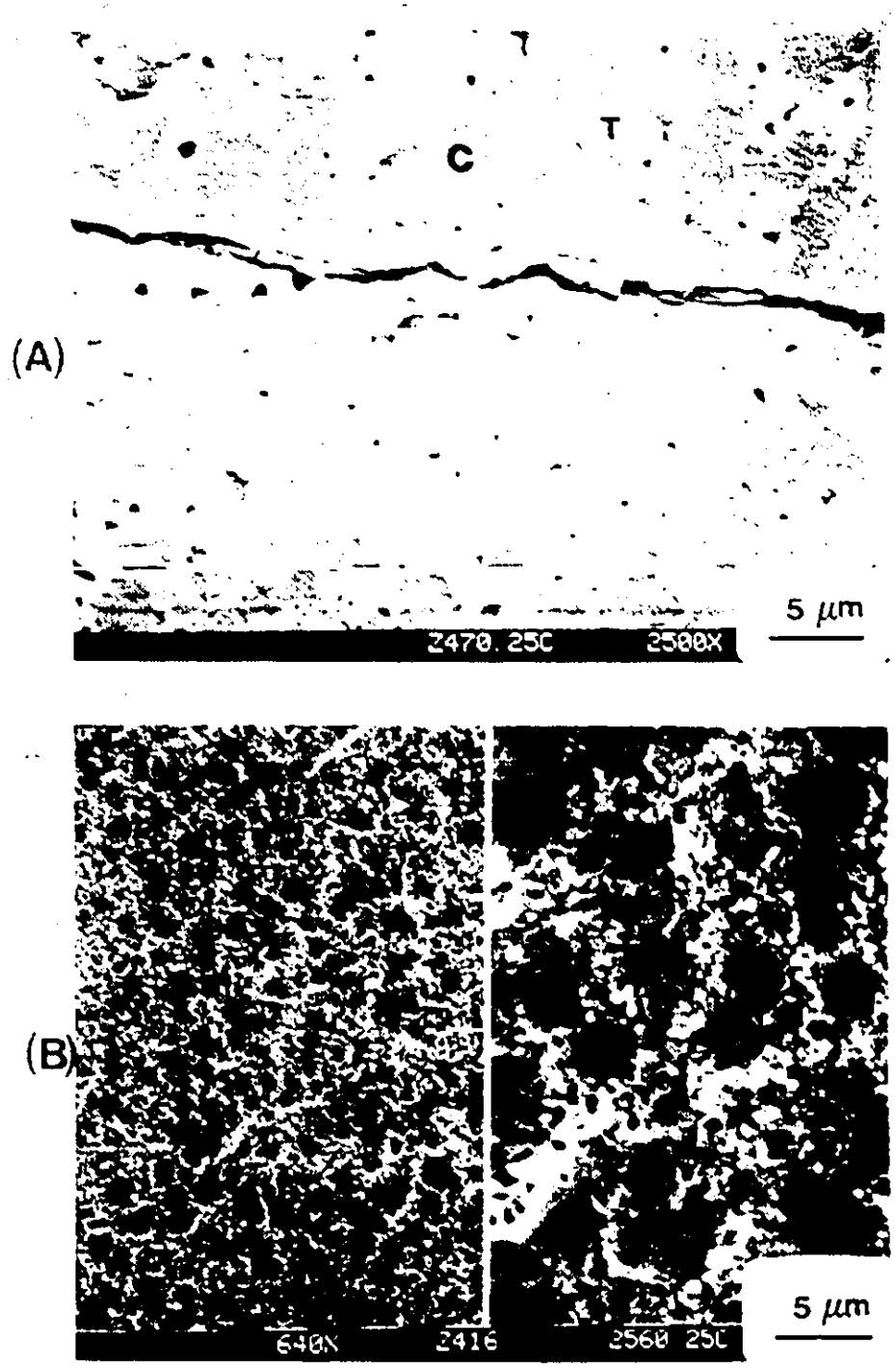

Fig. 5-34 Fractography of PSZ : (A) Arrested crack ; (B) Fracture surface.

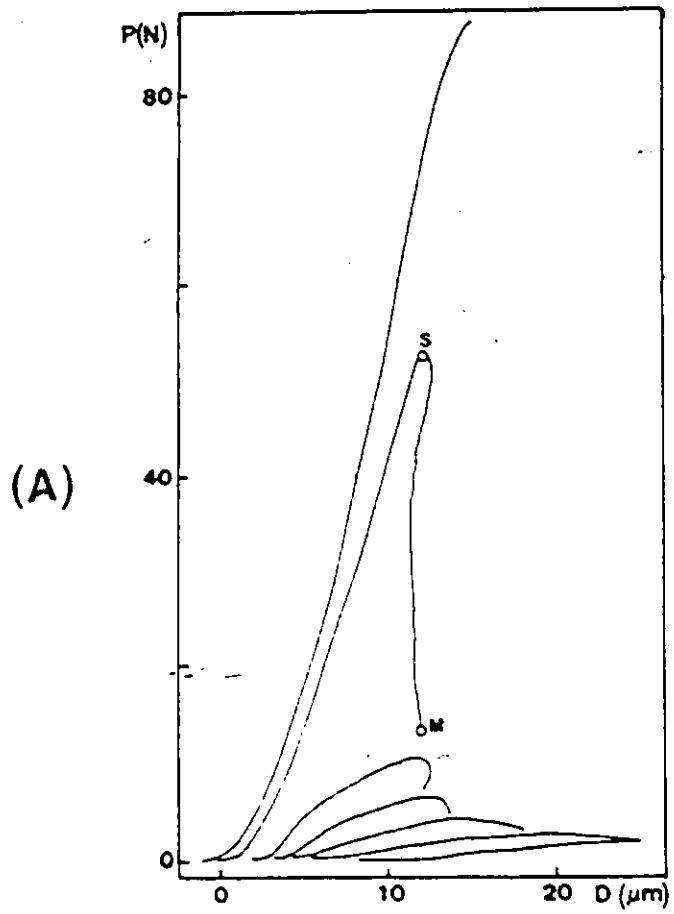

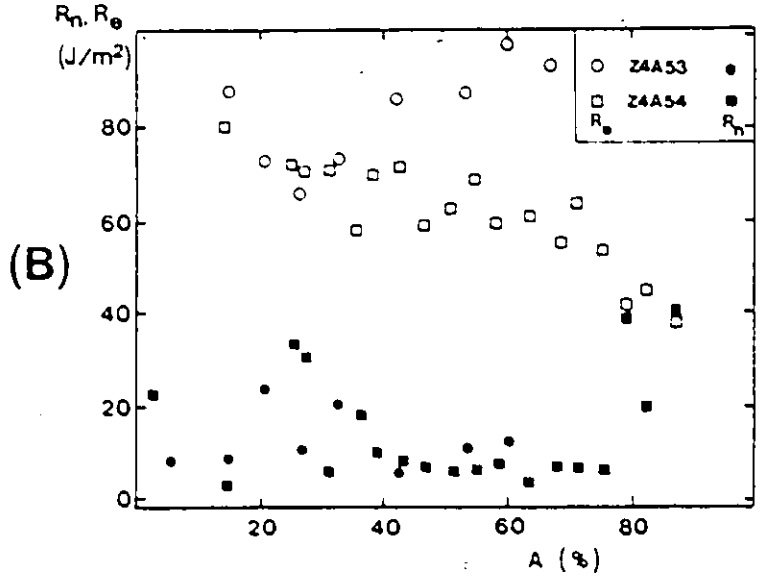

Fig. 5-35 Fracture testing results for Z4A50 type ceramics ; (A) Load-displacement record ; (B) Resistance to fracture compiled for two specimens.

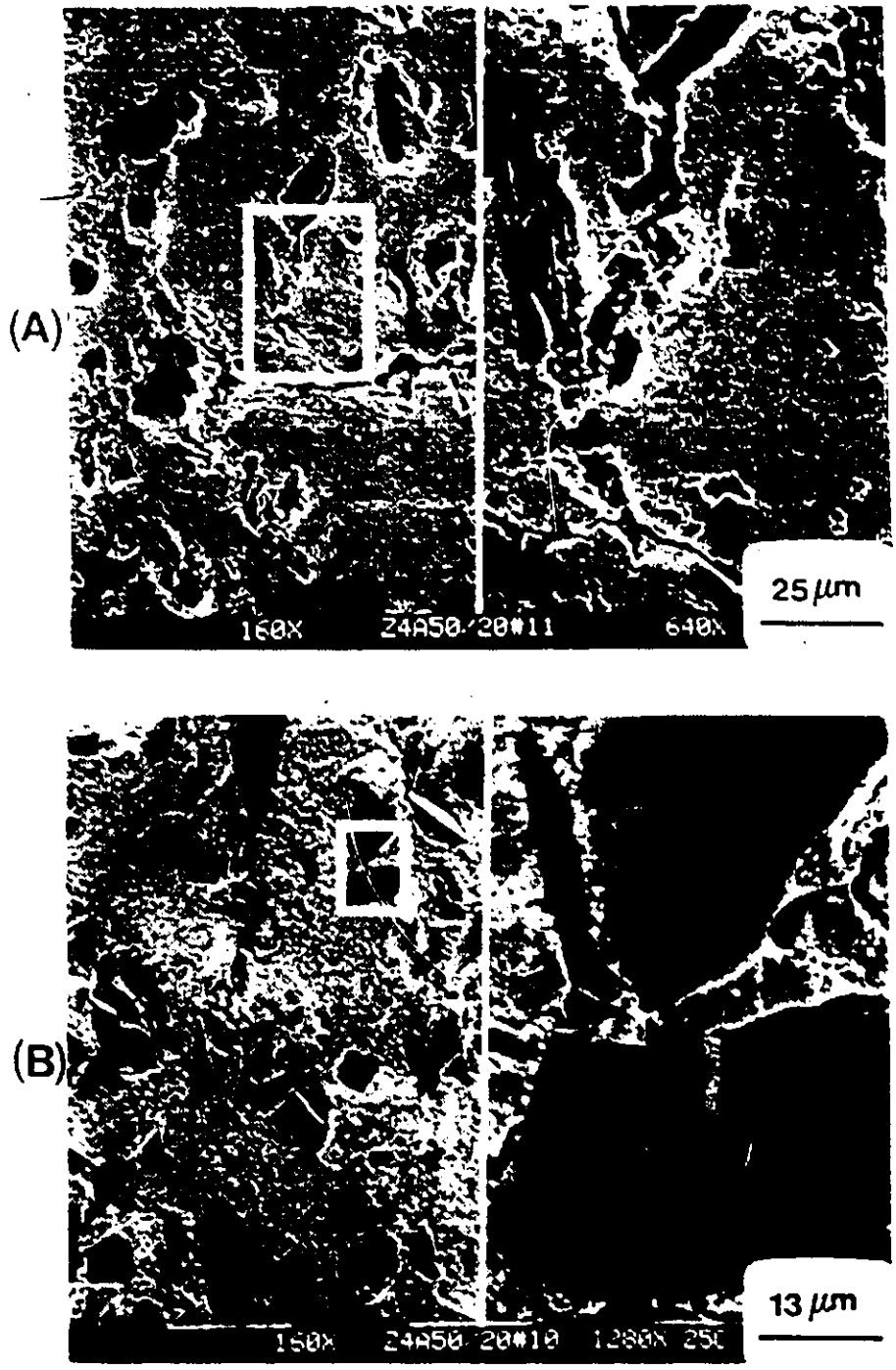

Fig. 5-36 Fractography of Z4A50 type ceramics : (A) Arrested crack ; (B) Fracture surface.

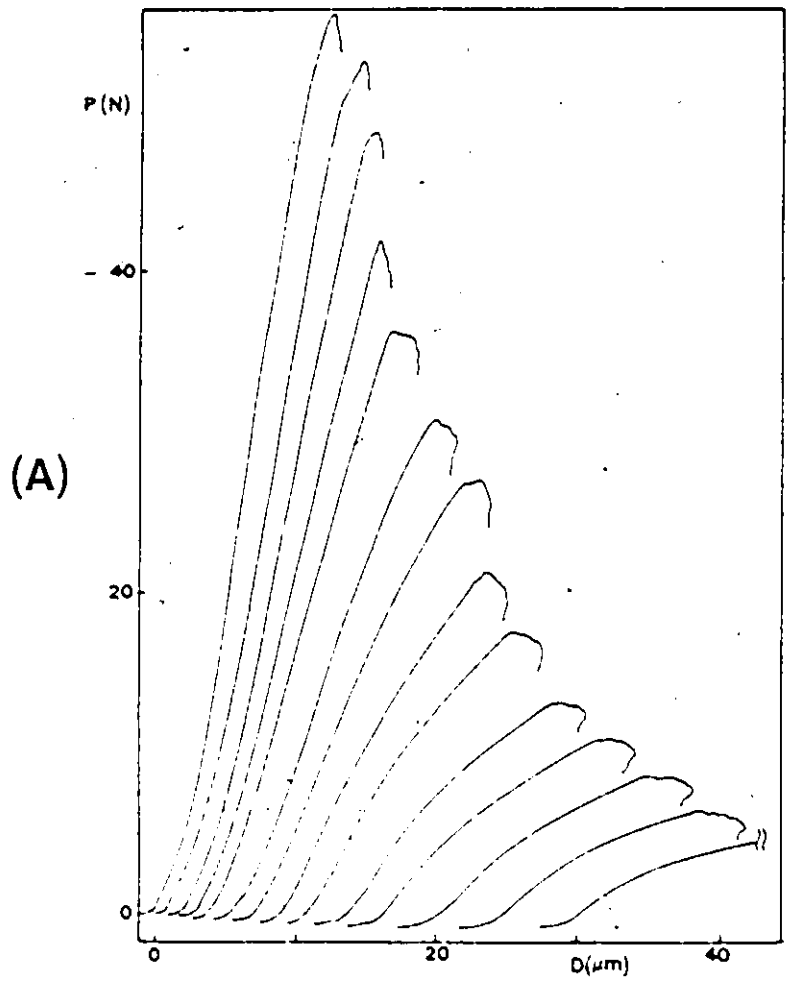

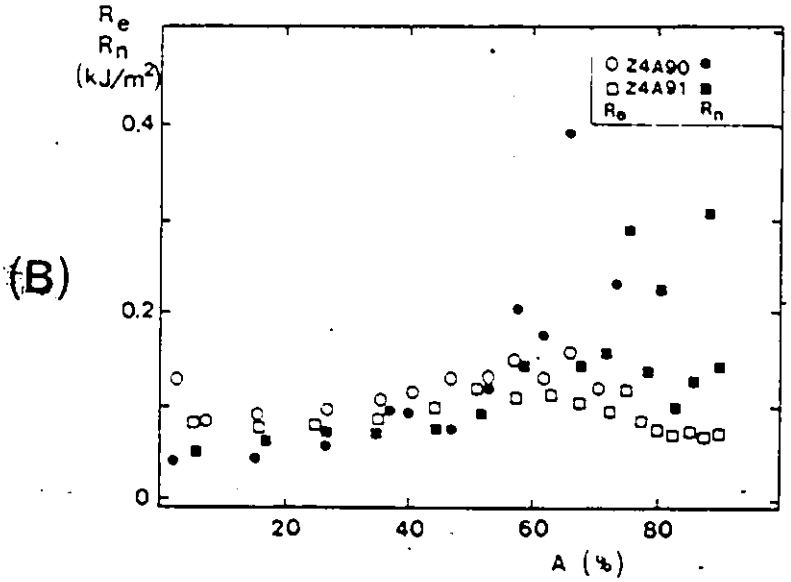

Fig. 5-37 Fracture testing results for Z4A90 type ceramics : (A) Load-displacement record ; (B) Resistance to fracture compiled for two specimens.

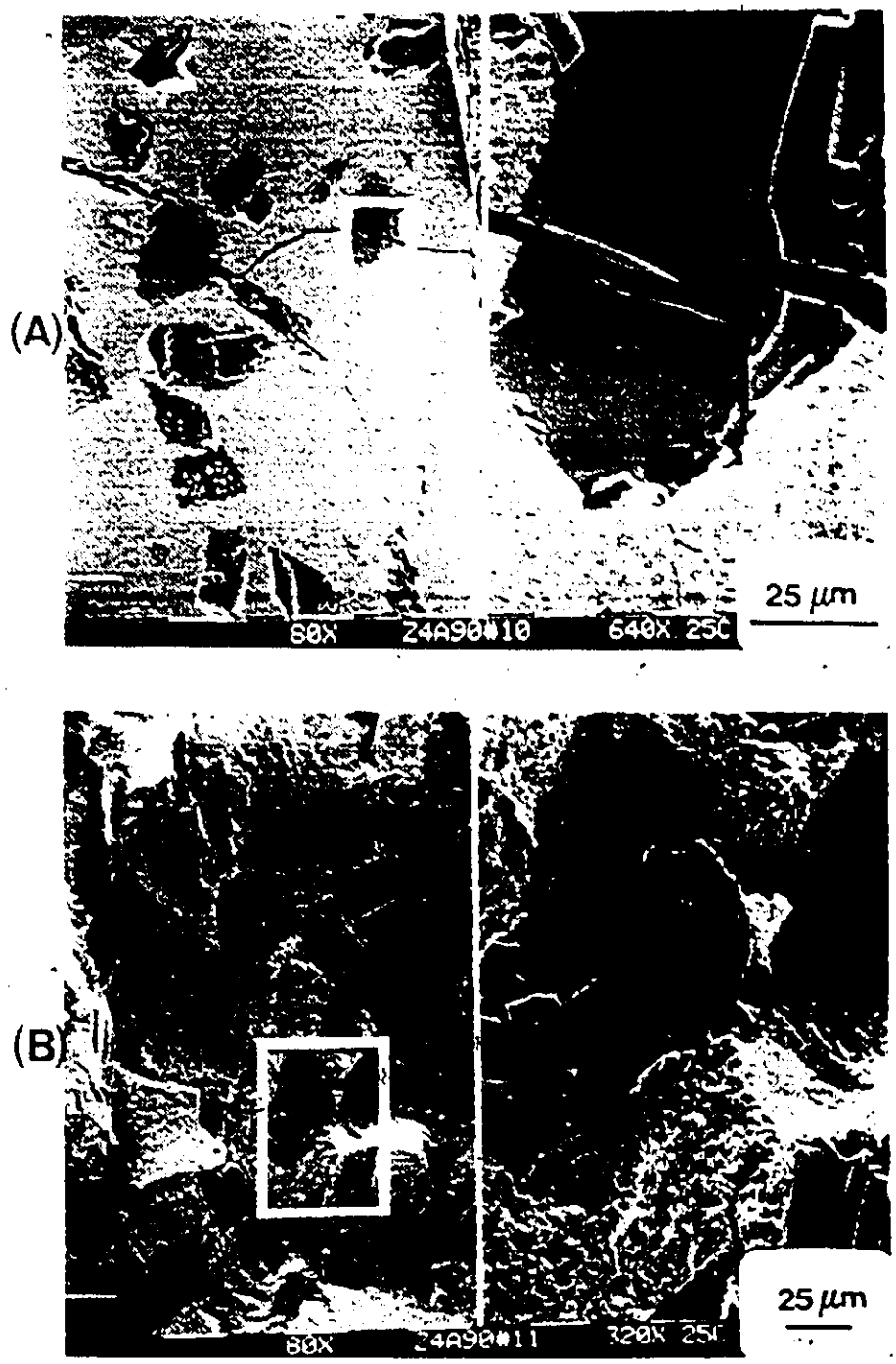

Fig. 5-38 Fractography of Z4A90 type ceramics :
(A) Arrested crack ; (B) Fracture surface.

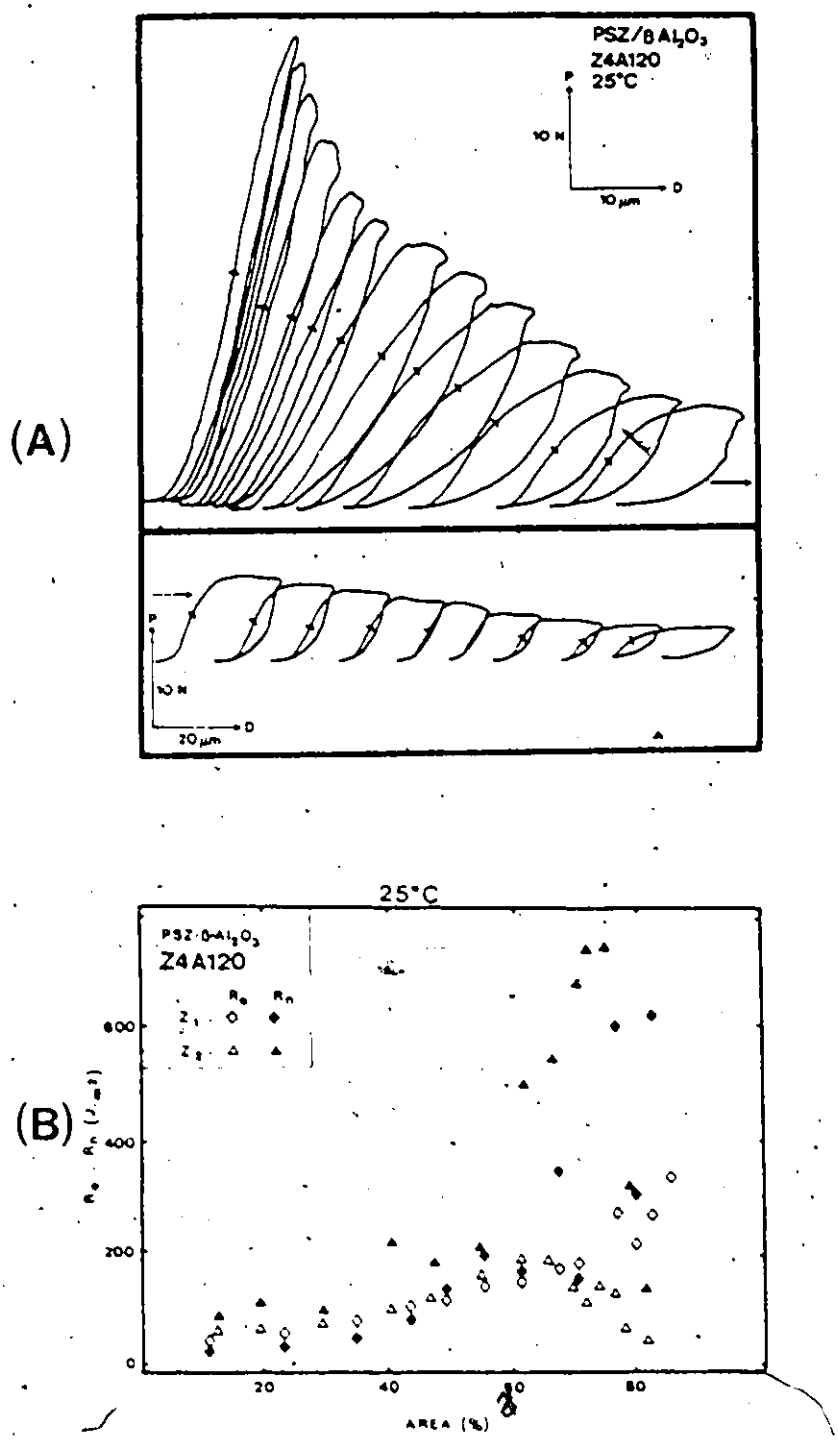

Fig. 5-39 Fracture testing results for Z4A120 type ceramics : (A) Load-displacement record ; (B) Resistance to fracture compiled for two specimens.

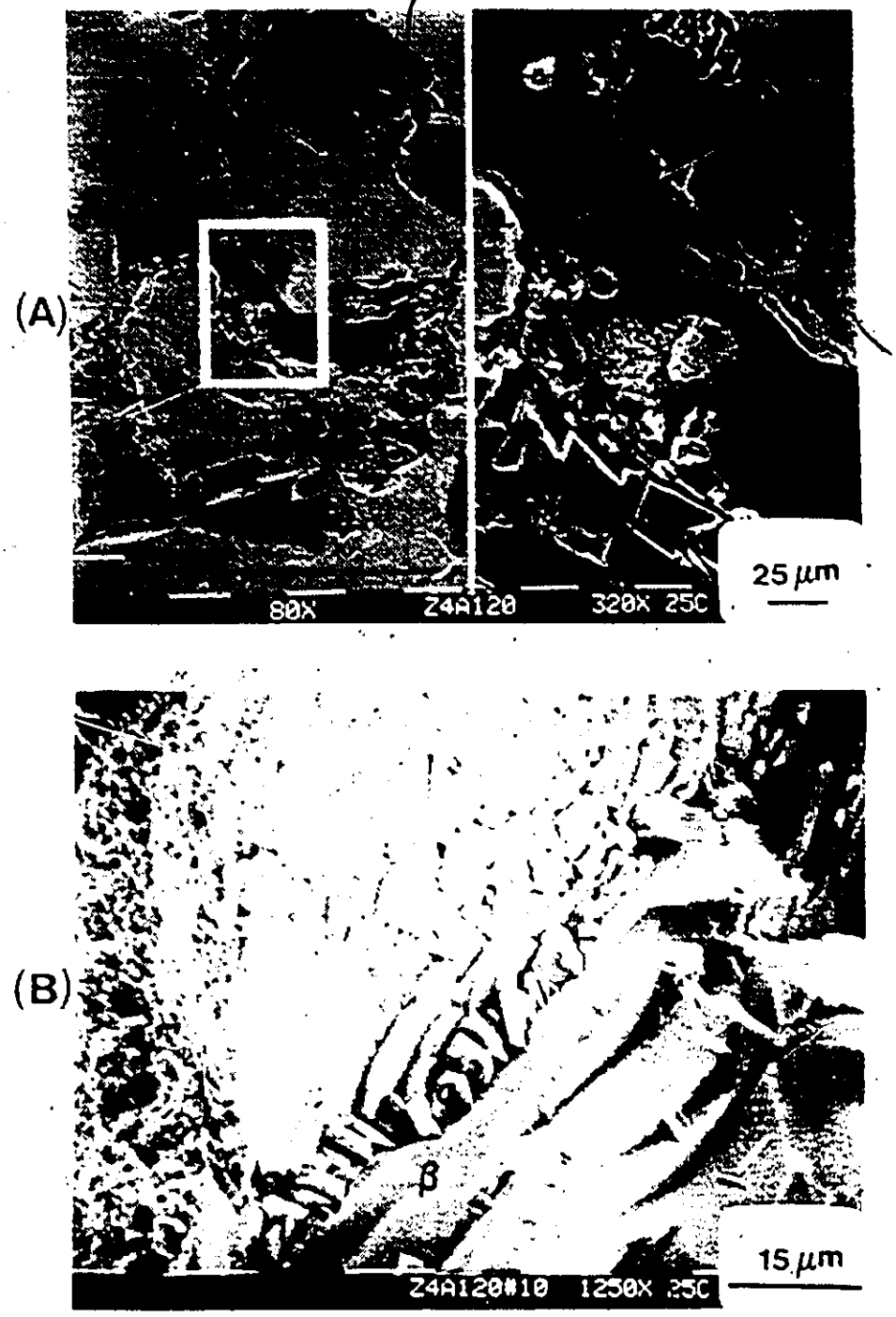

Fig. 5-40 Fractography of Z4A120 type ceramics :
(A) Arrested crack ; (B) Fracture surface.

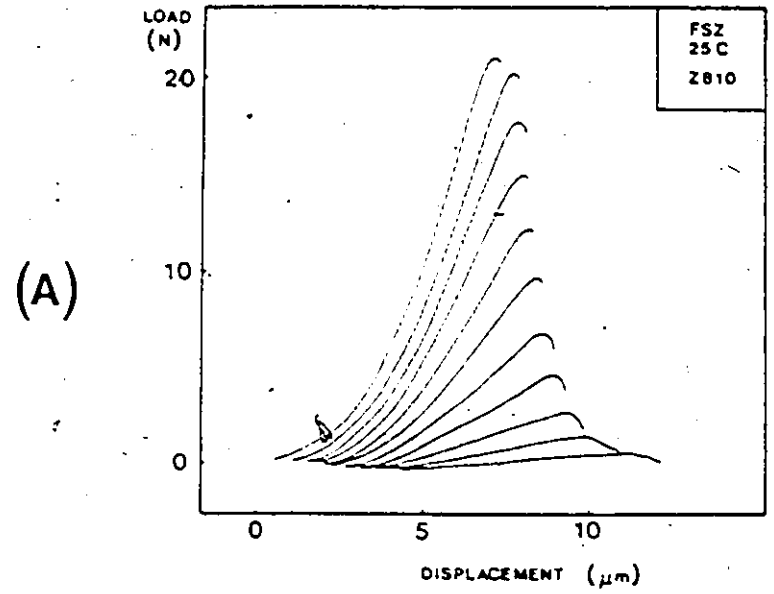

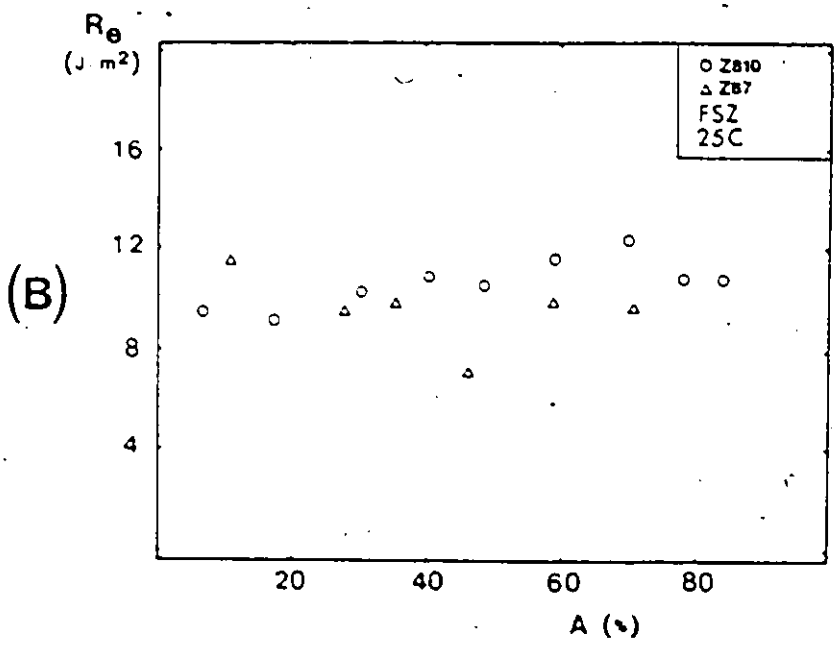

Fig. 5-41 Fracture testing results for FSZ :
(A) Load-displacement record ; (B) Resistance to fracture compiled for two specimens.

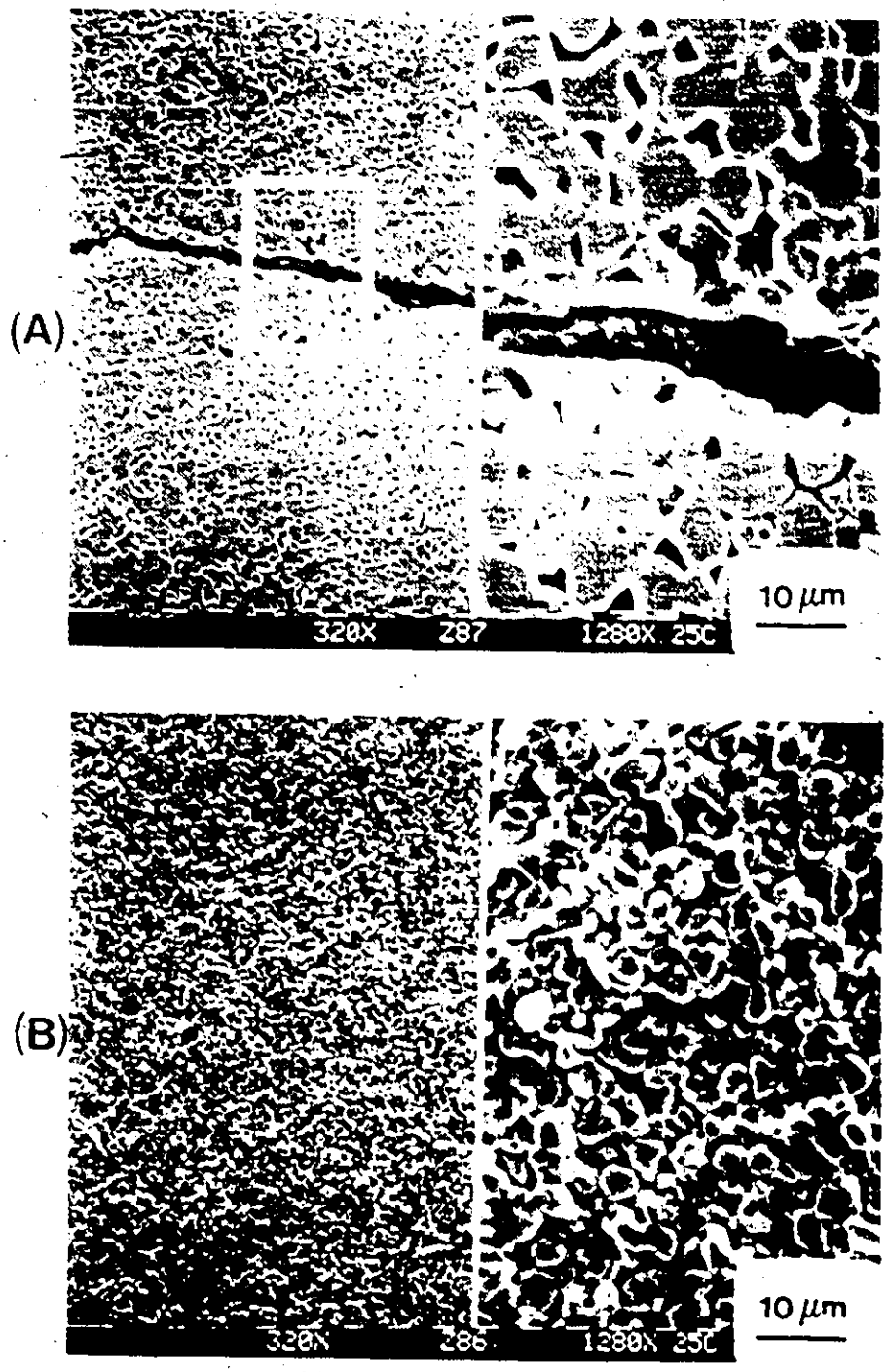

Fig. S-42 Fractography of FSZ : (A) Arrested crack ; (B) Fracture surface.

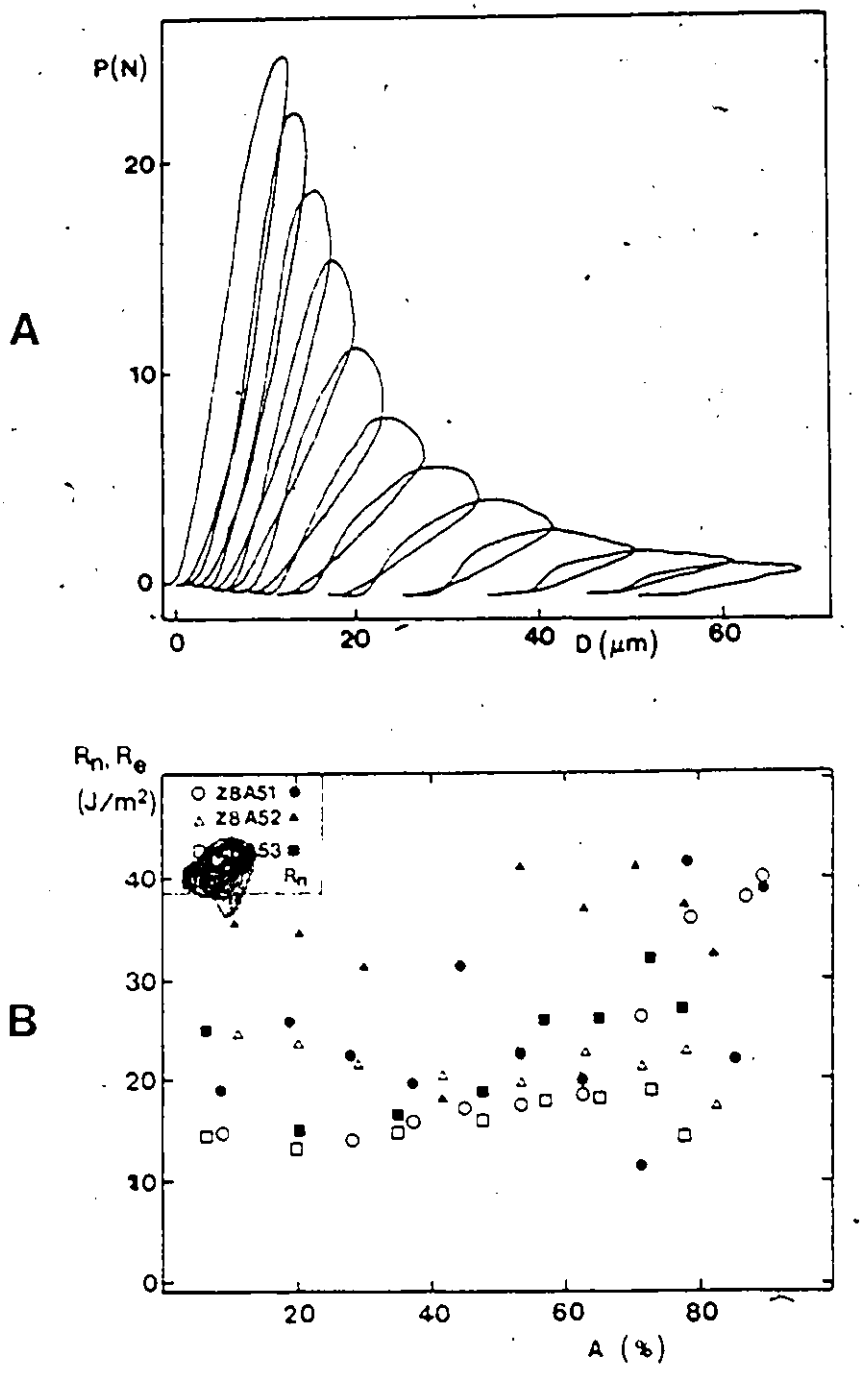

Fig. 5-43 Fracture testing results for Z8A50 type ceramics : (A) Load-displacement record ; (B) Resistance to fracture compiled for three specimens.

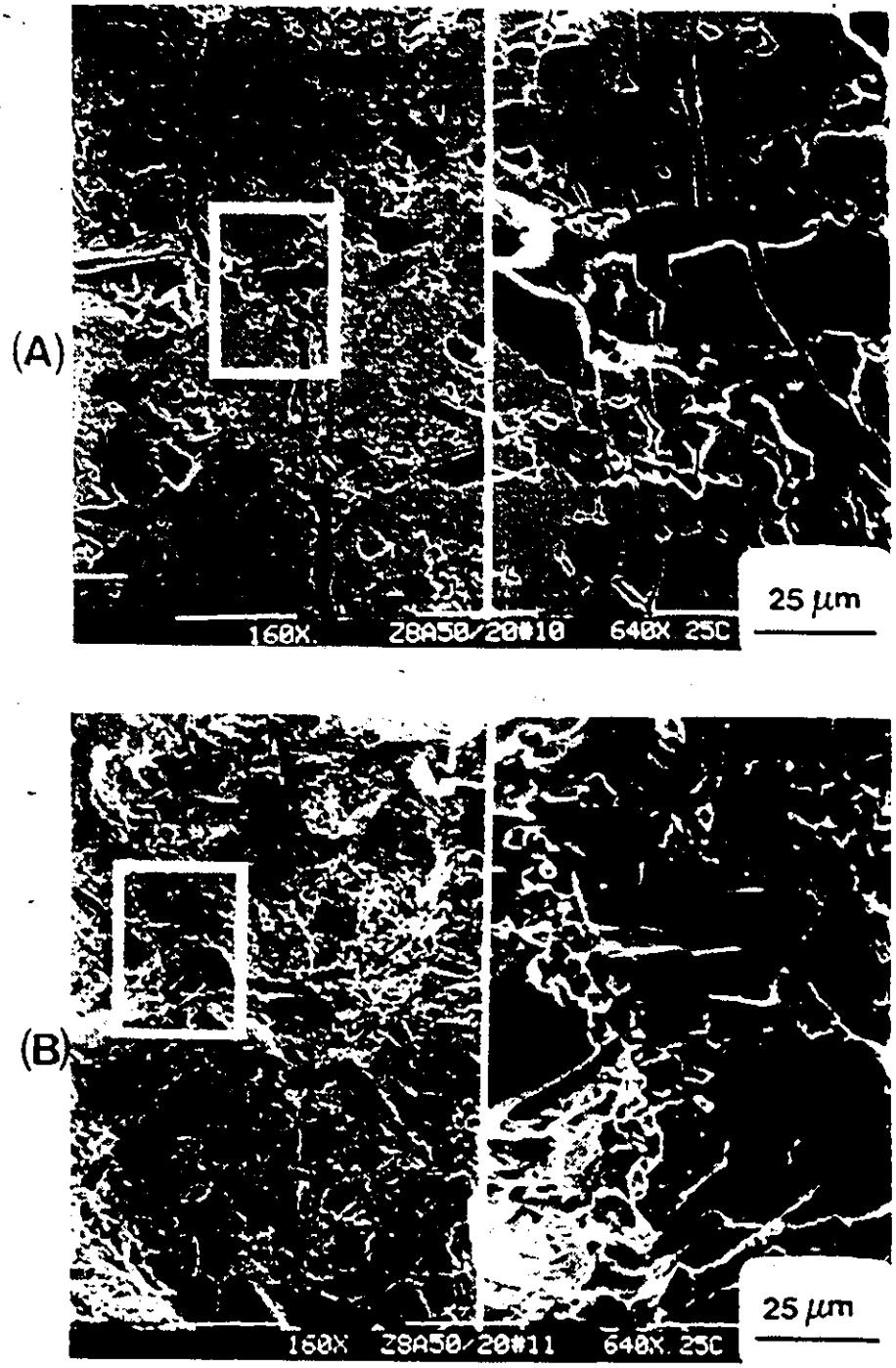

Fig. 5-44 Fractography of Z8A50 type ceramics :
(A) Arrested crack ; (B) Fracture surface.

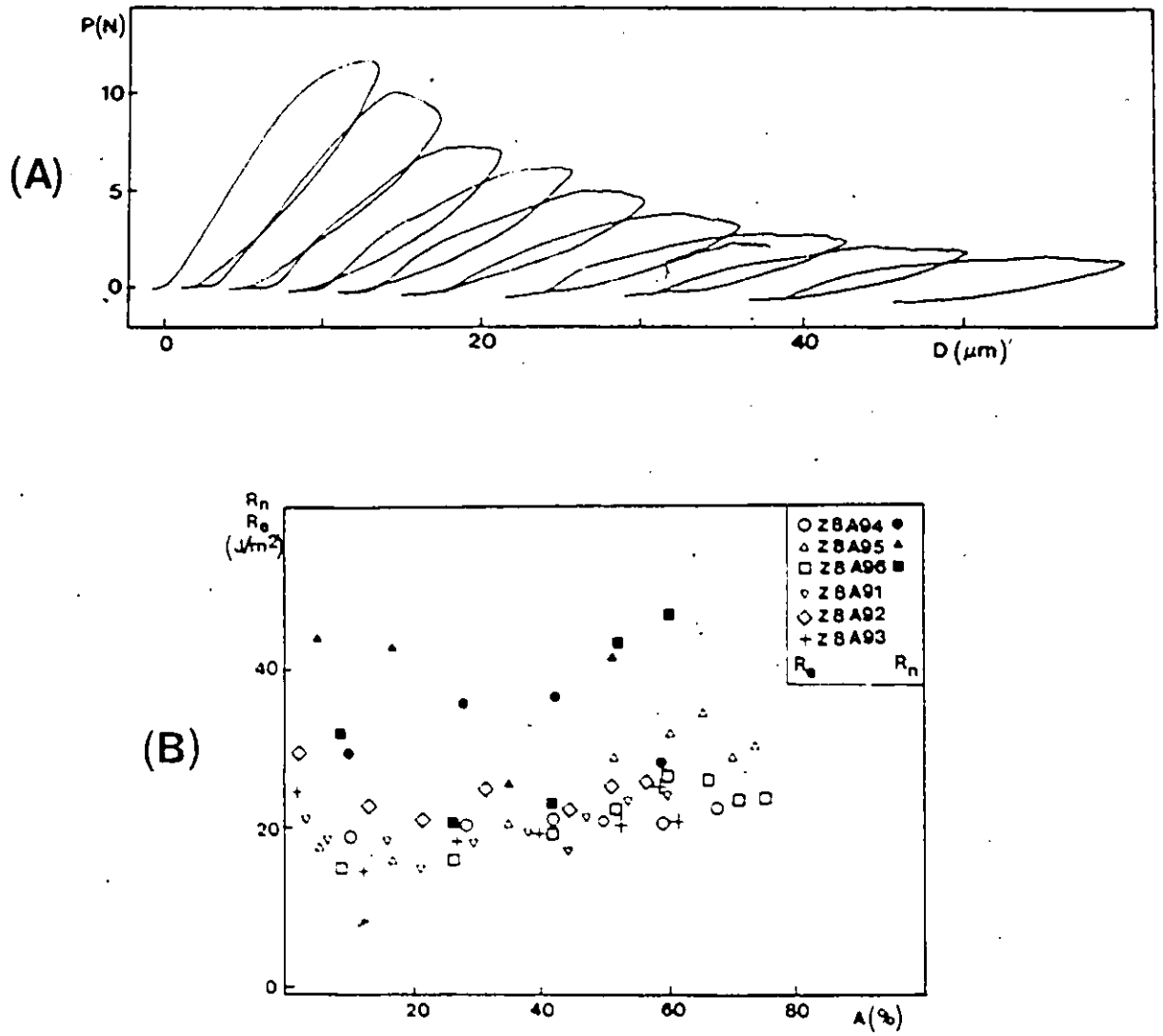

Fig. 5-45 Fracture testing results for Z8A90 type ceramics : (A) Load-displacement record ; (B) Resistance to fracture compiled for six specimens.

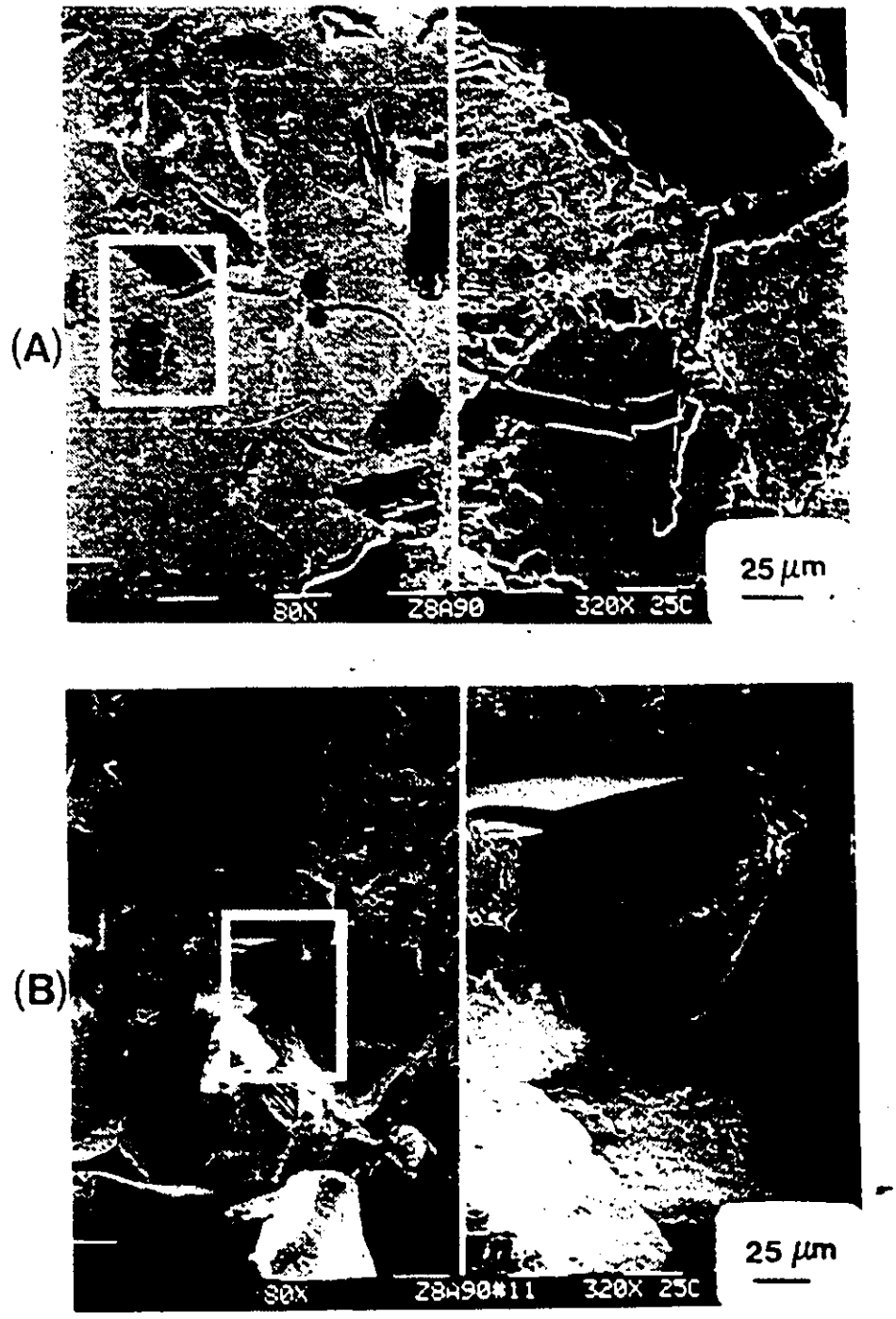

Fig. S-46 Fractography of Z8A90 type ceramics :
(A) Arrested crack ; (B) Fracture surface.

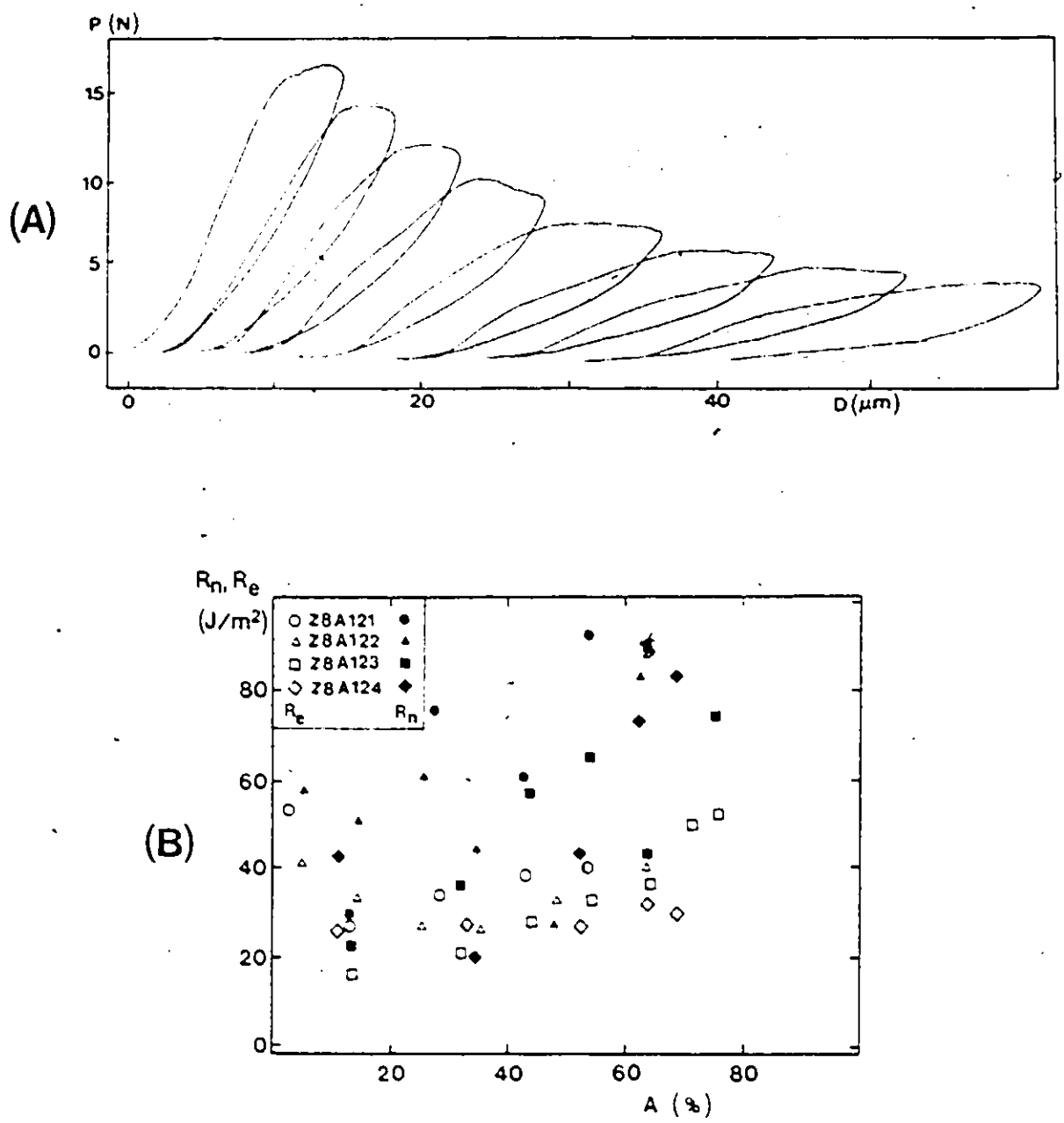

Fig. 5-47 Fracture testing results for Z8A120 type ceramics : (A) Load-displacement record ; (B) Resistance to fracture compiled for four specimens.

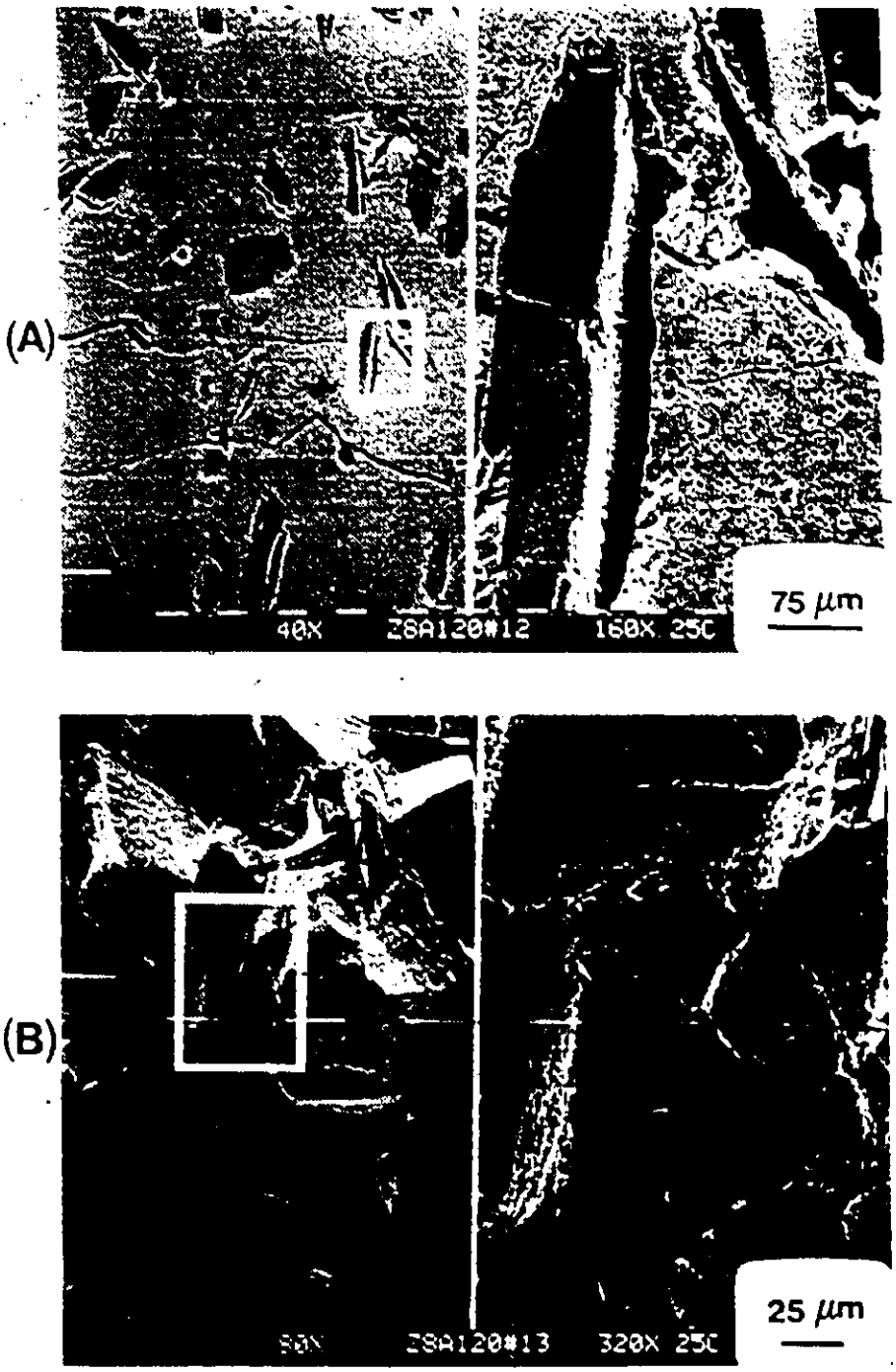

Fig. 5-48 Fractography of Z4A120 type ceramics :
(A) Arrested crack ; (B) Fracture surface.

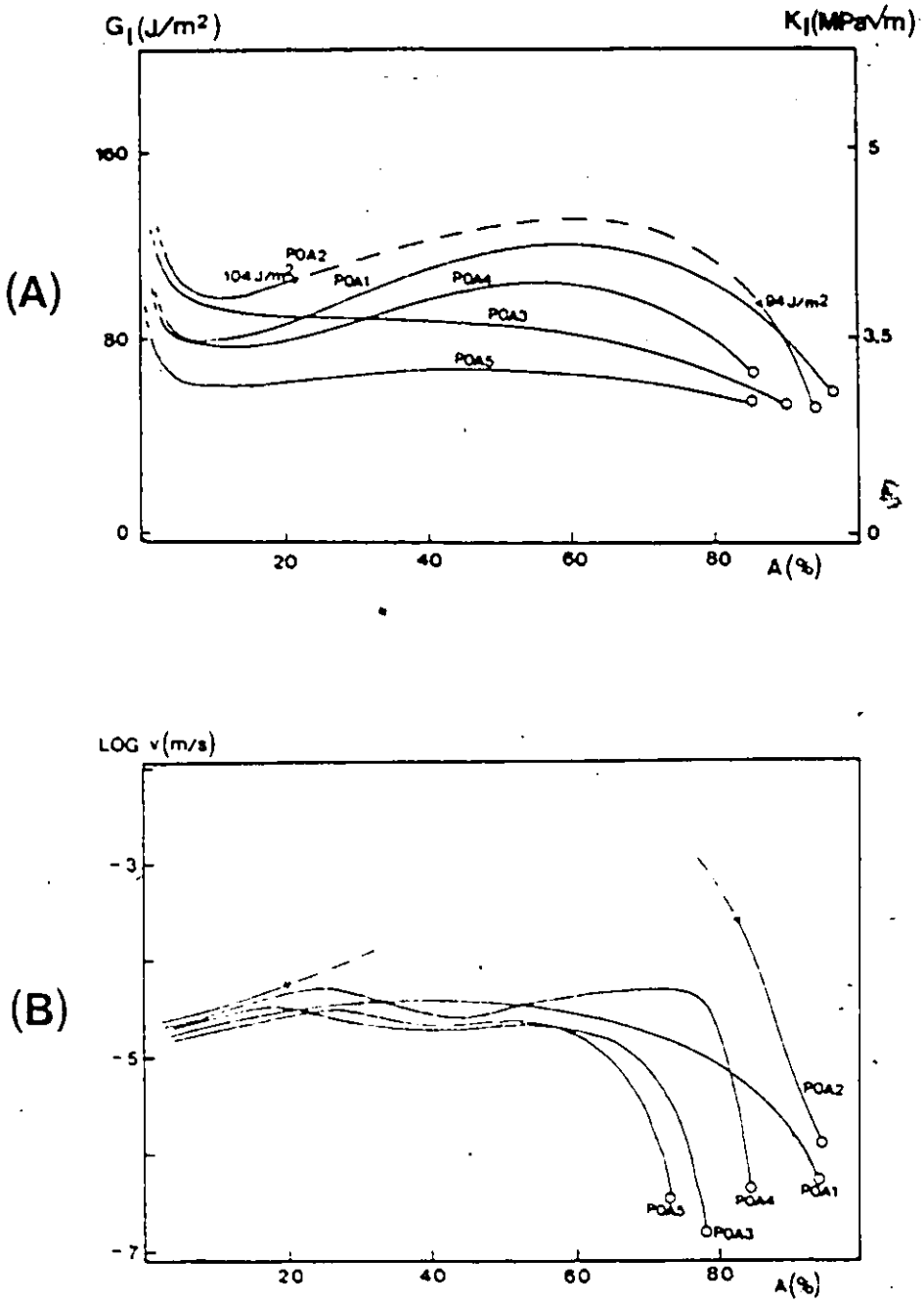

Fig. 5-49 Load-relaxation results for POA type ceramics : (A) Crack driving force ; (B) Crack velocity.

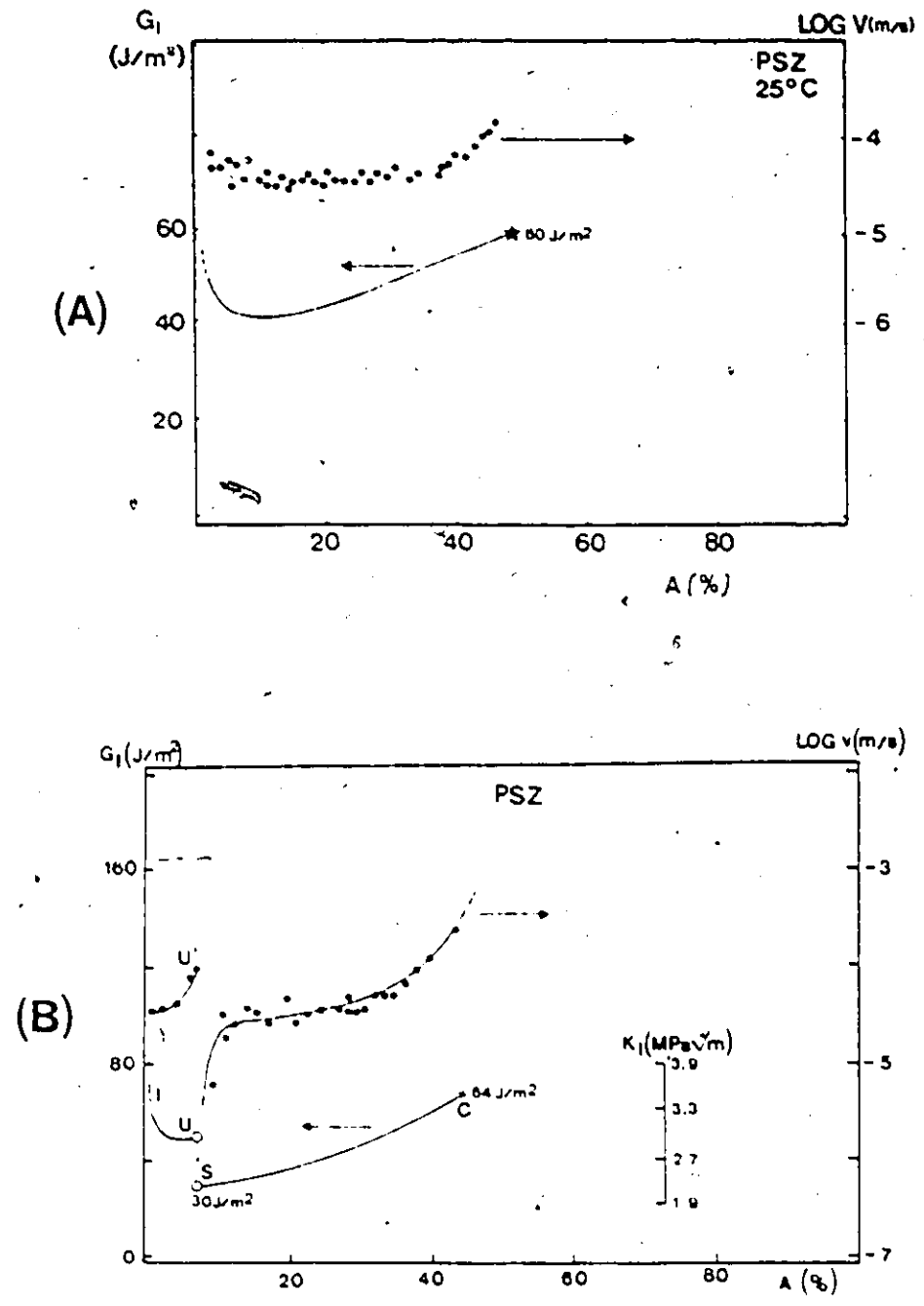

Fig. 5-50 Load-relaxation results for commercial PSZ:
(A) Continuous test up to critical conditions ;
(B) Specimen unloaded and reloaded.

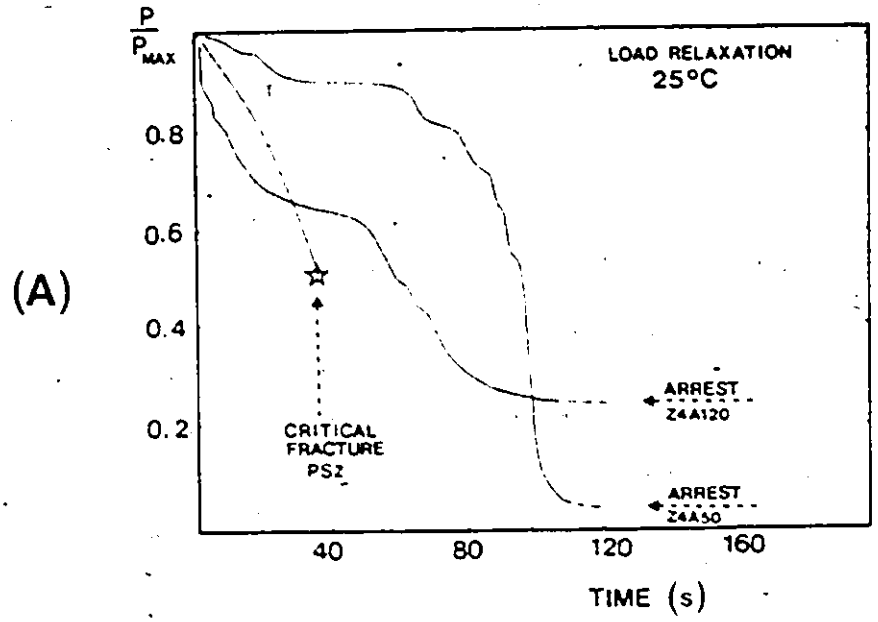

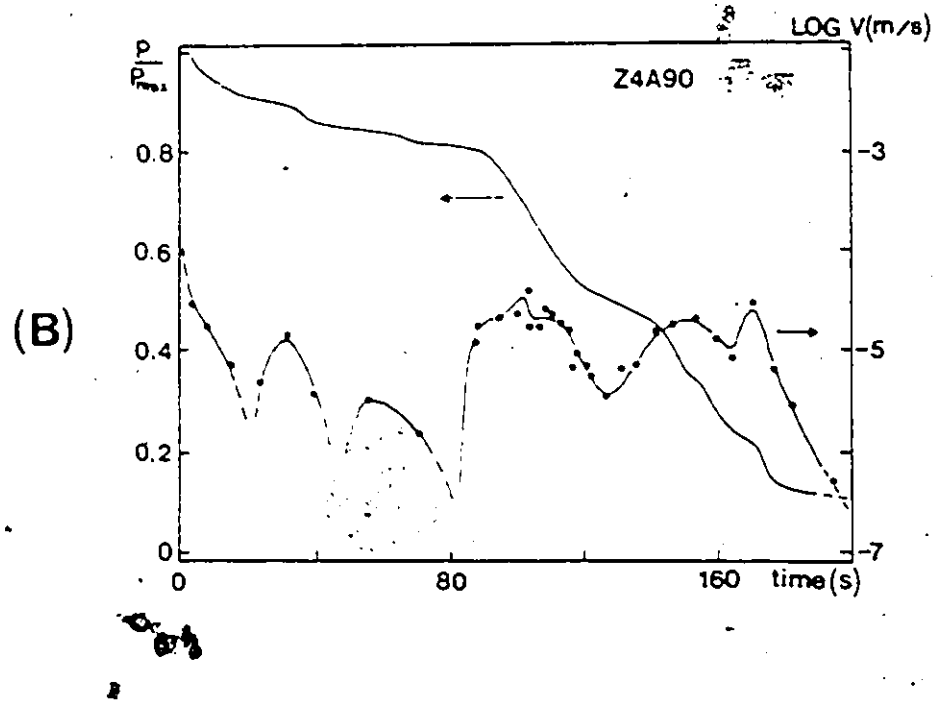

Fig. S-51 Load-relaxation records for PSZ and PSZ-beta-alumina composites : (A) PSZ, Z4A50, Z4A120 ; (B) Z4A90, with the crack velocity curve.

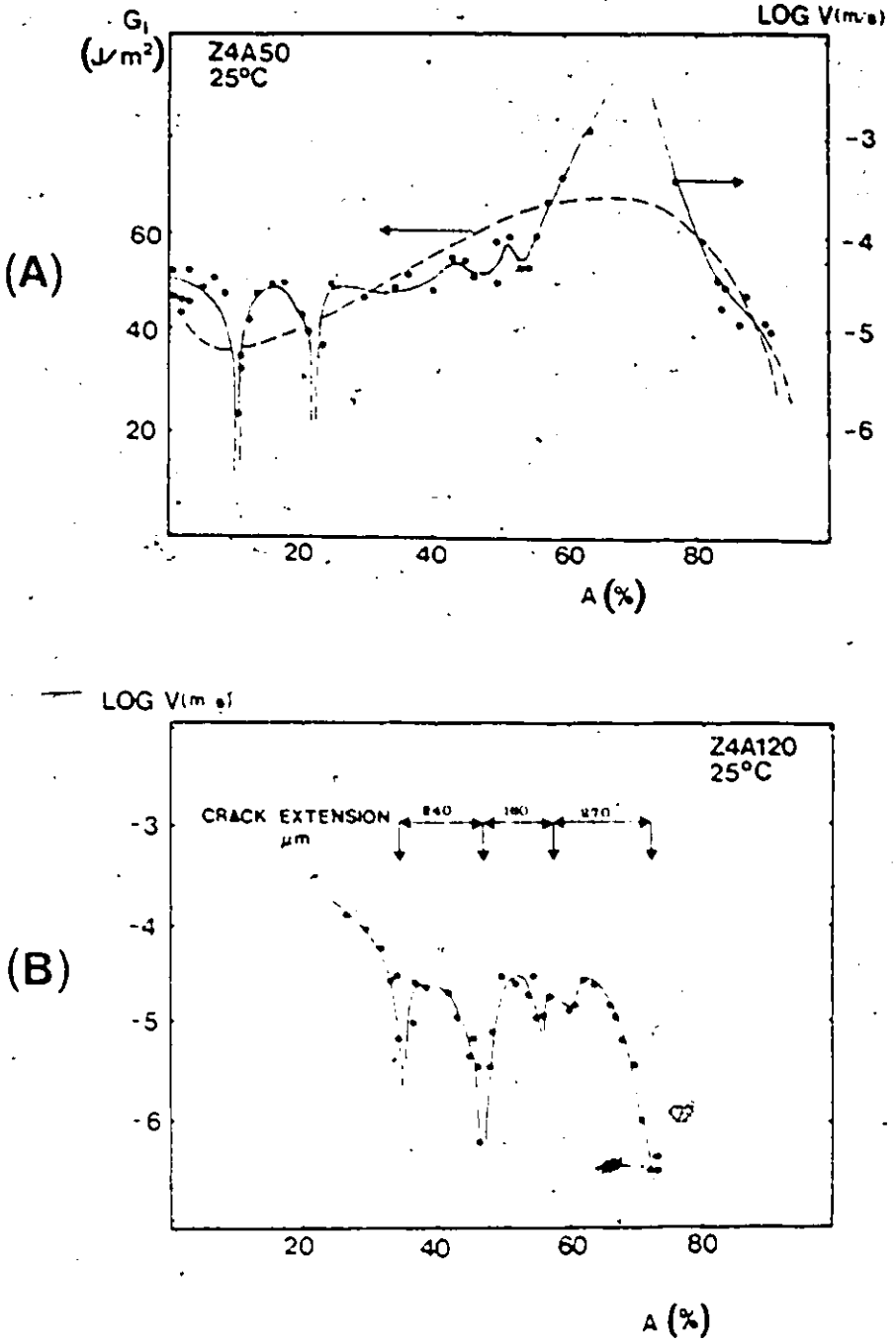

Fig. 5-52 Crack velocity variation against fracture area, for PSZ-beta-alumina composites: (A) For Z4A50 (accompanied by an approximate crack driving force graph) ; (B) For Z4A120.

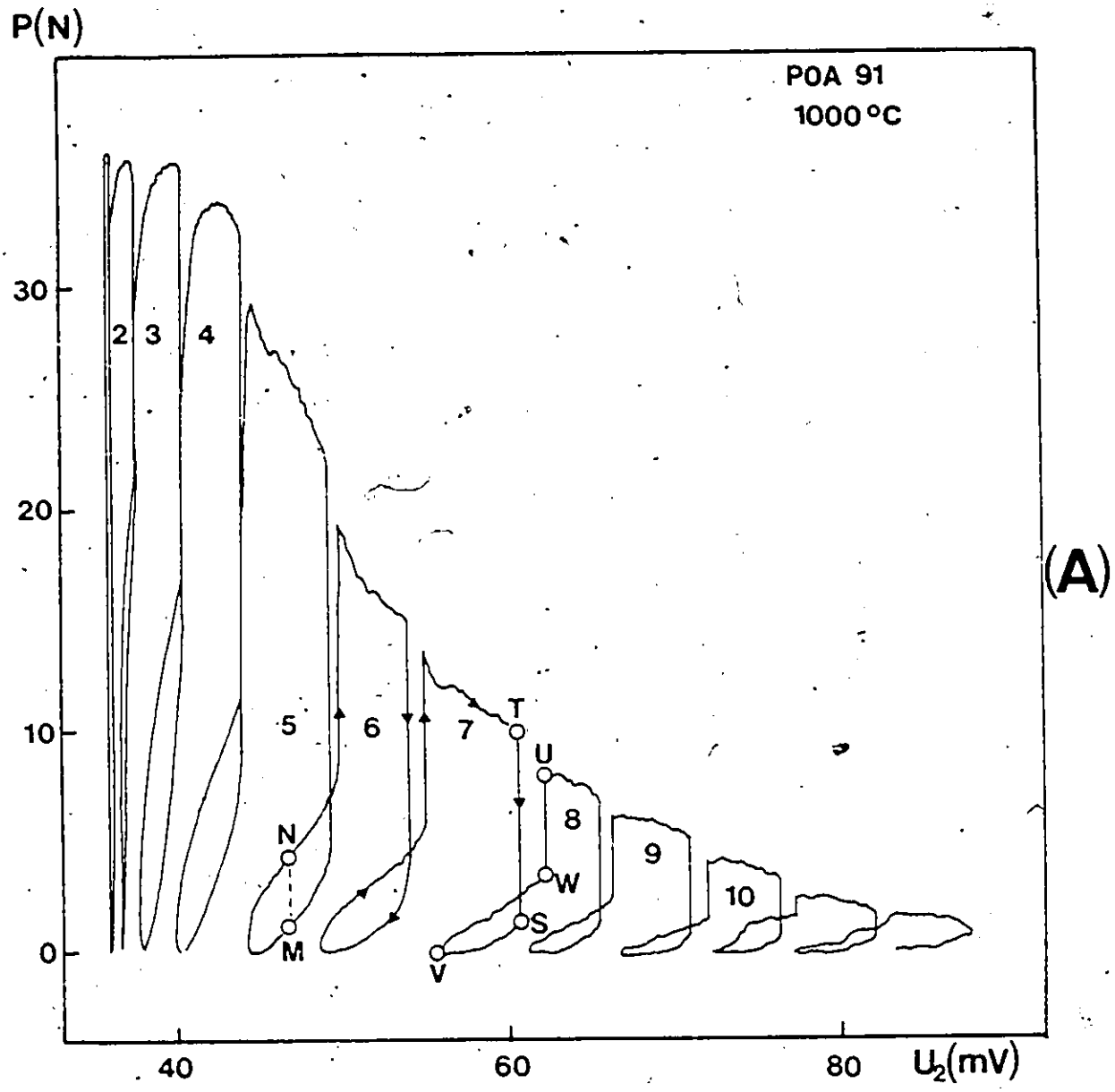

Fig. 5-53 Elevated temperature fracture testing results for P0A type ceramics: (A) Load vs. potential drop at 1000°C, i=1 mA ; (B) Load vs. potential drop at 1300°C, i=5 mA ; (C) Resistance to fracture.

(B)

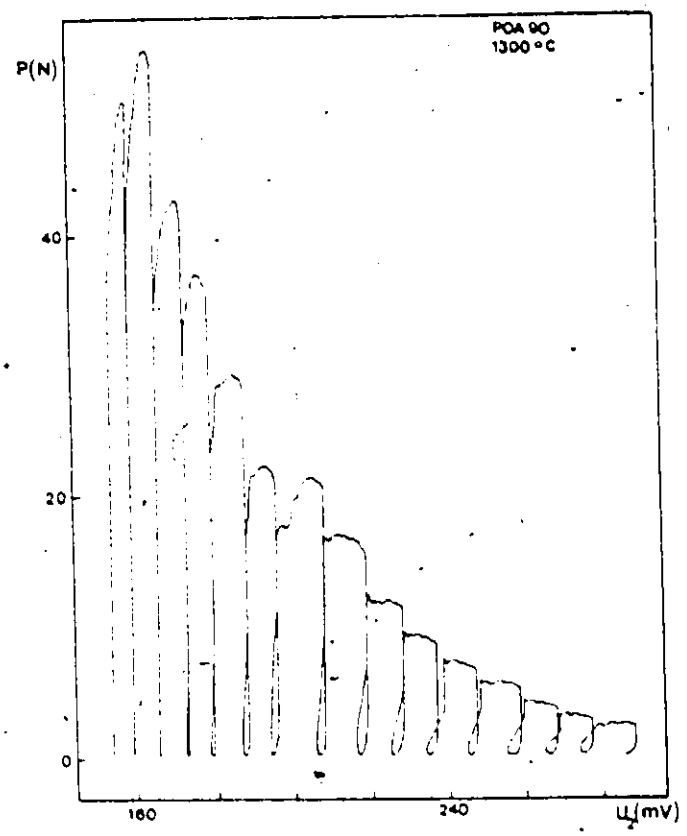

(C)

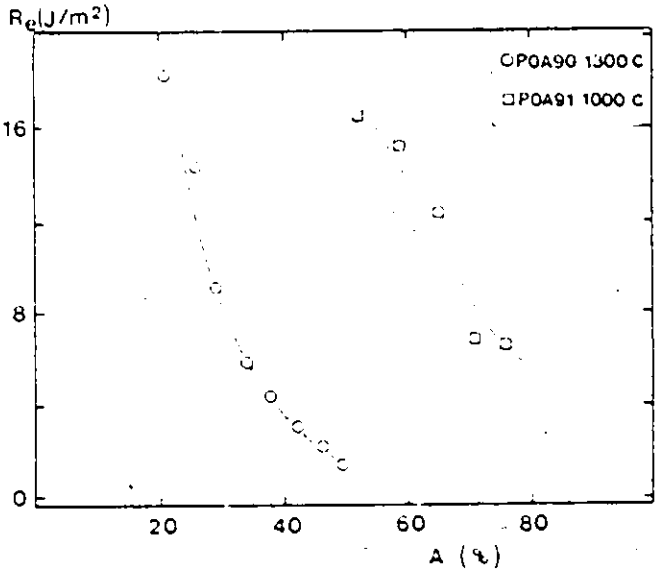

Fig. 5-53 Continued

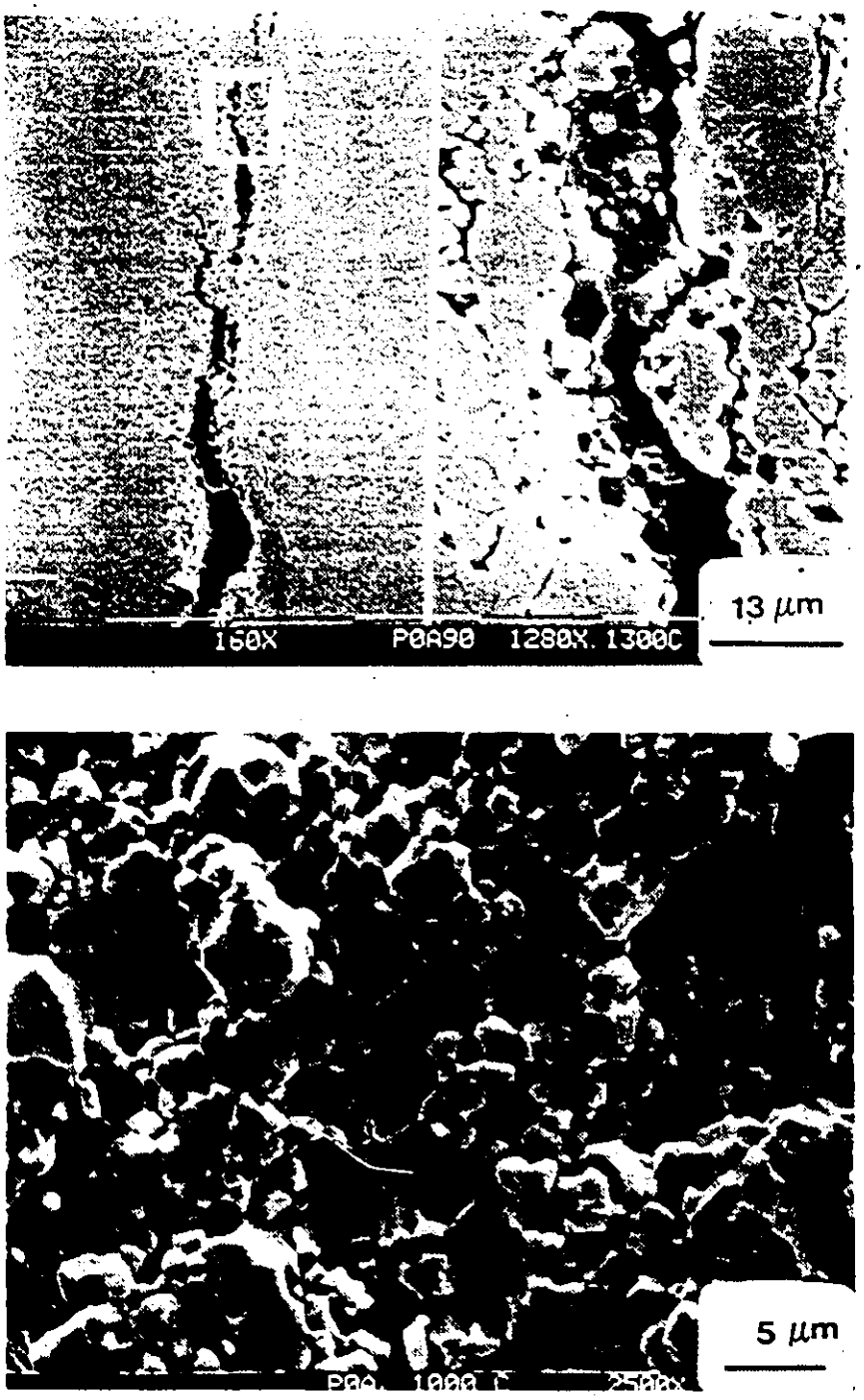

Fig. 5-54 Fractography of POA type ceramics : (A) Arrested crack at 1300°C ; (B) Fracture surface at 1000°C.

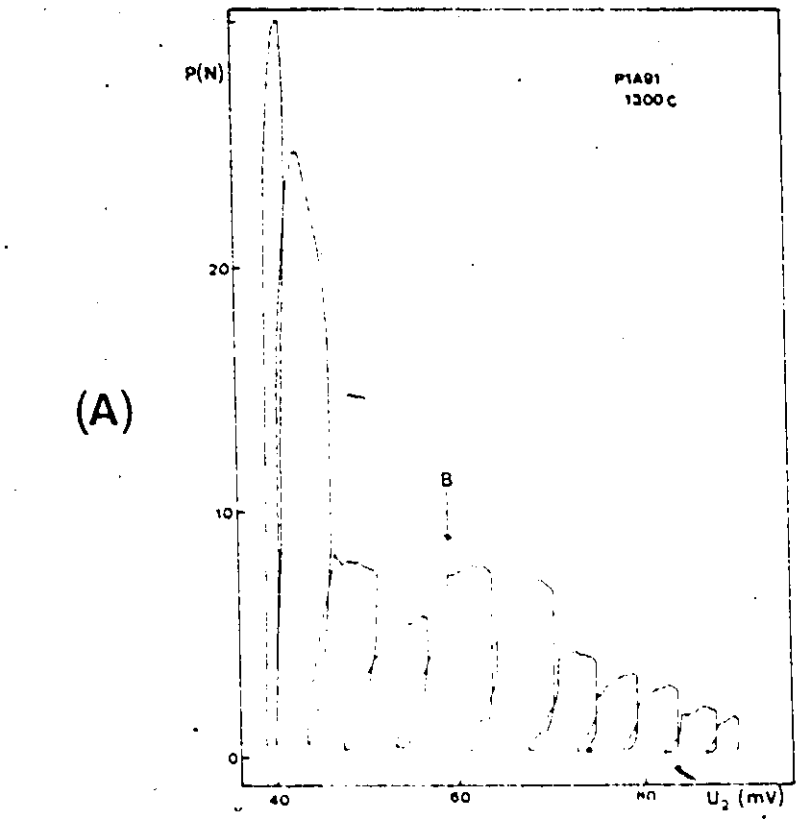

Fig. 5-55 Fracture testing results for P1A type ceramics:
(A) Load vs. potential drop record at 1300°C;
(B) Resistance to fracture at 1000 and 1300°C.

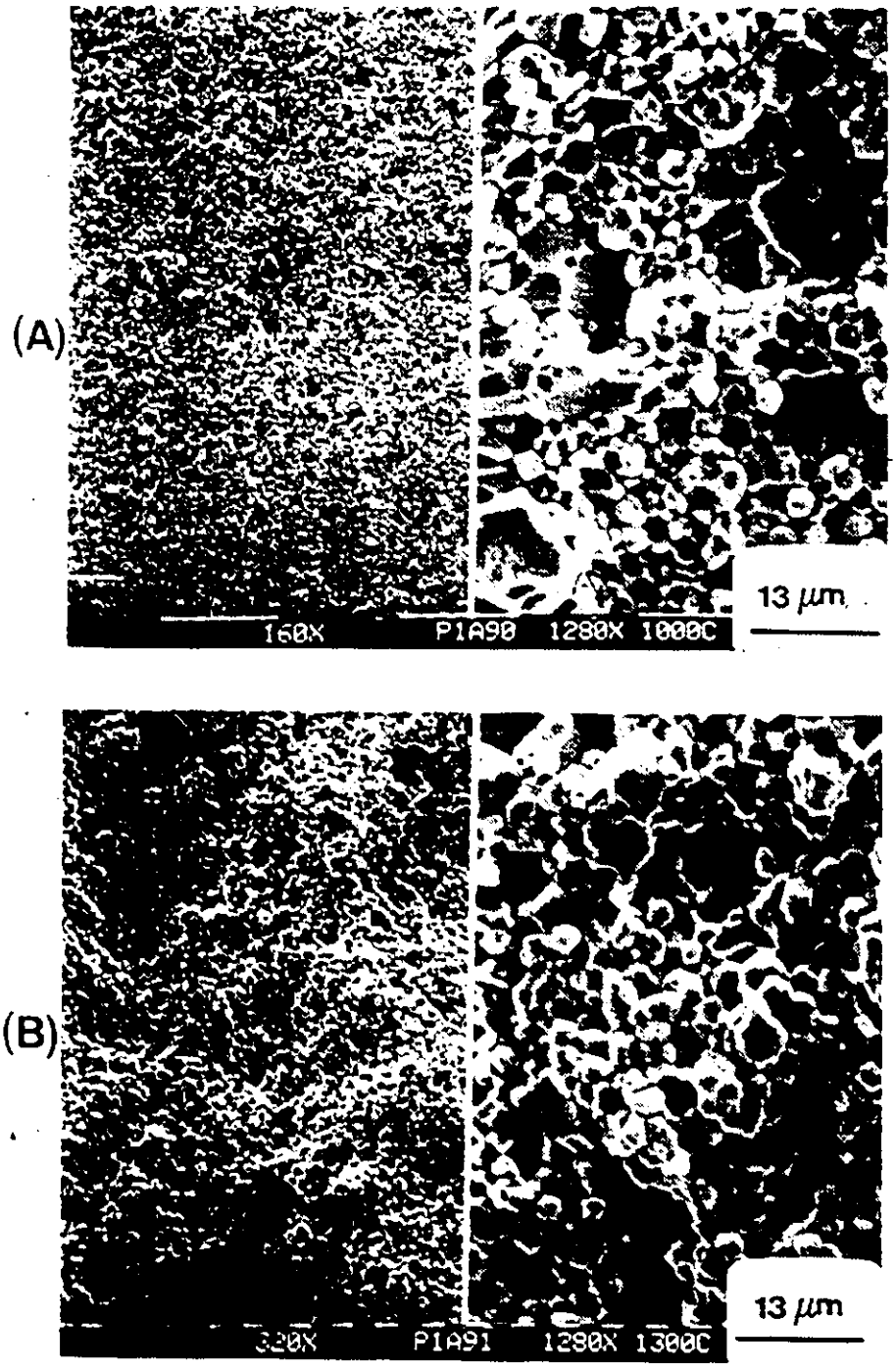

Fig. S-S6 Fracture surface of P1A type ceramics: (A) At 1000°C ; (B) At 1300°C.

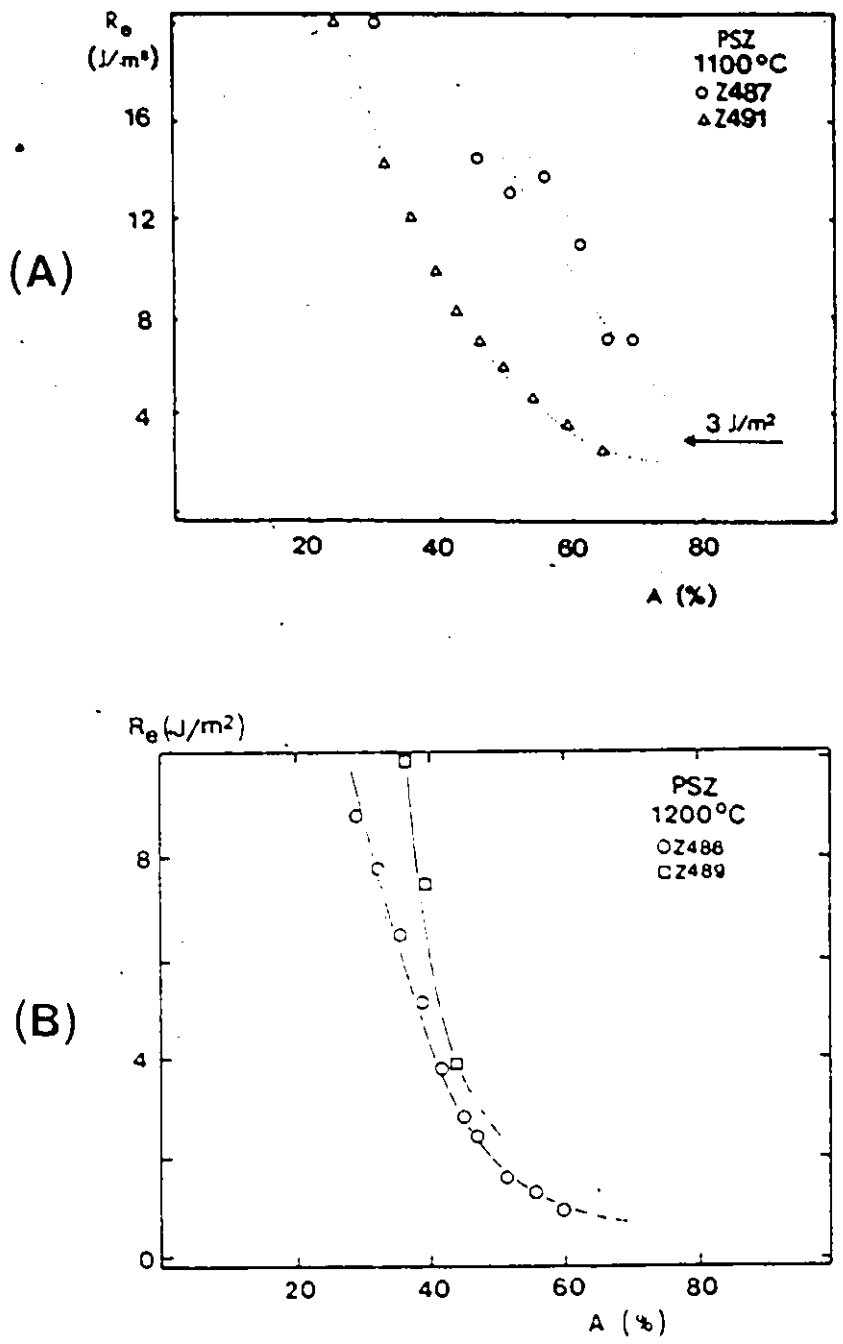

Fig. 5-57 Elevated temperature fracture testing results for PSZ : (A) Resistance to fracture at 1100°C ; (B) Resistance to fracture at 1200°C ; (C) Load vs. potential drop at 1300°C ; (D) Resistance to fracture at 1300°C.

(C)

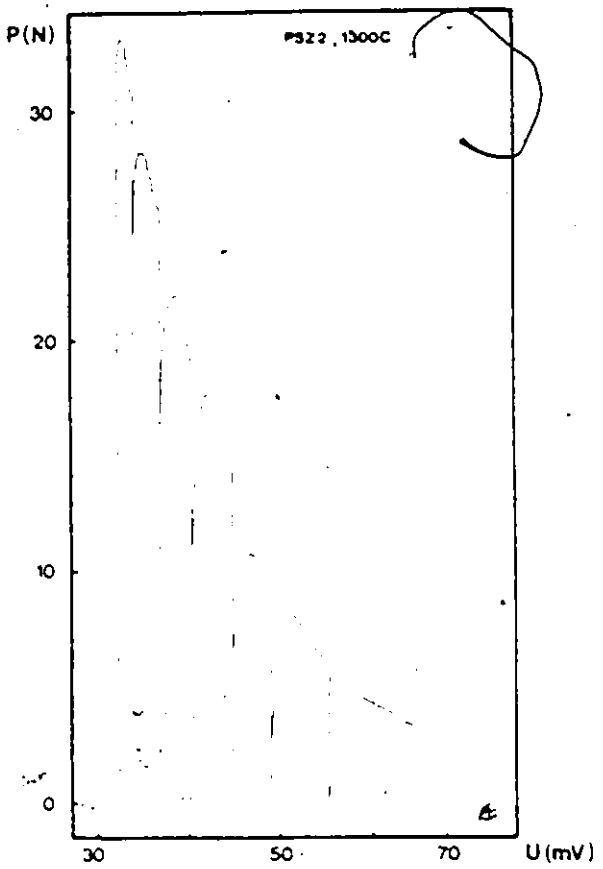

(D)

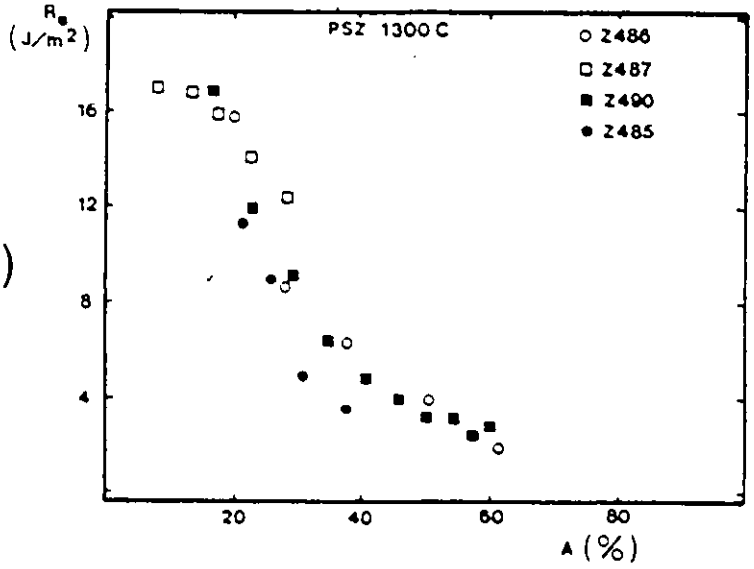

Fig. 5-57 Continued

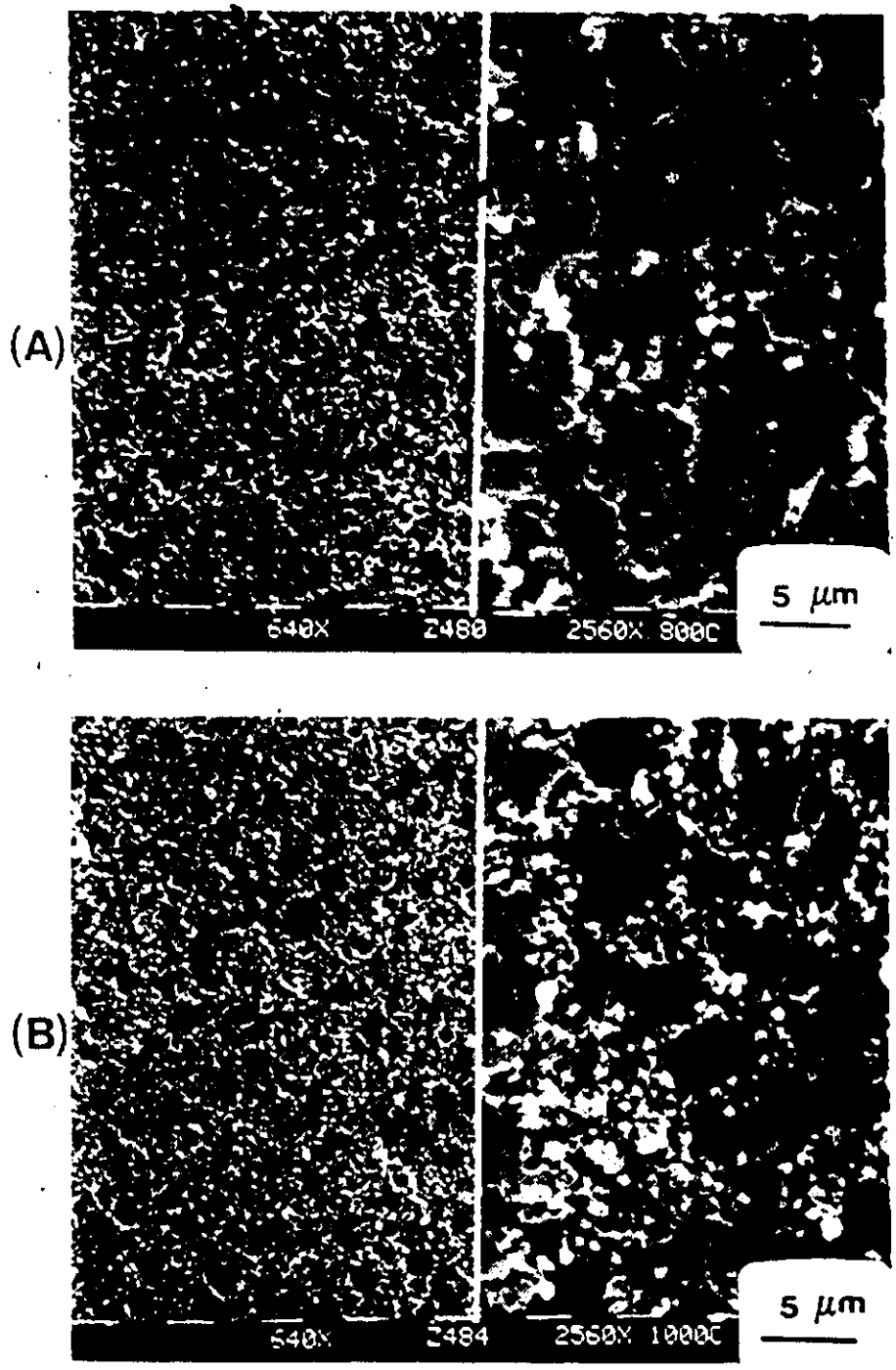

Fig. 5-58 Elevated temperature fractography of PSZ :
(A) 800°C ; (B) 1000°C ; (C) 1100°C ; (D) 1200°C ;
(E) 1300°C ; (F) Crack arrested at 1300°C ;
(G) Crack arrested at 1100°C.

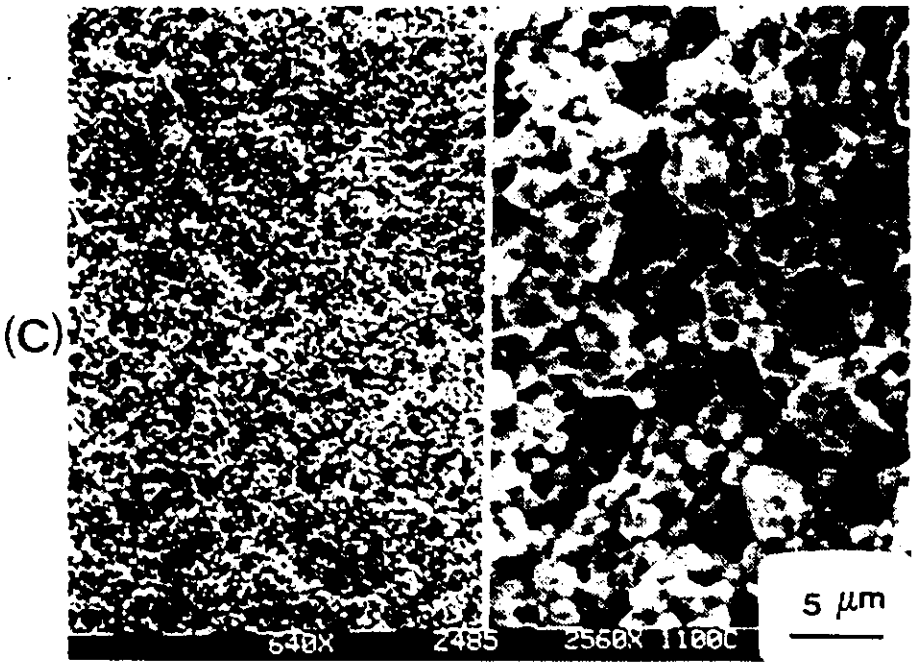

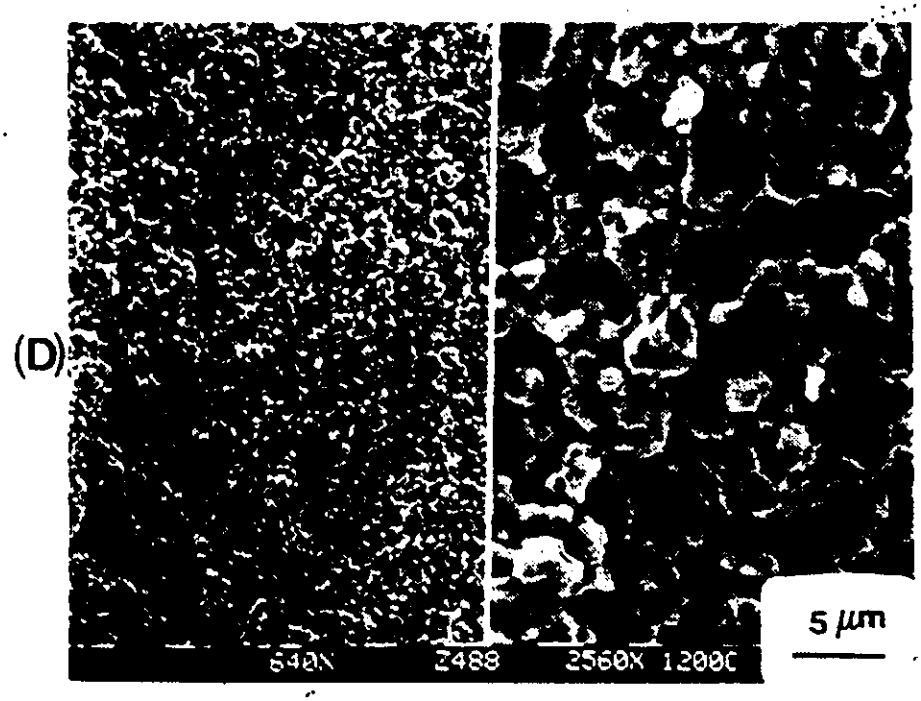

Fig. S-S8 Continued

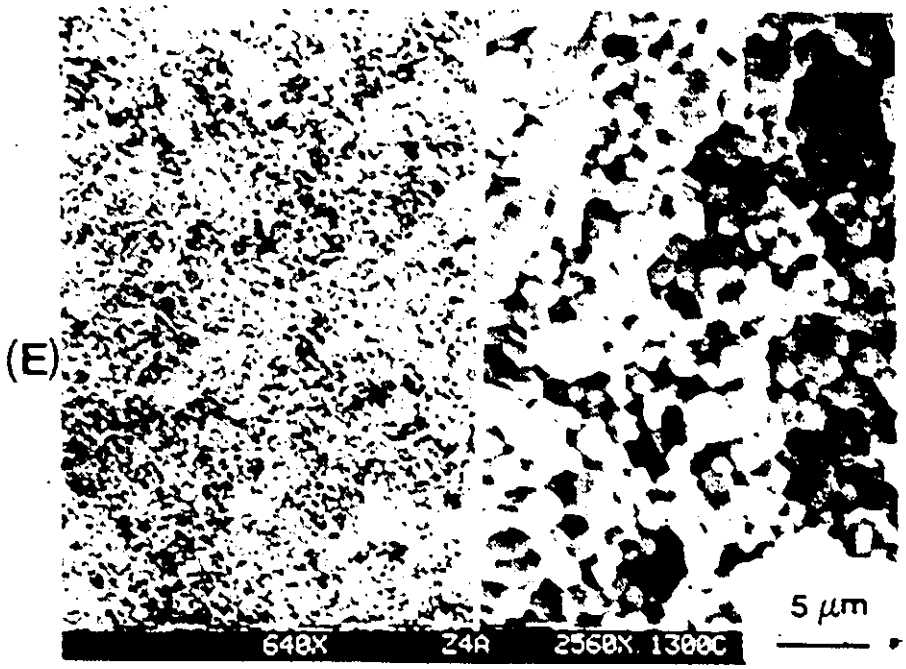

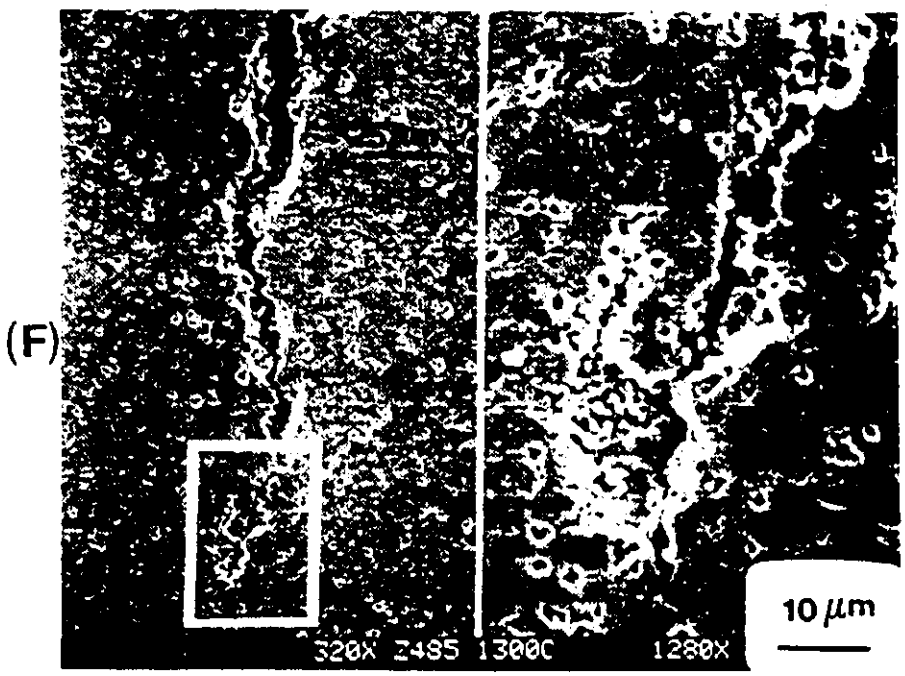

Fig. S-58 Continued

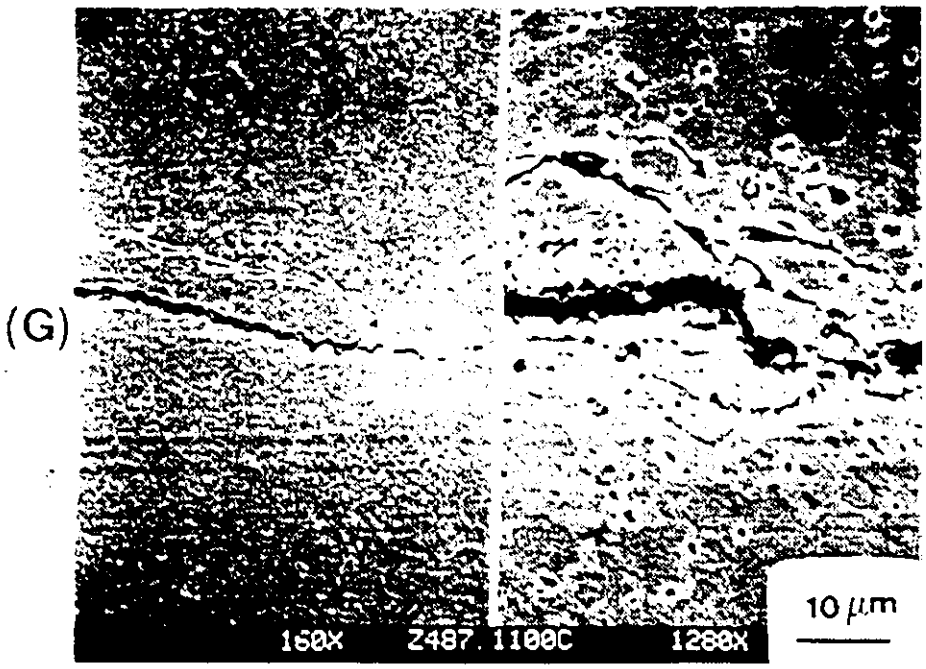

Fig. 5-58 Continued

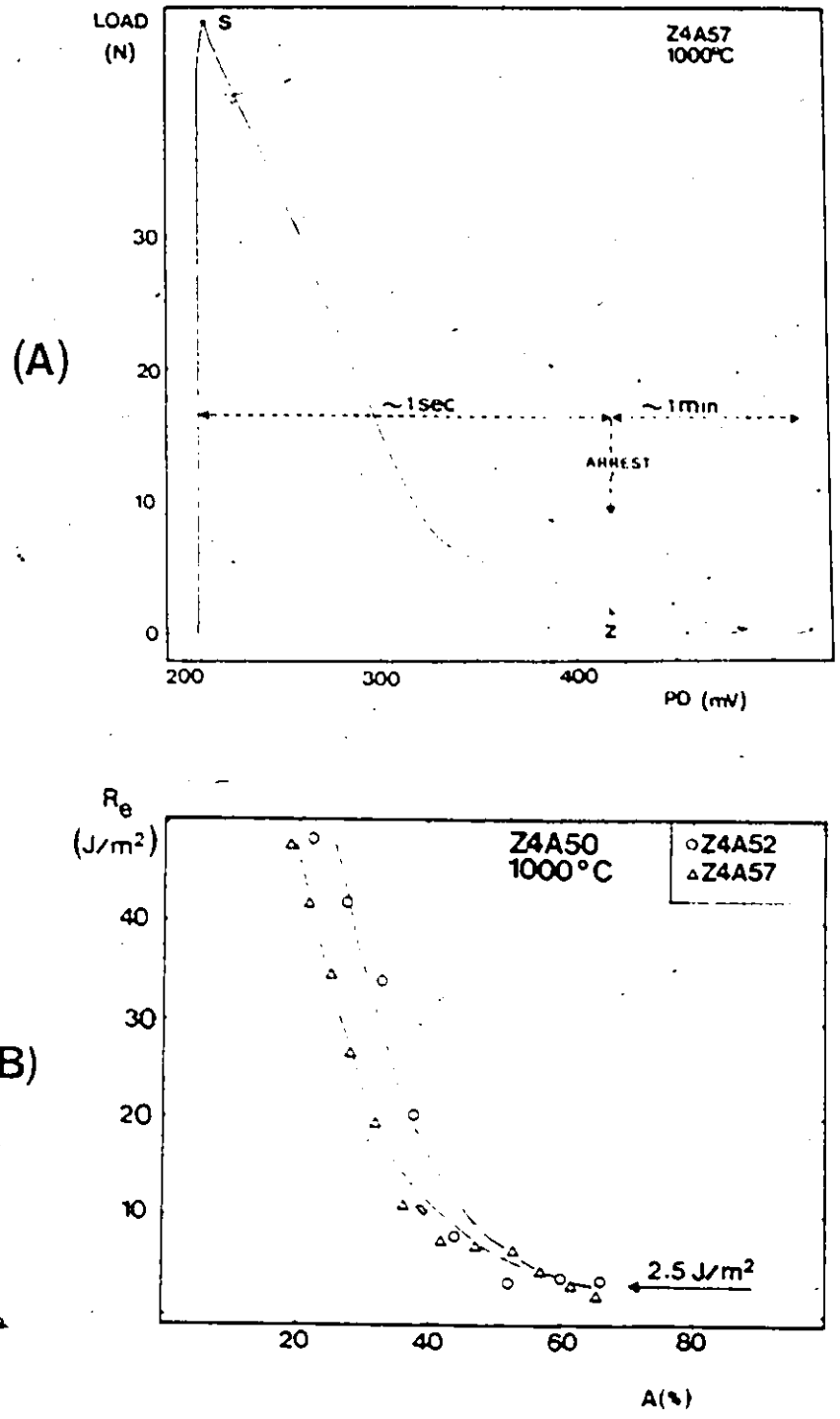

Fig. 5-59 Fracture testing results for Z4A50 type ceramics at 1000°C : (A) Load vs. potential drop record ; (B) Resistance to fracture (two specimens).

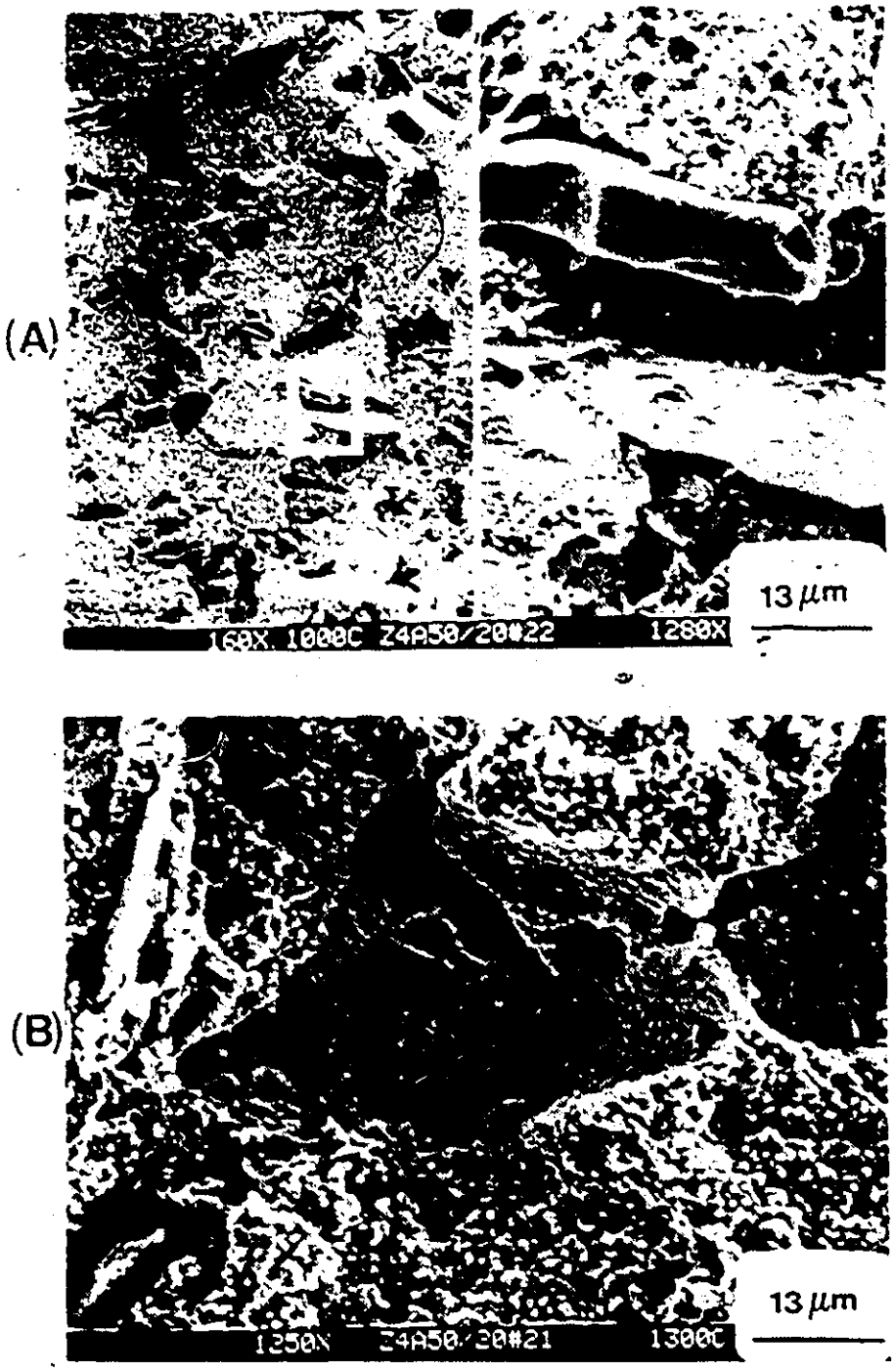

Fig. S-60 Fractography of Z4AS0 composite : (A) Fracture surface at 1000°C ; (B,C) Particles pull-out at 1300°C ; (D) Crack-particle interaction at 1300°C.

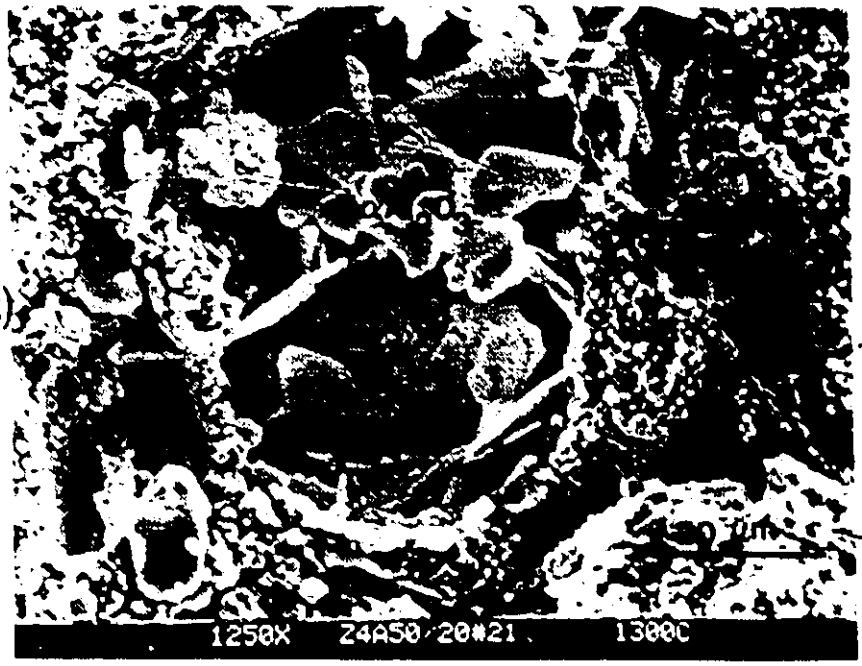

Fig. 5-60 Continued

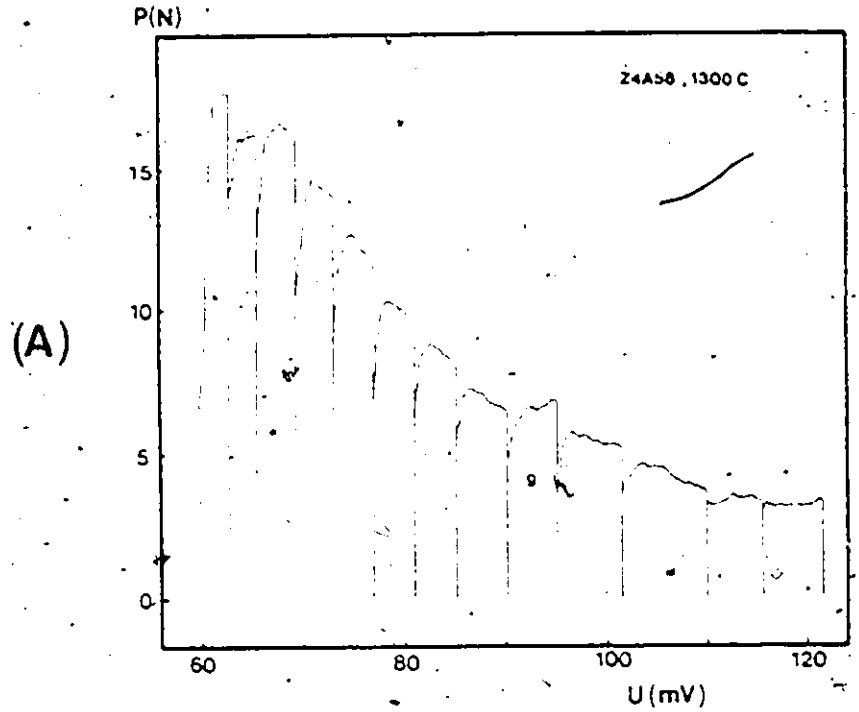

(A)

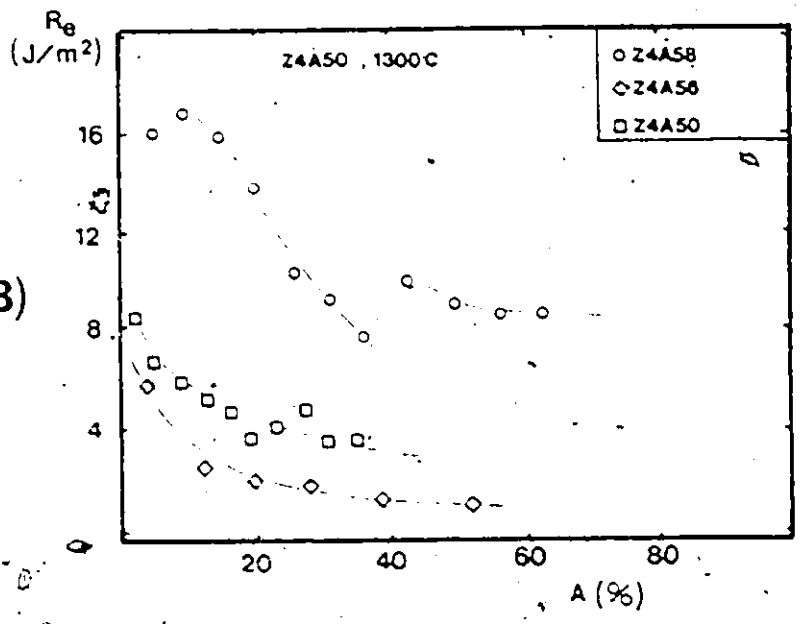

(B)

Fig. 5-61 Fracture testing results for Z4A50 type ceramics at 1300°C : (A) Load vs. potential drop record ; (B) Resistance to fracture (three specimens).

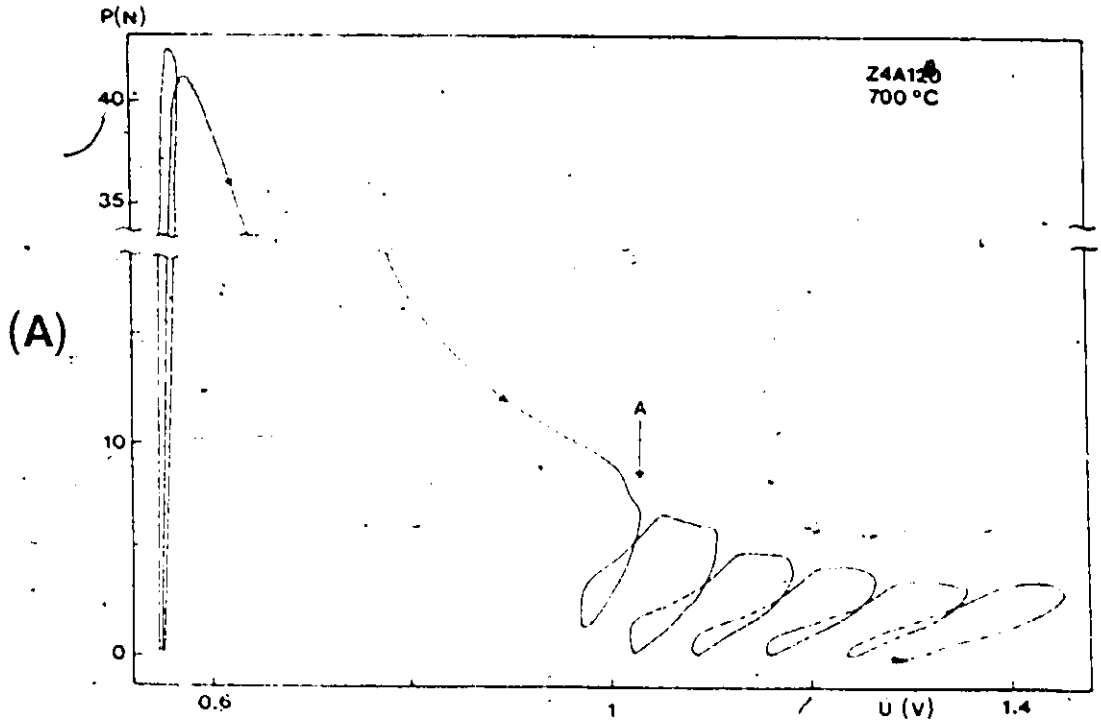

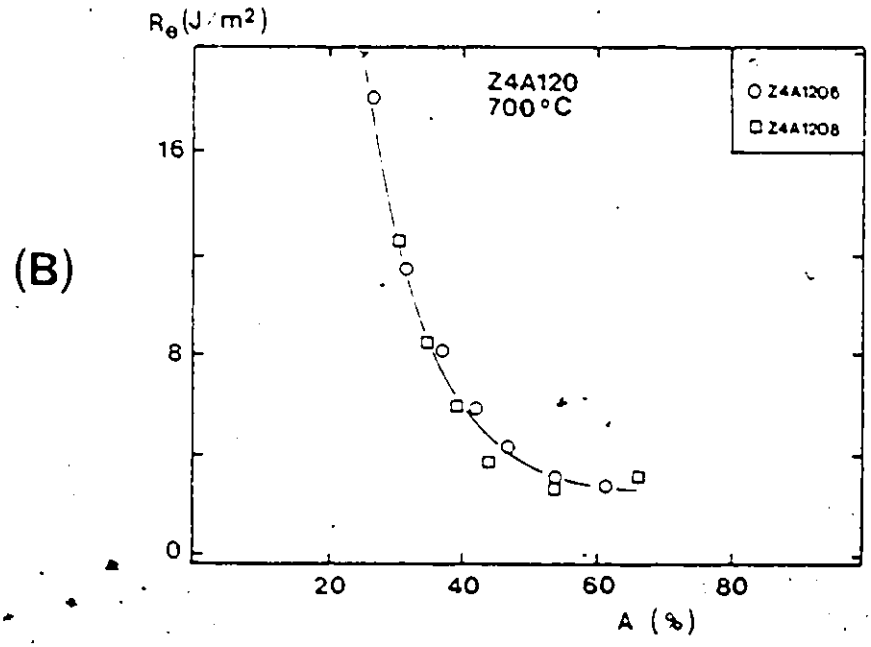

Fig. 5-62 Fracture testing results for Z4A120 type ceramics at 700°C : (A) Load vs. potential drop record (i=1 mA) ; (B) Resistance to fracture (two specimens).

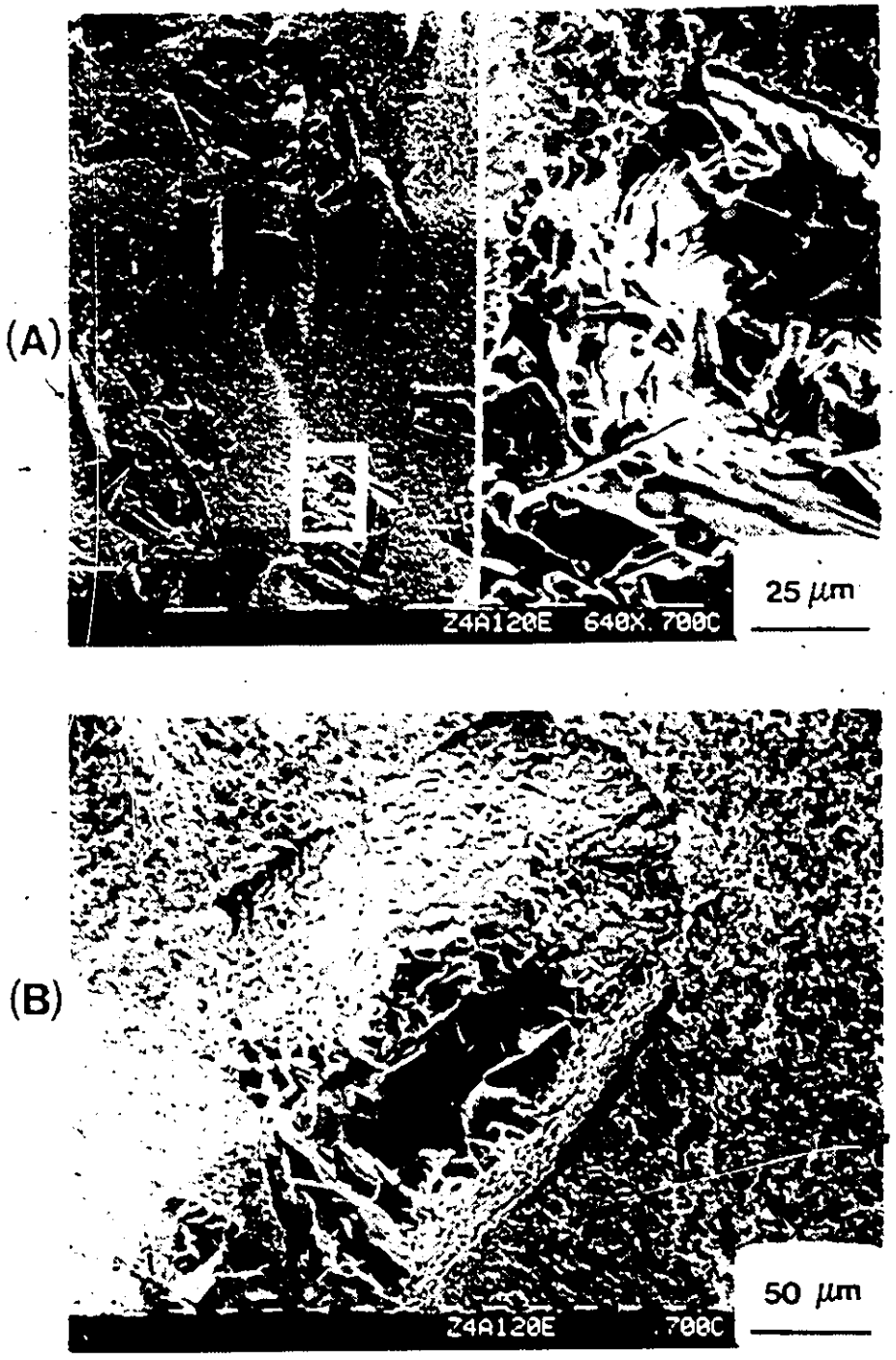

Fig. 5-63 (A,B) Fracture surface of Z4A120 composite at 700°C.

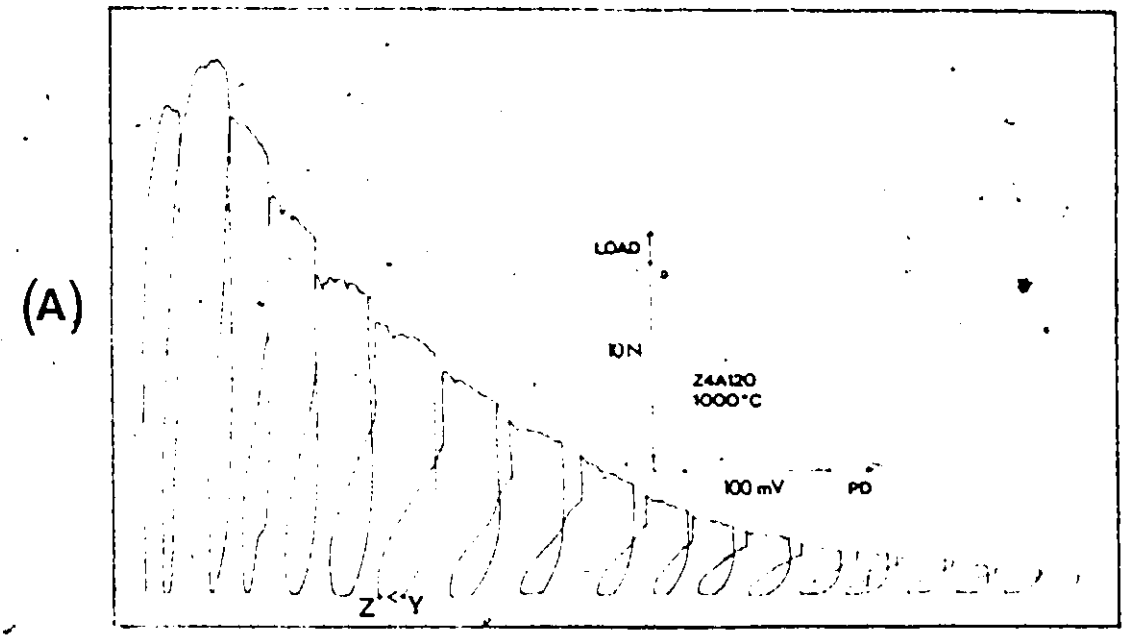

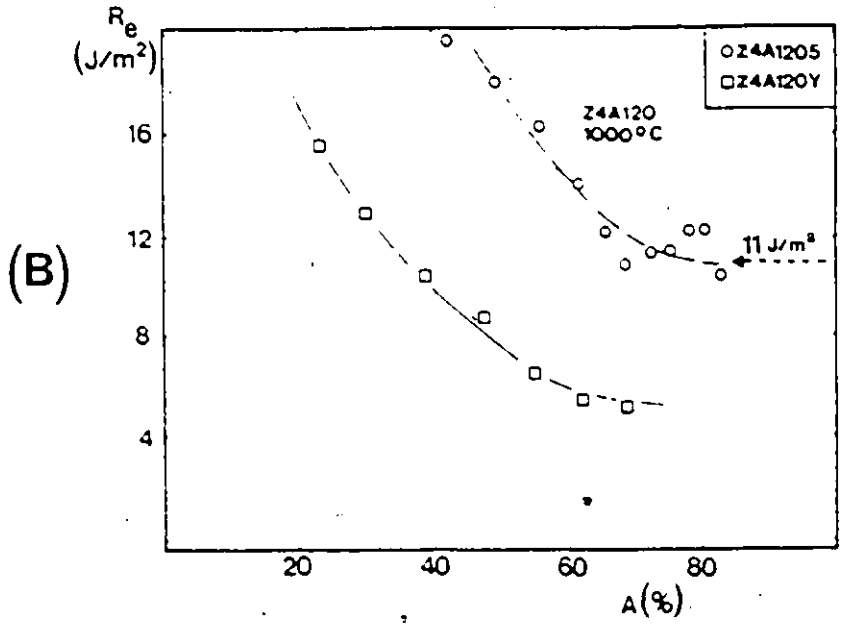

Fig. 5-64 Fracture testing results for Z4A120 type ceramics at 1000°C : (A) Load vs. potential drop record ; (B) Resistance to fracture (two specimens).

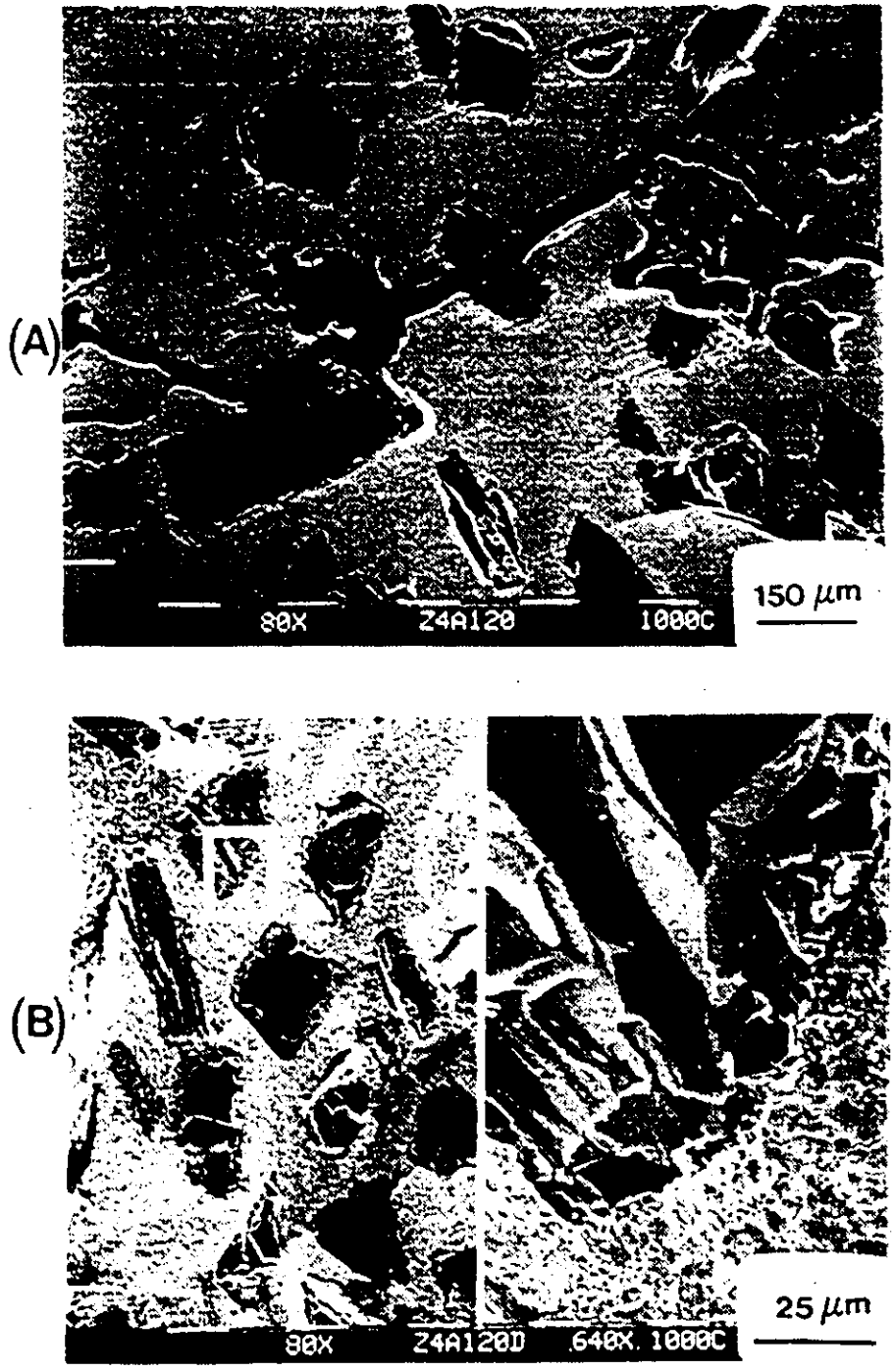

Fig. 5-65 Fractography of Z4A120 composite tested at 1000°C : (A) Arrested crack ; (B) Fracture surface.

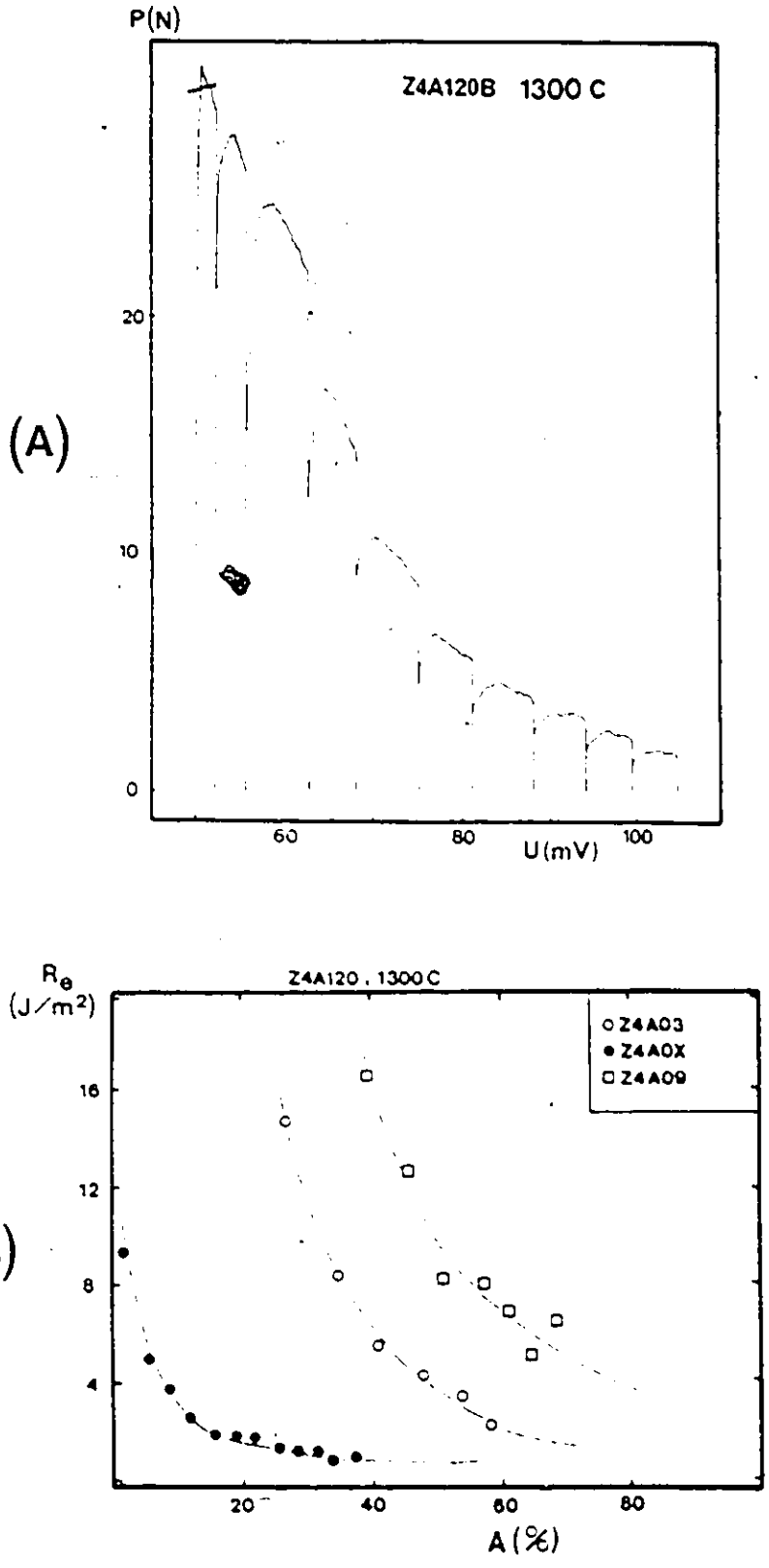

Fig. 5-66 Fracture testing results for Z4A120 type ceramics at 1300 °C : (A) Load vs. potential drop record ; (B) Resistance to fracture (three specimens).

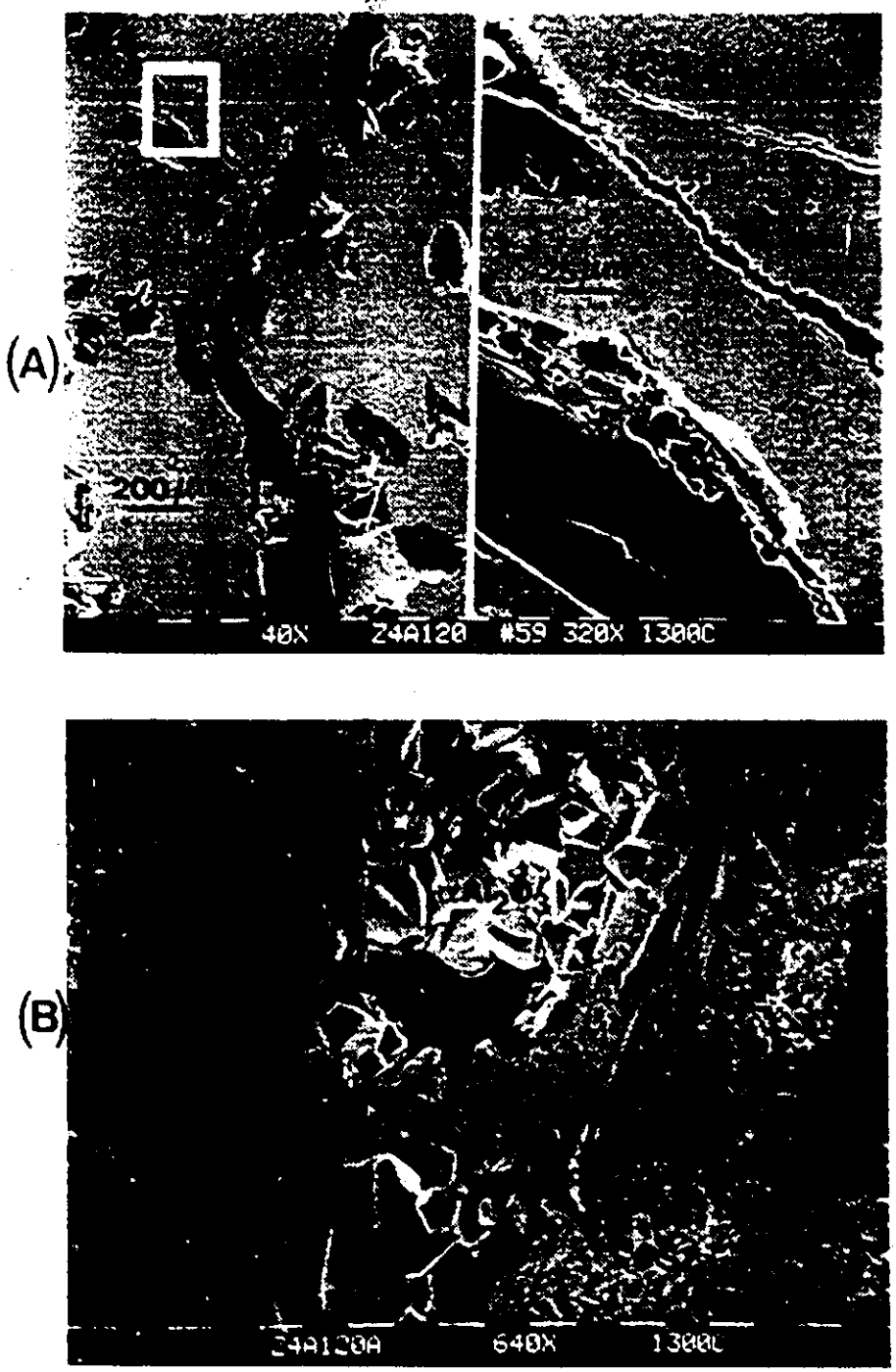

Fig. 5-67 Fractography of Z4A120 composite tested at 1300°C : (A) Arrested crack ; (B) Fracture surface.

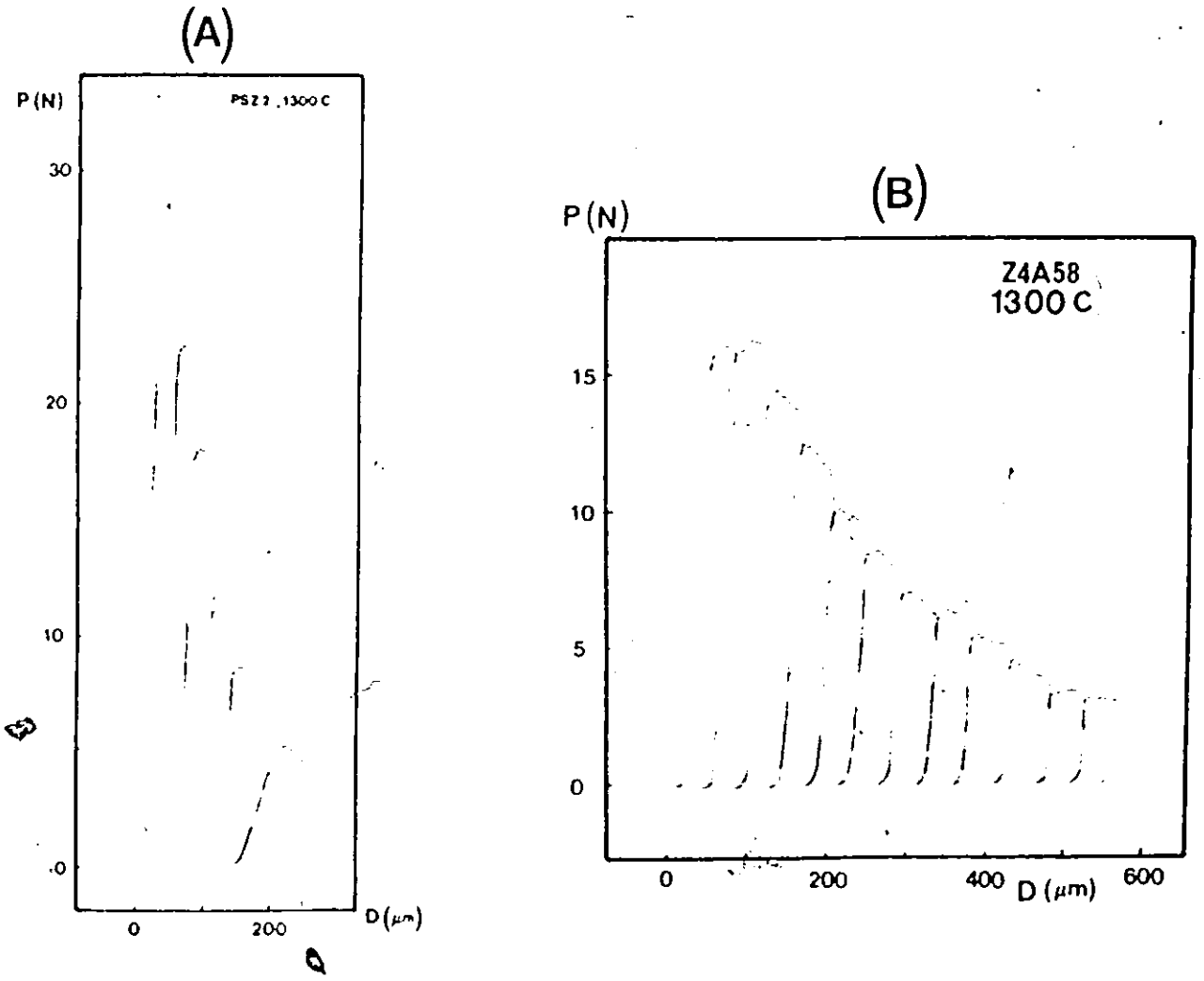

Fig. 5-68 Determination of the nonelastic energy dissipation rate, R_n, at 1300 °C : load-displacement graphs for PSZ (A) ; Z4A50 (B) and Z4A120 (C) ; (D) R_n compiled for seven specimens.

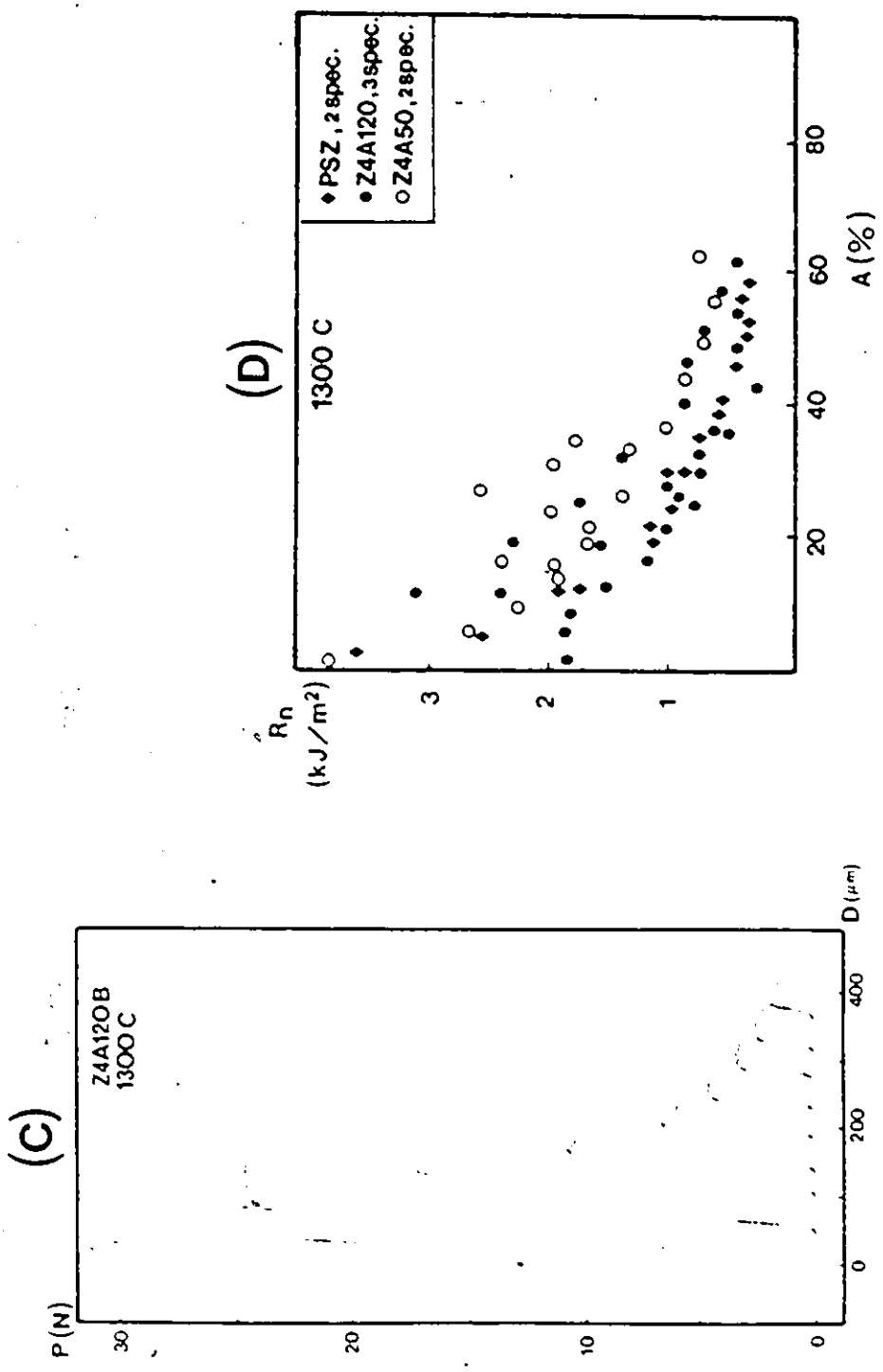

Fig. 5-68 Continued

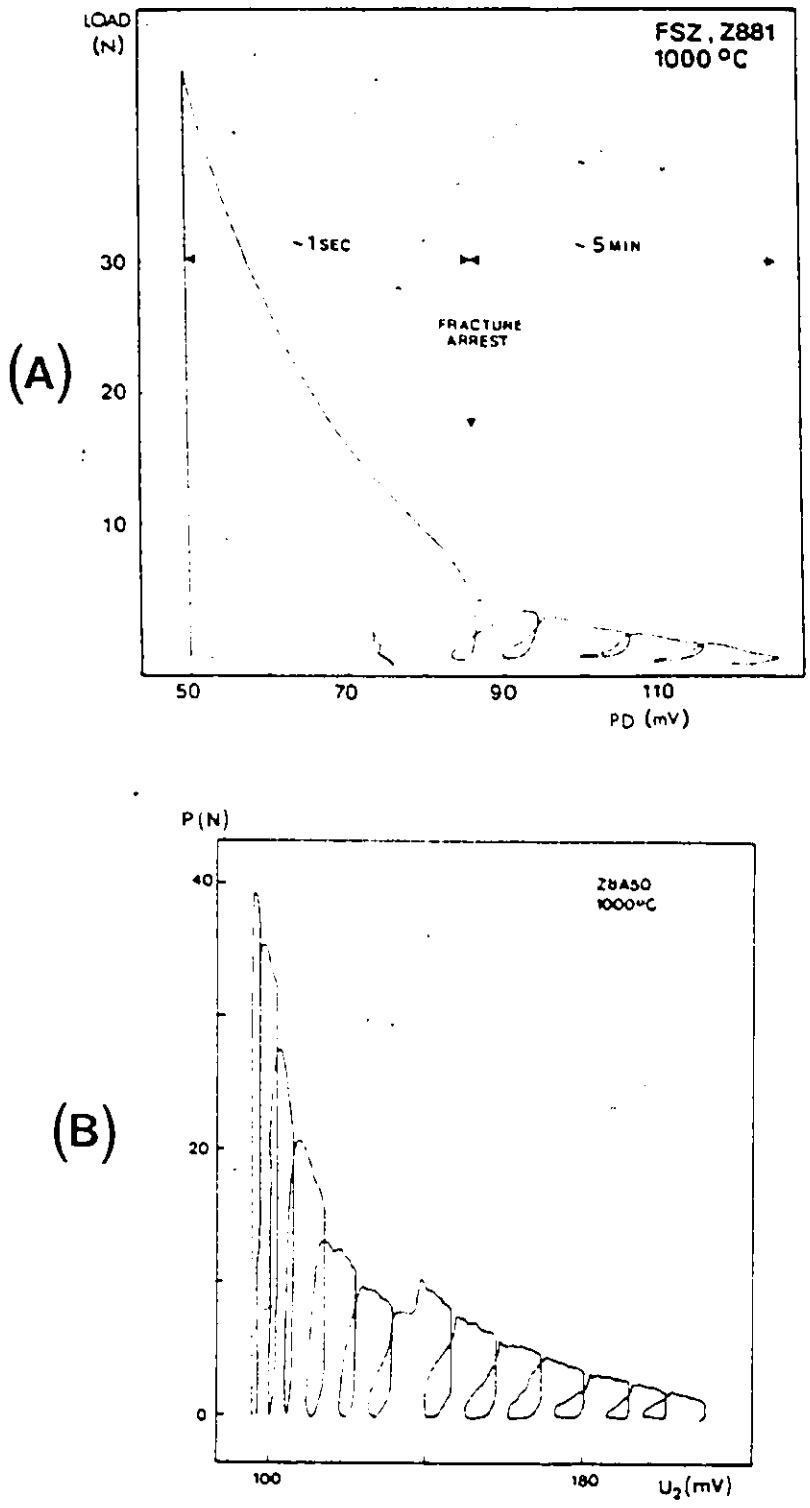

Fig. 5-69 Load against potential drop at 1000 °C for FSZ (A) and Z8A50 (B).

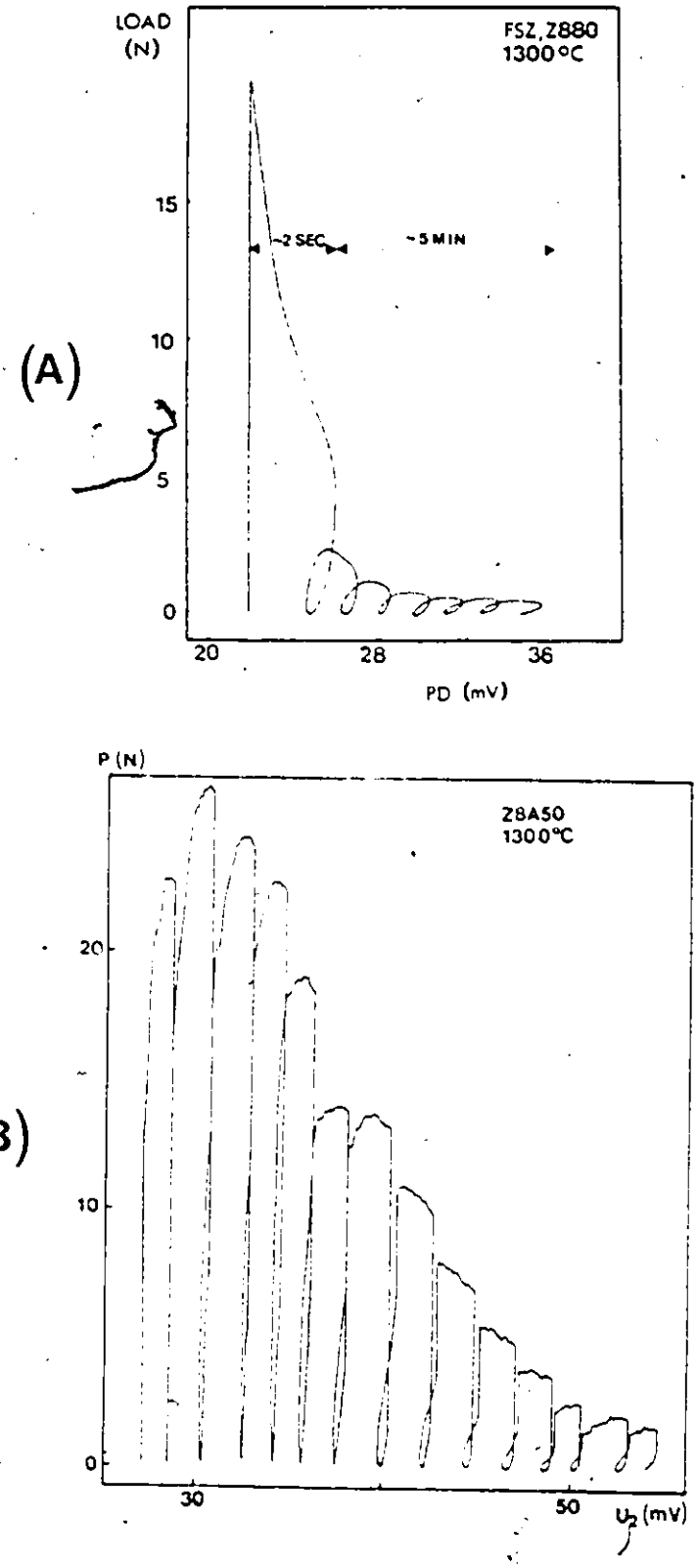

Fig. 5-70 Load against potential drop at 1300 °C for FSZ (A) and Z8A50 (B).

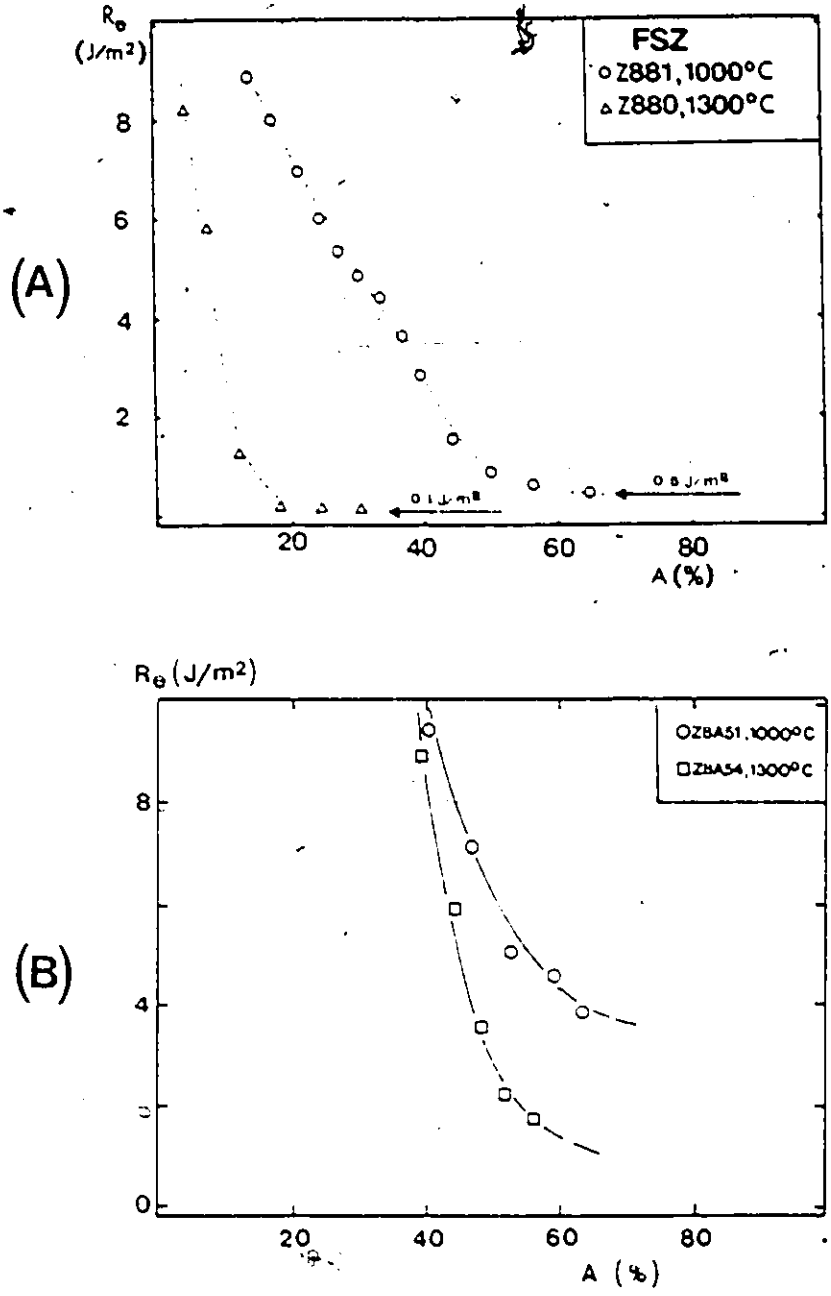

Fig. 5-71 Resistance to fracture at 1000 and 1300°C of FSZ (A) and Z8A50 (B).

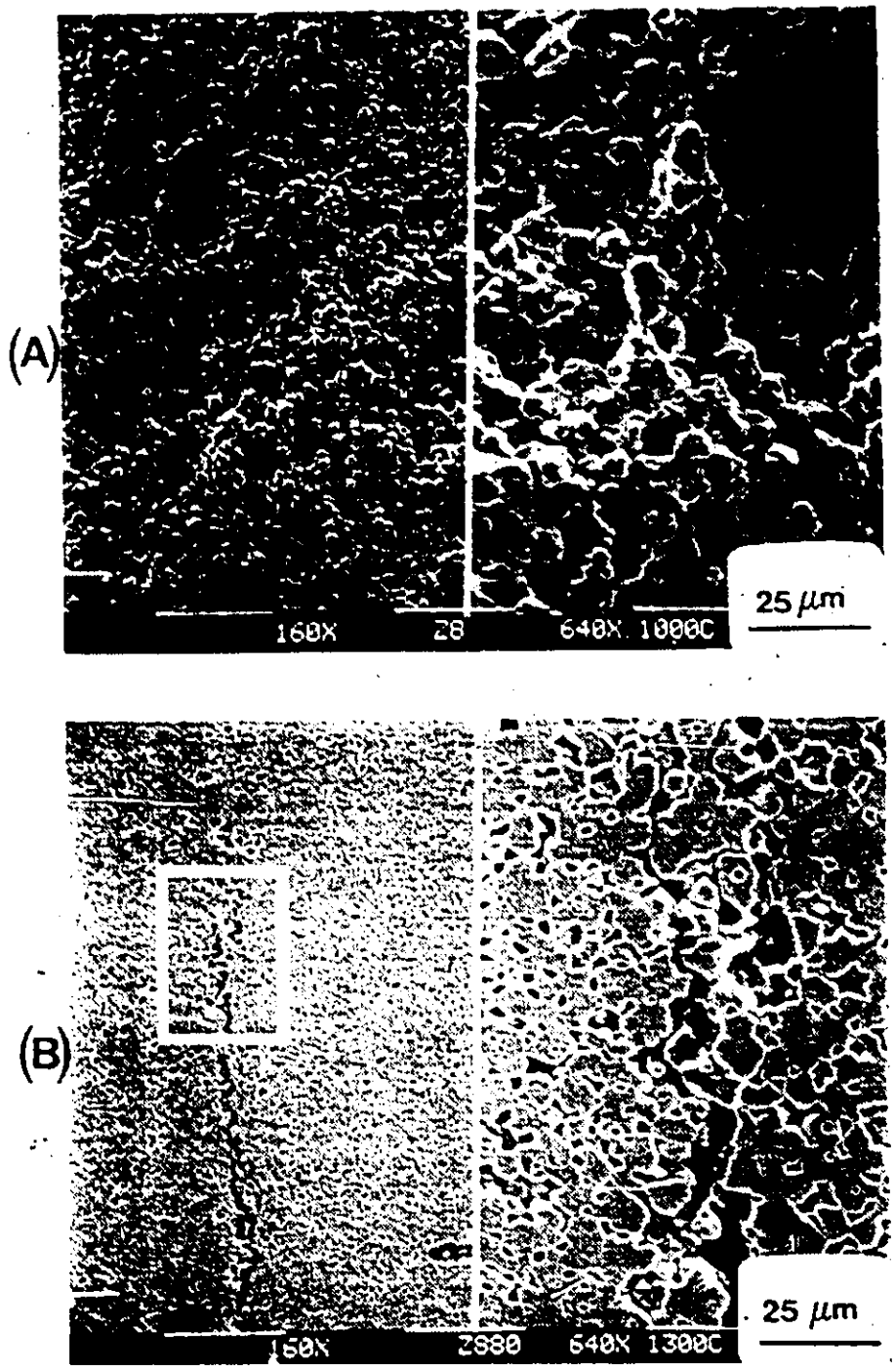

Fig. 5-72 Fractography of FSZ at elevated temperatures : (A) Fracture surface at 1000°C ; (B) Crack arrested at 1300°C.

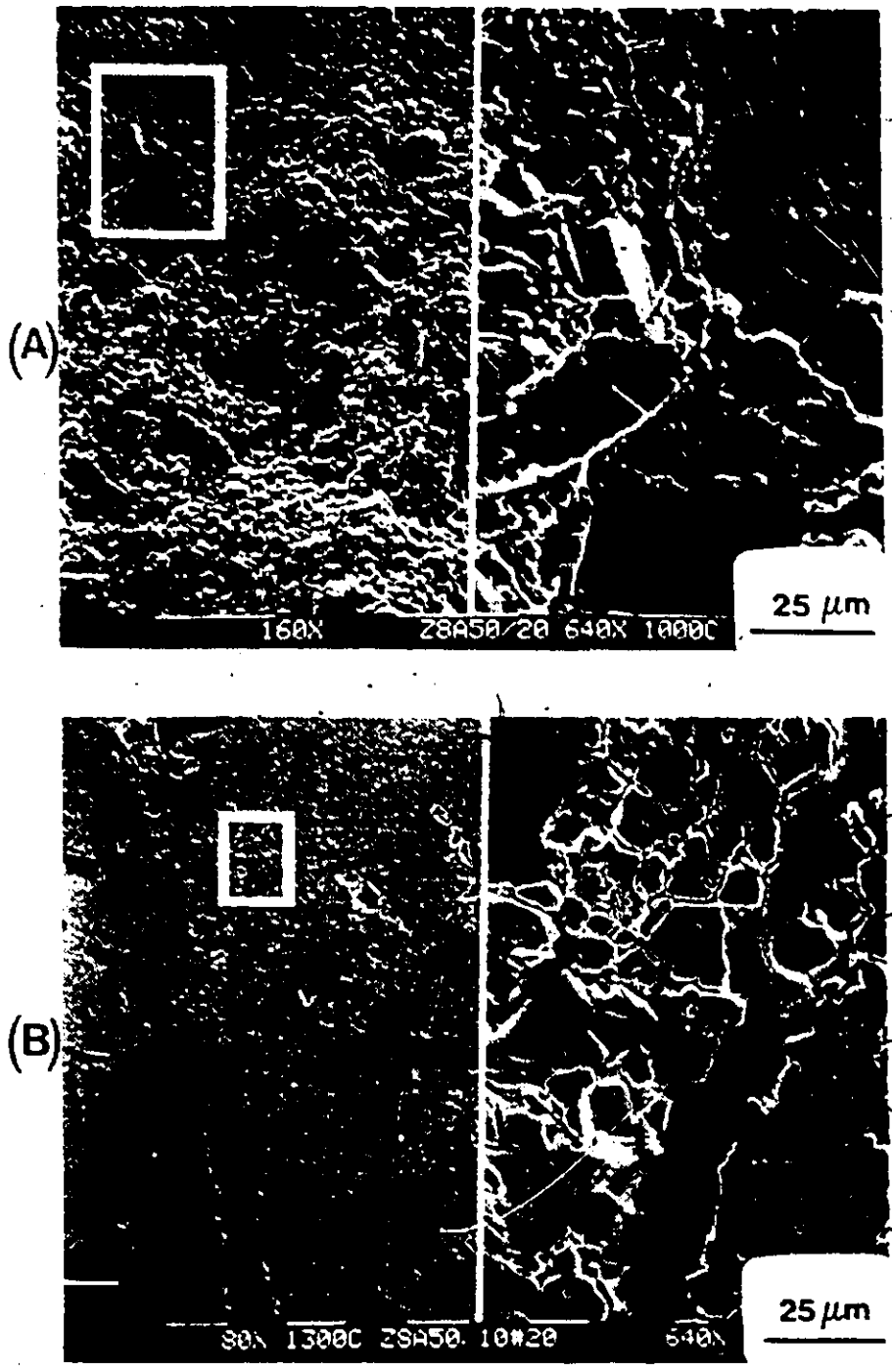

Fig. 5-73 Fractography of Z8A50 at elevated temperatures : (A) Fracture surface at 1000°C ; (B) Crack arrested at 1300°C.